Dissertation

submitted to the

Combined Faculties of the Natural Sciences and Mathematics

of the Ruperto-Carola-University of Heidelberg, Germany

for the degree of

Doctor of Natural Sciences

Put forward by

Oliver Joachim Georg Porth

born in: Frankfurt am Main

Oral examination: November 9$^{\text{th}}$, 2011

Formation of Relativistic Jets: Magnetohydrodynamics and Synchrotron Radiation

Referees: Priv. Doz. Dr. Christian Fendt
Prof. Dr. Max Camenzind

Zusammenfassung

In der vorliegenden Arbeit werden speziell-relativistische magnetohydrodynamische Simulationen in Verbindung mit Synchrotron-Strahlungstransport benutzt, um die Entstehung relativistischer, kollimierter Plasmaströmungen (Jets) zu untersuchen. Unsere Ergebnisse belegen das Paradigma der magnetischen Selbstkollimation auch im relativistischen Fall. Im ersten Teil der Arbeit untersuchen wir Plasmaströmungen ausgehend von heißen, rotierenden Akkretionsscheibenkoronen. Wir erhalten quasi-stationäre, gut kollimierte aber nur schwach relativistische Jets. Im Vergleich zu nicht-relativistischen Scheibenwinden führt die relativistische Feldlinienrotation zu einer reduzierten Effizienz der Beschleunigung und Kollimation. Im zweiten Teil untersuchen wir elektromagnetisch dominierte Strömungen mit unterschiedlichen elektrischen Stromverteilungen. Indem wir der Strömung über 3000 Schwarzschildradien weit folgen, erhalten wir hoch-relativistische Jets, mit Lorentzfaktoren $\Gamma \gtrsim 8$ und halb-Öffnungswinkeln unter 1°, die als dynamische Modelle für Jets von aktiven Galaxienkernen auf Parsec-Skalen dienen. Wir verwenden die magnetohydrodynamische Jet-Struktur der quasi-stationären Simulationsmodelle, um den relativistischen Synchrotron-Strahlungstransport zu berechnen. Im Ergebnis erhalten wir synthetische Strahlungskarten und Polarisationsmuster, die mit hochaufgelösten Radio- und (Sub-)mm-Beobachtungen naher aktiver Galaxienkerne verglichen werden können. Die relativistische Geschwindigkeit und die helikalen Magnetfelder des Jet-Entstehungsgebiets prägen die beobachtete Polarisation und Faraday-Drehung. Insbesondere verraten Asymmetrien der Polarisationsrichtung die Händigkeit der magnetischen Helix und dadurch den Drehsinn des zentralen Körpers. Schließlich zeigen wir erste Ergebnisse von dreidimensionalen, hochaufgelösten Simulationen der Jet-Entstehung; dabei wird adaptive Gitterverfeinerung angewendet. Die elektrische Ladungstrennungskraft, die durch relativistische Feldlinienrotation induziert wird, wirkt der magnetischen Lorentzkraft entgegen, so dass wir eine erhöhte Stabilität relativistischer Strömungen erhalten. Entsprechend saturieren nichtaxialsymmetrische Störungen der Feldlinienfußpunkte schnell entlang des Jets und keine Anzeichen von erhöhter Dissipation oder Unterbrechung der Strömung nahe der Ausstoßstelle sind beobachtet.

Abstract

In this thesis, the formation of relativistic jets is investigated by means of special relativistic magnetohydrodynamic simulations and synchrotron radiative transfer. Our results show that the magnetohydrodynamic jet self-collimation paradigm can also be applied to the relativistic case. In the first part, jets launched from rotating hot accretion disk coronae are explored, leading to well collimated, but only mildly relativistic flows. Beyond the light-cylinder, the electric charge separation force balances the classical trans-field Lorentz force almost entirely, resulting in a decreased efficiency of acceleration and collimation in comparison to non-relativistic disk winds. In the second part, we examine Poynting dominated flows of various electric current distributions. By following the outflow for over 3000 Schwarzschild radii, highly relativistic jets of Lorentz factor $\Gamma \gtrsim 8$ and half-opening angles below 1° are obtained, providing dynamical models for the parsec scale jets of active galactic nuclei. Applying the magnetohydrodynamic structure of the quasi-stationary simulation models, we solve the relativistically beamed synchrotron radiation transport. This yields synthetic radiation maps and polarization patterns that can be used to confront high resolution radio and (sub-) mm observations of nearby active galactic nuclei. Relativistic motion together with the helical magnetic fields of the jet formation site imprint a clear signature on the observed polarization and Faraday rotation. In particular, asymmetries in the polarization direction across the jet can disclose the handedness of the magnetic helix and thus the spin direction of the central engine. Finally, we show first results from fully three-dimensional, high resolution adaptive mesh refinement simulations of jet formation from a rotating magnetosphere and examine the jet stability. Relativistic field-line rotation leads to an electric charge separation force that opposes the magnetic Lorentz force, such that we obtain an increased stability of relativistic flows. Accordingly, the non-axisymmetric modes applied to the field-line foot-points saturate quickly, with no signs of enhanced dissipation or disruption near the jet launching site.

Contents

Conventions

- Throughout, we will follow the convention that Greek indices used for four-tensors run from 0 to 4.
- Latin indices used for three-space range from 1 to 3.
- In addition, Einstein's sum convention for equal indices is used.
- The signature of the Minkowski metric is (-,+,+,+).
- Vectors are typeset **boldface**
- Gauß CGS units are used for all physical quantities with rare exceptions that are specified explicitly.

Acknowledgements

I would like to express my dearest gratitude to my supervisor Christian Fendt who treated all my minor and major concerns with the highest priority. I thank him for support in every possible way and for showing interest and insight in uncounted motivating discussions. I am grateful for having an excellent colleague, Bhargav Vaidya, with whom I cracked many numerical and physical nuts, on the blackboard, the whiteboard and the plain grid of the wall. It also has been a great pleasure to work with Somayeh Sheiknezami, I am deeply thankful for her curiosity and trust. To my collaborators in Leuven and Paris, Zakaria Meliani, Christophe Sauty and Rony Keppens, I would like to express my gratitude for sharing ideas and future plans – and in particular for letting me be part of the plans.

I express my gratitude to Klaus Meisenheimer and Max Camenzind for being part of my thesis committee and for advice during the early phase of this work. I acknowledge a fellowship by the International Max Planck Research School (IMPRS) and especially thank Hans-Walter Rix for the additional financial support of my travels to unconventional places, such as Nepal.

For being great office mates I give credit to Tessel van der Laan and Natalie Raettig, thanks for sharing a desk with me (twice). I am happy to thank the entire fourth IMPRS *(lost-/party-)* generation for being a great community; it has been a pleasure! In particular, I enjoyed the daily lunch and table soccer with Gisella de Rosa, Mario Gennaro, Mauricio Cisternas and Kasper Borello Schmidt. Thanks guys!

At last I may think of the ones closest to my heart of which Fanny is the first. You always succeed to dispel my doubts and bring me down to earth when I am lost in thought. Thank you for being wonderful! With deep gratitude I thank my parents Rita and Wolfgang for believing in me also during the last years of studies. This is for you.

Chapter 1

Introduction

Collimated supersonic flows are observed in numerous astrophysical contexts. These *jets* emerge as an accompaniment of the accretion process in the formation of stars as well as in black hole systems. Launched from the vicinity of a black hole, jets can be accelerated to highly *relativistic* velocities and remain collimated for a tremendous spatial range.

1.1 Astrophysical Jets

The first documented visual observation of an astrophysical jet was the outflow of the young star TTauri, performed at the Lick observatory by Burnham (1890). For half a century the fuzzy nebulae in star-forming regions lay at rest until they kindled the interest of Herbig and Haro in the 1950's. Nowadays, the jets of Herbig-Haro objects are recognized as an ubiquitous phenomenon of star formation (Fig. 1.1; for a historical overview, see Reipurth & Heathcote 1997). The collimated outflows can extend from 100 AU to 10^6 AU away from the central star with velocities up to $500\,\mathrm{km\,s^{-1}}$ (e.g. Bally 2007).

Curtis (1918) was the first to observe a relativistic jet as “a curious straight ray” emanating from the center of the giant elliptical galaxy M87. Other than the stellar jets which emit radiation in shock-heated (forbidden) molecular lines, relativistic jets are seen as a featureless power-law spectrum. This fact and the high degree of linear polarization, which can obtain values of $\sim 30\%$, strongly suggest the synchrotron process as emission mechanism of the radio and optical flux (e.g. Meisenheimer & Roeser 1986). In conclusion, the presence of a magnetic field can be inferred, furthermore, it is now well established that magnetic fields even play a major role in the jet phenomenon. The manyfold appearance active galactic nuclei (AGN) and the associated jets will be reviewed in detail in section 1.2.

Relativistic jets within the galaxy were first recognized by Mirabel & Rodríguez

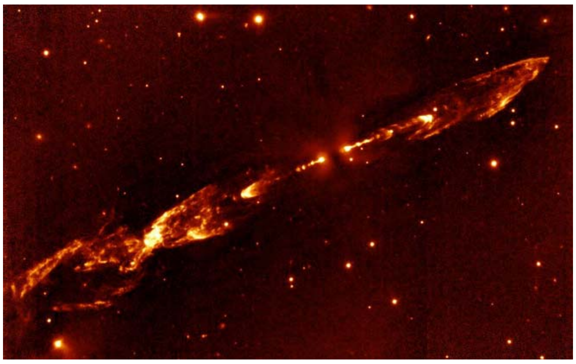

Figure 1.1 *left:* False color image of HH 47 (adapted from Reipurth & Bally (2001)). A bipolar jet plows through a dense star-forming cloud (bok globule). *right:* The pulsed symmetric jet of HH 212 in the H_2 emission line observed by VLT, adapted from Bally (2007); (see Zinnecker et al. (1998), Codella et al. (2007)).

(1994) in the vicinity of X-ray binaries (XRBs). Immediately, the galactic *superluminal* sources were postulated as scaled-down versions of the extragalactic jets discovered in the early days of radio-interferometry, the 1960's. Hence the term

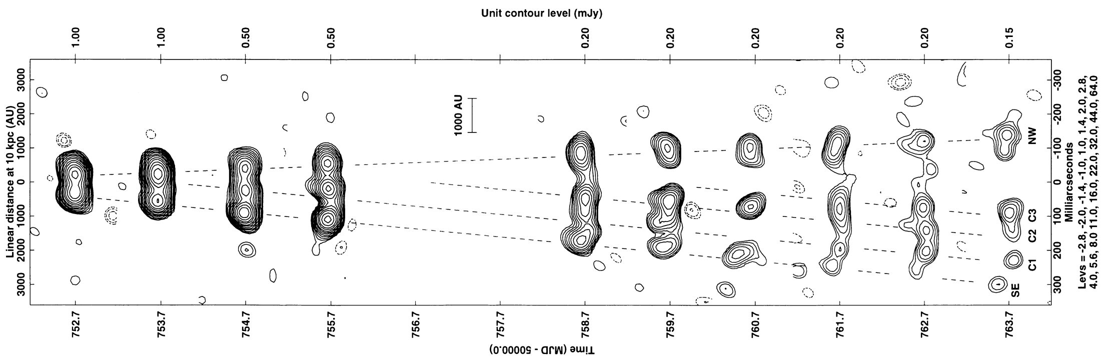

Figure 1.2 Superluminal ejection from the μ-quasar GRS1915+105 (adapted from Fender et al. (1999))

μ-quasar signifies a galactic radio source in the vicinity of a $\sim 10M_\odot$ accreting black hole, contrasting the supermassive black holes $> 10^7 M_\odot$ hosted by quasars or active galactic nuclei (AGN, see section 1.2). The lower mass of the central object also implies a shorter dynamical time-scales and thus processes that take millions of years in quasars are accessible to human perception in μ-quasars. State transitions in the accretion flow are thus observed by weekly variations in the "X-ray-hardness - intensity" relation of XRBs (Belloni et al. 2005). The state of a given XRB does not wander erratically within the hardness-intensity diagram (HID), but performs cycles along clear paths.[1] Customarily, a distinction between

[1]Interestingly the cycles not only occur in black hole systems but also also in accretion flows around neutron stars and white dwarfs (Körding et al. 2008).

two states is made: the low intensity, hard X-ray spectrum state called low/hard and the converse high/soft state (Dhawan et al. 2000). Compact stationary jets are typically observed in the low/hard state while in the high/soft state episodic jets occur (Fender 2001).

For the prototypic source GRS 1915+105, Chaty et al. (1996) and Fender et al. (1999) computed a distance of $12.5 \pm 1.5\,\mathrm{kpc}$ with a mass of the central object of $14.0 \pm 4.4 M_\odot$ (Greiner et al. 2001). Another nearby source is XTE J1550-564 with a black hole of $12 - 15 M_\odot$ and a distance of approximately $5\,\mathrm{kpc}$ (Titarchuk & Shrader 2002; Orosz et al. 2002). μ-quasars are thus closer by approximately three orders of magnitude than the next extragalactic jet of the galaxy Centaurus A at $3.4 \pm 0.15\,\mathrm{Mpc}$ (Israel 1998). However, in terms of Schwarzschild radii (r_S), the highest angular resolution can actually be achieved in an extragalactic jet: originating at the colossal $6.6 \times 10^9 \pm 0.4 M_\odot$ black hole of M87 at a distance of $\sim 16\,\mathrm{Mpc}$ (Gebhardt et al. 2011). High resolution radio observation can thus probe within $\simeq 20 r_\mathrm{S}$ of M87 (Krichbaum et al. 2006; Ly et al. 2007), whereas galactic sources are (un-) resolved far worse by a factor of $\sim 10^5$.

Merloni et al. (2003) suggested a unification of galactic and extragalactic jet sources onto a *Fundamental plane of black hole activity* by connecting the luminosities in the radio and X-ray band with the black hole mass: $\log L_R = (0.6^{+0.11}_{-0.11}) \log L_X + (0.78^{+0.11}_{-0.09}) \log M_\bullet + 7.33^{+4.05}_{-4.07}$. This scheme is very successful in unifying hard state XRBs with low power AGN (Falcke et al. 2004; Markoff et al. 2008) and raises hope that a complete unification, placing the current state of an individual AGN onto its position in the HID cycle, will become possible in the future. The combination of appropriate time resolution in XRBs and sufficient spatial resolution in nearby AGN thus gives a promising vista on the formation of relativistic jets in the universe.

Jets play a key role in the extreme gamma-ray burst (GRB) objects that light up the γ-ray sky for a duration from 10^{-3}s to 10^3s. The energy released by the burst is of the order $10^{51} - 10^{54}\mathrm{erg\,s^{-1}}$, approaching the rest mass of the sun. From causality arguments it follows that the energy must be confined to a volume equal or less than the sun. The nature of these cosmological objects is still mysterious, however, evidence is mounting that the GRB progenitors are massive collapsing or merging stars (Fig. 1.3; see the review by Piran (2004)). Energetics suggests that the burst occurs via internal shocks in a highly collimated flow with strongly beamed emission. Typically, Lorentz factors of $\Gamma \sim 100$ are required to explain the observed spectra. Via fading X-ray and optical afterglow emission, GRBs could be localized within (star-forming) galaxies at cosmological distances (e.g. Fruchter et al. 1999; Price et al. 2003; Gorosabel et al. 2005). GRBs share many properties with the most extreme AGN jets known as TeV-blazars, for example: a synchrotron origin of the radiation, collimated (ultra-) relativistic flows and the emission of γ-rays. This indicates that also GRBs can be understood within the same framework.

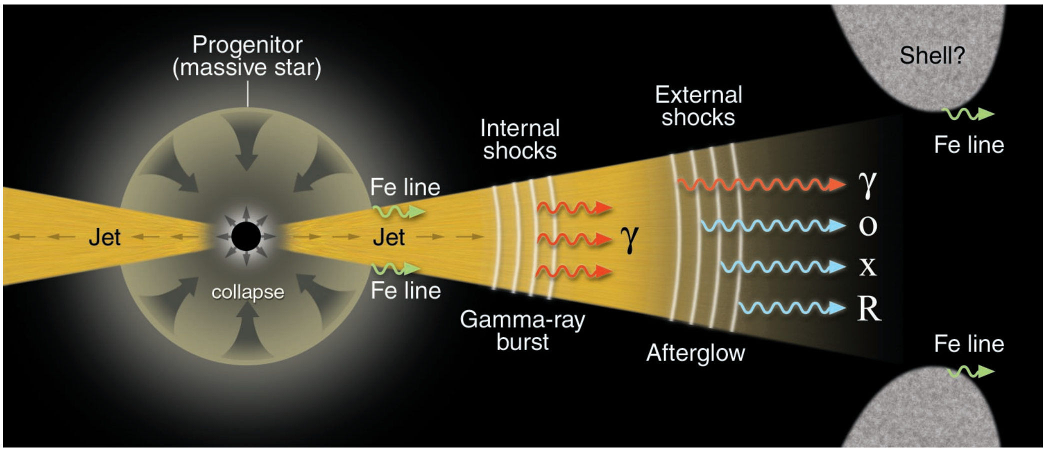

Figure 1.3 Schematic view of a GRB triggered by the collapse of a massive star. Internal shocks within a relativistic jet produce a burst of γ-rays and an external shock with the environment is thought to be responsible for the afterglow emission (adapted from Mészáros (2001)).

Still today, elementary questions posed by relativistic jets are unanswered, these comprise:

- the jet-disk connection and triggering of a jet via state transitions in the disk
- the determination of acceleration and collimation scales (tightly linked to the so-called σ-problem)
- the mechanism of particle acceleration within the jet
- the matter content of the jet and mass-loading
- the details of jet-environment interaction such as entrainment and feedback
- the fundamental question of jet stability

Above all these pressing issues hovers the question of the origin of the astrophysical magnetic field itself.

1.2 Jets in AGN

It is now well established that most galaxies harbor a supermassive black hole (SMBH, $M_\bullet = 10^5 - 10^{10} M_\odot$ e.g. Kormendy & Richstone (1995)) in their center. The energy released by the accretion process onto a black hole leads to an excess of electromagnetic radiation from the galactic core which, in its most dramatic manifestations, can exceed the luminosity of thousand "normal" galaxies (e.g. $\sim 10^{46}\mathrm{erg\,s^{-1}}$). In these AGN, jets can be launched and accelerated to relativistic velocities with Lorentz factors ranging up to $\Gamma \sim 40$ in extreme cases (Jorstad et al. 2005). The majority of AGN jets however has lower Lorentz factors, with at least 83% of the population below $\Gamma = 10$ (Lister & Marscher 1997; Lister et al. 2009).

1.2.1 The AGN Story

In the inventory of the AGN bestiary, objects meet one or more of the following criteria: pointlike central emission, broad-band spectrum, broad emission lines / narrow emission lines, radio loudness, variability and polarization.[2] Unlike any other astronomical object, the electromagnetic radiation from an AGN can be extremely broad-band, in the case of NGC 4151, the almost flat spectrum covers a range of ten orders of magnitude in frequency.

In the radio frequency range, jets radiate via the synchrotron process (see below), thus early radio surveys such as the 3C catalogue by Edge et al. (1959) were highly successful in detecting radio-loud AGN (radio galaxies) or quasi-stellar radio sources known as *quasars*. The high success-rate comes at no surprise, as a large fraction of all bright radio sources in fact are AGN.

The first quasar where a star-like optical counterpart could unambiguously be determined was 3C 48. The unfamiliar blue colors and broad emission lines at unusual frequencies of the 16 magnitude star were a puzzle for the discoverers Matthews & Sandage (1963).

Unusual emission lines in "spiral nebulae" were already reported by Fath (1909) – in retrospect the first documented observation of an AGN. Together with five other "emission line nebulae", Fath's object (now known as NGC 1068) was compiled in Carl K. Seyfert's seminal publication (Seyfert 1943). It led to the class of Seyfert galaxies: characterized by their broad emission lines in high ionization states confined to a small nucleus of the visible host galaxy. Seyferts are the most numerous type of AGN in the local universe, residing in $5 - 10\%$ of all galaxies (e.g. Maiolino & Rieke 1995; Ho et al. 1997), the obscured fraction could even be substantially higher.

It was Maarten Schmidts breakthrough discovery (Schmidt 1963) that connected the peculiar quasars with the emission line galaxies by the realization that the Balmer-series and MgII lines of 3C-273 were shifted by the redshift of $z = 0.158$.

[2]see R. D. Blandford et al. (1990), Peterson (1997) or Krolik (1998) for a full description of the phenomenology.

Quasars thus represent highly luminous galactic nuclei, their cosmological nature makes them valuable tools for the investigation of the history of our universe.

Before the rapid development of optical surveys, most of the known AGN were radio selected and spectroscopically confirmed like 3C-273, hence they fell into the jet featuring radio-loud class. We should however keep in mind that the occurrence of jets is only one part of the AGN story and the intrinsic abundance of radio-quiet objects is 10-30 times higher than radio-loud objects (e.g. Sandage 1965). In contrast to radio selection, optical surveys find both the radio loud and -quiet objects. With the advent of large optical surveys such as the Sloan digital sky survey (SDSS), a run on cosmological AGN has started. Beginning in the year 2000, the SDSS has now (data release 8, Eisenstein et al. (2011)) identified more than 120 000 quasars based on photometric selection and spectroscopic classification. The most distant object discovered this way is a $z = 6.42$ quasar (Fan et al. 2003). Cross correlation with modern radio surveys such as FIRST (Gregg et al. 1996) however proved successful for only $\sim$2000 objects (e.g. Best et al. 2005), while the majority of known sources are now radio-quiet quasars.[3]

For a complete census of active galactic nuclei, also the sources obscured by dust extinction in the host galaxy have to be taken into account. For Compton thin sources, hard X-ray selection (e.g. Sazonov et al. 2007) proves successful as similar to the radio case – starting at $\sim$ 2keV – AGN also dominate the bright X-ray sky (e.g. Della Ceca et al. 2004). Highly obscured AGN re-radiate a part of the absorbed optical and X-ray flux in the mid-infrared due to reprocessing of the nuclear radiation by dust. Thus infrared selection (Grazian et al. 2006) is the key to detect also these well hidden AGN. Ultimately, to establish an inventory of the AGN population along cosmic time demands to exploit the full multi-wavelegth information (e.g. Yan et al. 2011).

One of the major discoveries of the last decade is the tight coupling of black hole mass with the properties of the host galaxy. Over four orders of magnitude in galaxy bulge mass, the black hole mass scales as $M_\bullet \approx 0.002 M_{\mathrm{bulge}}^{1.12\pm0.06}$ with an observed scatter of 0.3dex (Magorrian et al. 1998; Häring & Rix 2004). Also the bulge velocity dispersion is tightly correlated to the black hole mass via the $M_\bullet - \sigma$ relation $M_\bullet \propto \sigma^\beta$ (Gebhardt et al. 2000; Ferrarese & Merritt 2000). As pointed out by Tremaine et al. (2002), the adopted value of β however depends on the measurement systematics and varies between $3.75 - 5.3$.

The tight correlation of two entities separated by at least six orders of magnitude in spatial scale has motivated the postulation of a feedback mechanism

[3]Today, the term quasar is mostly used synonymously for "high luminosity AGN with broad optical and UV emission lines" and sometimes also for "generic AGN". In this sense, a radio-quiet quasar is not an oxymoron – a more common notation for these objects is however "QSO".

between black hole growth and the star formation rate (Silk & Rees 1998). Also to explain the demography of massive black holes in the local universe – the puzzling "downsizing", first described by Cowie et al. (1996) – a negative feedback mechanism breaking the hierarchical build-up can be employed (Granato et al. 2001; Quilis et al. 2001). Powerful radio jets have been proposed to provide such a feedback loop by disturbing the intergalactic cooling flows (McNamara et al. 2000; Di Matteo et al. 2005). On the other hand, jets could in principle also lead to positive feedback, whereby the jet cocoon pressure compresses the interstellar medium to trigger star formation (Klamer et al. 2004; van Breugel et al. 2004). However, on the whole the effect is now believed to decrease the star formation rate (Antonuccio-Delogu & Silk 2008). While a very appealing scenario, the feedback mechanism should be regarded with caution, as also a purely non-causal origin of the correlations could prevail. In hierarchical growth scenarios, statistical convergence following the central limit theorem can thus also account for the observed correlations in the present universe (Peng 2007; Hirschmann et al. 2010; Jahnke & Macciò 2011).

1.2.2 Radio Jets

As a qualitative measure of the jet power, the radio-loudness has become a standard diagnostic. It is defined via the ratio of luminosities at a given radio frequency to the optical B-band: $\mathcal{R} \equiv L_{\mathrm{R}}/L_{\mathrm{B}}$. With an increasing number of black hole mass estimates, it became possible to relate the radio-loudness to the normalized accretion rate $\lambda \equiv \dot{M}/\dot{M}_{\mathrm{Edd}}$ (Ho 2002; Sikora et al. 2007); Figure 1.4. It shows that jets are more common for low Eddington ratios and additionally, features a bimodality of jet power depending on source morphology. While the authenticity of the dichotomy is highly debated (e.g. Strittmatter et al. 1980; Sramek & Weedman 1980; Sikora et al. 2007) as it could also result from selection effects (Singal et al. 2011; Broderick & Fender 2011), the implications are intriguing: It hints to the existence of a third parameter next to the Eddington ratio and black hole mass to determine the jet power. The dimensionless black hole angular momentum or *spin* parameter a is a natural choice, which led to the *spin paradigm* proposed by Wilson & Colbert (1995). Taking into account the spin history due to episodic accretion events leading to low spins (predominantly in late-type Seyferts) and major mergers leading to high spins (giant ellipticals), the spin paradigm can be quite successful in reproducing the observed radio phenomenology (e.g. Fanidakis et al. 2011). Though mostly attributed to the jet power due to the Blandford &

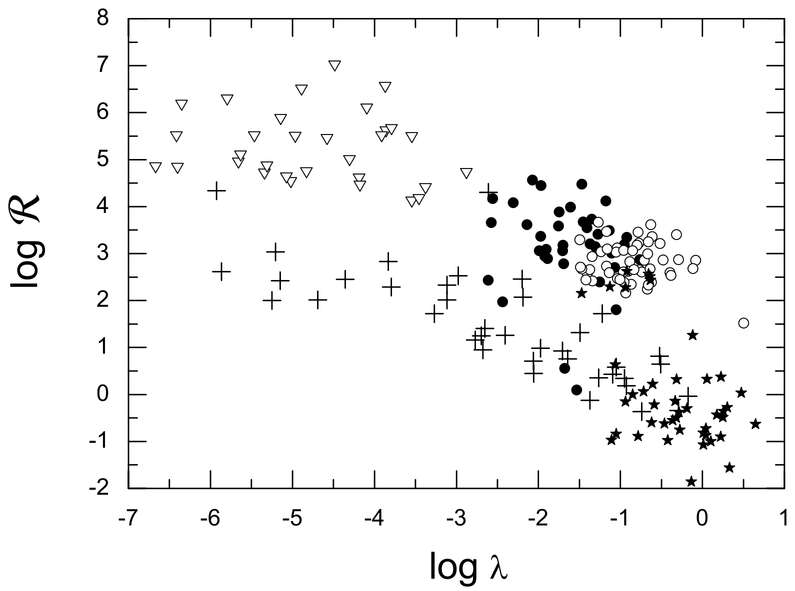

Figure 1.4 The apparent dichotomy in (total) radio-loudness $\mathcal{R}$ against Eddington ratio λ for various morphologies: BLRGs are marked by filled circles, radio loud quasars by open circles, Seyfert galaxies and LINERs by crosses, FR I radio galaxies by open triangles, and PG quasars by filled stars (adopted from Sikora et al. (2007)).

Znajek (1977) process

$$L_{\rm jet} \simeq 10^{42} \left(\frac{B_p}{3{\rm KGauss}}\right)^2 \left(\frac{M_\bullet}{10^8 M_\odot}\right)^2 a^2\,{\rm erg\,s^{-1}} \qquad (1.1)$$

(see Tchekhovskoy et al. (2010a) for a more general formulation) also for relativistic jets launched from the inner region of the accretion disk, the spin can have a governing influence. For example, the black hole spin determines the location of the innermost stable circular orbit (ISCO) and therefore the maximum rotational velocity of the disk. Observationally, the spin paradigm had to suffer some recent setbacks as in addition to the disputed radio power dichotomy, also in galactic XRBs no correlation between the jet power and spin estimates could be found so far (Fender et al. 2010). Evidence is mounting that the radio loudness and jet formation process could also depend on other factors such as the state of the accretion disk or the nuclear gas environment.

A great advantage of radio observations of jets is the unmatched resolution obtainable with interferometry. Radio interferometric imaging of jets often shows extended structure on the Kpc to Mpc scale, so called lobes (Fig. 1.5). To quantify the lobe morphology, Fanaroff & Riley (1974) measured the distance of the two brightest features in terms of the overall source size. This lead to the FR classification where FR1 sources have size ratios less than 0.5 while FR2 sources are extended

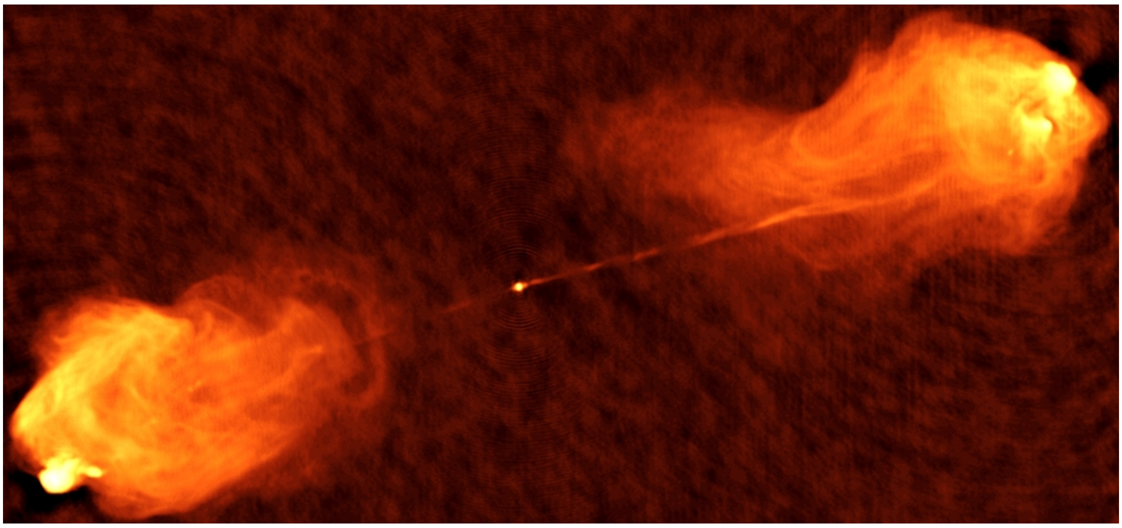

Figure 1.5 Radio image of the extragalactic radio source Cygnus A with lobes, hot spots, jet and core. The linear extent of the source is $\simeq$ 120Kpc (image courtesy of C. L. Carilli (Carilli & Barthel 1996)).

with ratios greater than 0.5. Fanaroff & Riley (1974) already realized that their classification is correlated with the radio luminosity, where FR2 sources feature higher luminosities than FR1s. The original classification, based on the 3CR catalogue with a frequency of 178Mhz, sets the dividing line at $\approx 2 \times 10^{25}\mathrm{W\,Hz^{-1}\,sr^{-1}}$, hence quasars are FR2 sources. Later it was realized that the division is also a strong function of the optical luminosity of the host galaxy (e.g. Ledlow & Owen 1996). This dependence is generally seen as the influence of the galactic environment on the jet deceleration (e.g. De Young 1993), but also jet-intrinsic mechanisms are proposed (e.g. Baum et al. (1995), also Meliani & Keppens (2009)).

The jet formation region can be probed with very large baseline interferometry (VLBI) reaching resolutions of milliarcseconds to the *parsec scale* or less. Even with VLBI, the *core* region appears as an unresolved blob which often shows an extension generally aligned with the large scale features, the *core-jet* (Figure 1.6). Unlike the lobe emission which is mostly two-sided (FR2) or isotropic (FR1), the core-jet is almost always one-sided which is interpreted in terms of relativistic beaming (see below).

To overcome the noise-level in VLBI observations, a brightness temperature for the cores of least 10^{10}K is required. The very fact that VLBI is possible for a large number of sources is thus a first indication for the non-thermal emission of jets. For sources dominated by the core emission, the radio-spectrum is typically flat in F_ν in contrast to the steep spectrum $F_\nu \propto \nu^{-\alpha}$ ($0.5 \lesssim \alpha \lesssim 1$) of lobe dominated sources (e.g. Tornikoski et al. 1993).

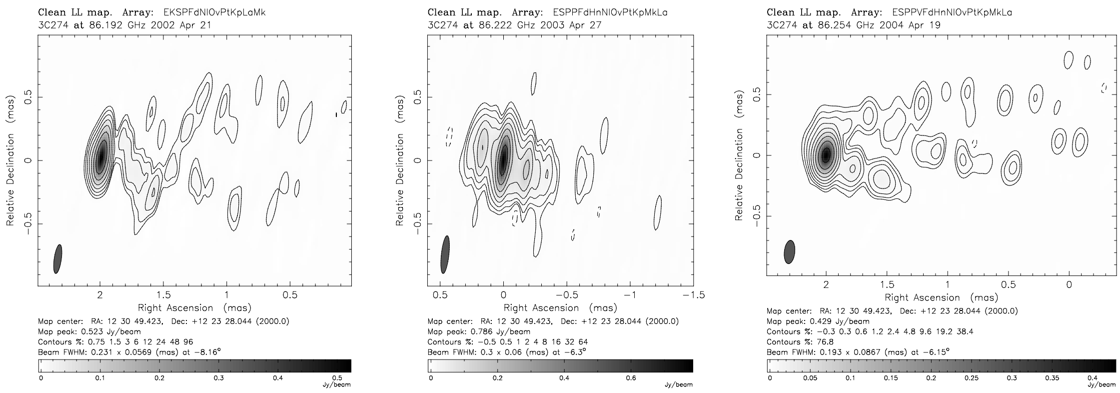

Figure 1.6 86GHz observations of the M87 core with a resolution of 27.8 Schwarzschild radii. A counter-jet appears in the 2003 image, however, the yearly sampling is yet too sparse for a kinematic analysis. (adopted from Krichbaum et al. (2006)).

Within the core dominated objects, a subset exists with high optical polarization and variability. For these sources (BL Lac objects, high polarization quasars (HPQ) and optically violently variable (OVV) quasars) the spectrum extends smoothly into the infrared and optical continuum, suggesting a common emission mechanism for the entire range. Although a peak in νF_ν exists mostly, it can be found anywhere from the mm-band to the soft X-rays. In addition, BL Lac and OVV objects often exhibit a second, more energetic peak in νF_ν at energies around ~ 100MeV (Figure 1.7).

Little is known about the matter content of extragalactic jets. The observation of synchrotron radiation merely determines the emitting particles to be electrons, whether the charge is balanced by positrons or ions is however (embarrassingly) still unresolved. In principle, the baryon content could be assessed by the simultaneous observation of radio spectrum and an independent measure of the jet power (e.g. Reynolds et al. 1996; Bicknell & Begelman 1996; Dunn et al. 2006). Alas, due to the uncertain distribution of the relativistic particles, especially the unknown position of the *lower cutoff* $\gamma_{\rm min}$, the models still allow for both possibilities. It has been suggested that the pair annihilation process is responsible for the ~ 100 Mev γ-rays from blazars (Henri et al. 1993). However, extreme pair densities $> 10^9\,{\rm cm}^{-3}$ are required for annihilation to dominate over the inverse Compton photons (e.g. Boettcher & Schlickeiser 1996) and accordingly, no clear signature of the process can be observed.

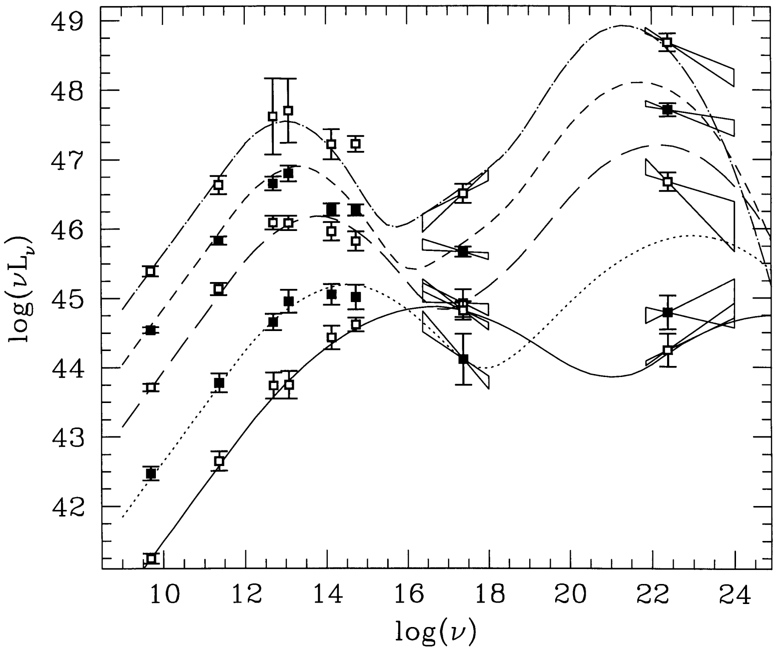

Figure 1.7 Average SED of a blazar sample binned by radio luminosity with analytic models of the spectra shown as lines (adapted from Fossati et al. (1998)).

1.3 Radiation Mechanisms

So far, we reviewed the manyfold appearance of AGN jets, commenting only little on the emission mechanisms responsible. This shall be provided in the following sections.

1.3.1 Synchrotron Radiation

The synchrotron process was initially considered by Schwinger (1949) to account for the radiation from terrestrial particle accelerators – just in time for the application to the newly found astrophysical radio sources (Alfvén & Herlofson (1950), independently: Shklovsky (1953)). Today, the synchrotron origin of the radio emission from relativistic jets is well established. Synchrotron radiation arises due to the alternating field of electric charges gyrating relativistically around a magnetostatic field. An electron with a Lorentz factor γ thus emits electromagnetic radiation peaked around a characteristic frequency

$$\nu_c = 1.2\gamma^2 B_\perp \text{MHz} \tag{1.2}$$

where $B_\perp$ (measured in gauss) signifies the component of the magnetic field perpendicular to the electron momentum. The power radiated by an individual particle is given by the relativistic Larmor formula

$$P_S = 2\gamma^2 \sigma_{\mathrm{T}} c (B_\perp^2/8\pi) \tag{1.3}$$

where σ_{T} denotes the Thomson electron cross section and c the speed of light as customary. Typically, the distribution of relativistic electrons in radio sources is non-thermal and can be parametrized by a *power-law* $dn_e/d\gamma \equiv K\gamma^{-p}$ within a certain range of electron Lorentz factors $\gamma_{\min} \leq \gamma \leq \gamma_{\max}$. The emissivity and thus the optically thin spectrum is immediately given by the integration

$$\epsilon_\nu \propto \int d\gamma \, dn_e/d\gamma \, P_S \, \delta(\nu - \nu_c) \tag{1.4}$$

$$\propto K \, B_\perp^{1+\alpha} \, \nu^{-\alpha} \tag{1.5}$$

where the *spectral index* $\alpha = (p-1)/2$ was introduced. The giant radio lobes exhibit such a power-law spectrum with $\alpha \approx 0.7$ (e.g. Blundell et al. 1999). Optically thin synchrotron radiation is highly linearly polarized with an electric $\mathbf{e}$ vector oscillating perpendicular to the sky-projection of the magnetic field. In the uniform case, the polarization degree is ~ 0.7 (for $p = 2$) depending mildly on p (see also: Pacholczyk 1970a).

While extended radio lobes are well described by optically thin synchrotron radiation, sufficiently compact cores will become opaque due to *self-absorption*. The opacity can be derived equally well from Kirchoff's law or from quantum mechanical principles using Einstein coefficients. It becomes

$$\kappa_\nu \propto K \, B_\perp^{(2\alpha+3)/2} \, \nu^{-(2\alpha+5)/2} \tag{1.6}$$

such that the optically thick source function reads

$$S_\nu = \epsilon_\nu/\kappa_\nu \propto B_\perp^{-1/2} \nu^{5/2}. \tag{1.7}$$

The corresponding brightness temperature is $T_{\mathrm{b}} = 10^9 (\nu/\mathrm{MHz})^{1/2} B^{-1/2}\mathrm{K}$ up to coefficients of order unity. At the spectral peak, T_{b} is only a modest function of B and approximately $T_{\mathrm{b}} \simeq 4 \times 10^{11}\mathrm{K}$ (e.g. Krolik 1998) which matches the observed values from radio jets well. Also optically thick synchrotron radiation can be highly polarized with a degree up to ~ 0.1 (for $p = 2$); the direction of polarization is perpendicular to the optically thin case.

We see that the optically thick contribution per se can not account for the flat spectrum of core-jets, instead the flux is as steep as $\propto \nu^{5/2}$. In fact, no known physical process leads to an entirely flat spectrum. A generally accepted way out of this dilemma is to assume that the core-flux is composed of a superposition from several unresolved emitting components. The individual spectra are likely to be offset which leads to a broadening of the superposed spectrum. In addition to opacity effects, spectral aging due to radiation losses ($t_S \propto \gamma^{-1}$) and adiabatic expansion steepens the spectrum at the high frequency end. At frequencies below $\nu_c(\gamma_{\min})$, the emission occurs according to $\propto \nu^{1/3}$, however this flattening most likely falls below the self-absorption turnover, in which case a source function $\propto \nu^2$ is adopted.

1.3.2 Faraday Rotation

Electromagnetic waves traveling in a plasma are subject to birefringent propagation effects. The strength of the wave-dispersion is determined by the relation of wave-frequency ν to the plasma-frequency and the electron gyro-frequency

$$\nu_0 = n_e e^2/(\pi m_e) = 8.89 \times 10^3 n_e^{1/2} \text{ Hz} \tag{1.8}$$

$$\nu_G = eB/(2\pi m_e c) = 2.8 \times 10^6 B \text{ Hz}. \tag{1.9}$$

In astrophysical applications (e.g. $n_e \sim 1\text{cm}^{-3}$, $B \sim 1$gauss – for core-jets), the refractive index can thus often be approximated by the high frequency regime of the cold plasma

$$n^2 \simeq 1 - \frac{\nu_0^2}{\nu^2} \tag{1.10}$$

and refraction has only marginal influence. However, a difference in refractive index for transverse left-handed and right-handed circularly polarized waves (ordinary and extraordinary wave modes) promotes a phase shift proportional to the path length l

$$\Delta\phi = \omega/c(n_{\text{ord}} - n_{\text{ext}})\ l \tag{1.11}$$

which can become large for astrophysical applications. This effect is known as *Faraday rotation* (FR) and leads to a frequency dependent rotation of the linear polarization plane by the angle

$$\chi_{\text{F}} = 2.35 \times 10^4 \frac{n_e B\ l}{\nu^2}. \tag{1.12}$$

In extragalactic jets, polarization and Faraday rotation are valuable diagnostics to estimate the source geometry. For example, the depolarization associated with (unresolved) differential Faraday rotation could be used to constrain the orientation of double-lobed FR2 sources. Laing (1988) and Garrington et al. (1988) found for all sources within their sample that the brighter side of the jet showed less depolarization than the fainter side. A likely explanation is “The side with the stronger jet is closer to us, is seen through a smaller amount of material and therefore shows less depolarization." (Laing (1988)).

Consistent detections of $\Delta\chi \propto \lambda^2$ are found in resolved jets as well as in unresolved radio cores (Zavala & Taylor 2003). Helical magnetic fields are generally perceived to promote transversal Faraday rotation measure (RM) *gradients* owing to the toroidal field component. Observationally, such gradients were first detected by Asada et al. (2002) and Zavala & Taylor (2005) in the jet of 3C 273. The RMs are generally found to follow a monotonic profile across jets (Gabuzda et al. 2004; O'Sullivan & Gabuzda 2009; Croke et al. 2010), supporting the helical field conjecture.

1.3.3 Compton Scattering

According to the standard models, the AGN accretion disk itself is not hot enough to account for the X-ray flux via thermal emission (see Malkan & Sargent 1982). This motivated the invention of an accretion disk *corona* or *jet base* which generates the X-radiation via inverse Compton up-scattering of the thermal disk photons (e.g. Corbel et al. 2000; Markoff et al. 2003a). High variability of the X-ray emission of some Seyfert galaxies also implies an origin from the innermost accretion disk.

The radiation pressure due to Compton scattering limits the luminosity of sustained accretion to the Eddington luminosity

$$L_{\mathrm{Edd}} = \frac{4\pi c G M_\bullet m_p}{\sigma_{\mathrm{T}}} = 1.3 \times 10^{46} \frac{M_\bullet}{10^8 M_\odot} \mathrm{erg\,s^{-1}} \tag{1.13}$$

for a spherical accretion flow. A limiting accretion rate is obtained when the Eddington luminosity is equated to the accretion luminosity

$$L_{\mathrm{acc}} = \frac{1}{2}\frac{G M_\bullet \dot{M}}{r_{\mathrm{in}}} = \epsilon(a)\dot{M}c^2 = 5.7 \times 10^{46}\,\epsilon(a)\frac{\dot{M}}{M_\odot \mathrm{yr}^{-1}}\,\mathrm{erg\,s^{-1}} \tag{1.14}$$

where the *radiative efficieny* $\epsilon(a)$ parametrizes the position of the ISCO in terms of the gravitational radius.[4] With this, the Eddington limited accretion rate becomes

$$\dot{M}_{\mathrm{Edd}} = 2 \times 10^{-1}\epsilon^{-1}\frac{M_\bullet}{10^8 M_\odot} M_\odot \mathrm{yr}^{-1}. \tag{1.15}$$

Throughout this work we will often parametrize the mass-loss due to the jet in terms of $\dot{M}_{\mathrm{Edd}}$. The ratio of accretion luminosity and Eddington luminosity, the so-called Eddington ratio

$$\lambda = L_{\mathrm{acc}}/L_{\mathrm{Edd}} \tag{1.16}$$

[4]For the Schwarzschild case it is $\epsilon(0) = 0.06$ and $\epsilon(1) = 0.42$ in the extreme Kerr metric.

is one of the fundamental parameters in black hole accretion theory and can be measured to compare a large variety of accreting black holes (see e.g. Fig. 1.4). Values of λ range from 10^{-7} to $\gtrsim 1$, however such super-Eddington objects are very rare.

Within the jet, also Compton up-scattering of the radio photons and thus *Synchrotron self Compton* (SSC) prevails (Jones et al. 1974). When the energy density of relativistic particles trumps the energy of the radiation field, photons will gain energy according to

$$P_C = 4/3\,\gamma^2\,\sigma_\mathrm{T}\,c\,u_r \tag{1.17}$$

which corresponds to the Larmor formula for synchrotron radiation (Eq. 1.3; for an isotropic electron distribution $B_\perp^2 = 2/3B^2$), only that the field energy is now replaced by the energy density of the radiation field u_r. Hence the ratio of inverse Compton luminosity to synchrotron luminosity is simply $u_r/(B^2/8\pi)$. Since the same electrons are responsible for synchrotron and inverse Compton radiation, and $P_S \sim P_C \propto \gamma^2$, the up-scattered spectrum has exactly the same shape as the original synchrotron spectrum. SSC modeling augmented with additional external seed photons is now a standard practice able to explain the double-humped spectrum of core jets and BL Lac objects (e.g. Abdo et al. 2010a).

The dependence of the inverse Compton power on u_r can lead to a catastrophic cooling called the "inverse Compton catastrophe" (Kellermann & Pauliny-Toth (1969); more recently: Tsang & Kirk (2007)). It occurs when the Compton cooling time becomes shorter than the Synchrotron loss time: $u_r \gtrsim B^2/8\pi$. The cascade of secondary scatterings is either stopped at the Klein-Nishina limit[5] or when the energy of the relativistic electrons is diminished. In the stationary case on the other hand, the radio brightness temperature is expected to obey the *inverse Compton limit* $T_b \lesssim 10^{12}$K.

1.4 Signatures of Relativistic Motion

The appearance of extragalactic jets is intimately connected with their relativistic nature. Here the observational indications of relativistic jet flows are reviewed briefly.

[5]At the Klein-Nishina limit, the photon energy surpasses the electron rest-mass and the scattering becomes inelastic.

1.4.1 Superluminal motion

Evidence for relativistic motion in AGN was discovered by Gubbay et al. (1969), Whitney et al. (1971) and Cohen et al. (1971) using time resolved VLBI experiments. In great foresight, Rees (1966) predicted the effect of *superluminal motion* in radio sources already three years in advance of the actual detection. The telltale motion of enhanced emission regions called *knots*[6] is subject to a relativistic illusion: due to time dilation, the observed transverse velocity can appear as high as Γv for an "optimal" viewing angle of $\sin(i_{\mathrm{max}}) = \Gamma^{-1}$. Superluminal motion thus gives a lower limit on the Lorentz factor of the knots.

Measurements of v_{app} in quasars gives values ranging from $1 - 30c$ with a peak around $8 - 9c$ (Lister et al. (2009), Jorstad et al. (2001); Fig. 1.8). For the source PKS 1510, Jorstad et al. (2005) reported the record value of 46c. For BL Lacs, the distribution is more extended and peaks at lower values compared to quasars, around $2 - 3c$ (Gabuzda et al. 1994).

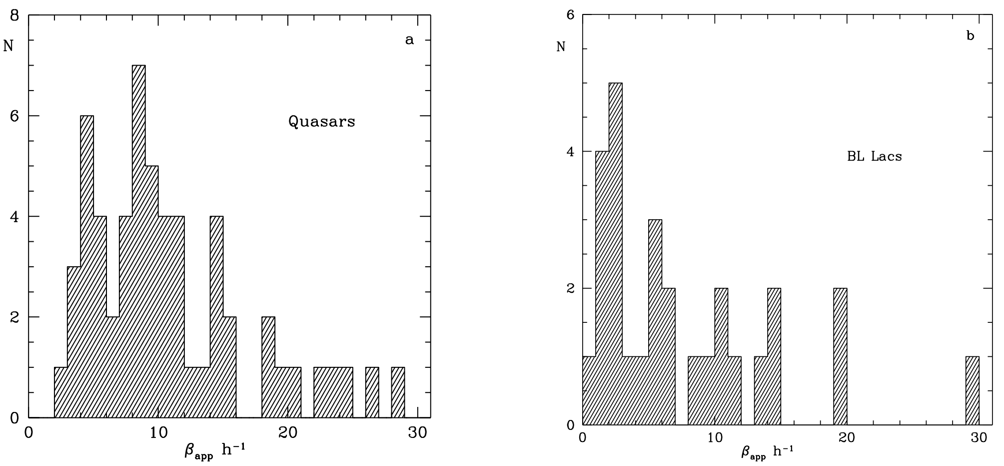

Figure 1.8 Distribution of the superluminal motion, $\beta_{\mathrm{app}} = v_{\mathrm{app}}/c$ detected in 33 γ-ray bright sources (adopted from Jorstad et al. (2001)).

Also in galactic μ-quasars, superluminal motion was detected (Mirabel & Rodríguez 1994). The radio source GRS 1915+105 showed ejection of two components, apparently moving at $2-3c$ (Figure 1.2). The fact that a receding component could be observed as well allowed to place the source within our galaxy. It also suggests a large viewing angle $\sim 70°$ and thus a Lorentz factor as high as $\Gamma \simeq 5$ (see also: Tingay et al. 1995; Mirabel & Rodríguez 1998).

Most likely, the knots are caused by traveling relativistic shocks in the jet flow (Rees 1978) and as such, the pattern speed ($< c$) does not directly correspond to bulk kinetic motion. For high Lorentz factors however, the shock speed Γ_{S} is only

[6]sometimes also casually called "blobs".

a slight overestimation of the flow value Γ_{P} with a ratio $\Gamma_{\mathrm{P}} \simeq \Gamma_{\mathrm{S}}/\sqrt{2}$ (Blandford & Königl 1979). Thus the pattern speed argument can not rule out relativistic bulk flow with $\Gamma \gtrsim 10$ (e.g. Marscher 2006).

Observationally, multiple indications support the notion that the knot motion reflects the underlying flow. These are for example: the observation of bidirectional knots, nearly no inwardly moving features, multiple knot ejections of the same speed and the tight correlations of jet speeds with $\gamma-$ray emission and luminosity (see also: Lister et al. 2009).

1.4.2 Beaming

Only few sources are known to feature a two-sided core-jet (e.g. Feretti et al. 1993; Wilkinson et al. 1994; Sudou et al. 2000), while most sources appear one-sided in VLBA imaging. The widely accepted reason is *doppler beaming* of the intrinsically symmetric jets. For an observer of a source moving with relative velocity $\boldsymbol{\beta}\, c$, the emitted frequency ν' will appear boosted by the doppler factor D:

$$\nu = D\nu' = \left(\Gamma\left(1 - \beta \cos i\right)\right)^{-1} \nu' \tag{1.18}$$

where the inclination i is measured between photon path and the velocity of the source. The bulk of the emission is beamed to a cone of opening angle $\sim 1/\Gamma$, leading to relativistic aberration. Also the direction of polarization is subject to aberration which can lead to viewing angle dependent *polarization swings* (e.g. Blandford & Königl 1979).

From the Lorentz invariance of the photon occupation number it follows the well known relation for the specific intensity

$$\frac{I_\nu}{\nu^3} = inv. \tag{1.19}$$

which gives rise to a strong *doppler favoritism* of the approaching side, as $I_\nu = D^3 I'_{\nu'}$. The corresponding ratio of jet to counter jet surface brightness can be computed to

$$R = \left(\frac{1 + \beta \cos i}{1 - \beta \cos i}\right)^{2+\alpha} \tag{1.20}$$

with the spectral index α (e.g. Blandford & Königl 1979). Hence for intrinsically symmetric sources, a measurement of R can yield the parameter-combination $\beta \cos i$ and thus a lower limit of β and $\cos i$ (since both quantities are bounded by one).[7] Also the non-detection of a counter-jet can be used for lower limits on β.

[7] In connection with Equation (1.20) we should note that an other version for unresolved "blobs" with the exponent $3 + \alpha$ exists in the literature. The difference is based on the fact that in the modeling of blobs, the co-moving volume is considered, while for jets the radiation transport is conveniently cast in the observer system. See also the extended discussion on the matter by Jester (2008).

For example in M87, the existence of a counter-jet was long under debate. From the lower limit of $R > 28$, Reid et al. (1982) derived $\beta > 0.6$ and $\cos i > 60^{\circ}$. Also Biretta et al. (1989) drew their conclusions from the non-detection of a counter-jet with limit $R > 380$. In the more recent VLBI studies from Ly et al. (2004), Krichbaum et al. (2006) and Ly et al. (2007) a transient counter-jet could finally be detected and confirmed (see also Figure 1.6). The latter authors combined the measured 43GHz brightness ratio with the apparent velocity measurement v_{app} to obtain a jet speed of $0.6 - 0.7c$. However, given the considerable uncertainties involved in defining R from the data, these numbers should only be taken as a rough guideline.

In an accelerating jet, each emitting element can be understood as its own inertial system. Hence it is helpful to define a common frame for the radiation transport. In the *observer frame* it becomes

$$\frac{dI_\nu}{dl} = D^{2+\alpha}\epsilon'_\nu - D^{1.5+\alpha}\kappa'_\nu I_\nu \tag{1.21}$$

where ϵ'_ν and κ'_ν are the co-moving (synchrotron) emissivity and opacity, respectively (e.g. Begelman et al. 1984). In this thesis, the polarized radiation transport will be solved for the stationary jet models in accordance with relation 1.21. Under the assumption of stationarity, time dilation effects other than doppler boosting of the frequency can safely be neglected.

For non-stationary sources on the other hand (e.g. knots), reconstruction of the physical *world map* would require taking into account the various photon travel times that lead to the *world picture* imaged by an observer (see also: Jester 2008).

1.4.3 Intra Day Variability and the Compactness Problem

Quasars closely aligned with the line of sight (*blazars*) frequently exhibit rapid temporal "daily" flux variations with an amplitude of up to $\sim 25\%$ (Quirrenbach et al. (1992); see also Figure 1.9). Multiple intrinsic and extrinsic models for the variability have been proposed, based for example on the microlensing effect (Chang & Refsdal 1979), accretion disk (Chakrabarti & Wiita 1993) and shock-in-jet models (Marscher & Gear 1985). A kinematic "Lighthouse"-model of orbiting blobs accounting for quasi-periodic flaring was suggested by Camenzind & Krockenberger (1992).

It is now well established that in order to explain the high intrinsic variability of blazars, relativistic length and time compression has to be invoked. When the source is unresolved as in the case of AGN cores, its size can only be estimated based on light travel times. A variation on the timescale Δt can thus not originate in a source larger than $c\Delta t$ due to causality constraints. The length scales obtained

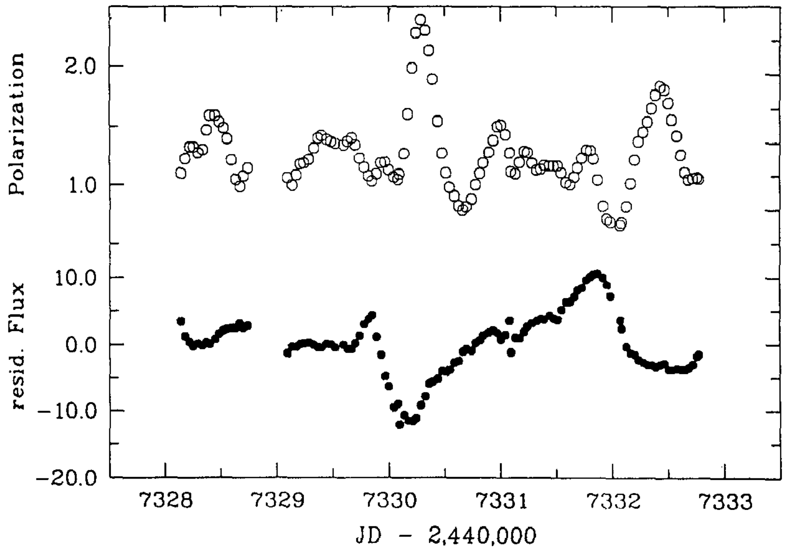

Figure 1.9 Intra day variations in residual radio flux density in percent (•) and polarization (◦) in the compact flat spectrum source 0917 + 624 discovered by Quirrenbach et al. (1989) (adopted from Wagner & Witzel (1995)).

this way however tend to underestimate the source size giving rise to a *compactness problem*: Brightness temperatures inferred from variability $T_{\rm b} = F_\nu D^2 \nu^{-2} c^{-2} \Delta t^{-2}$ frequently obtain values as high as $\approx 10^{19}$K (Quirrenbach et al. 1992) – well above the inverse Compton limit.

An elegant solution to this problem was proposed by Rees (1967): in the case of a relativistically moving source, the intrinsic time difference is compressed via $\Delta t = D^{-1}\Delta t'$ and thus doppler boosting can be invoked to reconcile the observed T_b with a model of the co-moving $T'_{\rm b}$. This way, the compactness problem can be circumvented, however, the required Doppler factors are typically larger than the values obtained by alternative methods. For example, by naively enforcing the (stationary) inverse Compton limit $T'_{\rm b} \leq 10^{12}$K, Doppler factors as high as $D \sim 100$ are inferred.

In TeV emitting blazars, the variability can be as short as 3-5 minutes (Albert et al. 2007; Aharonian et al. 2007) which requires high Lorentz factors (> 50) derived from the pair creation opacity (Henri & Saugé 2006). The discrepancy between Doppler factors obtained from superluminal motion versus simple stationary radiation modeling is sometimes called the *Doppler factor crisis*. It can be resolved by assuming more complex geometries or allowing time-dependence in the dynamical and spectral modeling (e.g. Georganopoulos & Kazanas 2003; Chiaberge et al. 2000; Gopal-Krishna et al. 2004; Ghisellini et al. 2005; Lyutikov & Lister 2010).

A similar version of the compactness problem is present in Gamma ray burst sources (GRB) (Ruderman 1975; Schmidt 1978). In order to reconcile the pair production opacity with the optically thin non-thermal spectrum, the Lorentz factor has to be higher than $\gtrsim 100$ (e.g. Baring & Harding 1997; Fenimore et al. 1993; Piran 1999; Lithwick & Sari 2001). The jets of GRBs are thus the fastest known macroscopic objects in the universe.

1.5 Formation of Relativistic Jets

After illustrating the observational evidences, it is now time to review the physical mechanisms capable of producing collimated relativistic jets. The generation of a jet is customarily divided into *1. launching* of the flow from a central engine, *2. acceleration* to high velocity and *3. collimation.* We shall see that the acceleration and collimation is in fact tightly connected such that the divide occurs only for structural convenience.

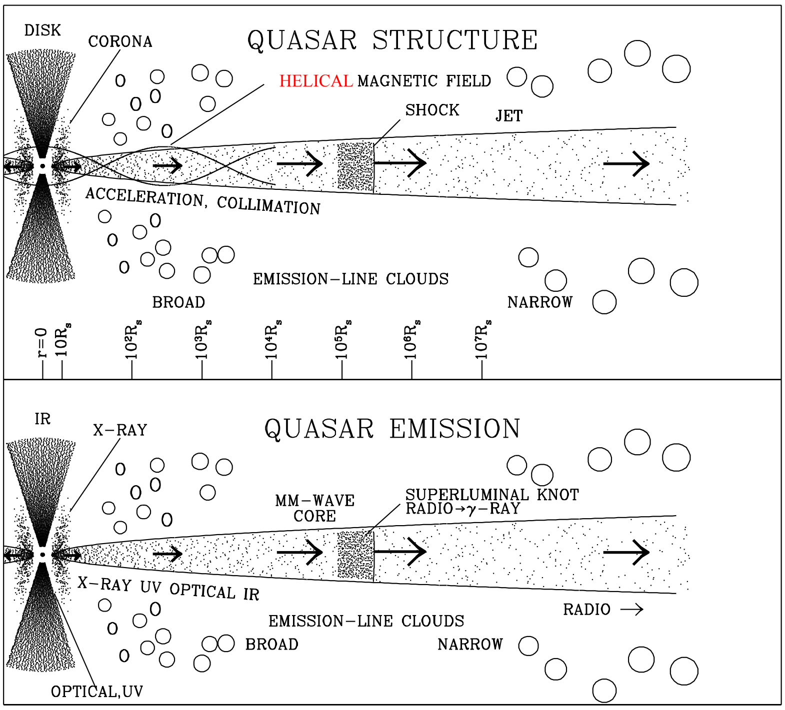

Figure 1.10 Sketch of the physical structure and emission regions of a radio-loud AGN (adapted from Marscher (2005)). The poloidal field of the original cartoon was replaced by a *helical* field geometry. Extended radio lobes on Kpc-Mpc scales are not included.

1.5.1 Central engines

In order to power a jet from the vicinity of a compact object, two possible energy reservoirs can be tapped: the potential energy released from accreting matter (according to 1.14) or the rotational energy of a black hole. The available spin energy can be expressed in the reducible mass

$$E_{\rm spin} = M_{\rm red}c^2 = M_\bullet \left(1 - \left((1+\sqrt{1-a^2})/2\right)^{1/2}\right) c^2 \tag{1.22}$$

and for a maximally spinning black hole one finds $E_{\rm spin} = 0.29 M_\bullet c^2 = 5.2 \times 10^{61} M_\bullet/(10^8 M_\odot)\,{\rm erg}$. This energy theoretically suffices to power an AGN with $10^{46}{\rm erg\,s^{-1}}$ over a typical duty cycle of 100 Myrs. The most appealing process by which spin energy can be extracted was suggested by Blandford & Znajek (1977) (BZ). In a purely electrodynamic model, they demonstrated that a large-scale magnetic field can transport Poynting flux away from the ergosphere, much like the mechanical energy extraction suggested earlier by Penrose (1969)[8]. The power depends crucially on the magnetic field strength (according to 1.1) which is not known from first principles. Most likely, the structure of the magnetic field is determined by the surrounding accretion disk, either by dynamo processes or by accretion of the surrounding field. Recently, numerical general relativistic magnetohydrodynamic (GRMHD) simulations including a disk have become possible, first in two dimensions (Koide et al. 1998; Gammie et al. 2003; De Villiers et al. 2003; Komissarov 2005; Hawley et al. 2007; Nagataki 2009) and also in full 3D (McKinney & Blandford 2009).

With great success, the GRMHD simulations demonstrated the feasibility of highly relativistic jets launched from the vicinity of a black hole. However, a number of unsolved problems remain. One is connected to the mass-loading of the tentative BZ jet, since due to flux freezing, the ionized material can not pass onto the field lines rooted on the black hole. As a way out, a density floor is imposed to replenish the mass in the outflow with readily created $e^\pm$ pairs. So far, it remains to be proven that the jet energy of the simulations really stems from spin or in fact from the accretion potential. Another challenge for present BZ jet models is the fact that left alone, they show little tendency to collimate and rely on external collimating agents. This also impedes the ability of the BZ jet to accelerate to highly relativistic speeds. In the case of GRBs, the collimator can be found in the stellar envelope pressure (Tchekhovskoy et al. 2010b; Komissarov et al. 2010), for an AGN or μ-quasar, a *disk wind* is frequently suggested (e.g. McKinney & Narayan 2007).

The launching of a wind or jet from a thin accretion disk threaded by a large scale magnetic field was initially suggested by Blandford & Payne (1982) (BP). In the seminal paper, the associated magnetic torque of the wind was also found to aid in the accretion process itself by the transport of (magnetic) angular momentum.

[8] A comprehensive review is provided by Komissarov (2009) and Krolik & Hawley (2010).

The jet power can constitute a sizable fraction of the accretion lumiosity, as high as 50% (see the review by Ferreira 1996). Hence a disk around a maximally spinning $10^8 M_\odot$ SMBH accreting at a rate of $1 M_\odot \mathrm{yr}^{-1}$ can power an outflow of $10^{46} \mathrm{erg\,s}^{-1}$, similar to the BZ case considered before. Whereas the early works on magnetized accretion ejection structures (MAES) were performed under the assumption of self-similarity, self-consistent simulations of jet launching Shakura & Syunyaev (1973) - type disks (SS73) recently became possible (Casse & Keppens 2002; Meliani et al. 2006a; Zanni et al. 2007; Tzeferacos et al. 2009; Murphy et al. 2010).

In contrast to the puffed up advection dominated accretion flows (ADAF) of the BZ - type jet models, the vertical density profiles in a SS73 disk are very steep, up to $\rho(z) \propto \exp(-(z/z_0)^2)$ which so far can not be resolved by the dynamical simulations. Accordingly, MAES simulations tend to over-estimate the mass-flux when approaching the low mass loading regime, in contradiction to the analytic results. Unfortunately this also limits the terminal velocities adopted by the simulations (see also the discussion by Murphy et al. 2010). So far, all such studies are performed in non-relativistic MHD. In the relativistic case, a further complication impedes the applicability of jet launching from necessarily resistive disks: the naive adoption of resistivity in RMHD leads to an a-causal parabolic equation where perturbations grow exponentially. A few studies have addressed this general problem (Komissarov 2007; Palenzuela et al. 2009; Takamoto & Inoue 2011), however, causal resistive RMHD is still in its infancy an no application to jet launching exists to date.

One way to circumvent this problem is to resign on the disk structure and consider the ideal RMHD outflow only from the disk surface onwards. In such *disk as boundary* simulations, acceleration and collimation of an initially slow wind can be studied. In the non-relativistic case, numerous disk as boundary simulations have proven jet self-collimation (chronologically: Ustyugova et al. 1995; Ouyed & Pudritz 1997; Romanova et al. 1997; Krasnopolsky et al. 1999; Ustyugova et al. 1999, ...) for a wide parameter-space (Fendt 2006; Pudritz et al. 2006). The first extension of disk as boundary simulations to the relativistic case was presented by Porth & Fendt (2010), the results will be discussed in detail in chapter 4 of this thesis.

1.5.2 Acceleration

Once an outflow is launched from the central object, it can be accelerated by magnetic, thermal, centrifugal or radiative forces. Naturally, any process worth considering should be capable of accelerating flows to Lorentz factors of $\Gamma \sim 10$ as inferred from observations.

Lets first consider radiative driving. Most likely, the gas at the jet base is fully ionized, leaving only electron scattering and a contribution of bound-bound and bound-free transitions to the radiation pressure. Accordingly, only in super-Eddington objects the radiation can be of dynamical importance (e.g. Lynden-Bell 1978; Proga 2007; Takeuchi et al. 2010). In addition, due to relativistic aberration, only photons within a cone $\lesssim 1/\Gamma$ behind the flow actually contribute to the acceleration, while all other inclinations decelerate. In fact, for $\Gamma = 10$, the ratio of collimated intensity to the isotropic component needs to be as high as $\sim 10^4$ which puts extreme constraints on the geometry (Krolik 1998). Thus radiation is hardly a viable mechanism to achieve high Lorentz factors (see also Phinney 1982).

Also thermal acceleration in analogy to the de Laval nozzle has been proposed early on (e.g. Blandford & Rees 1974). Due to irradiation and Compton heating, the upper layers of an accretion disk are likely to assume a temperature $\sim 10^7$K. This suffices to drive gas beyond the escape temperature at radii of $\sim 10^3 r_{\rm S}$ (Begelman et al. 1983) and thus account for slow winds $\sim 0.1c$ often observed in X-radiation absorption (e.g. Chelouche & Netzer 2005). However, to thermally accelerate to relativistic velocities, temperatures in excess of the plasma rest-mass energy are required. For a pair-plasma, this signifies $\sim 10^{10}$K, which clearly demands a different heating mechanism. In the direct vicinity of the black hole, a hot corona could form due to an accretion shock or a so-called CENBOL shock (CENtrifugal pressure supported BOundary Layer shock) (see also Kazanas & Ellison 1986; Das & Chakrabarti 1999). Also Blandford (1994) has proposed a mechanism of dissipation near the ergosphere as a consequence of the Lense-Thirring effect. However uncertain the mechanism of heating, acceleration out of thermal enthalpy is a robust mechanism capable of achieving high Lorentz factors via expansion $\Gamma \propto r$ (e.g. Meliani et al. 2010a; Komissarov 2011).

The leading paradigm of steady jet formation takes into account magnetohydrodynamic processes, either via the BZ or the BP mechanism. In both processes, a rotating magnetosphere gives rise to a global current system that accelerates the flow via the Lorentz force. Beyond the escape surface, the differences are reflected only in the underlying rotation law of the field lines. As a first order approximation to the BZ effect, a solid-body rotation law is frequently adopted (e.g. Komissarov et al. 2007; Tchekhovskoy et al. 2008), while in the BP scenario a Kepler rotation profile is most likely preserved by the field lines. To achieve high Lorentz factors, the flow at the base is necessarily *Poynting dominated* with large values of the magnetization parameter σ which signifies the ratio of electromagnetic to kinetic energy flux (Michel 1969). The problem of accelerating to relativistic speeds thus can be seen as a matter of mass loading of the flow.

The accelerating Lorentz force can be decomposed into a magnetic pressure force and a "tension" term, depending on which dominates, two kinds of jets are possible: magnetic tower jets, propelled by magnetic pressure gradient (see Kato 2007, for a definition) and the classical BP jets, *magnetocentrifugally* accelerated by the tension and centrifugal forces. As the Lorentz force can also account for jet *collimation*, acceleration and collimation are intricately coupled. For example, in a stationary cylindrical flow, no acceleration due to the $\mathbf{j} \times \mathbf{B}$ force is possible. Also in the conical case which yielded $\Gamma \propto r$ for thermal acceleration, no MHD acceleration is possible as the magnetic energy $\propto B^2 V$ is conserved. Efficient acceleration demands a special geometry of the flux surfaces called *differential collimation*, requiring a delicate balance of forces across the flow (for a review, see Komissarov 2011).

1.5.3 Collimation

The magnetohydrodynamic (MHD) self-collimation of non-relativistic jets has been proven in general by time-dependent simulations (Ustyugova et al. 1995; Ouyed & Pudritz 1997) and has been investigated in further detail considering additional physical effects as magnetic diffusivity by Fendt & Čemeljić (2002), a variation in Ouyed & Pudritz (1999), non-axisymmetric instabilities in the launching region (Ouyed et al. 2003), or a variation in the mass flow profile or the magnetic field geometries (Fendt 2006; Pudritz et al. 2006), or the influence of a central magnetic field (Fendt 2009; Matsakos et al. 2008).

In the case of relativistic jets the efficiency of MHD self-collimation is under debate. The main reason is the existence of electric fields which are negligible for non-relativistic MHD and which are commonly thought to have a net de-collimating effect on the jet. Essentially, Chiueh et al. (1991) have demonstrated the current carrying relativistic jet can be highly collimated (also Heyvaerts & Norman 1989; Appl & Camenzind 1993; Begelman & Li 1994; Heyvaerts & Norman 2003a; Vlahakis 2004). However, the actual structure of these jets still remains unclear - mainly due to the need for simplifying assumptions to solve the corresponding set of MHD equations.

So far, a variety of theoretical models have been developed for the case of *self-similar* jets (Li et al. 1992; Contopoulos 1994, 1995; Vlahakis & Königl 2003; Meliani et al. 2006b), although it seems clear that relativity does not obey self-similarity. Fully 2.5D theoretical solutions for the internal magnetic jet structure could be obtained by neglecting matter inertia (Fendt 1997a; Fendt & Memola 2001). These force-free solutions for the field structure can in principle be coupled to the dynamical wind solution along the field lines (Fendt & Camenzind 1996;

Fendt & Greiner 2001; Fendt & Ouyed 2004).

Relativistic MHD simulations of accelerating and collimating jets have been presented by Komissarov et al. (2007), spanning over a huge range of length scale and providing jets of large Lorentz factor $\Gamma \sim 10$. Their simulations, however, did not start from the very base of the jet - the accretion disk, but at some fiducial boundary above the equatorial plane. Since the jet has been launched already with super-escape speed, gravity has not been considered. The jet flow has been confined within a rigid wall of predefined shape which naturally affects the opening angle of the MHD jet nozzle and thus jet collimation and acceleration.

Simulations of jet self-collimation have been presented by Porth & Fendt (2010) for mildly relativistic flows and by Porth et al. (2011) for the highly relativistic case. These results confirm the early analytic studies on jet self-collimation and present a flexible modeling framework for observations of jets from AGN or μ-quasars.

1.6 Outline of the Thesis

In this thesis, the prevailing paradigm of *magnetohydrodynamic* relativistic jet formation is investigated using special relativistic MHD simulations.

Chapter 2

Reviews the equations of relativistic magnetohydrodynamics that are manipulated in the course of this work. Useful conservation laws and analytic expressions are derived. The implementation of a gravitational source term to the conservation laws is detailed.

Chapter 3

Sets the stage for the numerical treatment of the equations. Details of the numerical setup such as boundary conditions are provided. The Stokes vector transport routine is extensively tested against analytical expectations and literature results.

Chapter 4

Discusses the results obtained for the formation of relativistic disk winds from hot accretion disk coronae. Special attention is given to the position of the light cylinder and the force balance across the field. This chapter follows from our publication Porth & Fendt (2010).

Chapter 5

Shows simulations of self-collimating Poynting dominated jets reaching Lorentz factors ~ 8 modeling radio-loud AGN jets. Open and closed current models are discussed and the details of the acceleration regime are shown. This chapter follows from our publication Porth et al. (2011).

Chapter 6

Provides mock observations of the AGN jet models obtained in chapter 5 by means of a newly developed polarized synchrotron radiation transport code. Standard diagnostics such as core-shift, polarization structure and Faraday rotation gradients are performed for the model jets. This chapter also follows from our publication Porth et al. (2011).

Chapter 7

Provides fully three dimensional simulations of the jet formation site with focus on stability. Two different kinds of non-axisymmetric perturbations are developed. The non-axisymetric modes of the flow are obtained and a stabilizing mechanism for astrophysical jets is discussed.

Chapter 8

Summarizes the main conclusions of this thesis and gives an outlook on future directions of research.

Chapter 2

Principles of Relativistic Magneto-Hydrodynamics

In this chapter, we derive the fundamental equations of relativistic magneto-hydrodynamics and introduce conservation laws and other relations used throughout this work. We discuss the concept of critical points and characteristics.

2.1 Relativistic MHD Equations

We solve the time dependent non-linear system of special relativistic conservation laws. In a covariant formulation (see Landau & Lifshitz 1960), the equations naturally follow as a set of hyperbolic equations. For convenience, we adopt a flat Minkowski metric while for a general relativistic formulation, the partial derivatives of Equations (2.1) to (2.3) should be replaced by covariant derivatives. The signature of the metric used in the following is given by $(-,+,+,+)$ and thus the square of the four velocity, $(u^\alpha) \equiv (\Gamma c, \Gamma \mathbf{v})^T$, becomes $u^\alpha u_\alpha = -c^2$.

2.1.1 Covariant MHD

The MHD equations describe conservation of energy, momentum and mass, coupled to the evolution of the magnetic field given by the homogenous Maxwell equation. In four-vector notation[1] this is satisfied by the vanishing four-divergence of the energy-momentum tensor $T^{\alpha\beta}$, the mass current density ρu^α and the dual Faraday

[1]following the convention that Greek indices run from 0 to 4 whereas Latin indices go from 1 to 3. In addition, Einsteins sum convention for equal indices is used.

tensor $F^{*\alpha\beta}$ leading to the fundamental relations

$$\partial_\alpha T^{\alpha\beta} = 0 \tag{2.1}$$

$$\partial_\alpha F^{*\alpha\beta} = 0 \tag{2.2}$$

$$\partial_\alpha (\rho u^\alpha) = 0. \tag{2.3}$$

We assume that the energy-momentum tensor is composed of an ideal fluid part

$$T^{\alpha\beta}_{\mathrm{f}} = \rho h u^\alpha u^\beta + p g^{\alpha\beta} \tag{2.4}$$

with the co-moving specific plasma enthalpy h, gas density ρ and pressure p. In addition, the electromagnetic part is added

$$T^{\alpha\beta}_{\mathrm{em}} = F^{\alpha\delta} F^\beta_\delta - \frac{1}{4} g^{\alpha\beta} F^{\delta\epsilon} F_{\delta\epsilon} \tag{2.5}$$

where we have absorbed the additional factor $1/4\pi$ in the definition of our fields. The final energy-momentum tensor of the ideal magneto-fluid can then be written as

$$T^{\alpha\beta} = (\rho h + b^2) u^\alpha u^\beta + \left(p + \frac{1}{2} b^2\right) g^{\alpha\beta} - b^\alpha b^\beta. \tag{2.6}$$

In the latter relation, we have introduced the magnetic field pseudo vector

$$b^\alpha = -\frac{1}{2} \epsilon^{\alpha\beta\gamma\delta} u_\beta F_{\gamma\delta} \tag{2.7}$$

that depends on the four-velocity. Its components read $b^0 = B^i u^i$; $b^i = (B^i + b^0 u^i)/u^0$ and we note the useful relation

$$b^\alpha b_\alpha = \frac{1}{2} F^{\alpha\beta} F_{\alpha\beta} = B^2 - E^2. \tag{2.8}$$

The *ideal MHD condition* enters by assuming infinite conductivity in the co-moving plasma frame $\sigma \to \infty$, hence negligible electric fields given by $F^{\alpha\beta} u_\beta = 0$. Therefore the dual Faraday tensor can be expressed solely in terms of the velocity and magnetic vectors as

$$F^{*\alpha\beta} \equiv \frac{1}{2} \epsilon^{\alpha\beta\gamma\delta} F_{\gamma\delta} = b^\alpha u^\beta - b^\beta u^\alpha \tag{2.9}$$

and for the field three-vector components it follows

$$B^i = F^{*i0} = b^i u^0 - b^0 u^i \tag{2.10}$$

$$E^i = \epsilon^{ijk} b^j u^k \tag{2.11}$$

with latin indices running from 1 to 3. Equation 2.11 is equivalent to the classical ideal MHD condition $\mathbf{E} = -\boldsymbol{\beta} \times \mathbf{B}$ and the reason why electric fields can be eliminated from the equations. We highlight here that the relativistic MHD system is completely described by the homogenous Maxwell equations (2.2) and thus no assumption about the displacement current is made.[2]

[2]The inclusion of the displacement current limits the Alfén velocity to the speed of light. This can also be exploited in "semi-relativistic" MHD where the displacement current is included

2.1.2 Continuity Equation

For a numerical treatment, a component-wise notation is necessary. The relativistic continuity equation (2.3) written in components becomes

$$\partial_t(\Gamma\rho) + \partial_j\left(\Gamma\rho v^j\right) = 0. \tag{2.12}$$

2.1.3 Induction Equation

Having a closer look at the homogenous Maxwell equation (2.2), we see as $F^{*00} = 0$, only the spatial components are actually equations of evolution and the time component merely yields the solenoidal constraint

$$\nabla \cdot \mathbf{B} = 0. \tag{2.13}$$

The spatial components result in the ordinary induction equation

$$\partial_t \mathbf{B} - \nabla \times (\mathbf{v} \times \mathbf{B}) = 0 \tag{2.14}$$

or equivalently

$$\partial_t B^i \mathbf{e^i} = \partial_j (v^i B^j - B^i v^j)\mathbf{e^i}. \tag{2.15}$$

2.1.4 Momentum Equation

The spatial components of (2.1) result in the relativistic momentum equation

$$\begin{aligned} &\partial_t \left[\left(\rho h + \frac{B^2}{\Gamma^2} + (\mathbf{vB})^2\right)\Gamma^2 v^i - b^0 b^i\right]\mathbf{e^i} \\ +&\partial_j\left[\Gamma^2 v^j v^i \left(\rho h + \frac{B^2}{\Gamma^2} + (\mathbf{vB})^2\right) + p + \frac{1}{2}\left(\frac{B^2}{\Gamma^2} + (\mathbf{vB})^2 - b^i b^j\right)\right]\mathbf{e^i} = 0 \end{aligned} \tag{2.16}$$

For convenience, we introduce the terms

$$\begin{aligned} w_t &\equiv \left(\rho h + \frac{B^2}{\Gamma^2} + (\mathbf{vB})^2\right) && (2.17) \\ \mathbf{m} &\equiv w_t \Gamma^2 \mathbf{v} - b^0 \mathbf{b} && (2.18) \\ p_t &\equiv p + \frac{1}{2}\left(\frac{B^2}{\Gamma^2} + (\mathbf{vB})^2\right) && (2.19) \\ \mathcal{E} &\equiv \Gamma^2 w_t - p_t - b^0 b^0 && (2.20) \\ D &\equiv \Gamma\rho && (2.21) \end{aligned}$$

Thus written in component-notation, the momentum equation reads

$$\partial_t m^i \mathbf{e^i} + \partial_j\left(\Gamma^2 v^i v^j w_t + p_t - b^i b^j\right)\mathbf{e^i} = 0. \tag{2.22}$$

and c is artificially limited to facilitate the computation (known as "Boris correction" after Boris (1970)).

2.1.5 Energy equation

Energy conservation follows naturally from the time components of (2.1). It is

$$\partial_t \left(\Gamma^2 w_t - p_t - b^0 b^0\right) + \nabla \left(w_t \Gamma^2 \mathbf{v} - b^0 \mathbf{b}\right) = 0 \tag{2.23}$$

or

$$\partial_t \mathcal{E} + \nabla \mathbf{m} = 0. \tag{2.24}$$

2.1.6 Conservation of State Vector

When considering the state and flux vectors

$$\mathbf{U} \equiv \begin{pmatrix} D \\ m^i \mathbf{e^i} \\ \mathcal{E} \\ B^i \mathbf{e^i} \end{pmatrix}; \qquad \mathbf{F}^j \equiv \begin{pmatrix} D v^j \\ (w_t \Gamma^2 v^i v^j + p_t - b^i b^j)\mathbf{e^i} \\ m^j \\ (v^i B^j - B^i v^j)\mathbf{e^i} \end{pmatrix} \tag{2.25}$$

the equations of special relativistic MHD are summarized by

$$\partial_t \mathbf{U} + \partial_j \mathbf{F}^j = 0 \tag{2.26}$$

$$\partial_j B^j = 0. \tag{2.27}$$

This signifies a conservation equation for the state vector $\mathbf{U}$. Its variables are customarily called conservative variables. The variables that are usually of interest for the physical application are however

$$\mathbf{V} = (\rho, p, \mathbf{v}, \mathbf{B})^T, \tag{2.28}$$

called primitive variables. While the map from primitive variables to conserved variables is simply given by the relations (2.18), (2.20) and (2.21), the inverted map becomes a set of highly non-linear equations that are tightly coupled via the appearance of the Lorentz factor Γ in all conserved variables (see also: Noble et al. 2006).

2.1.7 Equation of State

The MHD equations have to be closed with an equation of state (EoS) relating the gas pressure with other quantities such as density or entropy. The EoS thereby models the underlying thermodynamics and depends on the plasma composition. The simplest EoS is the isothermal relation $pc^2 = c_{\mathrm{s}}^2 \epsilon$ with $c_{\mathrm{s}}^2 \equiv const$ which can be used to eliminate the energy equation from the set of equations. The isothermal EoS has its application for example in the ultra-relativistic limit or when the pressure is dominated by radiation, in which case the sound speed approaches the value $c_{\mathrm{s}}^2 = 1/3c^2$. Even for degenerate matter in white dwarfs and neutron stars, the isothermal case is sometimes applied (e.g. Nicotra et al. 2006).

Typically, equilibrium thermodynamics and thus an ideal gas-law[3] $p = k_{\mathrm{B}}\rho T/(\mu m_{\mathrm{p}})$ is assumed. The ideal gas law remains applicable also for relativistic temperatures $k_{\mathrm{B}}T \gg m_{\mathrm{p}}c^2$ where the equilibrium is then described by the Juttner distribution (e.g. Anile 1989). The internal energy density composed of internal degrees of freedom and particle rest-mass reads

$$\epsilon = \frac{f}{2}p + \rho c^2 = \frac{p}{\gamma - 1} + \rho c^2 \tag{2.29}$$

where the adiabatic index $\gamma \equiv c_p/c_V = (f+2)/f$ for a number of degrees of freedom f was introduced. The specific enthalpy is then

$$h \equiv \frac{\epsilon + p}{\rho} = \frac{\gamma}{\gamma - 1}\frac{p}{\rho} + c^2 \tag{2.30}$$

which implicitly defines the *ideal gas EoS* for a given adiabatic index. From the first law of thermodynamics one can derive the relation

$$p = Q(S)\rho^{\gamma} \tag{2.31}$$

between pressure, density and a quantity $Q(S) = \exp((\gamma-1)S)$ that solely depends on the entropy S. It is called pseudo-entropy and is customarily used instead of S. By assuming $S \equiv const.$ (isentropic flow), relation (2.31) defines the *polytropic EoS*. Just like the isothermal case, the polytropic EoS can be used to eliminate the energy equation, however the constancy of entropy forbids irreversible thermodynamic processes such as shocks. The sound-speed of the ideal gas EoS reads

$$c_{\mathrm{s}}^2 \equiv \left.\frac{\partial p}{\partial \epsilon}\right|_S = \frac{\gamma p}{\rho h}c^2 = c^2 \frac{\gamma}{\rho c^2 p^{-1} + \frac{\gamma}{\gamma - 1}} \leq (\gamma - 1)c^2. \tag{2.32}$$

We see that the high-temperature limit, the constant $\gamma > 2$ law encounters a problem, as c_{s} becomes super-luminal in conflict with causality.

2.1.7.1 Synge Gas

For a non-relativistic mono-atomic gas the number of degrees of freedom yield $f = 3$, or $\gamma = 5/3$, whereas a relativistic kinetic plasma theory yields the adiabatic index $\gamma = 4/3$ for the high temperature limit. Like the photon gas, a hot relativistic plasma thus features $\epsilon = 3p$. For intermediate temperatures, the EoS is bound

[3] where $k_{\mathrm{B}}, T, m_{\mathrm{p}}$ signify the Boltzmann constant, temperature and particle mass, respectively.

between the two limiting cases to the gas law found by Synge (1957). In terms of the inverse temperature $z \equiv \rho c^2/p$, the enthalpy of the *Synge gas* is given by

$$h_{\mathrm{S}}(z) = c^2 \frac{K_3(z)}{K_2(z)} \tag{2.33}$$

where K_n denotes the modified Bessel function of the second kind.

The adiabatic index of the Synge gas smoothly varies between $(4/3, 5/3)$ and it is customary to define an effective index valid for the local temperature. At least two alternative definitions exist in the literature. One way is to write the enthalpy in analogy to (2.30) and solve for the *effective adiabatic index*

$$\hat{\gamma}(z) \equiv \frac{h - c^2}{h - c^2 - z^{-1}} \tag{2.34}$$

(e.g. Anile 1989; Mignone & McKinney 2007). An alternative is to obtain the exponent from the functional form of (2.31) via

$$\hat{n} \equiv \left. \frac{\partial \ln p}{\partial \ln \rho} \right|_S , \tag{2.35}$$

(e.g. Meliani et al. 2004). To avoid confusion, we shall refer to $\hat{n}$ as the *polytropic index* which in general differs from the previous definition for the effective adiabatic index. Its limiting behavior however is identical. Using the thermodynamic identity $d\epsilon = hd\rho$ $(dS = 0)$, we can relate the sound speed to the polytropic index

$$c_{\mathrm{s}}^2 = \hat{n} \frac{p}{\rho h} c^2 \tag{2.36}$$

in analogy to the ideal gas (2.32).

In relativistic hydrodynamics, EoS of the form $h = h(z)$ are adopted in most cases. Let us therefore state the following useful

Corollary 1 *For an EoS given by $h = h(z)$, the sound speed takes the form*

$$c_{\mathrm{s}}^2 = \frac{1}{h} \frac{h'}{zh' + z^{-1}} c^2 \tag{2.37}$$

where h' is the derivative $h' = dh/dz$ (Mignone & McKinney 2007).

Proof: With the isentropic relations $d\epsilon = hd\rho$ and $pdh = z^{-1} c_{\mathrm{s}}^2 dp$ the sound speed defined by (2.32) becomes

$$c_{\mathrm{s}}^2 = z \frac{p}{hc^2} \frac{\partial h}{\partial \rho} \tag{2.38}$$

and (2.37) simply follows from the application of the chain rule $\partial h/\partial \rho = \partial h/\partial z \partial z/\partial \rho$.

The sound speed corresponding to the Synge gas thus reads

$$c_{\mathrm{s,S}}^2 = \frac{1}{G}\frac{G'}{zG' + z^{-1}}c^2 \tag{2.39}$$

where the derivative of the Bessel ratio $G(z) = K_3(z)/K_2(z)$ is given by $G'(z) = G^2 - 1 - 5G/z$ due to the recurrence relations. In the limit $z \to 0$, the squared sound speed approaches its maximum value $c_{\mathrm{s}}^2 = 1/3c^2$. The variation of the effective adiabatic index $\hat{\gamma}$ and sound speed with inverse temperature is shown in figure 2.1.

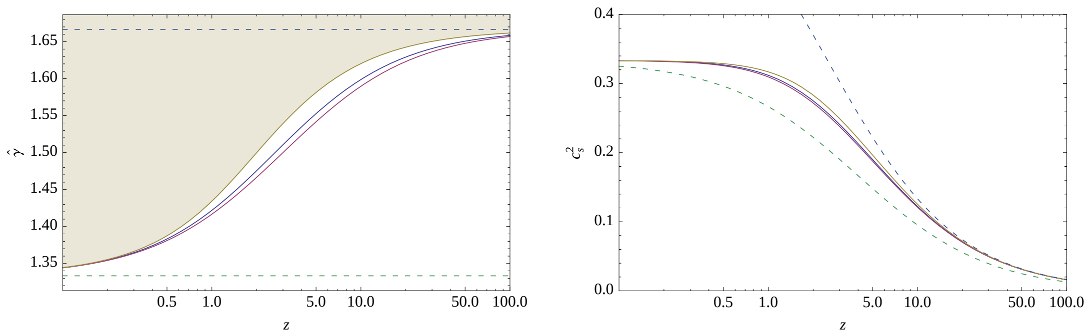

Figure 2.1 *Left:* effective adiabatic indices as a function of $z = \rho c^2/p$ for various equations of state. Blue: Synge gas, red: RC EoS, beige: TM EoS. The ideal gas laws for $\gamma = 4/3$ and $\gamma = 5/3$ are shown dashed and the region forbidden by the Taub inequality is shaded beige. *Right:* Corresponding squared sound speeds in units of c^2.

In addition to the causality constraint $\hat{n} < 2$, relativistic kinetic theory provides another more rigorous stability condition known as Taub's fundamental inequality (Taub 1948)

$$(h - c^2 z^{-1})(h - 4c^2 z^{-1}) \geq c^2. \tag{2.40}$$

By taking the equal sign in latter relation, Mathews (1971) introduced the TM EoS where the enthalpy and corresponding sound speed are given by

$$h_{\mathrm{TM}}(z) = c^2 \frac{5z + z\sqrt{9 + 4z^2}}{2z^2} \tag{2.41}$$

$$c_{\mathrm{s,TM}}^2 = c^2 \frac{c^2}{3\,h\,z}\frac{5h\,z - 8c^2}{h\,z - c^2}. \tag{2.42}$$

The admitted physical states are bound by the Taub criterion, $\gamma \leq \hat{\gamma}_{\mathrm{TM}}(z)$. It provides a very good approximation to the Synge gas. In a numerical code, the frequent evaluation of the Bessel functions renders a direct implementation of the Synge EoS costly (see e.g. Falle & Komissarov 1996), therefore fast approximations like the TM EoS are commonly used in numerical codes. It is implemented in

PLUTO and AMRVAC (Mignone et al. 2007; Meliani & Keppens 2010) as the Synge-type relativistic EoS.

Another even faster and more accurate approximation to the Synge gas was introduced by Ryu et al. (2006), hereafter called RC. The enthalpy reads

$$h_{\mathrm{RC}}(z) = 2c^2 \frac{6 + 4z + z^2}{3z + 2z^2}. \tag{2.43}$$

As depicted in figure 2.1, Synge gas, RC EoS and the $\gamma = 4/3$ law obey Taub's inequality everywhere. The difference between the sound speed derived from the RC EoS and the Synge gas is barely visible in the curves. Further discussion of various alternative EoS and their impact in relativistic (M)HD can be found in Falle & Komissarov (1996), Mignone et al. (2005), Ryu et al. (2006) and Mignone & McKinney (2007).

2.2 Relations in Axisymmetric MHD

The region of jet formation may be fairly well approximated in *axisymmetry*. In fact, non-axisymmetric distortions may actually hinder the formation of powerful jets as probably demonstrated by the existence of a variety of strongly magnetized, rapidly rotating accretion disk systems which, however, do not exhibit jets (e.g. cataclysmic variables or most pulsars). Whenever axisymmetry is invoked, the coordinates are divided into *poloidal* part in the (r, z)-plane, indicated by subscript $(\cdot)_p$ and the *toroidal* part in ϕ-direction, indicated by subscript $(\cdot)_\phi$.

Under the assumed symmetry in a cylindrical coordinate system, the magnetic field vector can be split as

$$\mathbf{B} = \mathbf{B}_p + B_\phi \mathbf{e}_\phi, \tag{2.44}$$

where B_ϕ can now be an arbitrary function of r and z, as the solenoidal condition translates to $\nabla \cdot \mathbf{B_p} = 0$. The poloidal field can be conveniently associated to the stream function $\Psi(r, z) = (1/2\pi) \int \mathbf{dS} \cdot \mathbf{B_p}$, which measures the magnetic flux through the surface area S. The poloidal field $\mathbf{B_p}$ thus follows alternatively from the toroidal component of the vector potential

$$\mathbf{B_p} = \nabla \times \mathbf{A}_\phi, \tag{2.45}$$

or the stream function to read

$$\mathbf{B_p} = \nabla \times \frac{\Psi\ \mathbf{e}_\phi}{r} = \frac{1}{r} \nabla\Psi \times\ \mathbf{e}_\phi. \tag{2.46}$$

2.2.1 The Electric Field

A major difference between relativistic MHD and non-relativistic MHD is the occurrence of the *electric field* in the equations. This not at all in contradiction to the ideal MHD condition which merely assumes negligible *co-moving* electric fields. In the lab-frame, the electric field $\mathbf{E} = \mathbf{B} \times \boldsymbol{\beta}$ couples to the charge density $\rho_{\mathrm{e}} \equiv 1/4\pi \nabla \cdot \mathbf{E}$ and thus enters into the Euler equation introducing an additional term $\propto \beta^2$. Naturally, the non-relativistic limit is obtained for $v \ll c$.

In axisymmetry, the ideal MHD condition $\mathbf{E} = \mathbf{B} \times \boldsymbol{\beta}$ gives

$$\mathbf{E} = \frac{r\Omega}{c} \mathbf{B_p} \times \mathbf{e}_\phi = \frac{r}{r_{\mathrm{L}}} \mathbf{B_p} \times \mathbf{e}_\phi \tag{2.47}$$

in terms of the so called angular velocity of the field line

$$r\Omega \equiv v_\phi - v_p B_\phi / B_p \tag{2.48}$$

or the *light cylinder radius* $r_{\mathrm{L}} \equiv c/\Omega$. At the light cylinder $r/r_{\mathrm{L}} = 1$, the hypothetic rotational velocity of the field line $r\Omega$ supersedes the speed of light. In terms of the light cylinder, the electric charge becomes

$$\rho_{\mathrm{e}} = \frac{r}{r_{\mathrm{L}} c} j_\phi + \frac{B_p}{4\pi r c} \nabla \left(r^2 / r_{\mathrm{L}} \right) \tag{2.49}$$

and is of importance only for $r > r_L$.

The direction of the electric field is given by $-\nabla \boldsymbol{\Psi}$ and therefore the magnetic flux surfaces also represent equipotentials of the electric field. The ideal MHD condition guarantees $E < B$ everywhere in the flow, however the magnitude of E surpasses the *poloidal* field strength B_p at the light cylinder from where it begins to execute a governing influence over the dynamics. The (de-) collimating influence of the electric field will be discussed in detail by means of the force-balance along the jet solutions in chapter 4. With the equipotential nature of the flux surfaces, the electric field has no component in direction of the flow and can thus influence flow acceleration only via effecting on the (differential) collimation of the flow.

With the magnetic and electric fields introduced, it remains to define the Poynting flux $\mathcal{S} \equiv (c/4\pi) \mathbf{E} \times \mathbf{B}$. In stationary axisymmetry, $\mathcal{S}$ simplifies to

$$\mathcal{S} = -\frac{c}{4\pi} \frac{r}{r_{\mathrm{L}}} B_\phi \mathbf{B_p} = -r\Omega \frac{B_\phi \mathbf{B_p}}{4\pi}. \tag{2.50}$$

This is the main energy reservoir out of which flow acceleration can be fed. In order to acquire relativistic speeds, the base of the flow has to be in fact *Poynting dominated*, which simply states that the Poynting flux trumps rest-mass energy at the launching site of the jet.

2.2.2 Field Line Constants

Stationary axisymmetric MHD flows conserve the following five quantities along the magnetic flux-function $\Psi = \Psi(r, z)$. From the iso-rotation law together with the ideal MHD condition follows the rest mass energy-flux per magnetic induction,

$$k(\Psi) \equiv \frac{\rho u_p}{B_p} \tag{2.51}$$

and the iso-rotation parameter can be deduced from Faradays law to

$$\Omega(\Psi) \equiv \frac{1}{r}\left(v_\phi - v_p \frac{B_\phi}{B_p}\right). \tag{2.52}$$

This is often interpreted as angular velocity of the field lines. In absence of shocks the (pseudo-) entropy

$$Q(\Psi) \equiv \frac{p}{\rho^\gamma} \tag{2.53}$$

is conserved, as well as the angular momentum flux

$$l(\Psi) \equiv -\frac{I}{2\pi kc} + r u_\phi \tag{2.54}$$

and the flux ratio of total energy to rest-mass energy,

$$\mu(\Psi) \equiv \frac{\mathcal{S} + \mathcal{K} + \mathcal{M} + \mathcal{T} + \mathcal{G}}{\mathcal{M}} \tag{2.55}$$

where we identify the individual terms as (purely) kinetic energy flux $\mathcal{K} \equiv (\Gamma - 1)\rho\ u_p c^2$, rest-mass energy flux $\mathcal{M} \equiv \rho\ u_p c^2$, thermal energy flux $\mathcal{T} \equiv \Gamma \frac{\gamma}{\gamma-1} p\ u_p c^2$, and gravitational energy flux $\mathcal{G} \equiv \rho\ \phi\ u_p$, respectively. The cold limit of (2.55) is particularly of interest, it reads

$$\mu = \Gamma(\sigma + 1) \tag{2.56}$$

where $\sigma = \mathcal{S}/(\mathcal{K} + \mathcal{M})$ is the customarily defined magnetization parameter - the ratio of Poynting to kinetic flux. This simple relation provides a theoretical maximum for the Lorentz-factor $\Gamma_\infty = \mu$, when the entire energy is converted into kinetic energy, hence $\sigma \to 0$.

2.2.3 Critical Points of the MHD Equations

In stationary flows, critical points arise in the wind equation where the derivatives of the conserved quantities with respect to the parametrization vanishes and thus the "solution speed" becomes zero. Passing smoothly through the critical points is thus a big challenge when dealing with the stationary fluid equations. Although this problem is less severe in time-dependent MHD, we shall demonstrate that knowledge about the positions of the critical points is still required in order to formulate a well posed boundary value problem.

Whereas hydrodynamical flows exhibit one critical point at the sonic surface, MHD possess three critical points associated with the three wave speeds: the slow magnetosonic velocity $v_{\rm SL}$, the Alfvén velocity $v_{\rm A}$ and the fast magnetosonic velocity $v_{\rm FM}$. By considering the relativistic wind equation, Camenzind (1986b) presented the critical velocities in the axisymmetric Minkowski space. They follow from the dispersion relation

$$u_p^4 - u_p^2\left(u_{\rm A}^2 + \frac{B_\phi^2}{4\pi\rho h} + u_{\rm s}^2\right) + u_{\rm s}^2 u_{\rm A}^2 = 0 \tag{2.57}$$

where u_s^2 describes the sound four velocity $u_s^2 = c_s^2/(1-c_s^2)$ and $u_{\rm A}$ the critical Minkowski Alfvén speed

$$u_{\rm A}^2 \equiv \frac{B_p^2(1-(r/r_{\rm L})^2)}{4\pi\rho h}. \tag{2.58}$$

In analogy to the non-relativistic case[4] , we can write the defining equation for the slow and fast magnetosonic critical point as

$$(u_p^2 - u_{\rm FM}^2)(u_p^2 - u_{\rm SL}^2) = 0. \tag{2.59}$$

In a cold flow $u_{\rm s} \ll u_{\rm A}$, the critical velocities assume the simple form:

$$u_{\rm FM}^2 \simeq u_{\rm A}^2 + \frac{B_\phi^2}{4\pi\rho h} + u_{\rm s}^2 \tag{2.60}$$

$$u_{\rm SL}^2 \simeq \frac{u_{\rm s}^2 u_{\rm A}^2}{u_{\rm FM}^2} \tag{2.61}$$

which we will adopt for the rendering of the Mach surfaces in sections 4 and 5.

The occurrence of critical points is closely linked to the concept of characteristics. In MHD, seven characteristics corresponding to the wave speeds $\pm u_{\rm SL}$, $\pm u_{\rm A}$, $\pm u_{\rm FM}$ and the entropy disturbance $u_E = 0$ have to be taken into account (for a derivation, see Goedbloed & Poedts 2004). These convey the information of the physical state at the boundaries (encoded in the associated Riemann invariants, e.g. Landau & Lifshitz 1959) up- and downstream of the flow. Due to the $\nabla \cdot B = 0$ condition, the eight variables of MHD are in fact determined by just seven waves arising in the system. An interesting situation occurs where the flow

[4]Early works on relativistic pulsar winds claimed the existence of an additional *pure* Alfvén critical point, or the light-cylinder as an additional critical point (see e.g.: Okamoto 1978). However, based on the method of characteristics, it can be shown that the number of critical points in a hyperbolic partial differential equation like the time-dependent set of MHD exactly equals the number of allowed wave solutions in the system. Ergo no additional critical point is allowed to occur in the time-dependent and also in the stationary system (see also Bogovalov 1997).

speed v corresponds to the characteristic velocity v_c: the upstream characteristic $v - v_c$ can not traverse over this critical point from the super-critical region, instead both characteristics point in the down-stream direction. In the sub-critical region, the upstream characteristic can only extend to the critical point and therefore the physical state *at the critical surface* is encoded in its Riemann invariant. For this reason, critical points constitute *internal boundaries* of the flow. This can be nicely visualized in the Minkowski-type x-t diagram shown in figure 2.2.

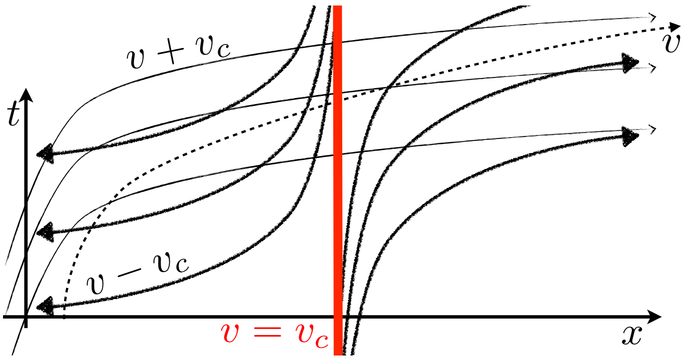

Figure 2.2 x-t (Minkowski) diagram illustrating the run of the $v + v_{\rm c}$ and $v - v_{\rm c}$ characteristics in the vicinity of a critical point. The $v - v_{\rm c}$ characteristic conveys the critical point information up- and downstream of the flow. The critical point given by $v - v_{\rm c} = 0$ constitutes an internal boundary condition.

A special situation occurs in the super-fast magnetosonic region of the flow: all characteristics are pointing downstream and hence no communication back across the critical point is permitted. This has profound implications for the causality of the flow upstream of the fast point which is thus independent of anything happening in the super-fast magnetosonic region.[5] For example, violent (recollimation-) shocks occurring in the causally disconnected region could thus not perturb the upstream bulk-flow acceleration region. The causally disconnected region is thus a promising site for the production of shock accelerated particles in relativistic jets (e.g. Polko et al. 2010). In addition, global flow instabilities like the kink instability (e.g. Bateman 1978) are largely suppressed. By steepening of the mach cones, the super-fast flow could become completely causally decoupled, allowing no communication even across the flow which ultimately sets an end to the gradual acceleration of jets in relativistic MHD (see also: Zakamska et al. 2008).

The existence of the full set of characteristics is guaranteed by the hyperbolicity of the (time-dependent) ideal MHD equations. In special cases however, degeneracies in the characteristic waves occur: *1.* for wave propagation parallel to the

[5] As pointed out by Sauty et al. (2002), with the transformation $r \to 1/r$, the structure of the equations and causality at the fast magnetosonic point can be seen in close analogy to the light cones at the event horizon of a rotating black hole.

field, either the slow or the fast characteristic correspond to the Alfvén wave, *2.* for perpendicular propagation, both slow and Alfvén wave vanish. If in addition to *1.*, the Alfvén speed also equals the sound speed, then all waves travel with the same velocity (Goedbloed & Poedts 2004). These situations have to be handled with extra care when numerical solutions are obtained with modern Riemann solvers that take the characteristic wave speeds into account (e.g. Komissarov 1999; Koldoba et al. 2002).

One could argue that the inclusion of time-dependence in the equations allows for the characteristics to negotiate the critical point self-consistently and thus simulations appear to have no difficulty in crossing the critical points. However, also in the setup of time-dependent simulations, one important corollary has to be met:

Corollary 2 *The number of conditions to be assigned at a given boundary has to correspond to the number of characteristic waves traveling through the boundary to the simulation domain.*

"Proof:" In a well posed boundary value problem, the number of constraints equals the number of independent variables. For a proper determination of the system, the constraints given at the internal boundary (critical points) have to be allowed by the numerical boundary. Therefore each downstream critical point reduces the number of necessary constraints at an *inflow* boundary by one, while it adds one constraint to be given at an *outflow* boundary.

While there exists broad consensus on the number of allowed boundary constraints, the nature of the constraints can not be readily derived. This is largely due to the fact that the MHD Riemann invariants depend on a combination of the flow variables such that no simple relation between wave and associated constraint can be given directly. In addition, the complexities involved in deriving the invariants for MHD are considerable. An analytic solution to the relativistic MHD Riemann problem has only recently been obtained – for a special case by Romero et al. (2005) and for the general case by Giacomazzo & Rezzolla (2006). In practical applications, the boundary conditions for a given scenario have to be motivated by the physics of the problem, where care must be taken that the conditions of corollary 2 are met. Naturally, different authors make different choices for the constraints to describe the "same" physical problem. This is especially apparent in "disk-as-boundary" simulations which we will discuss in further details in section 3.2.

In the three-dimensional case, the ensemble of critical points describe a critical surface. It is interesting to note that for critical surfaces which cross the flow lines at an inclination, the internal boundary defined by the convergence of characteristics in general does not correspond to the positions where the velocities of the flow and wave-speeds coincide. Instead, it is given by the *separatrix characterisitc* defining a limiting surface for the upstream characteristics $\mathbf{v} - \mathbf{v}_c$. In time-steady flows, this corresponds to the new algebraic critical point and we can finally understand the difference between the critical velocities defined via Equations (2.57) and (2.58) and the "ordinary" wave speeds of RMHD (given by e.g. Keppens & Meliani 2008). At the classical critical point $\mathbf{v} - \mathbf{v}_c = 0$, the information transport via the upstream characteristic changes from the upstream to the downstream direction. Therefore, for small deviations from the critical point, it must be directed perpendicular to the flow. Since characteristics of the same family can not cross, the upstream characteristics have to asymptotically approach each other at the separatrix surface. Only when the critical surface is perpendicular to the flow lines, both surfaces coincide. We illustrate the split of the critical surface at the example of the fast magnetosonic Mach surface (FMS) in Figure 2.3. The new

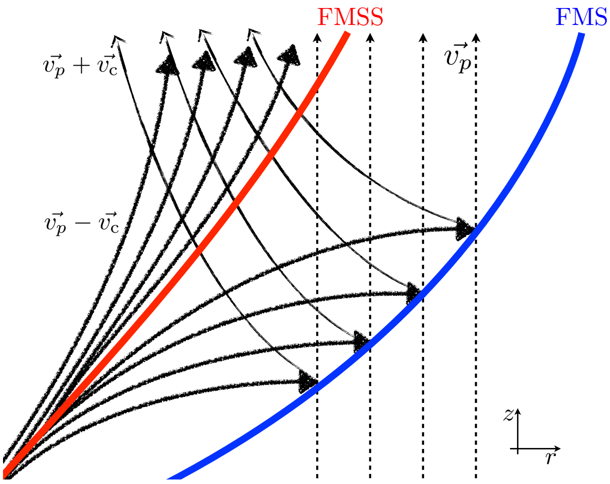

Figure 2.3 Sketch of the split between fast magnetosonic surface (FMS) and fast magnetosonic separatrix surface (FMSS). No communication "back" across the FMSS is allowed.

fast magnetosonic separatrix surface (FMSS) also defines the causal horizon of the flow (Bogovalov 1994; Tsinganos et al. 1996). In $r-$ self-similar models, the FMSS coincides with the so-called *modified fast point* (MFP) where the velocity component *towards the axis* equals the fast magnetosonic velocity and the flow causally decouples. Due to the restriction of self-similarity, the MFP is also the algebraic critical point (e.g. Ostriker 1997; Vlahakis et al. 2000; Vlahakis & Königl 2003). By construction, $r-$ self-similar models that cross over the MFP therefore always select solutions exhibiting a *recollimation* towards the axis.

2.2.4 Perpendicular Force-Balance and the Light Surface

The processes leading to flow collimation can be identified directly from the (steady-state) trans-field force-balance equation (Chiueh et al. 1991; Appl & Camenzind 1993). Here, we adopt the notation of the latter authors when investigating the collimation behavior in the quasi steady-state time domain of our simulations. Projecting the stationary momentum equation 2.22 perpendicular to the flux surface $\mathbf{n} = -\nabla\boldsymbol{\Psi}/\Psi$ and applying cylindrical coordinates, the curvature $\kappa \equiv \mathbf{n}\,(\mathbf{B_p}\cdot\nabla)\,\mathbf{B_p}/B_p^2$ of a flux surface $\Psi(r,z)$ can be written in terms of a the summation over the forces

$$\begin{aligned}
\kappa\frac{B_p^2}{4\pi}\left(1-M^2-\frac{r^2\Omega^2}{c^2}\right) = & \\
+\left(1-\frac{r^2\Omega^2}{c^2}\right)\nabla_\perp\frac{B_p^2}{8\pi}+\nabla_\perp\frac{B_\phi^2}{8\pi}+\nabla_\perp p & \\
+\left(\frac{B_\phi^2}{4\pi r}-\frac{\rho h u_\phi^2}{r}\right)\nabla_\perp r-\frac{B_p^2\Omega}{4\pi c^2}\nabla_\perp\left(r^2\Omega\right) & \\
+\Gamma\rho\nabla_\perp\phi, &
\end{aligned} \tag{2.62}$$

where we have added the collimating component of the gravitational force. For the ease of use in section 4.4.2.1, we label the terms as

$$(F_{\text{curv}}, F_{\text{pbp}}, F_{\text{pbphi}}, F_{\text{p}}, F_{\text{pinch}}, F_{\text{cf}}, F_{\text{el}}, F_{\text{grav}})$$

in the order of their appearance in Equation 2.62. In the adopted notation, the (poloidal) Alfvén Mach number M is relativistically defined as

$$M^2 \equiv \frac{4\pi\rho h u_p^2}{B_p^2}. \tag{2.63}$$

The gradient $\nabla_\perp \equiv \mathbf{n}\cdot\nabla$ is projected perpendicular to the magnetic flux surfaces Ψ, and thus along the (inward pointing) electric field.

The *light surface* of a magnetosphere is located where $r_{\text{L}}(\Psi) = r_{\text{L}}(r,z) \equiv c/\Omega(\Psi)$ [6], hence it depends on the flux-geometry as well as on the rotation profile Ω. Each flux surface / magnetic field line crosses the light surface at most once (see also the discussion in Fendt (1997b)). Some field lines $\Psi(r,z)$ never cross the light surface, indicating an asymptotic radius $r_\infty(\Psi) < r_{\text{L},\Psi}$. For these field lines relativistic effects due to rotation (electric fields) are less important. The light surface constitutes a critical point of the stationary axisymmetric wind equation

[6] Thus, the light surface consists of the points of intersection between the field lines with their corresponding light cylinder

only in the mass-less limit in which it is identical to the critical poloidal Alfvén surface $M_A^2 = 1 - (r_A/r_L)^2$ (Camenzind 1986a,b). However, it is essential to note that at the light surface the dynamical behavior of the poloidal magnetic pressure term changes, implying a sign change of the force. This leads to the existence of three dynamically different regimes in the asymptotic (collimated) region of a relativistic jet (see Fig. 2.4). In region I, for all field lines $r_\infty(\Psi) < r_{\mathrm{L},\Psi}$

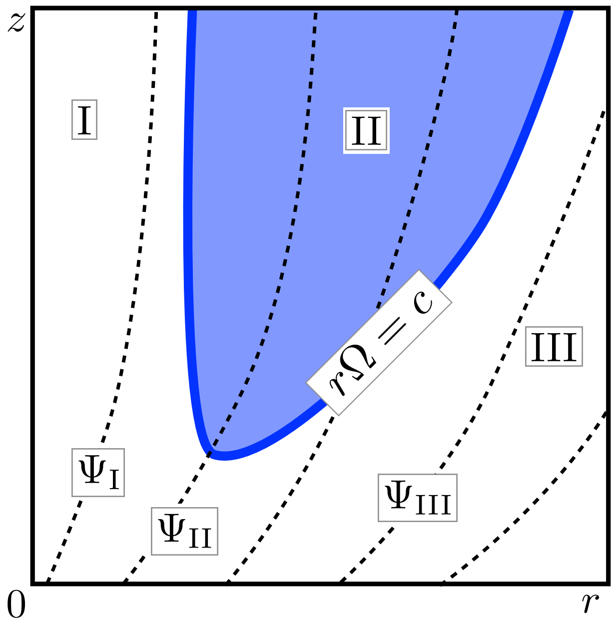

Figure 2.4 The different dynamical regimes in special relativistic disk-winds. Region I and III stay sub-relativistic, while region II is relativistic, i.e. electric forces are not negligible (see Sect. 2.2.4 for a discussion).

corresponding to $(1 - (r/r_\mathrm{L})^2) > 0$, and, thus, a de-collimating magnetic pressure term. Field lines in region II do cross their light cylinder, and, since $r > r_\mathrm{L}$, the magnetic pressure term acts as collimating for $r > r_\mathrm{L}$. Field lines in Region III never reach their light cylinder, and here the magnetic pressure term is de-collimating again. The slope of the outer part of the light surface critically depends on the dynamics and the magnetic field structure of the outflow in the very inner part.

Similarly, the forces due to the electric field $E = r/r_\mathrm{L} B_\mathrm{p}$ (second last term in Eq. 2.62) scale with the relative position to the light surface, hence they are important in region II of the jet formation region only.

Equation 2.62 together with Fig. 2.4 once again demonstrates the need to resolve the whole acceleration and collimation region of a jet in radial and vertical direction. Only when the light surface is taken into account self-consistently, the proper force-balance is applied along and across the flow.

2.2.5 Parallel Force-Balance

Projecting the momentum equation along the flow yields the parallel-field force equation, it reads:

$$\begin{aligned} \frac{B_p^2}{4\pi}\nabla_{||}M^2 = \kappa_{||}\frac{B_p^2}{4\pi}\left(1-M^2\right) \\ -\nabla_{||}\left(p+\frac{B_p^2}{8\pi}+\frac{B_\phi^2}{8\pi}\right) \\ -\left(\frac{B_\phi^2}{4\pi r}-\frac{\rho h u_\phi^2}{r}\right)\nabla_{||}r \\ -\Gamma\rho\nabla_{||}\phi \end{aligned} \tag{2.64}$$

with the necessary definitions $\nabla_{||} \equiv \mathbf{B_p}/B_p\nabla$ and $\kappa_{||}B_p^2 \equiv \mathbf{B_p}/B_p\left(\mathbf{B_p}\cdot\nabla\right)\mathbf{B_p}$. We see how the change in the Mach-number is mediated by the interplay of tension-, pressure-, pinch-, centrifugal- and gravitational- acceleration. Electric fields (pointing in the perpendicular direction) don't contribute and the equation reduces to the Newtonian case: In steady-state, there is no acceleration due to the electric field!

A number of self-similar approaches to the relativistic jet formation have been published (eg. Vlahakis & Königl (2003)). While the self-similar Ansatz is a powerful and highly successful tool to solve the non-relativistic MHD problem (starting with the Blandford-Payne solution), we believe that using self-similarity for relativistic MHD jets is problematic.

We note that neither the light surface nor the relativistic Alfvén surface obeys a self-similar structure. It is well known that forcing self-similarity into the relativistic MHD equations constrains the rotation law for the magnetosphere $\Omega^F(r) \propto r^{-1}$. (see also discussion in Li et al. 1992; Li 1993). This is a major difference to the non-relativistic self-similar approach. We further note that also the scaling for the electric field depends on the radial position of the light surface (see Eq. 2.47). This is, however, of uttermost importance for the structure of relativistic magnetospheres as the electric field forces play a leading role in the trans-field force-balance (equation 2.62). Similar arguments hold for the inner light surfaces around Kerr black holes or the geometry of the black hole ergosphere.

We therefore believe that a steady-state self-similar relativistic MHD approach is intrisically inconsistent with the relativistic characteristic of the flow.

2.3 Gravity in Special Relativity

The outcome of MHD simulations is mainly determined by the boundary conditions and great care is needed to provide a boundary that describes the physical state of interest. Since the jet in our simulations is considered to be launched as a sub-escape velocity wind from a rotating disk, it is essential to take into account a proper disk model as boundary condition. In particular, gravity is needed to counter-act disk rotation in the boundary as well as to stratify an atmosphere in the initial domain. This is the main reason why we have added gravity to our special relativistic treatment.

A way to mimic general relativistic effects in special relativity is to resort to so called Pseudo-Newtonian potentials introduced by Paczynsky & Wiita (1980) (PW). By conjecture, Bohdan Paczynsky found the potential

$$\phi_{\mathrm{PW}} = -\frac{GM}{R - r_{\mathrm{S}}} \tag{2.65}$$

which reproduces exactly the position of the marginally bound orbit, the marginally stable orbit (ISCO) and the form of the Keplerian angular momentum (see Abramowicz 2009, for a derivation).[7] An other pseudo-potential for the Schwarzschild metric was proposed by Nowak & Wagoner (1991) (NW). It was designed to yield a better fit for the Kepler and epicyclic frequencies than PW and reads

$$\phi_{\mathrm{NW}} = -\frac{GM}{R}\left(1 - 3\frac{GM}{Rc^2} + 12\left(\frac{GM}{Rc^2}\right)^2\right). \tag{2.66}$$

The effective potentials $V_{\mathrm{eff}} = \phi + L^2/(2r^2)$ and corresponding Kepler angular velocities Ω_{K} are shown in Figure 2.5 in comparison to the Newtonian and Schwarzschild case. Due to its conceptual simplicity, the PW potential has found widespread application in dynamical simulations of disk accretion (e.g. Hawley & Krolik 2001; Armitage et al. 2001; McKinney & Gammie 2002; Proga & Begelman 2003; Machida & Matsumoto 2003; Kato et al. 2004; Ohsuga & Mineshige 2011). A number of pseudo potentials for the Kerr metric have been proposed (e.g. Chakrabarti & Khanna 1992; Semerák & Karas 1999; Mukhopadhyay & Misra 2003; Ghosh 2004), however the expressions approximate the Kerr space-time only in the equatorial plane and none has acquired the popularity of the PW potential. Today, the increasing prevalence of (3+1 split) general relativistic codes reduces the need for more sophisticated pseudo potentials.

In this work, we do not focus on the region very close to the horizon of the central object, but on the long-term dynamics and evolution of a disk wind into a relativistic jet. As the outflow is accelerated to super escape speed quickly, the direct impact of gravity on the jet dynamics is marginal. Therefore we can safely neglect general relativistic effects in our simulation domain.

[7] The capital $R = \sqrt{r^2 + z^2}$ denotes the spherical radius throughout this work.

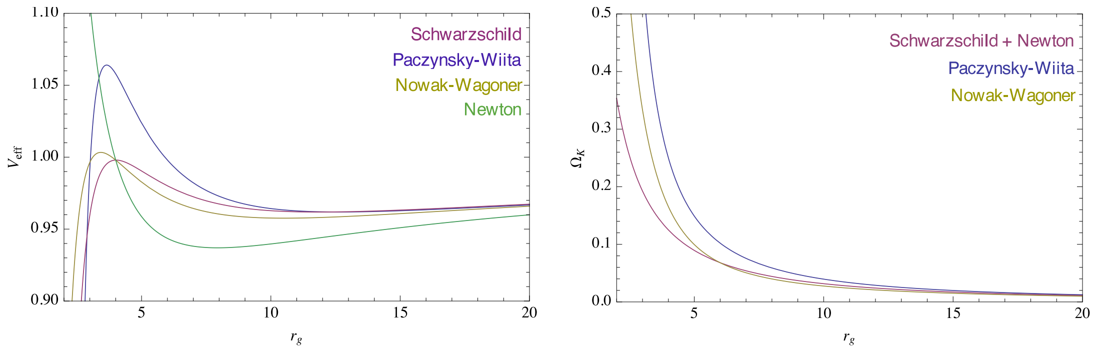

Figure 2.5 Pseudopotentials emulating a Schwarzschild metric. *Left:* Effective Potentials for $L = 1.15\, L_{\mathrm{ISCO}}$. The two extrema give rise to different kinds of circular orbits: unstable (inner) and stable (outer). For $L = L_{\mathrm{ISCO}}$ the two branches meet, defining the innermost stable circular orbit with radius $r_{\mathrm{ISCO}} = 6r_{\mathrm{g}} = 3r_{\mathrm{S}}$. All Pseudopotentials reproduce this behavior. *Right:* Corresponding Keplerian angular velocities. The NW potential is designed to reproduce the GR case at the ISCO and gives a better fit than the PW potential. The Schwarzschild and Newtonian cases match exactly.

In a special relativistic code, the (pseudo-) Newtonian acceleration can be added as a source term. Thus instead of equation 2.1, we solve

$$\partial_\alpha T^{\alpha\beta} = f^\beta \tag{2.67}$$

with the four force density

$$(f^\beta) = \Gamma\rho(-\nabla\phi \cdot \mathbf{v}, -\nabla\phi)^T \tag{2.68}$$

as a local source term on the right-hand side. This is incorporated in the numerical code PLUTO as a "body force" $\mathbf{a} = -\nabla\phi$ using the infrastructure of the code.

Due to the steep gradients in the $\propto 1/R$ potential close to the origin, we apply a softened potential

$$\phi = -\frac{GM}{R + r_{\mathrm{S}}} \tag{2.69}$$

for the study of section 4. Omission of softening would lead to numerical errors piling up to produce artificial acceleration along the spine of the jet close to the axis. Once the gradients are resolved properly, either via softening or increased resolution, the artificial effects vanish. The specific value of the softening length then has no influence on the jet dynamics.

The simulations of chapter 5 are performed with an alternative approach. Instead of providing an explicit softening, we simply offset the singular origin slightly from the domain by the vector $(\Delta r, \Delta z) = (0, -1/3)$ and thus adopt the potential

$$\phi = -\frac{GM}{\sqrt{r^2 + (z + r_{\mathrm{S}})^2}}. \tag{2.70}$$

Note that the usage of a PW potential would re-introduce a singularity in the simulation domain. It is better suited for spherical domains where the singularity can conveniently be cut out by the choice of the inner grid radius.

Chapter 3

Numerical Treatment

3.1 Grid Based MHD Codes

The equations of MHD are essentially hyperbolic conservation laws and can be solved with the numerical methods developed for this type of partial differential equations. Modern high resolution shock capturing schemes usually harness the finite volume spatial discretization which solves the integral form of the differential equations and advances the volume averages of the variables. Therefore, discontinuities and shocks are treated self-consistently and the *conservative* structure of the equations can be accounted for in a natural way. The latter property ensures that, upon convergence, the scheme actually approaches a weak solution of the conservation law. A review of the numerous numerical schemes devised for the simulation of relativistic astrophysical flows can be found by Martí & Müller (2003) and a comprehensive introduction to the matter is provided in Goedbloed et al. (2010). In this section, we shall only briefly review the principal ideas underlying the codes that are applied in the following chapters.

Following the method proposed by Godunov, the computational domain is divided into discrete cells and at the interfaces a (linearized) Riemann problem is solved to obtain the numerical flux between the cells $\mathbf{F}_{i\pm1/2}$. These are then used to update the conserved variables in the cell $\mathbf{U}_i^{n+1}$ according to

$$\mathbf{U}_i^{n+1} = \mathbf{U}_i^n - \frac{\Delta t}{\Delta x}\left[\mathbf{F}_{i+1/2} - \mathbf{F}_{i-1/2}\right]. \tag{3.1}$$

This is in fact the defining equation of a conservative scheme. A flow diagram of the PLUTO code is shown in Figure 3.1 which illustrates the general strategy in all Godunov-type schemes. By assuming constant values within the cells, Godunov's original scheme was at most first order accurate in space. Higher order can be obtained by a monotonous *reconstruction* of the values within the cell (and the fluxes at the interfaces). The spatial order then depends on the degree of the polynomial used for reconstruction, a linear interpolation will obtain second order accuracy, the piece-wise parabolic method (PPM) of Colella & Woodward (1984) is third order accurate and so on. Instead of solving the Riemann problem exactly, as this is

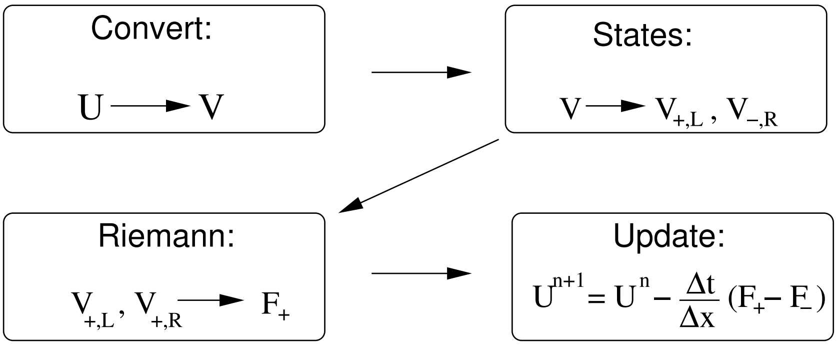

Figure 3.1 Simplified flow chart of a Godunov-type scheme for conservation laws, in particular the PLUTO code. The strategy is to 1. *convert* the conserved variables to primitive form, 2. *reconstruct* the left and right interface states, 3. *solve* the Riemann problem approximately to obtain the cell-interface fluxes and 4. *time-update* the conserved variables. (adopted from Mignone et al. (2007)).

computationally and theoretically very challenging, *approximate* Riemann solvers are employed. These substitute the 7-wave Riemann fan by a reduced number of characteristics, taking into account only the fastest wave speeds. Approximate Riemann solvers that are generalized to special relativistic MHD range from taking in to account only one wave in form of the TVDLF solver up to the five waves treated by the HLLD Riemann solver (Mignone et al. 2009). This full spread of Riemann solvers is implemented in the PLUTO and AMRVAC codes and the choice between one or the other is a matter of robustness and requirements on numerical diffusion.

In practice, the Riemann problem demands the knowledge of the inner cell primitive variables that enter into the flux calculation (see also Toro 1999). This calls for a *conversion* from a set of conservative to the corresponding primitive variables which, due to its highly non-linear nature, is the “Achilles heel” of all conservative relativistic fluid codes. Typically, the conversion is performed with a Newton-Raphson solver over the non-linear system of equations defined by the inversion of (2.18), (2.20) and (2.21). Since conserved and primitive magnetic field are identical, a 5×5 system has to be solved. This was illustrated by Balsara (2001) by directly considering the Jacobian matrix of the transformation. By rearranging the equations, Komissarov (1999) could reduce this to a 3×3 system and Del Zanna et al. (2003) reduced further to a 2×2 system of equations. Finally, Mignone & Bodo (2006) presented a single equation that needs to be solved iteratively. Especially for high $\sigma-$ flows, the iteration however does not always converge to the required accuracy. In these cases a special treatment is called for that typically involves an increase of numerical diffusion or the solution of supplementary conservation laws such as the entropy equation.

Although the induction equation $\partial_t \mathbf{B} = \nabla \times (\mathbf{v} \times \mathbf{B})$ analytically preserves a solenoidal magnetic field ($\nabla \cdot \mathbf{B} = 0$), the numerical scheme could still generate spurious monopoles. The accumulating numerical errors can then lead to unphysical solutions and instabilities. Therefore extra attention is needed to handle the divergence of $\mathbf{B}$. Many strategies to ensure solenoidal fields were developed in the past and most are successful in maintaining a divergence with negligible influence on the solution. A detailed comparison of the schemes is provided by Tóth (2000) and we only mention the ones available in PLUTO, respectively AMRVAC. The constrained transport (CT) method going back to Evans & Hawley (1988) defines the magnetic fields on the cell interfaces leading to a *staggered* representation of the fields. By utilizing Stokes theorem, a solenoidal staggered field can thus be maintained within machine precision by the algorithm. This is capitalized by the codes in the tradition of ZEUS (Stone & Norman 1992) and also PLUTO has the capability of using staggered fields. A clear disadvantage of the staggering is the offset between magnetic fields and remaining variables which requires additional interpolation.[1] Another method was proposed by Powell (1994) and introduces an eighth wave to the set of existing characteristics. Since this involves additional source terms, the strict conservation form of the scheme (3.1) is violated, which could result in incorrect solutions at discontinuities. As the divergence of $\mathbf{B}$ is merely advected by the eight wave scheme, it is advisable to add an additional diffusion term, leading the divergence cleaning algorithms put forward by Dedner et al. (2002). Divergence cleaning thus transports and damps the spurious monopoles, in addition, a cell-centered representation can be maintained (see also the comparison of divergence cleaning methods by Keppens et al. 2003).

It remains to mention the time-marching scheme. Although advanced methods have been developed for MHD, the schemes typically employed for relativistic flows rely on the robust but somewhat costly Runge-Kutta (RK) type schemes. Temporal accuracy can thus easily be obtained by using a $2nd$, $3rd$ or in the case of AMRVAC also a $4th$ order accurate RK scheme.

[1] As shown by Tóth (2000), a grid staggering is actually not necessary for the CT method and can be avoided by *temporal* averaging to obtain the staggered values.

3.1.1 PLUTO

The PLUTO code for numerical astrophysics[2], developed and maintained by Andrea Mignone and collaborators (Mignone et al. 2007) is a modular package written in the *C* language. Among other things, it is capable of ideal special relativistic hydro- and magnetohydrodynamics in various coordinate systems. Adaptive mesh refinement can be provided by the CHOMBO library[3]. The code is licensed under the GNU public license.

In the simulations of chapter 4 and 5 we use the PLUTO code in version 3.0.1, employing cylindrical coordinates. To follow the dynamics over large distances beyond the fast magnetosonic point, a (staggered) stretched grid is used. Much dedication is put into the proper treatment of the disk boundary and the development and testing of a current-free outflow boundary (detailed further in Appendix B.1). For robustness, we employ the rigid hll Riemann solver and rely on the RK3 time marching scheme. Using linear reconstruction, second order spatial accuracy is obtained. PLUTO is parallelized by means of the message passing interface (MPI) and the Arraylib library. The single block configuration is highly scalable, showing strong scaling up to 32.768 Blue Gene/P cores at 512^3 grid cells.

3.1.1.1 Scalability

We extensively use the parallel capabilities of the code. A typical production run of chapter 4 with 512×1024 grid cells is thus performed within two days on 16 cores of the PIA cluster of MPIA. Production runs shown in chpater 5 were performed with the JADE machine at CINES under the HPC-EUROPA2 project. The simulations with a domain size of 2555×2555 show strong scaling with over 85% efficiency up to 512 cores. A science-run can thus be obtained within two days and by consuming $\simeq 24$Kcpu h. Benchmarks and scaling of the production setups are shown in figure 3.2.

3.1.2 MPI-AMRVAC

The adaptive mesh refinement versatile advection code (AMRVAC) is a software package for astrophysical fluid dynamics developed by Rony Keppens and collaborators in Leuven/Belgium (Keppens et al. 2011). It offers special relativistic (M)HD capabilities. Block based adaptive mesh refinement (AMR) and MPI-parallelism is intrinsic to the code which is thus independent of additional libraries. For the expensive three-dimensional simulations outlined in section 7, we rely heavily on

[2] http://plutocode.ph.unito.it/
[3] https://seesar.lbl.gov/anag/chombo/

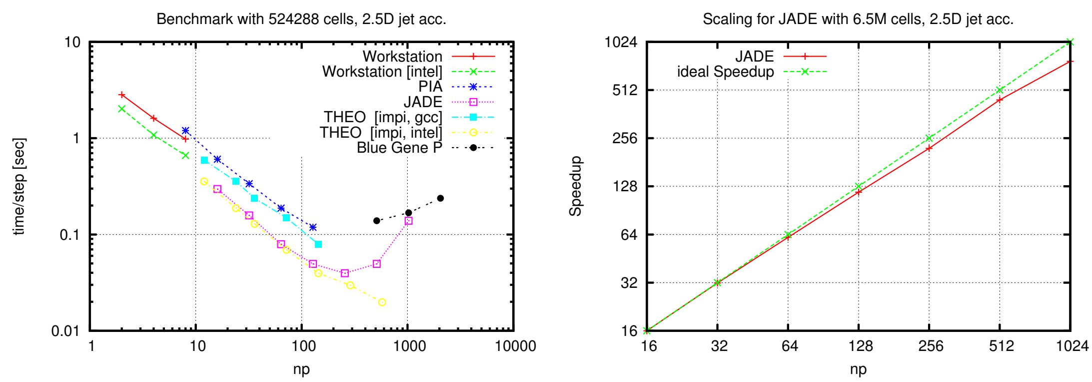

Figure 3.2 *Left:* Benchmark of PLUTO on various machines with MPI parallelization. The standard jet formation setup discussed in chapter 4 is used. Shown is the average time per step for an octo-core workstation, the former PIA cluster of MPIA, the SGI Altix machine JADE of CINES/Montpellier, the current THEO cluster of MPIA and the IBM Blue Gene/P at RZG/Garching (provided by Mario Flock). The usage of Intel compilers gives a significant speedup compared to the gcc. *Right:* Scaling of PLUTO using the production setup of section 5 on the JADE machine. A scaling with over 85% efficiency up to 512 cores is obtained.

the AMR and to optimally benefit from the mesh refinement, a special strategy has to be employed. In addition, the non-linear scaling of a mesh refinement code renders the cost estimation a non-trivial task which is thus investigated in more detail below.

3.1.2.1 Refinement Strategy

At the highest level, all simulations feature a resolution of 12 grid cells per unit radius ("inner disk radii"), leading to 240 cells[4] across the jet inlet diameter where the highest refinement level is enforced. In the production setup, cartesian coordinates are used which necessarily leads to additional $m = 4$ mode noise. Refinement of the jet is based on the scheme proposed by Lohner (1987) with weighted contributions of density, Lorentz factor and magnetic field strength.

As additional criterion, the initial domain is coarsened to the lowest level until the jet comes within reach. This decision is based on the Lorentz factor ($\Gamma > 1.05$) and a passive tracer scalar that is advected with the jet flow. Therefore an additional advection equation for passive scalars ι_n is implemented in the code:

$$\partial_t \iota_n + v^j \partial_j \iota_n = 0. \tag{3.2}$$

This is cast as conservation law

$$\partial_t \Gamma \rho \iota_n + \partial_j (v^j \Gamma \rho \iota_n) = 0 \tag{3.3}$$

[4] 480 for case 160M with double inlet size.

where took advantage of the conservation of mass given by the continuity equation (2.3). This is easily appended to the set of equations (2.25). At the jet inlet, the boundary condition of the tracer-scalar is set to one which thus "colors" the jet-material. The criterion in terms of the Lorentz-factor is however still required in order to avoid coarsening of the torsional Alfvén wave launched at the switch on of disk-rotation; it does not transport jet-inlet material. Thus the fast jet is always resolved appropriately, while the enforced coarsening significantly speeds up the simulations. Especially when the domain is initialized with a non-homogenous medium, the coarsening-strategy is crucial. A rendering of the grid-refinement at an exemplary jet solution is shown in Figure 3.3.

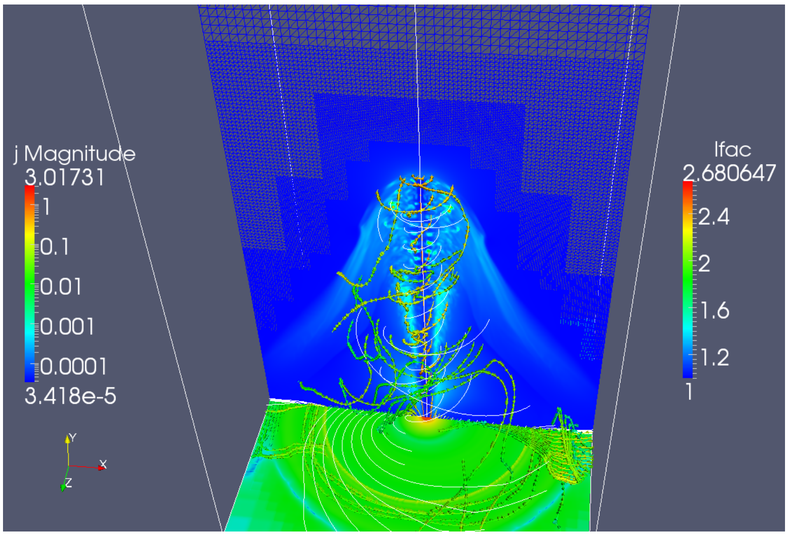

Figure 3.3 Slice through the jet showing Lorentz-factor and five-level mesh refinement. The current circuit and the field-lines within the jet are illustrated by stream-lines.

3.1.2.2 Scalability

Cost estimation of a single-block grid code is a simple exercise: based on a low-resolution, small-domain run, the execution time for a double resolution run will be increased by a factor of 2^{N_d+1}, where N_d is the number of spatial dimensions. The additional factor of two arrises due to the CFL criterion (Courant et al. 1928) which requires a decrease of the time-step in the high-resolution run. For a doubling of the domain, only a factor of two per dimension is required. In an adaptive code on the other hand, the number of active cells depends on the problem and typically increases with time when going from a simple initial state to an interesting final state. This calls for a scaling analysis directly with the production setup at a "meaningful" intermediate time.

We thus perform several test simulations and use the snapshots where the jet has traversed halfway through the simulation box for scaling analysis. This should give a fair impression on the actual timing of the simulations used for scientific production. The simulations are detailed in table 3.1. Two ghost zones are used on each side of the blocks. For the scaling analysis, one physical time unit ($\sim$ 100 timesteps) with subsequent snapshot output is computed. The code provides timings for the various tasks such as re-grid, IO and boundary condition calculation.

Table 3.1 Simulations for scaling analysis

ID	Domain	base cells	Blocks	T_{snap}	level population	# active
40M	32 x 64 x 32	48 x 96 x 48	12^3	40	48 196 900 21216	40M
40MnoAMR	32 x 64 x 32	48 x 96 x 48	12^3	40	0 0 0 65536	40M
40Mb16	32 x 64 x 32	48 x 96 x 48	16^3	40	18 88 432 9344	40M
160M	64 x 128 x 64	48 x 96 x 48	12^3	100	48 228 1213 5911 86024	160M

Note. — 40MnoAMR enforces refinement to the highest level in order to estimate the AMR speedup.

To investigate the impact of block size and AMR, a comparatively small physical domain is run. The setup 40M with 10^8 effective cells scales to $\sim$ 256 cores. An increased block size should lead to lower computational overhead due to inter-block communication. Surprisingly, however, the simulation with increased block size (16^3), "40Mb16" shows very similar timing and scalability compared to 40M (see figure 3.4). In fact, the scaling and timing is slightly worse when a larger block size is used as illustrated in figure 3.5 (left), such that we will stick with fine-grained 12^3 blocks, allowing more refinement flexibility. To measure the impact of the AMR on the timing, the run 40MnoAMR is performed. At 256 cores, the comparison run 40M is faster by a factor of 2.8 which denotes the "AMR speedup".

Finally, the production setup "160M" is benchmarked, with $\sim 10^9$ effective cells in five grid levels. Neglecting IO, this run scales to 1024 cores with 86% efficiency. As the simulation progresses, more grid levels are filled such that we expect to still improve on the scalability towards the end of the simulation. Scaling is broken by the serial IO procedures of the AMRVAC code. The size of the T_{100} snapshot file amounts to 16GB which requires to limit the frequency of snapshot output to avoid performance losses and to meet disk space limitations.

To circumvent the IO bottleneck, we implemented the parallel .pvtu file format for post-processing which introduces virtually no computational overhead. However, to allow the restart of simulations, serial snapshot data still has to be written

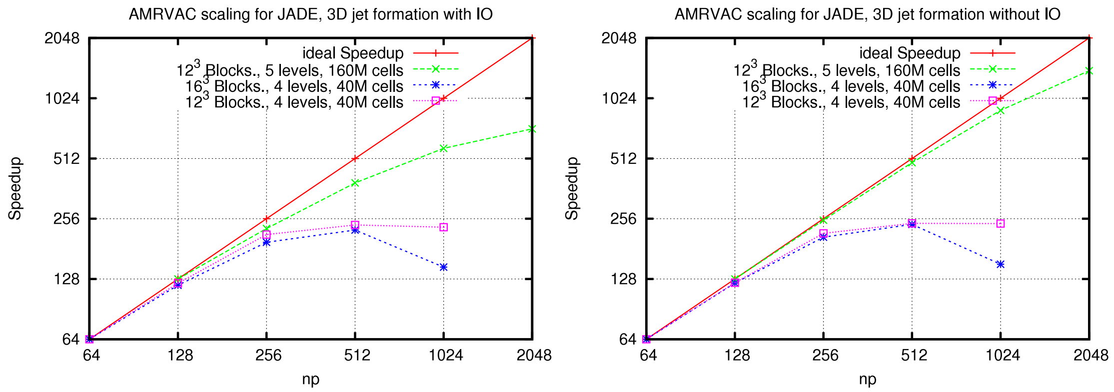

Figure 3.4 Scaling of the simulation setups. *Left:* including one IO cycle per physical time, *right:* without IO, the setup with 160M grid cells scales with over 85% efficiency to 1024 cores.

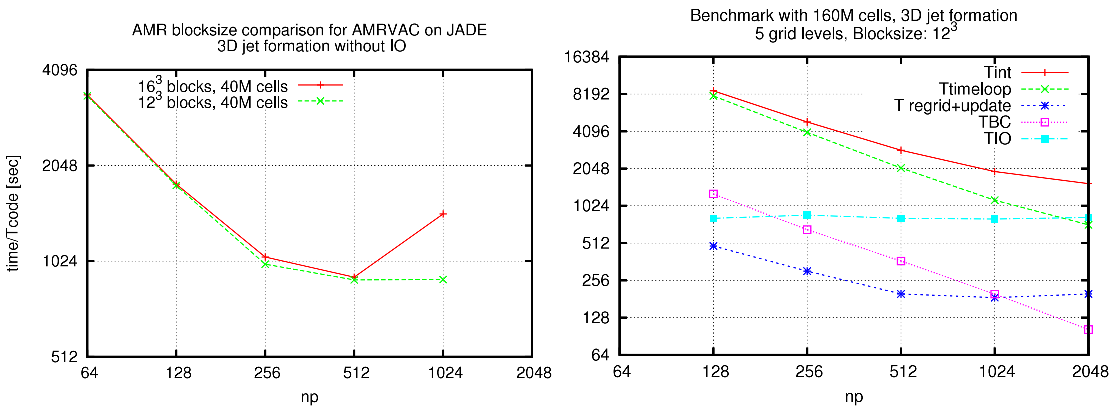

Figure 3.5 Block size comparison *(left)* and timing for case 160M *(right)*.

occasionally.

3.2 Injection in MHD Disk as Boundary Simulations

In disk as boundary simulations, the corona of a Keplerian accretion disk is modeled as a rotating boundary condition threaded by large scale magnetic fields. Matter is injected along the field lines and the acceleration of the plasma due to the Blandford & Payne (1982) mechanism is followed by the simulation.

Depending on the injection speed, the flow is expected to cross over fast, Alfvén or even the slow critical point downstream from the boundary. As outlined in section 2.2.3, the boundary conditions used to model the disk corona can not be chosen freely, but have to allow for the outgoing characteristics. Following Corollary 2, we see that the correct number of constraints for a sub-magnetoslow injection boundary is four, since the flow is expected to pass through three separatrix surfaces. In other words, there are four outgoing waves: the slow magnetosonic wave, the entropy wave, the Alfvén wave and the fast magnetosonic wave. Naturally, along a boundary where the flow is super magneto-slow the number of allowed constraints equals five due to the additional downstream slow wave. Within this limited freedom, those boundary conditions which best prescribe the astrophysical problem should be used. In the literature of "disk-as-boundary" jet formation simulations, a variety of choices for the injection boundary exist. Table 3.2 reviews a couple of them in chronological order.

Table 3.2 Injection conditions for disk-as boundary simulations

Authors	sub/super slow	# Out. Waves	# Const.	Nature of Const.
Ustyugova et al. (1995)[a]	sub	4	4	E_ϕ, E_r, v_z, s
Ouyed & Pudritz (1997)[b]	sub/super	4	6	$E_\phi, v_\phi, v_p, B_\phi, \rho, p$
Romanova et al. (1997)[c]	sub	3	3	E_ϕ, E_r, v_z
Krasnopolsky et al. (1999)[d]	super	5	5	$E_\phi, E_r, \rho, p, v_z$
Ustyugova et al. (1999)[e]	sub	4 - 5	4	E_ϕ, E_r, ρ, s
Komissarov et al. (2007)[f]	super	5	5	$E_\phi, B^\eta, \rho, v^\eta, \Omega$
Ramsey & Clarke (2011)[g]	sub	4	5	$E_\phi, \Omega, \rho, p, v_z$
Chapter 4	sub	4	4	E_ϕ, Ω, ρ, p
Chapter 5	super	5	5	$E_\phi, \rho, p, v_p, B_\phi$

Note. — ^{a} In the work of Ustyugova et al. (1995), mass flux is set as free parameter by allowing the disk density to evolve.
^{b} Ouyed & Pudritz (1997) and Fendt & Čemeljić (2002) allow no feedback from the jet to the disk and seem to over-determine their simulations. We were able to reproduce the consequences with our own simulations. A numerical boundary layer develops which creates a steep gradient $\partial_z \rho$ as the code tries to match the dense disk-boundary with the jet-solution (their figure 4). To conserve mass flux, the poloidal velocity will jump within a few grid cells, a spurious acceleration which is independent of resolution. Due to their additional Alfvén pressure, the injection velocity is not entirely clear to us, but we suspect it to be dynamically sub-slow.
^{c} Romanova et al. (1997) perform isothermal simulations without solving the energy equation. Since the sub-slow injection, constraints on the following three quantities are given, v_z, E_ϕ, E_r - just as Ustyugova et al. (1995).
^{d} Krasnopolsky et al. (1999) prescribe mass flux with the choice $(E_\phi, E_r, s, \rho, v_z)$ and super-slow injection.
^{e} Ustyugova et al. (1999) prescribe density ρ instead of the vertical velocity v_z (thus change from Ustyugova et al. (1995)). The injection speed is allowed to become super-sonic which strictly speaking results in an underdetermined system.
^{f} Komissarov et al. (2007) also inject super-slow. As the energy equation is not solved, one condition is already used for fixing the entropy. Constraints in the injection boundary (far from the disk) disk are $(E_\phi, B^\eta, \rho, v^\eta, \Omega^F)$ where the η-coordinate describes a "radial" direction ($\eta^2 = r^2/a + z^2$, $a \geq 1$) in elliptical coordinates.
^{g} Ramsey & Clarke (2011) comment on the apparent overdetermination by stating that the disk pressure should be left floating, which however lead to unrealistically high temperatures at the boundary and was therefore discarded.

We find that many different choices for the disk boundary exist, some interchange the assignment of density with the injection speed or the thermal pressure.

In the following we shall illustrate our considerations for the choice of the disk boundary. A necessary requirement for the outflow to settle into a steady state is a vanishing toroidal electric field $E_\phi = 0$ in the laboratory system. This is satisfied by $\mathbf{v_p}||\mathbf{B_p}$ and can be used to “freeze” the footpoints of the magnetic field: according to the poloidal part of Faradays law

$$\partial_t B_z = -1/r\partial_r r E_\phi; \qquad \partial_t B_r = \partial_z E_\phi \tag{3.4}$$

with $E_\phi = 0$, the evolution of $\mathbf{B_p}$ along the boundary is suppressed. The choice to constrain E_ϕ is shared by all authors, either via implementation as electromotive force or by the setting $\mathbf{v_p}||\mathbf{B_p}$ for the primitive boundary variables. Since the magnetic field within the domain changes during the evolution of the outflow, to avoid kinks and associated current sheets, at least one component of the poloidal field needs to be allowed to react to the simulation. When employing a staggered grid, it is customary to extrapolate the component parallel to the boundary (in this case B_r) to the ghost cells and let the flux across the boundary follow from the solenoidal condition. We follow this strategy in the simulations obtained with the PLUTO code. On the other hand, it would be desirable to prescribe the magnetic flux given by B_z entirely. The required radial field can then follow from extrapolation, where again the solenoidal condition should be enforced. For the simulations with AMRVAC we follow a potential field Ansatz for $\mathbf{B_p}$ by applying vanishing toroidal currents $j_\phi = \partial_z B_r - \partial_r B_z = 0$ at a given profile of B_z in the ghost zones. This has the advantage that no superfluous Lorentz force due to arbitrary extrapolation is created.

A number of authors prescribe in addition a fixed-in-time value for $E_r = -r\Omega/cB_z$. This is in fact very similar to conserving the iso-rotation parameter Ω constant in time, as the time evolution of B_z is already suppressed by the choice of E_ϕ. Since the iso-rotation parameter is a field-line constant (at least within ideal MHD), it reflects the rotation profile in the midplane of the underlying disk. Unlike often stated, the certainly appropriate choice of constraining (E_ϕ, E_r) is not dictated by the requirement of vanishing electric fields in the co-moving frame (as this is respected by design of MHD), but rather by the desire to reach a stationary state close to the initial configuration. To guarantee a smooth profile of Ω across the boundary calls for loosening constraints on either the rotation velocity v_ϕ or the toroidal field B_ϕ. Most authors let B_ϕ follow from the induction in the domain and also we adopt this approach in chapter 4. However, for the study of Poynting dominated flows discussed in chapter 5, we prefer to assign a given current-profile along the boundary. The rotation profile is then a consequence of the outflow evolution.

In stationary MHD, the mass-flux is determined by the sound speed at the slow magnetosonic point. Consequently, the statement: *"It is impossible to constrain mass-flux at a sub-slow magnetosonic injection boundary"* is often issued in the context of dynamical fluid simulations. This concept however does *not* directly carry over to dynamical simulations. Instead, as we have elaborated in section 2.2.3, it is the slow characteristic which should be allowed to traverse the boundary freely. To prove this point and on the way gain an intuitive understanding of several aspects of astrophysical jets, we devise the following thought experiment.

3.2.1 Nozzle Analogy

Before the proposition of the Blandford & Znajek (1977) and the Blandford & Payne (1982) process, models for relativistic jets were influenced by known mechanisms of the engineering world. The analogy with a convergent-divergent nozzle of the rocket engine (de-Laval nozzle) was first proposed by Blandford & Rees (1974). In their "twin exhaust model" for radio jets, Blandford & Rees (1974) considered the external thermal pressure distribution of a gravitationally-confined rotating gas-cloud to promote a favorable nozzle geometry. Camenzind (1989) and Li et al. (1992) took the analogy one step further and proposed a *magnetic nozzle*, where the magnetic field is responsible for shaping of the funnel wall. Still today, funnel walls are used as a governing parameter to model the medium external to the jet and promote collimation in relativistic MHD simulations (e.g. Komissarov et al. 2007; Tchekhovskoy et al. 2010a,b). Twenty five years after the initial idea, the twin-exhaust model has been resurrected by Heinz & Begelman (2000) who considered the inner energy of a tangled magnetic field structure instead of the thermal enthalpy as the main energy reservoir. Since a fully randomized magnetic field of this kind can be modeled like a gas endowed with an ultra-relativistic equation of state, efficient acceleration in analogy to the nozzle can also be found for this magnetically dominated plasma. For ordered field structures on the other hand, analogies can be best found in electrodynamics. For example, the well known attraction of current-carrying wires is often quoted as a descriptive explanation for jet collimation.

The many similarities between the paradigms borrowed from the engineering world and astrophysical jets yield an intuitive understanding of an otherwise complex phenomenon. It is therefore instructive to briefly consider the de-Laval nozzle flow and outline how and to which degree the concepts can be carried over to the astrophysical application.

Under the right conditions, the nozzle flow will experience a sonic transition which is localized exactly in the throat of the nozzle.[5] Therefore a hydrodynamic nozzle is the ideal laboratory to investigate the compatibility of various inflow boundaries with the constraints imposed by the fixed critical point. A nozzle with the differentiable shape-function $r(z)$ can be implemented to the PLUTO code by means of a reflective internal boundary condition in an otherwise cartesian grid. Hereby, the velocity component tangential to the boundary is mirrored while the remaining (primitive) variables follow from the domain.[6] We first consider a (non-relativistic) flow through a pipe with a cosine-shaped diminution. The nozzle shape is indicated by

$$r_{\mathrm{A}}(z) = \begin{cases} 1 & ; \quad z \leq 1 \\ \frac{3}{4} - \frac{1}{4}\cos(z\pi) & ; \quad -1 < z < 1 \\ 1 & ; \quad z \geq 1 \end{cases} \tag{3.5}$$

and we examine a domain of $r \in [0,1];\ z \in [-1,4]$ using 100×500 grid cells and adopt an ideal equation of state of adiabatic index 5/3. The initial domain is set to constant density $\rho = 1$ and the flow is started by a one-dimensional Riemann problem in the nozzles throat ($z = 0$). The setups shown here are summarized in Table 3.3. At the "outlet", all simulations assume zero gradient outflow boundaries for the variables except pressure which is set to p_{r}. Unconstrained boundary values at the inlet are also obtained by zero gradient extrapolation of the domain values. Simulation N7 constrains the mass-flux at the inflow boundary by the choice of $v_z\rho$,

Table 3.3 Hydrodynamic Nozzle setups, initial Riemann problems and inflow boundary constraints.

ID	Shape	p_{l}	p_{r}	$v_{z,\mathrm{l}}$	$v_{r,\mathrm{l}}$	$\rho_{\mathrm{l}} = \rho_{\mathrm{r}}$	Const.
N4	r_{A}	1	0.1	0	0	1	p_{l}, ρ
N7	r_{A}	1	0.1	1	0	1	$v_{r,\mathrm{l}}, v_{z,\mathrm{l}}, \rho$
N16	r_{A}	1	0.1	1	0	1	$v_{r,\mathrm{l}}, v_{z,\mathrm{l}}, p_{\mathrm{l}}, \rho$
N12	r_{B}	1	0.1	0	0	1	p_{l}, ρ

while N4 models a heat-bath with constant ($p,\ \rho$) and simulation N16 constrains all flow quantities at the inflow condition. We find that once settled into a stationary state, all setups promote very similar solutions if dimensionless quantities like the Mach number $M = v_p/(\sqrt{\gamma p/\rho})$ are considered (e.g. Figure 3.6). An axial cut of the flow quantities of all models is shown in Figure 3.7. Simulation N7 with given mass-flux shows some wave reflection at the inlet. Most likely, this stems

[5] see basic textbooks such as Landau & Lifshitz (1959).

[6] To cope also with very steep shape functions, we implemented a two-dimensional slope-weighted method of mirroring the values through the boundary.

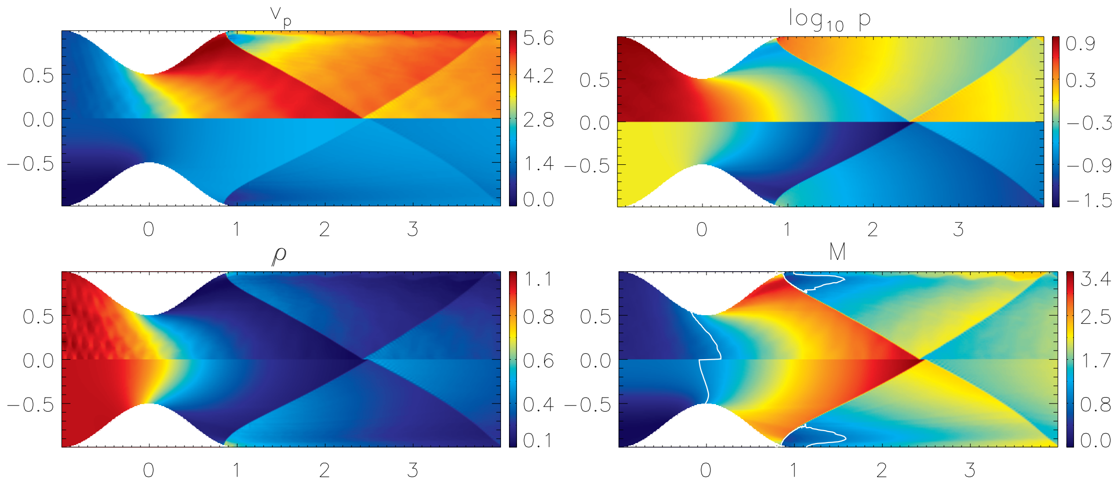

Figure 3.6 Choked flow in a nozzle-pipe, 2D hydrodynamic simulation with the PLUTO code. Top halves show (v_r, v_z, ρ) injection boundary (N7) and bottom halves show the (p, ρ) solution (N4). The Mach number M with a contour of the sonic surface is shown in the lower right panel. Although the boundary leads to differing v_p and p, in terms of the dimensionless Mach number, both approaches show comparable results.

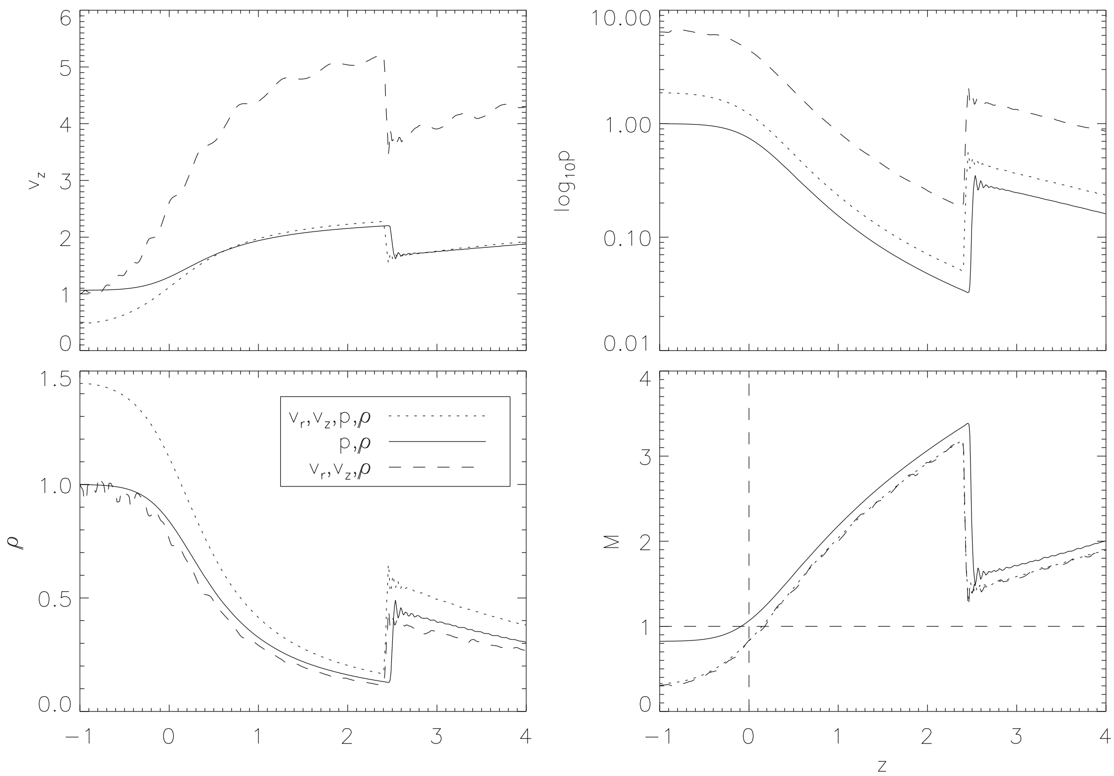

Figure 3.7 Quantities along the axis for runs N4,N7 and N16. Although for run N16 (dotted lines), the values $\rho = 1, p = 1, v_r = 0, v_z = 1$ are assigned to the boundary, the quantities obtained in the simulation are completely uncorrelated. The overdetermined simulation is thus not controlled by the injection boundary condition.

from the fact that we constrained both v_z and v_r and thus prohibited the injection angle to adapt to the geometry ahead. As long as the pressure is left free to adapt, no discontinuity at the inlet develops and the values provided for injection speed and density vary smoothly through the boundary. It is important to stress that the overdetermined simulation N16 on the other hand is completely uncontrolled by the boundary as none of the values provided for density, pressure and injection velocity are assumed within the simulation. By trying to exercise too much control over the simulation, all control is lost. This must be avoided in our jet simulations by all means!

In the post-nozzle flow, the high pressure exerted by the pipe wall promotes a *reconfinement shock* of the overexpanded flow. At the initially curved shock surface, the steepening sonic mach-cone can directly be observed. Such reconfinement shocks can also occur in super-fast magnetosonic relativistic jets (Sanders 1983). In expanding jets, the reconfinement occurs at the point when the sideways ram-pressure of the flow drops below the ambient pressure. At this point, a shock surface converges against the axis from where it is reflected back to the new jet boundary to be again reflected until the jet becomes sub-sonic (Falle 1991; Komissarov & Falle 1997). This process is often held responsible for the stationary knotty structure seen in some radio jets (see e.g. Cygnus A, shown in Figure 1.5).

An other interesting analogy is found in a separate simulation with the shape function

$$r_{\rm B}(z) = \begin{cases} -\sqrt{3}(z-a_2) - 3/2 & ; \quad 0 \leq 2 < a_1 \\ 5/2 - \sqrt{4-(z-a_2)^2} & : \quad a_1 \leq z < a_2 \\ a_0 + (z-a_2)^2/4 - (z-a_2)^3/(48m) & ; \quad a_2 \leq z < a_3 \\ a_0 + m(z-a_3) & ; \quad a_3 \leq z < z_{\max} \end{cases} \tag{3.6}$$

with $a_0 = 1/2,\ a_1 = (4-a_0)/\sqrt{3},\ a_2 = (7-a_0)/\sqrt{3},\ a_3 = a_2 + 4m, m = \tan 4^\circ$ which is adopted from the study of Heinbockel & Landry (1995). This setup (N12) leads to a stationary *termination shock* within the nozzle flow. In addition, the *shock corrugation* instability is clearly visible at the shock front (Figure 3.8). In astrophysical flows, such termination shocks occur in the context of stellar winds and Pulsar wind nebulae (e.g. Lyubarsky 2002).

From the analysis of the simple nozzle flow, we introduced several concepts that can directly be applied to the dynamics of astrophysical jets, these comprise: 1. thermal acceleration of supersonic expanding jets, 2. critical/separatrix points, characteristics and boundary constraints, 3. the causality of super (magneto-) sonic flows, 4. reconfinement and termination shocks as well as shock corrugation. In addition, we demonstrated that it is in fact possible to constrain mass-flux in subsonic injection and that comparable results can be obtained in principle. However,

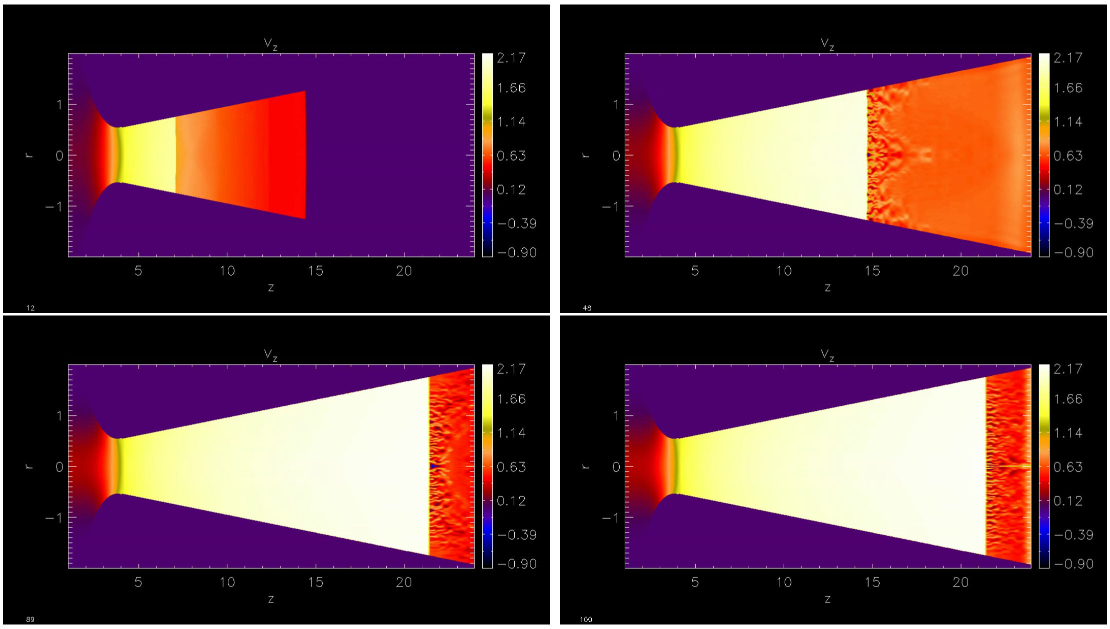

Figure 3.8 Shock structure in nozzle experiment, stills from a movie of the lateral flow velocity. The termination shock proceeds till $z \simeq 21$ where it remains stationary. Shock corrugation is observed at the termination shock.

we agree that the heat bath approach for the inlet boundary is the physically more sensible choice. We showed how an overdetermined boundary can result in complete loss of control over the simulation, therefore proper determination of the boundary conditions is crucial! We started out investigating the constraints imposed by the sonic transition which corresponds to the slow-magnetosonic point in MHD. However, it should be kept in mind that the concepts related to causality and shocks translate to the fast-magnetosonic point in MHD. As outlined in section 2.2.3, the additional waves of MHD require to loosen even more constraints at the sub-magnetosonic injection boundary which further complicates a direct application to jet formation.

3.3 Synchrotron Radiation Transport

Once the MHD solutions are settled into a stationary state, we solve the linearly polarized synchrotron radiation transfer equation taking into account self-absorption and Faraday rotation. While a derivation from first principles can be found in Appendix A, the implementation specific details are given here.

Let us define the Stokes parameters of linear polarization as $\mathbf{I} = \{I^l, I^r, U^{lr}\}^T$, where I^l can be defined as the polarized intensity measured in direction of the jet-axis projected on the sky, I^r is given by the perpendicular orientation across the jet and accordingly $U^{(lr)}$ describes the difference in the 45° orientations. The total intensity follows as $I = I^l + I^r$. In this basis, the transfer equation of linearly polarized light becomes a coupled ordinary differential equation of first order:

$$\frac{d\mathbf{I}}{dl} = \boldsymbol{\mathcal{E}} - \underline{\mathbf{A}}\ \mathbf{I}. \qquad \text{(Stokes vector transport)} \tag{3.7}$$

3.3.1 Key Ingredients

The coefficients of the emissivity vector $\boldsymbol{\mathcal{E}} = \boldsymbol{\mathcal{E}}(D, \epsilon'^{(e)}, \epsilon'^{(b)}, \chi_e)$ and opacity matrix $\underline{\mathbf{A}} = \underline{\mathbf{A}}(D, \kappa'^{(e)}, \kappa'^{(b)}, \chi_e, d\chi_{\mathrm{F}}/dl)$ depend on Doppler factor, co-moving emissivities/opacities and geometric information like the orientation of magnetic field with respect to the line-of-sight. In addition, the opacity matrix depends on the differential Faraday depth $d\chi_{\mathrm{F}}/dl$. We apply the standard expressions for the co-moving synchrotron emissivity and self-absorption opacity $\epsilon'^{(e,b)}$ and $\kappa'^{(e,b)}$ valid for isotropic power-law particle distributions following Pacholczyk (1970b).

The transformation of line of sight $\hat{\mathbf{n}}$ leads to the well known relativistic aberration

$$\hat{\mathbf{n}}' = D\hat{\mathbf{n}} - (D+1)\frac{\Gamma}{\Gamma+1}\boldsymbol{\beta}. \tag{3.8}$$

This supplies the projected co-moving magnetic field $B'_\perp = |\hat{\mathbf{n}}' \times \mathbf{B}'|$ which is responsible for emission and absorption (e.g. Equations A.16 and A.17). The co-moving field itself is given by $\mathbf{B}' = \mathbf{B}/\Gamma + \Gamma\,(\beta\mathbf{B})\cdot\boldsymbol{\beta}$ following the general definition (2.7).

The change between emitted photon $\hat{\mathbf{e}}'$ vector and its observed counterpart $\hat{\mathbf{e}}$ introduces a relativistic "swing" of the polarization (Cocke & Holm 1972). According to the short formulation discovered by Lyutikov et al. (2003), the "observer system" quantities follow as

$$\hat{\mathbf{e}} = \frac{\hat{\mathbf{n}} \times \mathbf{q}}{\sqrt{\mathbf{q^2} - (\hat{\mathbf{n}}\cdot\mathbf{q})^2}}; \qquad \mathbf{q} = \hat{\mathbf{B}} + \hat{\mathbf{n}} \times (\boldsymbol{\beta} \times \hat{\mathbf{B}}). \tag{3.9}$$

Hence the local observer-system angle of the emission χ_e as measured from the image axis $\hat{\mathbf{l}}$ (the projection of jet axis onto the plane of the sky) is given by

$$\cos\chi_e = \hat{\mathbf{l}}\cdot\hat{\mathbf{e}}\ ; \qquad \sin\chi_e = \hat{\mathbf{n}}\cdot\left(\hat{\mathbf{l}}\times\hat{\mathbf{e}}\right). \tag{3.10}$$

This rotation of the emitting plane along the photon path by χ_e is incorporated in the definition of $\boldsymbol{\mathcal{E}}$ and $\underline{\mathbf{A}}$ according to the transformation rules derived in Appendix A.3.

Similarly, Faraday rotation can be performed during the ray-casting. Faraday rotation of the relativistically moving plasma has first been considered by Broderick

& Loeb (2009b) and is directly fed into the opacity matrix via the observer system Faraday rotation angle

$$\frac{d\chi_{\mathrm{F}}}{dl} = \frac{e^3}{2\pi m_e^2 c^2} \frac{f(\gamma_t) n_e D^2}{\nu^2} (\hat{\mathbf{n}} - \boldsymbol{\beta}) \cdot \mathbf{B}' \tag{3.11}$$

in cgs units, where e, m_e, n_e denote the electron charge, mass and number density and ν the observed photon frequency. The dimensionless function $f(\gamma_t)$ takes into account that for high plasma temperatures the natural wave modes do not remain circular (Melrose 1997), suppressing Faraday rotation in favor of conversion between linear and circular polarization. We follow Huang et al. (2008) and Shcherbakov (2008) in defining

$$f(\gamma_{\mathrm{t}}) = \gamma_{\mathrm{t}}^{-1} \left(\gamma_{\mathrm{t}}^{-1} \left(1 - \frac{\ln \gamma_{\mathrm{t}}}{2\gamma_{\mathrm{t}}} \right) + \frac{\ln \gamma_{\mathrm{t}}}{2\gamma_{\mathrm{t}}} \right); \; \gamma_{\mathrm{t}} = 1 + \frac{k_B T_e}{m_e c^2} \tag{3.12}$$

in terms of the thermal electron Lorentz-factor γ_{t} to interpolate between the cold and relativistic limits.

With these considerations we solve the ordinary differential equation (3.7) using a fourth-order Runge-Kutta scheme for a grid of lines of sight. In practice this is realized by transforming the (r, z) plane information of the simulations into a coarsened cartesian grid with typically $100 \times 100 \times 500$ cells by means of a Delaunay triangulation. Along the ray, the coefficients of $\boldsymbol{\mathcal{E}}$ and $\underline{\mathbf{A}}$ are obtained by tri-linear interpolation of the primitive variables to the position given by photon path and step size. The photon path is found for flat Minkowski space and is therefore represented by straight rays. For numerical stability, the adaptive step size is chosen small enough to satisfy $\Delta l < 6 r_{\mathrm{S}}$, $\Delta\tau < 0.5$ and $\Delta\chi_{\mathrm{F}} < \pi/16$ yielding sufficient convergence of the solution as shall be demonstrated in the following. An illustration of our ray-tracing procedure with a rendering of an exemplary MHD solution of a collimating jet is shown in Fig. 3.9.

3.3.2 Test of the Ray-Casting Procedure

To test the implementation of the synchrotron transport, we compare the numerically obtained answer with known analytical solutions. These are however almost always restricted to homogenous media and can thus give only a small glimpse on the capabilities of the code. None the less, the ray-casting code should pass the simple tests before we proceed to more complex situations. We thus initialize the ray-casting domain with a purely vertical magnetic field, zero velocity and constant density and pressure. The homogenous domain reads

$$(\rho, p, v_x, v_y, v_z, B_x, B_y, B_z) = (10^{-24}, 9 \times 10^{-7}, 0, 0, 0, 0, 0, 1). \tag{3.13}$$

in cgs units.

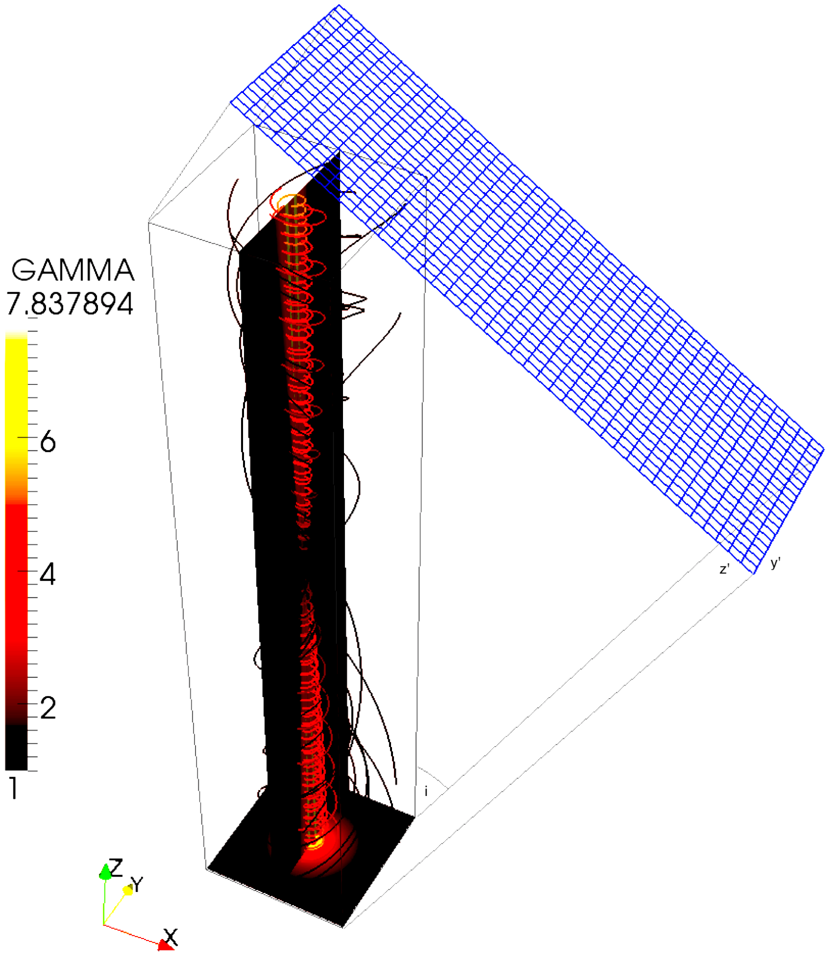

Figure 3.9 Illustration of the ray-casting geometry on an exemplary solution. Color-coding in slices ($x = 0$ and $z = -1000$) and field-lines represents the bulk Lorentz-factor. An inclination angle $i = 0$ corresponds to looking directly down the jet.

3.3.2.1 Internal Faraday Rotation

We first cast rays of 1GHz at an inclination of $i = 80°$ in absence of self-absorption to test the treatment of internal Faraday rotation. Field-lines thus have a component parallel to the line of sight as required by (3.11). Naturally, all lines of sight in the homogenous medium are equivalent. In Figure 3.10, we show the polarization degree along a photon path compared to the analytic expectation

$$\Pi = \Pi_{\max} \left| \frac{\sin \eta}{\eta} \right| \tag{3.14}$$

where $\eta \equiv d\chi_{\rm F}/dl \times l$ is the homogenous Faraday depth parameter (for a derivation, see e.g. Pacholczyk 1970b). We find that the period is conserved by the RK4-procedure to very good agreement, however the amplitude is not captured correctly leading to numerical depolarization for large step sizes. As a compromise between speed and accuracy, we hereafter choose the step-size of $\Delta\chi \leq \pi/16$. After 100rad,

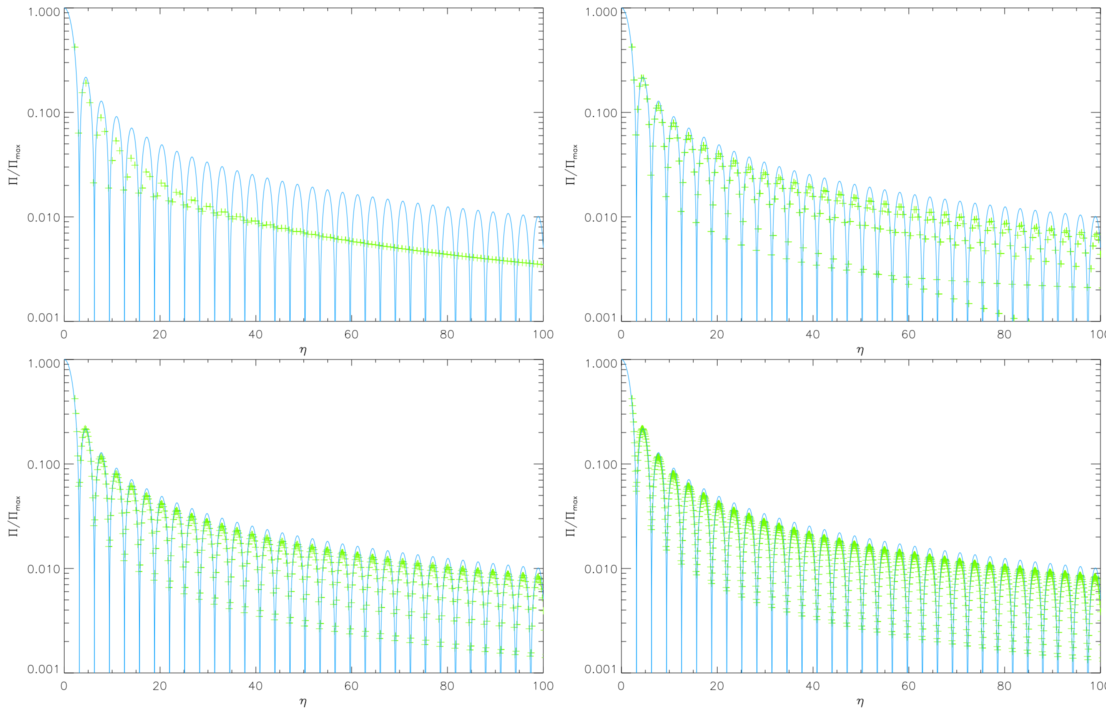

Figure 3.10 Optically thin internal Faraday rotation test (green crosses) with stepwidth $(\pi/4, \pi/8, \pi/16, \pi/32)$ compared to the analytical expectation of $\Pi(\eta) = \Pi_{\rm max}|\sin\eta/\eta|$ indicated by solid lines.

the numerical depolarization error therefore becomes $\simeq 10\%$. The absolute value of the polarization-amplitude at 100rad is thus $0.7 \pm 0.07\%$ which is more than sufficient for the aim of comparing with current radio observations (e.g. Lister & Homan 2005).

3.3.2.2 Self Absorption

We now test the code including self-absorption but in absence of Faraday rotation. To observe the optical depth transition within the domain, a ray of 40GHz is cast, again with an inclination of 80°. The analytical expectation for the unpolarized radiation transfer

$$\frac{dI_\nu}{dl} = \epsilon_\nu - \kappa_\nu\, I_\nu \tag{3.15}$$

is simply given by

$$I_\nu(l) = \frac{\epsilon_\nu}{\kappa_\nu}\left(1 - e^{-\kappa_\nu l}\right) \tag{3.16}$$

which can easily be found by variation of constants. With the adopted geometry and $d\chi_{\rm F}/dl \equiv 0$, the Stokes U^{lr} parameter vanishes and the polarized transfer equation decouples to the set

$$\frac{dI_\nu^l}{dl} = \epsilon_\nu^b - \kappa_\nu^b\, I_\nu^l \tag{3.17}$$
$$\frac{dI_\nu^r}{dl} = \epsilon_\nu^e - \kappa_\nu^e\, I_\nu^r \tag{3.18}$$

with solutions of the type (3.16). We note a peculiarity of polarized radiation transfer which we state as

Corollary 3 *In the presence of polarization dependent absorption $\kappa_\nu^e \neq \kappa_\nu^b$, the correct* total *intensity can only be found by solving the transfer equation of polarized radiation.*

Proof: The proof simply follows from adding 3.17 and 3.18 to find

$$\frac{dI_\nu}{dl} = \epsilon_\nu - \left(\kappa^b I_\nu^l + \kappa^b I_\nu^r\right) \tag{3.19}$$

which reduces to 3.15 only for $\kappa_\nu = \kappa_\nu^e = \kappa_\nu^b$ in contradiction to the prerequisite. The optically thin case however can be reproduced by the setting $\epsilon_\nu \equiv \epsilon_\nu^e + \epsilon_\nu^b$.

A mean opacity usually defined by $\kappa_\nu \equiv 1/2(\kappa_\nu^e + \kappa_\nu^b)$ can thus only yield an approximation to the real total intensity. A more useful definition of the effective opacity for power-law electron distributions of index p would be

$$\kappa_\nu^{\text{eff}}(p) \equiv \frac{2(7+3p)(8+3p)}{130+99p+18p^2}\,\kappa_\nu \tag{3.20}$$
$$\rightarrow \frac{91}{100}\kappa_\nu\ (p \rightarrow 2) \tag{3.21}$$

which at least reproduces the correct optically thick source function. This discrepancy between polarized and unpolarized transfer impedes a consistency check of the polarized solution with the one obtained from the simpler equation of type (3.15). Numerically obtained intensities are compared to the theoretical expectation in figure (3.11). For this simple test problem, the solutions are in excellent agreement. We also compare the solutions obtained by direct integration of the unpolarized equation for the total intensity using the mean opacity $I_\nu(\kappa_\nu)$ and the analytical solution for the effective opacity $I_\nu(\kappa_\nu^{\text{eff}})$. As expected, both functions reproduce the correct optically thin intensity and $I_\nu(\kappa_\nu^{\text{eff}})$ approaches the correct optically thick limit. In between, also $I_\nu(\kappa_\nu^{\text{eff}})$ differs from the true solution.

The expectation for the polarization degree for power-law electron distributions of index p immersed in a homogenous field can be found as

$$\Pi_{\text{h}} = \frac{(p+1)}{(p+7/3)} \rightarrow 0.69\ (p=2) \tag{3.22}$$

for the optically thin regime and

$$\Pi_{\mathrm{l}} = \frac{3}{(6p + 13)} \to 0.12 \ (p = 2) \tag{3.23}$$

for optically thick radiation. This is compared to the numerical value in the top panels of figure 3.11. Both limits are accurately approached by the transport code. The flip in polarization direction across the optical depth transition from the $\mathbf{r}$ direction perpendicular to the field ($I_\nu^r > I_\nu^l$) to the $\mathbf{l}$ direction parallel to the field ($I_\nu^l > I_\nu^r$) can be easily observed.

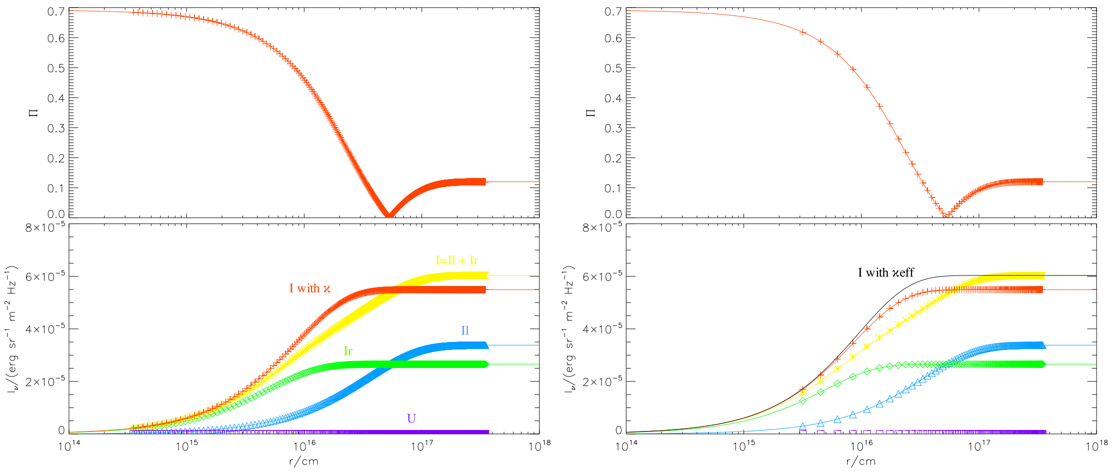

Figure 3.11 Test of the optical depth transition for step-width $\Delta\tau = (0.05, 0.5)$ compared to the analytical solutions for polarization (top) and intensity (below). Expected profiles are shown as solid lines and the numerical results are illustrated by various symbols. The unpolarized transfer with the effective opacity is shown as black solid line in the right-hand frame.

The step size needed for convergence of the solution should meet $\Delta\tau < 1$ and we choose $\Delta\tau \leq 0.5$ for the remainder of this study. Thus, the optical depth transition in the Stokes parameters is captured accurately by the numerical scheme.

Self absorption - oblique case To test the correct coupling of the Stokes parameters via Stokes U, we show an oblique field case with the setting

$$(\rho, p, v_x, v_y, v_z, B_x, B_y, B_z) = (10^{-24}, 9 \times 10^{-7}, 0, 0, 0, 0, 1/2, \sqrt{3}/2) \tag{3.24}$$

which is rotated by 30° around the x-axis with respect to the previous case. Thus the symmetry is broken and non-diagonal terms in $\underline{\mathbf{A}}$ enter into the calculation.

For brevity we omit the detailed prediction of the Stokes parameter and just compare total intensity and polarization degree with an analytical solution (Figure 3.12). As expected, the optical thick and thin limits are captured correctly and the polarization degree and total intensity match the analytical expectation along the ray.

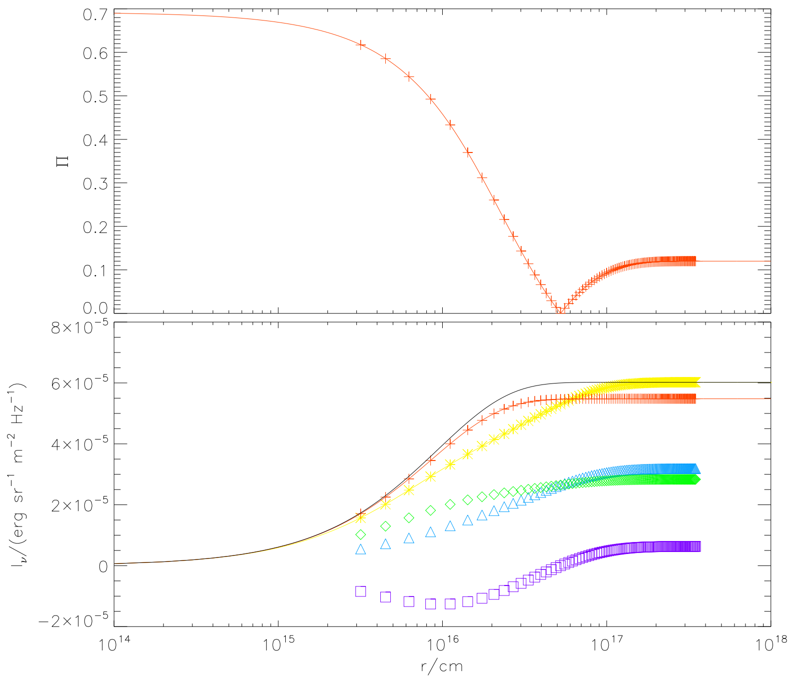

Figure 3.12 Test of the optical depth transition for step-width $\Delta\tau = (0.05, 0.5)$ compared to the analytical expectation for polarization (top) and intensity (below). The unpolarized transfer with the effective opacity is shown as a solid line in the right-hand frame.

As a final remark, it should be pointed out that in order to acquire radiation maps of the jet solutions, it is sufficient to follow the rays only till $\tau \approx 100$ where the medium becomes completely opaque. Deeper integration has no influence on the numerical solutions and hence also optically thick regions can be cast quickly with a limited amount of steps.

3.3.2.3 Lorentz Boost Test

We use an analytical jet model to test the proper treatment of the beaming effects and illustrate a number of basic points of synchrotron transport in jets. Therefore the ray-casting domain is initialized with the force-free helical "reverse pinch" jet model proposed by Lundquist (1950) and Taylor (1974). The rest-frame field reads

$$(B'_x, B'_y, B'_z) = (-J_1(r)\sin(\phi), J_1(r)\cos(\phi), J_0(r))$$

where J_0, J_1 signify the Bessel functions of the first kind. This cylindrical equilibrium field is transformed to the lab-frame with a Lorentz boost by $\Gamma = 10$ in the negative z-direction, in practice by using the field transformation law

$$\mathbf{B} = \Gamma(1 - \boldsymbol{\beta\beta})\mathbf{B}' \Leftrightarrow \mathbf{B}' = \frac{1}{\Gamma}(1 + \Gamma^2\boldsymbol{\beta\beta})\mathbf{B} \tag{3.25}$$

which yields

$$(B_x, B_y, B_z) = \Gamma(B'_x, B'_y, B'_z/\Gamma^2).$$

We find the transformation of the magnetic pitch angle defined as $\tan\Psi \equiv B_\phi/B_p$ to become

$$\tan\Psi = \Gamma^2 \tan\Psi' \tag{3.26}$$

such that the lab-frame field appears much more twisted than the co-moving counterpart (Figure 3.13).

Synchrotron radiation in this jet model was considered recently by Clausen-Brown et al. (2011) (hereafter CLK11), which allows us to compare our transport code to their results for the purpose of validation. As in the comparison paper, we initialize a top-hat profile for the relativistic electrons, confining the emission to the range of positive B_z.

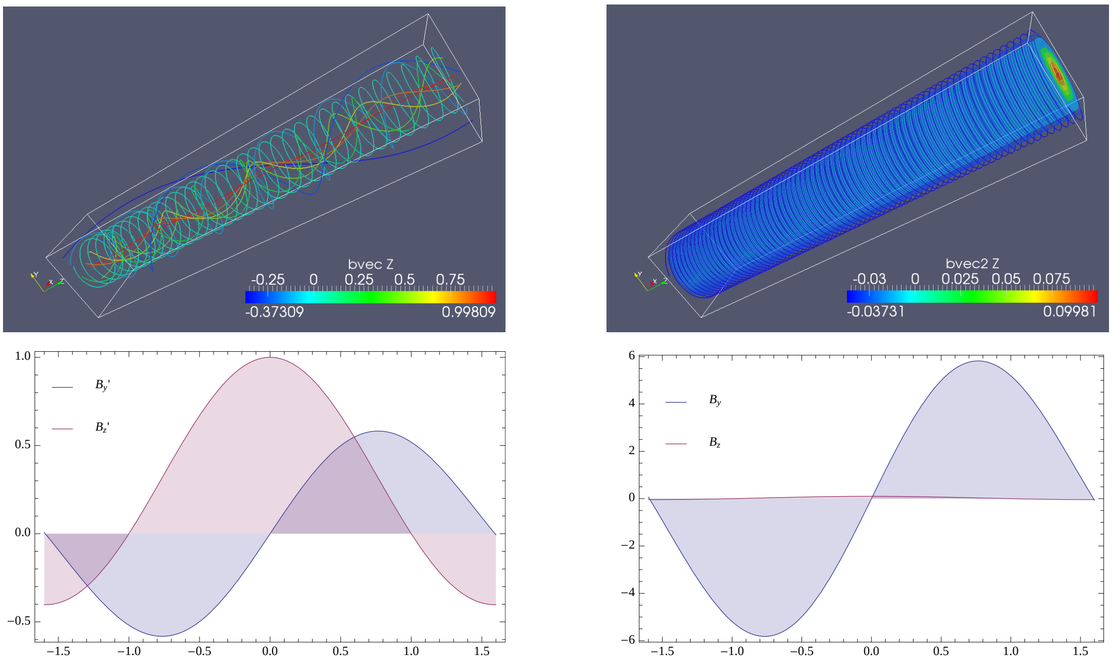

Figure 3.13 Inverse pinch configuration in the co-moving system (left) and moving with $u_z = 10$ in the lab system (right). Profiles of B_y and B_z along the x-axis are shown in the lower panels. Following CLK11 we restrict the emitting region to $B'_z > 0$.

According to the aberration of the line-of sight angle (A.47), photons emitted perpendicular to the jet axis with $\theta'_{\rm ob} = \pi/2$ define a cone in the observer system of opening angle $\theta_{\rm ob} \simeq 1/\Gamma$. Only within this small cone, the jet can be seen from the front-side. Jets at larger inclinations, for example in radio galaxies, are certainly seen from the back. If jets obey cylindrical symmetry, the front side image however directly corresponds to the back side view when reflected across the axis of symmetry. An image obtained by looking at viewing angles $1 < \theta_{\rm ob} < \pi$ could thus yield the view down the jet with $\theta_{\rm ob} \ll \Gamma$ by a symmetry operation.

We show the transverse intensity profiles calculated for optical thin synchrotron radiation in Figure 3.14. For the front-side inclinations we obtain excellent agree-

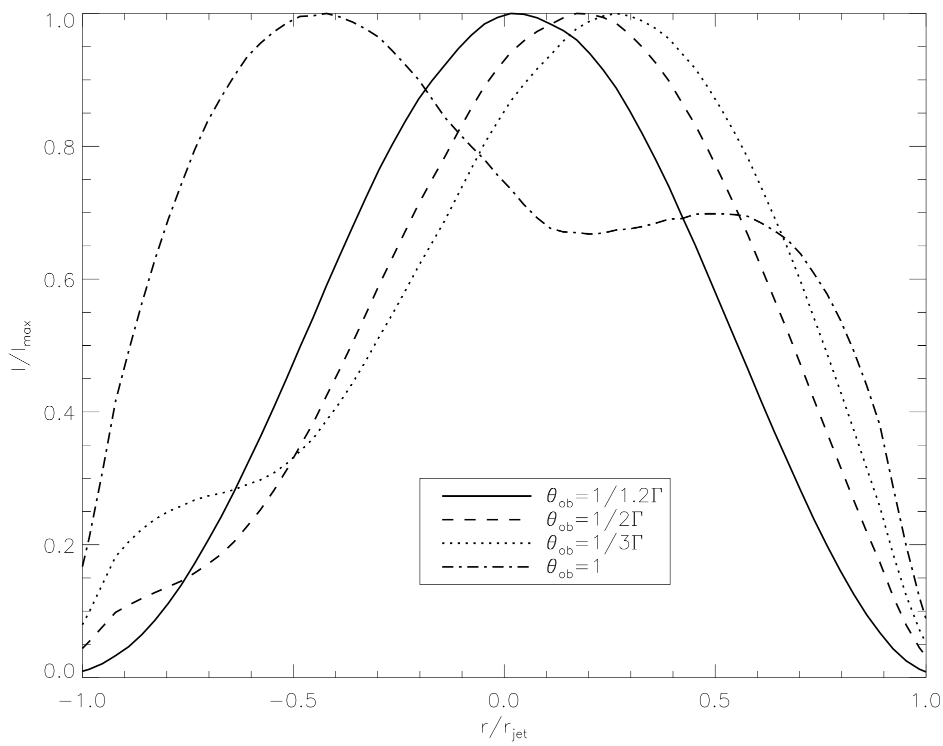

Figure 3.14 Profiles of the normalized intensity across the jet – to be compared with Figure 2 of Clausen-Brown et al. (2011). We find excellent agreement for the cases $\theta_{\rm ob} = (1/1.2\Gamma, 1/2\Gamma, 1/3\Gamma)$ while the double hump for the $\theta = 1$ case is more pronounced in the comparison paper.

ment with the model of Clausen-Brown et al. (2011). The profiles are identical as far as visual inspection is concerned. We also recover the double humped profile for the back-side viewing angle $\theta_{\rm ob} = 1$ (co-moving angle $\theta'_{\rm ob} = 170°$), however the secondary peak is more pronounced in the comparison paper. The reason for this difference is not clear to us.

In cylindrical optically thin jets, the polarization $\hat{\mathbf{e}}$ vector is either aligned or perpendicular to the projected jet direction (e.g. Pariev et al. 2003) such that the final Stokes U vanishes. A convenient notation for the polarization degree can thus be defined as $\Pi^* \equiv Q/I = (I^l - I^r)/(I^l + I^r)$. This quantity is positive for vectors aligned with the jet and negative for perpendicular polarization vectors. The magnitude of Π^* reduces to the ordinary linear polarization degree. In analogy to Figure 5 in CLK11, we show transversal profiles of the parameter Q/I obtained from our ray-casting procedure. Across the jet, the polarization is first perpendicular (with maximum degree of polarization), then flips to the parallel direction and flips again at the far side of the jet. This is customarily called a “spine and

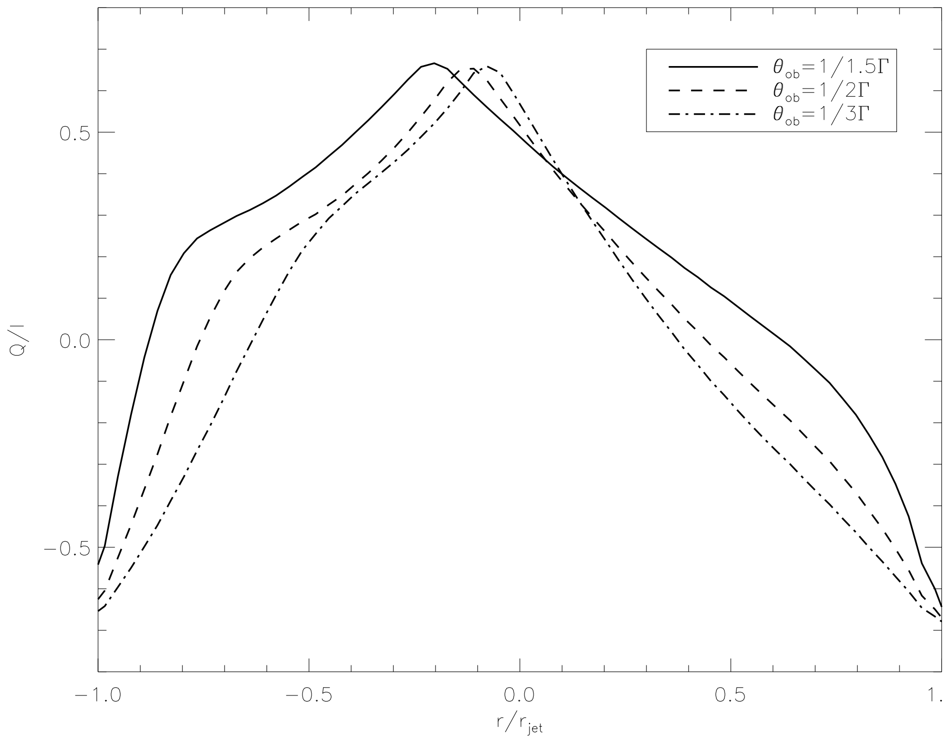

Figure 3.15 Transversal cut of polarization degree Q/I – in analogy to Figure 5 of Clausen-Brown et al. (2011). We find qualitative agreement in the magnitude, direction change of the polarization and ordering of the peaks, however the profiles in the comparison paper are more asymmetric with peaks distributed from ~ -0.8 to ~ -0.2.

sheath" polarization structure and is observed in our test case as well as in CLK11. Qualitatively, our solution thus agrees with CLK11, however the profiles in the comparison paper are stronger asymmetric with peaks distributed further on the left side of the jet. With decreasing viewing angle, the asymmetries become more pronounced also in our case. One explanation for the remaining discrepancy could be that a different electron index p was used to produce the polarization structure. We adopted the standard case of $p = 2$, while the value used by CLK11 is not specified in the paper. Prior to further discussion, the adopted values should be checked.

We can however affirm the main conclusions of CLK11 concerning the asymmetry of intensity and polarization and concerning the polarization flip. In addition, we also checked the numerical value of U/I and found it below 5×10^{-6}, in a very good agreement to the expectation from the geometric constraint. Hence we are assured that the synchrotron transport routine passes also this final test.

Chapter 4

Jets From Disk Coronae

4.1 Introduction

Astrophysical jets emanate from sources spanning a huge range in energy output or length scale - among them young stellar objects (YSO), stellar mass compact objects as X-ray binaries or μ-quasars, or the powerhouses of some active galactic nuclei (AGN) which host a super-massive black hole. In particular for radio-loud quasars, for which synchrotron emission dominates the radio spectrum, relativistic jets are a generic feature. Due to the omnipresent angular momentum conservation, mass accretion to all of these objects features a disk structure around the central mass. It is commonly believed that jets are launched as disk winds, which are further accelerated and collimated by magnetic forces (see Blandford & Payne (1982); Pudritz & Norman (1983); Camenzind (1986b); Heyvaerts & Norman (2003a); Pudritz et al. (2007). Relativistic jets may gain further energy by interaction with the black hole magnetosphere (Blandford & Znajek 1977; Ghosh & Abramowicz 1997; Komissarov 2005).

The focus this chapter is i) to concentrate on the formation and acceleration of a relativistic MHD jet right from the launching area the accretion disk surface, ii) to investigate the (self-) collimation of relativistic MHD jets under the influence of de-collimating electric forces and an "open" boundary condition for the outflow iii) to consider gravity as en essential gradient to provide a realistic disk boundary condition in equilibrium, iv) to run long-term simulations lasting more than 1000 inner disk rotations until the jet reaches steady state, v) to concentrate on MHD disk jets as disks are the natural origin for the mass load for AGN jets.

The outline of this chapter is as follows: in section 4.3 we outline the initial- and boundary conditions of the numerical simulations, whose results are shown in section 4.4. We conclude in section 4.5.

4.2 Accretion Disk Coronae

It is our ambition to connect the wind solutions to the ambiance of a realistic accretion disk. In our simulations, the flow originates in the high entropy atmosphere called a corona. Optically thin coronae are an integral part in models of the X-ray features of AGN (e.g. Mushotzky et al. 1993) and μ-Quasars (e.g. Nowak et al. 2002; Markoff et al. 2003b).

While Compton cooling can provide the observed spectra, the heating mechanism is not easily found. Just as in the case of the sun, the coronal heat cannot directly be transfered from the colder photosphere/accretion disk (according to the second law of thermodynamics) and the nature of vertical energy transport is an active field of research. External irradiation of flared disks by the central object (or central disk) is certainly present in a multitude of objects (see Czerny et al. 2008, for a review) but might not be the primary energy source. Among the most promising mechanisms we should highlight magnetic reconnection heating as proposed by Haardt & Maraschi (1991).

Between the mid-plane and the coronal point of injection in our simulations, ideal MHD can not provide a realistic picture. In order for an accretion disk to *work*, a torque of viscous or magnetic origin has to be exerted onto the material. Additionally, the flux-freezing constraint of ideal MHD must be relaxed since it would lead to an accumulating magnetic pressure that ultimately stops the accretion process in such magnetically arrested disks (MAD). Studies modelling both the accretion motion and the super Alfvénic jet based on a stationary self-similar approach (e.g. Wardle & Koenigl (1993); Ferreira & Pelletier (1993); Li (1995)) rely on global-scale magnetic fields and ad-hoc assumptions on the viscosity and (anisotropic) magnetic diffusion. In order for these models to be stable against strong magnetic compression on the one side and the magneto rotational instability (MRI; see Balbus & Hawley (1998)) on the other, Ferreira & Pelletier (1995) require equipartition for the thermal and magnetic pressure. Casse & Ferreira (2000) demonstrated the importance of heating for the mass-loading or the jet. Time-dependend numerical simulations of these magnetized accretion ejection structures (MAES) were presented by Casse & Keppens (2002, 2004); Zanni et al. (2007) and adopt a fixed in time anomalous resistivity profile in order to connect the two dynamical regimes.

Although the stationarity of the aforementioned simulations is possibly hampered by numerical diffusion and low resolution effects, MAES with global-scale fields are to date the most successful models to create collimated outflows.

It is now widely believed that the source of viscosity and resistivity in weakly magnetized disks is the turbulence seeded by the MRI. Local, stratified shearing box simulations by Miller & Stone (2000) suggest a quenching of the MRI in the strongly magnetized coronal region, as the magnetic scale height exceeds the thermal one. This is in contrast to the equipartition fields proposed for the MAES. Magnetic buoyancy of the large-scale fields eventually created by a turbulent dynamo could then provide the coronal heating. Typically, the MRI results in toroidally dominated coronal fields with $B_\phi^2 > 10 B_p^2$ and opening the field lines towards a topology favorable for wind acceleration remains a challenge. In the context of the solar corona this process is discussed by Wang & Sheeley (2003).

By restraining parts of the accretion disk structure, von Rekowski et al. (2003) could achieve outflows in time-dependend simulations of disk-corona structures where the magnetic field is sustained by a mean-field dynamo. Analytic models of this turbulent disk-corona-outflow connection are however in still its infancy (see the discussion by Kuncic & Bicknell (2004) and attempts by Blackman & Pessah (2009)).

4.3 Model Setup for the MHD Simulations

With the aforementioned considerations we choose the following model for our investigation. A global-scale poloidal field favorable of wind acceleration is adopted. Whether it is advected by the accretion flow or created by an underlying dynamo is not of our concern. The jet base resembles a corona in the sense that it is hot (electron temperature $\sim 10^9$K), has no mechanism of cooling, is non-turbulent (no viscosity) and highly ionized (infinite conductivity). We choose a Keplerian rotation profile for the field lines. The flow starts with sub-escape velocity and we investigate sub-magnetosonic injection where mass loading and energy fluxes are determined by the internal jet dynamics. We perform axisymmetric special relativistic MHD simulations of jet formation for a set of different magnetic field geometries and field strengths. In the following we discuss the numerical realization of our problem.

4.3.1 Boundary Conditions

Given the 2.5 dimensional nature of the problem, three geometrical boundaries have to be prescribed. These are the inlet boundary along $z = 0$ from which material is injected into the domain (*inflow*) and the two outer boundaries at $r = r_{\rm end}$ and $z = z_{\rm end}$ where we expect material to leave the computational domain (*outflow*). The boundary condition along $r = 0$ ($\rm r_{beg}$) follows from cylindrical symmetry. Figure 4.1 gives an overview of the different regions.

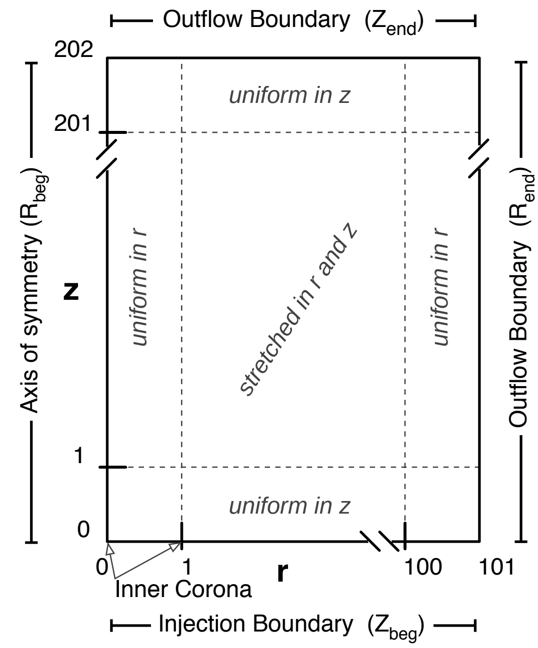

Figure 4.1 Sketch of the different regimes of our grid and boundary. In both directions we set 20 equidistant cells in $[0, 1]$. Then follows a stretched grid until we add five equidistant cells one unit-radius before the outflow boundary. For $r \in [0, 1]$, the hydrostatic corona is fixed to minimize the influence of the central region on the disk-wind.

4.3.1.1 Injection Boundary (Z_{beg})

Pursuing the aim to follow the acceleration of a disk wind from as close to the accretion disk as possible, we start with a sub slow-magnetosonic wind. We are hence free to choose four constraining boundary conditions without overdetermining the system (see Bogovalov (1997) and section 3.2 for more details).

Our choice is to fix the toroidal electric field component $E_\phi = 0$. This suppresses the evolution of the bounding poloidal magnetic field and is realized by requiring $\mathbf{v_p}||\mathbf{B_p}$. The field line iso-rotation is kept constant in time and follows a Keplerian rotation law $\Omega \propto r^{-1.5}$. The boundary condition starts out initially in a force-free state with zero toroidal field $\Omega = v_\phi(r)/r$ corresponding to a disk in hydrodynamic equilibrium. This is an essential ingredient as - within stationary ideal MHD - Ω just equals the mid-plane angular velocity of the material $\omega(r)$. Relaxation of the infinite conductivity constraint would, however, lead to an inequality $\Omega(r) \leq \omega(r)$ owing to the diffusion of magnetic field. For these reasons Ω should closely follow the expected disk rotational profile and should be limited by the maximal velocity in the mid-plane, typically at the inner edge of the disk located at $r = 1$.

A radial force-equilibrium along the whole boundary is enforced by balancing the centrifugal and pressure support against gravity via the sub-Keplerianity of the rotation $\sqrt{\chi} = v_\phi(r = 1)/v_K$ that also determines the inlet density, where v_K is the circular velocity that alone sustains against gravity at $r = 1$. A more convenient parametrization is in terms of the relative temperature $\epsilon \equiv c_s^2/v_\phi^2 = (\gamma-1)(1-\chi)/\chi$. We investigate two cases - a hot corona with $\epsilon = 2/3$ and a version with $\epsilon = 1/6$ ($\chi = 0.5$ and $\chi = 0.8$) .

If we interpret $r = 1$ as the innermost stable circular orbit (ISCO) around a black hole, $v_{\rm K}$ is a measure of the black hole spin. In the case of a Schwarzschild black hole it is $v_K \simeq 0.6c$ while we choose the scaling velocity $v_\phi(r = 1) = 0.5c$ for convenience.

The inner disk-edge is numerically difficult to model because of the transition to the inflow of the disk-wind and the steep gradients in gravity. Within $r < 1$, the so-called plunge region, a physical solution would allow for (radial and vertical) accretion onto the central object. Since the dynamics in this area would then require a general relativistic treatment which we cannot provide in this context, we simply minimize the dynamical effect of this region by freezing the hydrostatic solution initially present in the domain. Other authors have assumed a thin funnel flow along the axis (e.g. Krasnopolsky et al. (1999)) or added an internal sink-cell (like Casse & Keppens (2002)) to circumvent this problem. The transition between the "inner corona" and disk-wind is smoothed via the Fermi step function $F(x) = (1 + e^{(1-x)/0.1})^{-1}$. Rotational support is thus turned on by the setting

$$\rho_{\rm d}(r,z) = \frac{1}{1-\chi F^2(R)}(R + r_S)^{1/(1-\gamma)}, \tag{4.1}$$

$$v_\phi(r) = \sqrt{\chi} v_K F(R) R^{-0.5}. \tag{4.2}$$

Density given by Equation (4.1) and the coronal pressure p constitute the third and fourth fixed in time conditions.

Since pressure and density profiles are specified at the inlet, it is not possible to further constrain the mass-flux for sub-(magneto)sonic flows as this must follow from the sound speed at the sonic point. Therefore we match the vertical velocity v_z to the domain via $\partial_z v_z = 0$, while the radial component follows from the $E_\phi = 0$ condition. We limit the injection speed by the local slow magnetosonic speed in the case when the velocity just above the boundary becomes trans-sonic. This naturally provides the fifth constraint needed in that case.

With the induction of a toroidal magnetic field component in the jet, the rotational velocity needs to be adjusted in order to satisfy Equation (2.52),

$$v_\phi = r\Omega^F + \frac{v_p}{B_p} B_\phi \tag{4.3}$$

as we apply the condition $\partial_z B_\phi = \partial_z B_r = 0$ (while B_z then follows from $\nabla \cdot \mathbf{B} = \mathbf{0}$).

By letting the jet solution alone determine Poynting- and mass- flux, we loose control over the energy flux parameter μ and the limiting asymptotic Lorentz factor Γ_∞. It will rather be a consequence of the MHD under the constraints we have given, while we have used our freedom to provide a boundary most closely resembling a realistic hot disk corona. A graphical summary of the disk wind boundary conditions is shown in Fig. 4.2.

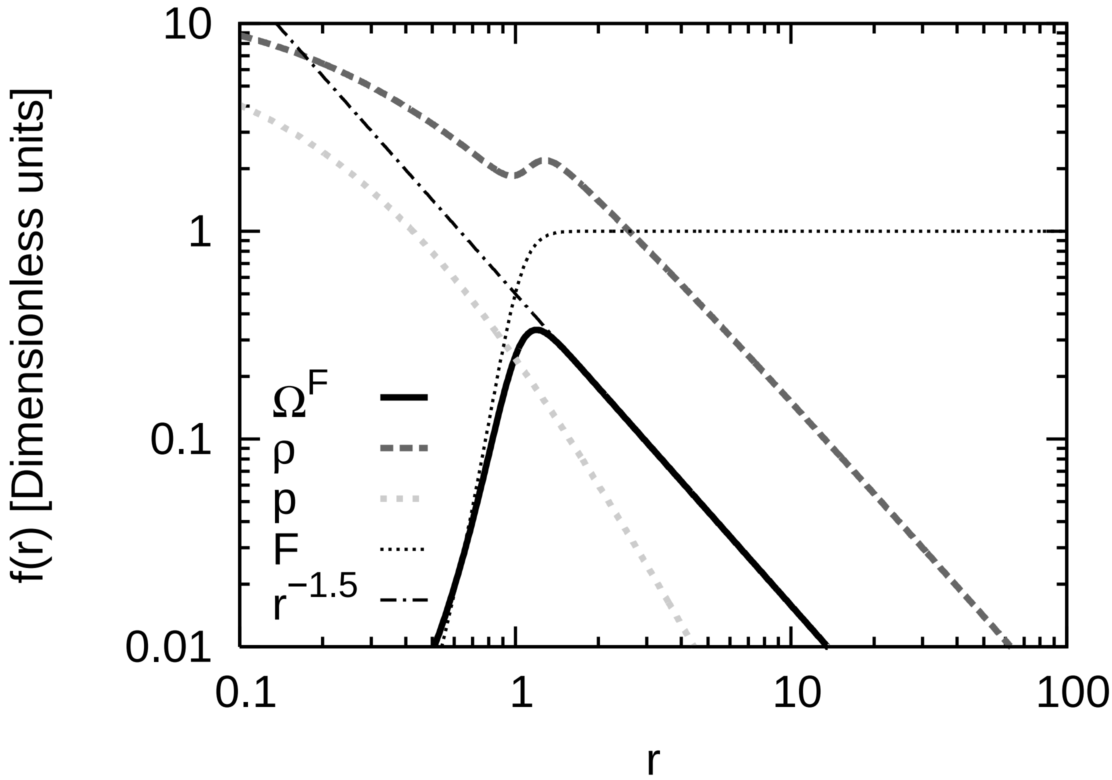

Figure 4.2 Profiles of the fixed in time variables for the inlet in hydrodynamic equilibrium. We give constraints on Ω, ρ, p, E_ϕ ($E_\phi = 0$ not shown). Parameters are $v_\mathrm{K} = 0.5, \epsilon = 2/3$. The thin dotted line is the Fermi step function used to smooth those variables experiencing a sharp transition at the inner disk radius $r = 1$.

4.3.1.2 Outflow Boundaries (R_{end}, Z_{end})

The standard outflow boundary conditions for many numerical codes are zero-gradient conditions, which are usually sufficient as the plasma velocities are constrained to be outward-pointing.

In the case of sub fast-magnetosonic outflows, this strategy is unfortunately insufficient as the flow inside of the domain will depend on the flow beyond the boundary via the incoming characteristics. Just as for the inlet boundary, the now missing information has to be supplied by constraints that describe best the physical conditions downstream of the boundary. In the case of an outflow, the conditions leading to an untampered flow are however impossible to know a priori. A way to circumvent this unphysical feedback is to avoid any causal contact by moving the boundary far away such that the characteristics will not enter the domain of interest within the simulated time.

When considering a boundary outside of causal contact "very far away", we estimate for Alfvén waves to travel over 10^3 scale radii within the anticipated simulation time. The computational effort of such huge grids does not allow a large parameter study and we leave this option for chapter 5.

In the absence of a substantially better solution, zero-gradients are used for the primitive variables except for magnetic fields for which this simple approach leads to artificial electric currents implying an inward-pointed Lorentz-force. Especially for low plasma-β this may result in a devastating artificial collimation - preventing any steady state to establish and artificially collimating the outflow increasingly thin with time.

Ustyugova et al. (1999) have performed a systematic study comparing different approaches for outflow conditions including a (toroidal) force-free condition $\mathbf{j_p}||\mathbf{B_p} = \mathbf{0}$ and a more sophisticated version including an additional numerical factor that needs to be determined a posteriori. For the outflow conditions in our simulations we instead recover the magnetic field components by imposing constraints on the poloidal ($j_r = -\partial_z B_\phi$, $j_z = r^{-1}\partial_r r B_\phi$) and toroidal ($j_\phi = \partial_z B_r - \partial_r B_z$) electric currents. For the toroidal magnetic field (poloidal electric current) we radially extrapolate the expected $1/r$ law of a marginal j_z at the radial end ($\mathrm{R_{end}}$). Using $\partial_z B_\phi = 0$ allows to specify j_r at the upper end of the domain ($\mathrm{Z_{end}}$). Concerning the poloidal magnetic field components we implement a current-free boundary condition by enforcing $j_\phi = 0$. This is a novel approach designed to minimize spurious effects of collimation. We convinced oursevels that boundary effects have only a marginal effect on the solution by varying the grid-size and geometry. For a detailed discussion and comparison of various outflow conditions we refer to Appendix B.1.

We note that, as a further complication, a fully relativistic version for a force-free or force-balance boundary conditions would also need to take into account electric forces. We have estimated the impact of such an upgrade and found that due to the geometry of our outflow (in particular the location of the light surface) it would play a minor role and is thus not worth the effort to implement.

4.3.2 Initial Conditions

As initial state we prescribe a force-free coronal magnetic field, $F^{\alpha\beta} j_\beta = 0$, together with a gas distribution in hydrostatic equilibrium. Both is essential in order to avoid artificial relaxation processes caused by a non-equilibrium initial condition. We apply an ideal equation of state $p = K\rho^\gamma$ with a "classical" adiabatic index of

$\gamma = 5/3$ since our flows are always cold when compared to the rest-mass energy. To further strengthen this choice, we performed a comparison simulation with the Taub (1948) equation of state as described by Mignone et al. (2005) which produced an identical jet once the hot shock has passed through the domain. The initially constant K is determined by the radial force-balance of the inlet.

For the initial magnetic field configuration we apply two different geometries. Field configuration A is a potential field of hourglass shape as applied by Ouyed & Pudritz (1997) and Fendt & Čemeljić (2002) with the magnetic field components

$$B_r(r,z) = \frac{1}{r}\left[1 - \frac{(z+z_d)}{\left(r^2+(z+z_\mathrm{d})^2\right)^{1/2}}\right] \quad (4.4)$$

$$B_z(r,z) = \frac{1}{\left(r^2+(z+z_\mathrm{d})^2\right)^{1/2}}, \quad (4.5)$$

corresponding to a vector potential

$$A_\phi(r,z) = \frac{1}{r}\left[\sqrt{r^2+(z+z_d)^2} - (z+z_\mathrm{d})\right] \quad (4.6)$$

in cylindrical coordinates with $B_r = -\partial_z A_\phi$ and $B_z = r^{-1}\partial_r\, rA_\phi$. The dimensionless disk thickness z_d with $(z_\mathrm{d}+z) > 0$ is introduced to avoid kinks in the field distribution for $z < 0$ (the ghost zones) and we choose $z_d = 1$ for convenience.

Our other option for the initial magnetic field (configuration B) is the "split monopole" (Sakurai 1987) with the magnetic field components

$$B_r(r,z) = \frac{r}{\left(r^2+(z+z_d)^2\right)^{3/2}} \quad (4.7)$$

$$B_z(r,z) = \frac{z+z_d}{\left(r^2+(z+z_d)^2\right)^{3/2}}. \quad (4.8)$$

In the split-monopole setup the parameter z_d defines the offset of the fictitious center of the monopole from the grid origin, and adjusts the initial angle of the field lines with respect to the disk-surface. We either adopt an angle of $\theta = 85°$ or $\theta = 77°$ for the field line passing through $r = 1$. Similar to Equation (4.6), the split monopole field can be described by a vector potential

$$A_\phi(r,z) = \frac{1}{r}\left[1 - \frac{z+z_\mathrm{d}}{\left(r^2+(z+z_\mathrm{d})^2\right)^{1/2}}\right]. \quad (4.9)$$

The fields are scaled to satisfy the the choice of the plasma-β

$$\beta \equiv \left.\frac{B_p^2}{2p}\right|_{r=1,z=0} \quad (4.10)$$

at the inner disk radius.

It should be kept in mind that plasma-β largely varies along the disk boundary. In configuration A, the profile $\beta(r)$ monotonically decreases until for large radii it is $\beta(r) \propto r^{-0.5}$ leading to a magnetically dominated outer corona. In the split-monopole, $\beta(r)$ decreases first to a minimum value (at $r^*(\theta = 77°) \approx 5$ and $r^*(\theta = 85°) \approx 15$) and increases for large radii according to $\beta(r) \propto r^{1.5}$ leading to thermal dominance.

In summary, for our injection boundary condition we are left with the following three dynamical parameters,

$$(v_{\rm K}, \beta, \epsilon). \tag{4.11}$$

An overview of the simulations performed in this parameterization is shown in Tab. 4.2.

4.3.3 Numerical Grid and Physical Scaling

We use a numerical grid of 512×1024 cells applying cylindrical coordinates. Onward from the inner region ($r < 1, z < 1$), which is resolved with 20×20 equidistant cells, we apply a stretched grid with the element size increasing by a factor of $\lesssim 1.005$. This leads to a domain size of $(r \times z) = (100 \times 200) r_{\rm i}$ corresponding to $(300 \times 600)\ r_{\rm s}$ if $r_{\rm i} = 3 r_{\rm s}$ (see sketch in figure 4.1). Staggered magnetic fields treated via constrained transport (Balsara & Spicer 1999) are used to ensure $\nabla \cdot \mathbf{B} = \mathbf{0}$.

Because of the constraints imposed on the cell aspect ratio by the zero-current boundary (appendix B.1), we set the last five grid cells to be equally spaced with maximal aspect ratios $< 3/1$.

The dimensionless nature of our simulations allows for various astrophysical interpretations. We provide a physical scaling of simulation variables (marked with a prime) in the following paragraph.

Since velocities are given in terms of the speed of light ($c' = 1$), relativistic simulations are in need of only two additional scales. The simulation variables are connected to their physical counterparts via

$$v = v'c; \quad l = l'l_0; \quad t = t't_0 = t'l_0/v_0; \quad \rho = \rho'\rho_0 \tag{4.12}$$

$$p = p'p_0 = p'\rho_0 c^2; \quad B = B'B_0 = B'\sqrt{4\pi\rho_0 c^2} \tag{4.13}$$

where we re-introduced the factor $1/\sqrt{4\pi}$ that was absorbed in the field strengths in Equation (2.5). If we assume a Schwarzschild black hole as central body, we may set the spatial scale $l_0 = 6 r_g$, equating the inner disk radius with the ISCO.

Then it becomes

$$
\begin{aligned}
v_0 &= 3 \times 10^{10}\mathrm{cm\ s^{-1}} && (4.14)\\
l_0 &= 9 \times 10^{5}\mathrm{cm}\left(\frac{\mathrm{M}_\bullet}{\mathrm{M}_\odot}\right) && (4.15)\\
t_0 &= 3 \times 10^{-5}\mathrm{s}\left(\frac{\mathrm{M}_\bullet}{\mathrm{M}_\odot}\right). && (4.16)
\end{aligned}
$$

Assuming a physical outflow mass-loss rate in terms of the Eddington limited accretion rate $\dot{M} = 0.01\dot{M}_{\mathrm{edd}}$ we can provide a scale for the density by comparison to the mass loss rate of the simulation $\dot{M}'$

$$
\rho_0 = 6 \times 10^{-7}\frac{1}{\dot{M}'}\left(\frac{M_\bullet}{M_\odot}\right)^{-1} \mathrm{g\ cm^{-3}} \qquad (4.17)
$$

where we applied a radiative efficiency of $\epsilon(a) = 0.1$. The scaling of pressure and magnetic fields then follows as

$$
\begin{aligned}
p_0 &= 5 \times 10^{14}\frac{1}{\dot{M}'}\left(\frac{M_\bullet}{M_\odot}\right)^{-1} \mathrm{g\ cm^{-1}\ s^{-2}} && (4.18)\\
B_0 &= 8 \times 10^{7}\ \dot{M}'^{-0.5}\left(\frac{M_\bullet}{M_\odot}\right)^{-0.5} \mathrm{Gauss}. && (4.19)
\end{aligned}
$$

Under these considerations, the only remaining scaling parameter is the mass of the compact object $M_\bullet$. Neglecting additional physical processes such as radiation pressure or radiative cooling leaves us with a scale-free model that can be applied to any disk-wind launched jet around compact objects. Table 4.1 provides a fiducial scaling for a microquasar with $M_\bullet = 10M_\odot$ and for an AGN with $M_\bullet = 10^8 M_\odot$. The scale-free nature becomes obvious if we recall the rest-frame temperatures for an ideal gas, $T = \frac{p'\ c^2}{\rho' k_{\mathrm{B}}}\langle\mu\rangle \mathrm{m_p}$ (Anile 1989), with the mean molecular weight $\langle\mu\rangle$, the proton mass $\mathrm{m_p}$, and the Boltzmann constant k_{B}. For ionized hydrogen $\langle\mu\rangle = 0.5$ one would find temperatures of $T = (p'/\rho')\ 5.45 \times 10^{12}$K, while for an electron-positron plasma ($\mu \simeq 1/2000$) the temperatures are lower by three orders of magnitude. These ultra-high scaling temperatures are only reached in the very inner corona between the central object and the inner disk radius. In this study we do not intend to follow the dynamics of the inner region and we will extend the modeling of this black hole corona in the next chapter. In principle, once $p/\rho \gtrsim c^2$, the equation of state transcends towards $\gamma = 4/3$ according to a Synge-gas (see section 2.1.7.1). In the jet, thermal pressure quickly looses importance and the temperatures are significantly lower.

Table 4.1 Fiducial scaling

$\frac{M_\bullet}{M_\odot}$	l/l' [cm]	t/t' [s]	ρ/ρ' [g cm^{-3}]	p/p' [g s^{-2} cm^{-1}]	B/B' [Gauss]
10^8	9×10^{13}	3×10^3	1.8×10^{-16}	1.5×10^5	1.4×10^3
10	9×10^6	3×10^{-4}	1.8×10^{-9}	1.5×10^{12}	4.4×10^6

Note. — Scaling for simulation WA05 ($\dot{M}' = 32.67$) assuming a physical mass loss rate of $\dot{M} = 1\%\dot{M}_{edd}$ with an efficiency of $\eta* = 0.1$.

4.4 Results and Discussion

We now present the results of our numerical simulations considering the formation of relativistic MHD jets from accretion disks. Each simulation consumed approximately 48 hours on 16 processors. The overall goal is to test whether the paradigm of MHD self-collimation of non-relativistic jets established from numerical simulations Ustyugova et al. (1995); Ouyed & Pudritz (1997); Krasnopolsky et al. (1999); Fendt & Čemeljić (2002) also holds in the relativistic case.

Table 4.2 Parameter summary of our disk-wind simulations.

ID	Top	β	ϵ	Remarks	$\Gamma_{\max}$	Γ_∞	ξ	$v_{p,\max}$	$r_{\rm jet}$	$\dot{M}$
WA01	A	0.2	2/3	-	1.23	1.33	18.84	0.54	20.26	23.77
WA02	A	1	2/3	-	1.27	1.37	11.47	0.58	21.86	26.62
WA03	A	2	2/3	-	1.26	1.34	10.69	0.57	22.21	24.15
WB01	B	1	2/3	$\theta = 77°$	1.33	1.41	8.27	0.64	24.19	16.48
WB02	B	1	2/3	$\theta = 85°$	1.29	1.33	8.19	0.60	21.27	15.66
WA04	A	0.2	1/6	-	1.27	1.38	13.40	0.58	21.14	36.08
WA05	A	1	1/6	-	1.25	1.33	9.84	0.57	22.77	32.67
WA06	A	2	1/6	-	1.25	1.32	9.34	0.57	22.92	29.27

Note. — Columns are from left to right: simulation ID; initial magnetic field distribution (Top): potential field (A) or split monopole (B); plasma-β; accretion disk temperature parameter ϵ; specific remarks; to the right we show values of the steady state, the maximum Lorentz factor $\Gamma_{\max}$ and asymptotic Lorentz factor Γ_∞, collimation degree ξ, maximal poloidal velocity $v_{p,\max}$, jet radius $r_{\rm jet}$ and the total mass flux out of the domain $\dot{M}$.

4.4.1 Overall Evolution of the Outflow

The initial evolution of the disk corona is governed by the propagation of toroidal Alfvén waves launched due to the rotation of the field line foot-points. The initial force-free magnetic field structure is adapted to a new dynamic equilibrium according to a rotating wind magnetosphere.

A wind is launched from the disk boundary and is continuously accelerated driving a shock front through the initial hydrostatic corona and sweeping this material out of the computational domain (Fig. 4.3). The disk wind evolves into a collimated outflow of super-magnetosonic speed. Along the symmetry axis the hydrostatic initial condition is very well preserved. Once the bow shock has passed through the domain, the jet mass flux declines to a value which is solely governed by the internal outflow dynamics and the injection boundary conditions. Similarly, the post-shock magnetic field distribution follows as well from the internal outflow dynamics and has in principle little in common with the initial setup. Certain combinations of boundary conditions for mass flux and magnetic field will result in a quasi-stationary[1] state of the outflow evolution (see next section). From this point onwards we can start our investigations of collimation and acceleration. In this paper we concentrate on analysis when the flow has reached a quasi-steady state. We usually terminate our simulations after 500 inner disk-rotations P, while a quasi-steady state is established over most of the domain after about 200 rotations.

Figure 4.3 shows the time evolution for two exemplary simulations with an initial hourglass-shaped potential field distribution (case A) and a split-monopole field distribution (case B), each for the parameter choice $(\beta, v_K, \epsilon) = (1, 0.5, 2/3)$.

The figure shows the Lorentz factor, the poloidal magnetic field lines, poloidal electric current flow lines and the critical MHD surfaces. In addition the light surface is drawn.

Phenomenologically, the solutions form a magnetic nozzle with, depending on the disk flux distribution, considerable difference in the width, but comparable final opening angles of the fast component. A broader initial field distribution (case B) also results in broader and faster winds where the material originating from the inner disk is more effectively thinned out. In analogy to hydrodynamic nozzles, the flow reaches the slow-magnetosonic speed directly above the throat. Collimation happens mainly before the fast-magnetosonic surface is reached. Afterwards, the opening angle of a given field line is approximately conserved.

Of particular interest is the electric current distribution (shown for the time step $T/P = 250$). The electric current distribution is a consequence of the dynamical evolution of the outflow and therefore a direct outcome of the disk boundary magnetic flux profile and the Keplerian field line rotation.

In general, the electric current leaves the outer disk to return within the fast component of the outflow. It is expected to enter the inner disk and then flow radi-

[1]We denote the dynamical state as *quasi* stationary as due to Keplerian disk rotation the disk outflow a large radii has evolved for a considerably lower number of disk rotations. Therefore, a slight change in the dynamical state of the outer outflow can be expected after another few outer, thus 1000s of inner rotations.

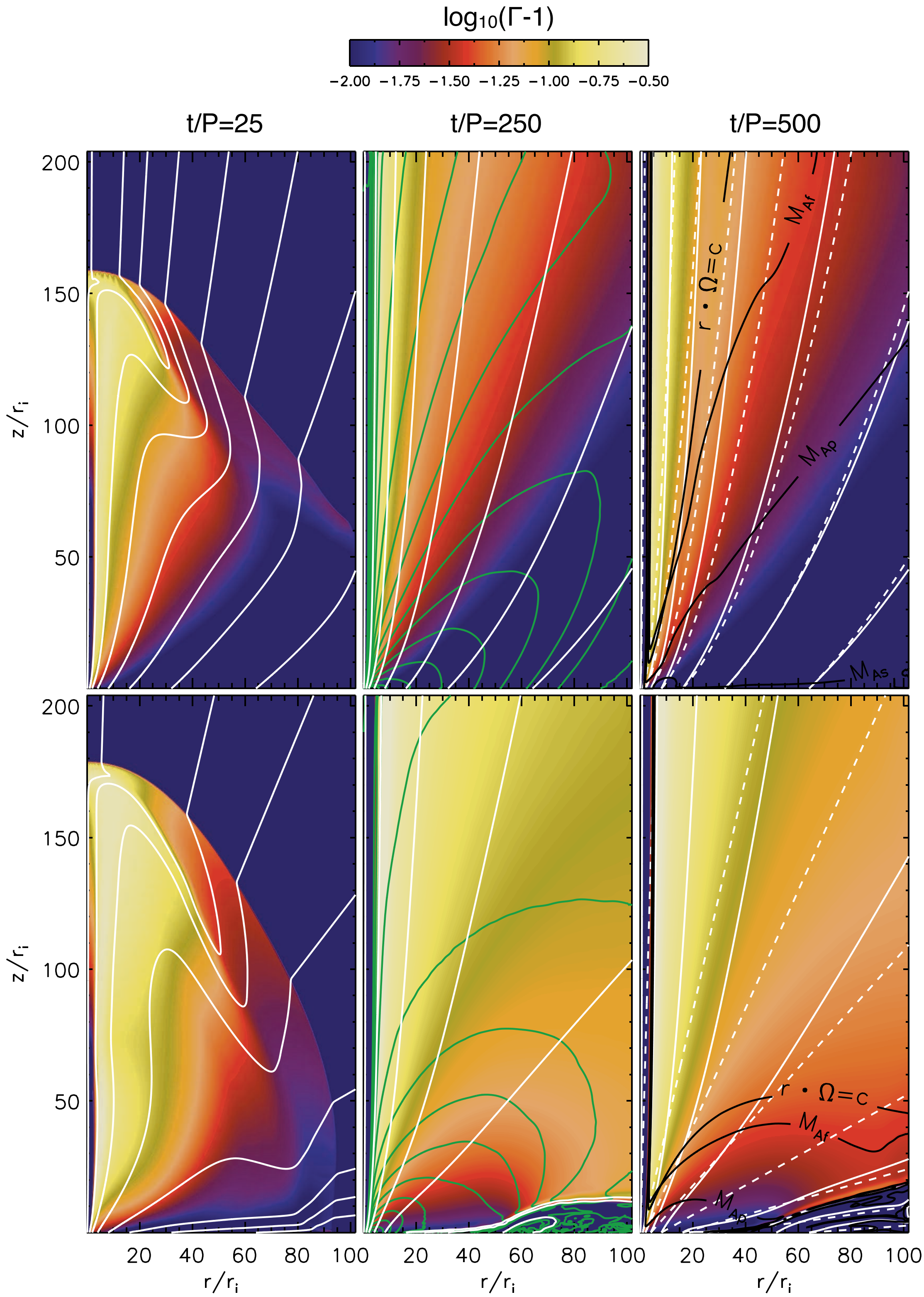

Figure 4.3 Formation of a relativistic MHD jet. Shown is the Lorentz factor (color gradient) in terms of $log_{10}(\Gamma - 1)$ at the time of 25, 250 and 500 (left to right) inner disk rotations. *Top:* Field distribution case A, hourglass-shape potential field (run WA02). *Bottom:* Split monopole initial field distribution case B (run WB01). Shown are poloidal magnetic field lines (solid white lines); the critical MHD surfaces (solid black lines); the light surface $r \cdot \Omega = c$ (solid black line). For time $T/P = 250$ electric current flow lines are added (solid green line). Time step $T/P = 500$ also show the initial field lines for comparison (dashed white lines).

ally outwards closing with the outgoing current. Such butterfly-shaped circuits are expected in Keplerian disks while the j_r plays a leading role in the disk-jet feedback (Ferreira 1997). A positive radial electric current in the disk-corona supports accretion by braking the disk material due to its magnetic torque $j_r \times B_z$ similar to a Barlow-wheel[2].

The inclination between the poloidal current vector and the magnetic field line indicates the direction of (de-) collimating magnetic forces acting on the flow. When the inclination becomes less than 90°, the Lorentz force $j_p \times B_\phi$ changes from collimation to de-collimation. In the actual field distribution, the field lines are somewhat pushed away from the surface $\mathbf{j_p} \perp \mathbf{B_p}$ (this is also where magnetic acceleration is most effective). For case B this happens beyond the light surface. As a result, both electric and magnetic forces deflect the flow towards the disk boundary which leads to a highly unstable layer just above the outer disk. We will provide an in-depth analysis including all forces acting on the flow in section 4.4.2.1.

The locations of the characteristic surfaces are signatures for the MHD flow. Depending on the initial magnetic flux distribution (case A,B) and the mass flux profile (see also Fendt (2006)), this location may vary a great deal. In our case B simulations, we generally observe surfaces which leave the domain in radial direction (parallel to the disk surface). For the case A simulations these surfaces tend to "collimate" leaving the domain in vertical direction. The latter implies a two-layered structure of the jet - a central super-fast magnetosonic jet surrounded by a sub-Alfvénic outflow. This is an interesting aspect for observational modeling and for stability analysis of sheath-spine jets (Pushkarev et al. 2005; Mizuno et al. 2007; Kovalev et al. 2007; Hardee 2007; Beskin & Nokhrina 2009). The broad wind launched from the outer regions of the disk has much lower velocities, decreasing continuously with increasing launching-radius. For example, the terminal velocity of the flow originating from $r_{\rm fp} > 32$ of the case A simulations drops below $0.2c$, consistent with the X-ray absorption features observed in a mounting number of AGN (Cappi 2006; Turner & Miller 2009). In principle, our dynamical models can provide basic ingredients (e.g. flow geometries and velocity gradients) for the modeling of spectral line profiles of disk winds (Knigge et al. 1995; Sim et al. 2008).

Following Fendt (2006), we may define an average collimation degree ξ of the outflow measured as the fraction of vertical and radial mass flux through equal-area

[2] However, this region is not resolved within our numerical domain, as it is located below our injection boundary as part of the underlying non-ideal MHD accretion disk. See Casse & Keppens (2002); Zanni et al. (2007) for non-relativistic simulations of the disk-jet interaction.

surfaces at a certain height (here at $z = z_m$),

$$\xi = \frac{\int_0^{r_m} r\Gamma v_z \rho|_{z_m}\, dr}{\int_{z_m - r_m/2}^{z_m} r_m \Gamma v_r \rho|_{r_m}\, dz}. \tag{4.20}$$

Similarly, we define a mass flux weighted jet radius,

$$r_{\rm jet} = \frac{\int_0^{r_m} r\Gamma v_z \rho|_{z_m}\, dr}{\int_0^{r_m} \Gamma v_z \rho|_{z_m}\, dr}. \tag{4.21}$$

The corresponding values for ξ and $r_{\rm jet}$ derived for $z_m = 200$ at the upper end of the domain and for time $t/P = 500$ are given in Tab. 4.2 along with the maximum Lorentz factor $\Gamma_{\rm max}$, the maximum poloidal velocity $v_{p,max}$, and the total mass flux $\dot{M}$. Figure 4.4 shows the time evolution of these quantities in the top panel. In general, we observe that the collimation degree ξ is the most sensitive tracer for secular trends among the observables mentioned. In the lower panel, we show the evolution of jet-power in the individual energy channels leaving the computational domain (radial and vertical). After the re-configuration of the initial stationary-state to the dynamical solution, the partitioning of energies is completed at around $t/P = 100$. Thermal energy-flux peaks when the hot bow-shock passes through the upper boundary. Far away from the central object, gravitational and thermal energy-flux are negligible. The integrated energy-flux is dominated by rest-mass, reflecting the fact that only the inner component reaches significant Lorentz-factors. The balance between Poynting and kinetic flux is of particular interest. Figure 4.4 shows merely the end result of the spatial conversion history with the remaining electromagnetic energy $\mathcal{S}$ above the purely kinetic part $\mathcal{K}$. More detailed insight into how this is established is provided in the following section using an individual field line.

4.4.2 Stationary State Analysis

Simulations starting from an initial field distribution A evolve into a quasi-stationary flow solution after about 200 inner disk rotations. Figure 4.6 shows our reference simulation WA04 at time $t/P = 250$, including an enlarged subgrid of the inner-most area of the domain.

Steady state solutions are helpful to understand the flow structure for a number of reasons. Firstly, by using MHD conservation laws, the conserved quantities (see Section 2.2.2) allow to identify the momentum and *energy channels* of the flow during acceleration and collimation. Secondly, by using the force-balance equations (2.62), (2.64) we may identify the leading forces on the material along the outflow. Thirdly, the cross-check for conserved quantities provides another test for the quality of our setup and the numerical approach. A secondary indicator of

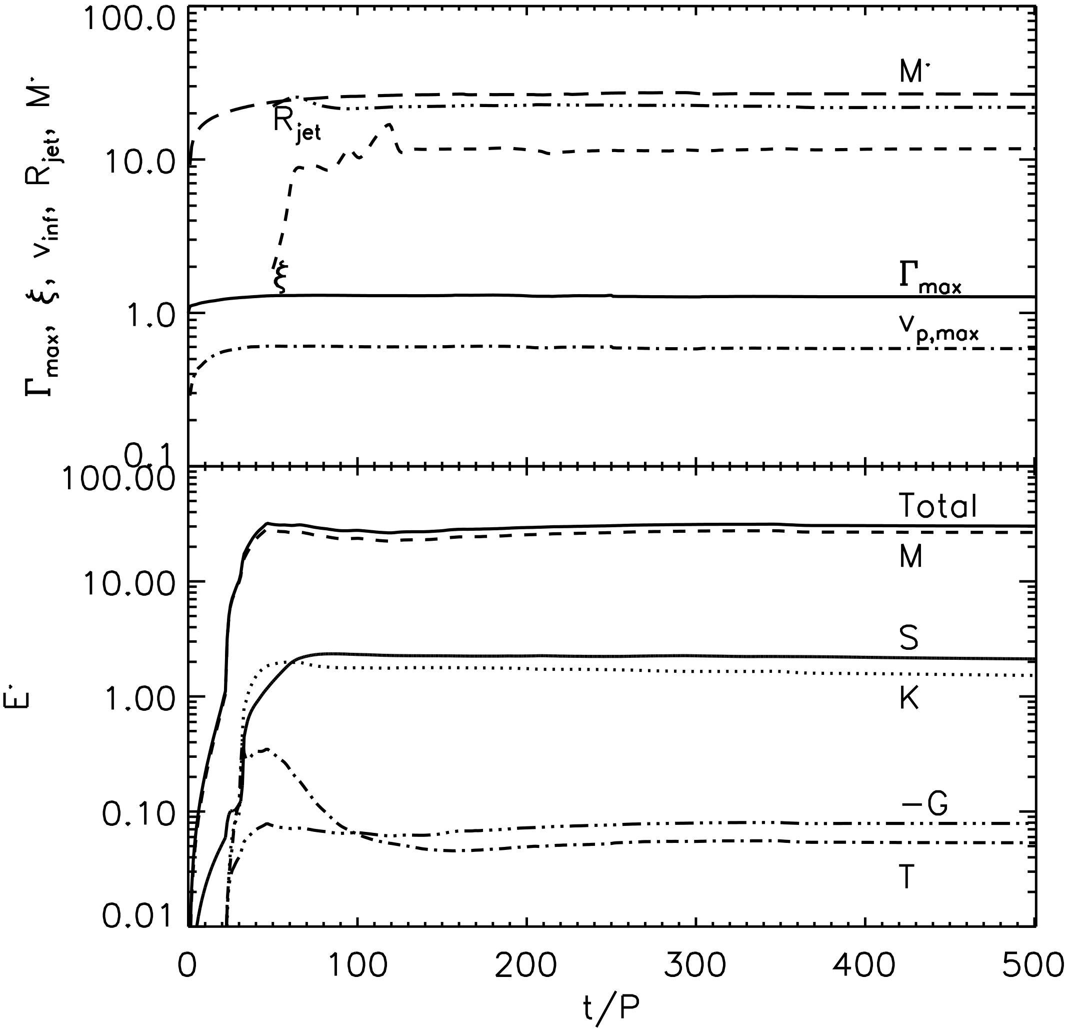

Figure 4.4 Time evolution of characteristic quantities. *Top panel:* After an initial adjustment till $t/P \simeq 200$, mass flux $\dot{M}$, jet radius r_{jet}, collimation degree ξ, maximal Lorentz-factor $\Gamma_{\max}$ and poloidal velocity $v_{p,\max}$ cease to evolve. *Lower panel*: Power in the individual energy chanels out of the domain. Thermal power (T) peaks when the shock reaches the upper boundary and is negligible otherwise. The total outgoing power (labeled accordingly) is dominated by rest-mass (M) and Poynting flux (S). Also shown are the gravitational (G) and (purely) kinetic (K) contributions (simulation run WA02).

stationarity is the alignment of poloidal velocities with the poloidal magnetic field lines, $E_\phi = 0$. This is why we included corresponding velocity vectors in Figure 4.6.

Stationarity is further confirmed by checking in detail the complete set of integrals of motion of the MHD-flow k, Ω, Q, l, μ as defined in Equations (2.51) − (2.55). Figure 4.5 shows the relative deviation of these quantities from their average value along a given field line after $t/P = 500$. The integrals are conserved within 1%-accuracy already right above the injection boundary - clearly demonstrating the quality of our numerical setup, in particular the injection boundary conditions carefully constructed from an equilibrium of Keplerian rotation and gas pressure.

Due to the differential rotation law, the number of Keplerian rotations $t/P(r)$ scales with radius as $t/P(r) = (t/P)r^{-3/2}$, implying that at the end of our simulations ($t/P = 500$), we have performed roughly one rotation at $r = 64$ and half a rotation at $r = 100$. Nonetheless the integrals of motion for the field line $r_{\rm fp} = 64$ are conserved within 0.1%.

4.4.2.1 Collimating and Accelerating Forces

In this section we identify the forces responsible for jet acceleration and collimation applying the steady-state parallel and transversal force-equilibrium Equations (2.62),(2.64).

Figure 4.7 compares these forces for a number of reference simulations (WB01, WA02, WA05) along a field line rooted at $r_{\rm fp} = 2$. As check for consistency, we also show the gradient of the Mach number $a \equiv B_p^2/4\pi\nabla_{||}M^2$ which just coincides with the summation of the parallel forces, indicating a steady state (see yellow solid and black dashed line).

In general, the outflow starts with sonic speed and is first launched by thermal pressure in the hot disk corona, respectively the centrifugal force in the colder version. Until the Alfvén point, the Lorentz-force of the poloidal electric current ($F_{\rm pbphi}+F_{\rm pinch}$) is the main magnetic driver. Ultimately the poloidal tension ($F_{\rm curv}$) keeps the acceleration up even above the fast surface.

Concerning the transverse force, we reproduce the expected sign-change of the curvature (tension) force (first collimating until the Alfvén surface, de-collimating beyond) and the poloidal pressure force (de-collimating until the light cylinder, collimating beyond). For the cross-field balance, we observe the following three regimes:

Just on top of the inlet, the main de-collimating forces besides poloidal magnetic pressure are thermal pressure in the hot case (WB02, WA02) and centrifugal support in the colder case (WA05). Gravity is here the strongest force towards the

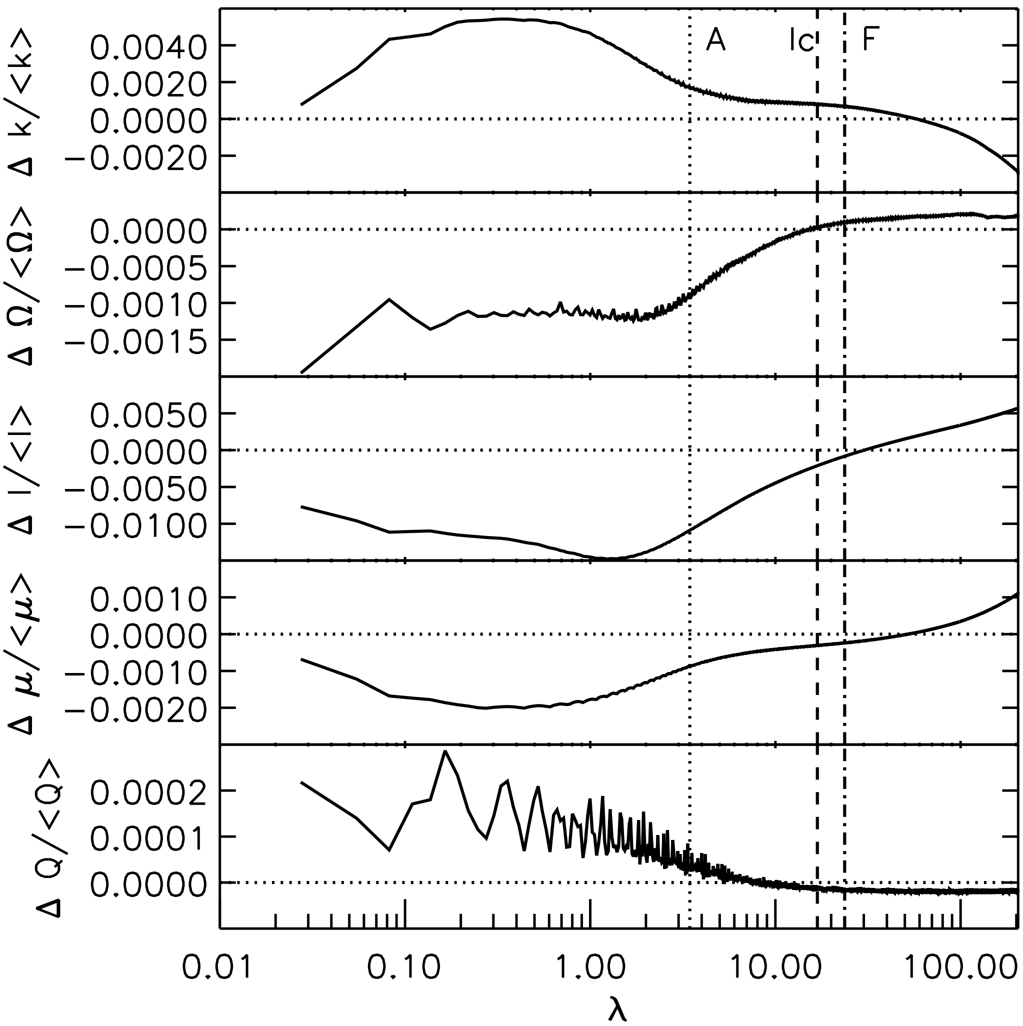

Figure 4.5 Field line constants (conserved quantities). Shown is the deviation from the average value along the field line rooted at $r_{\mathrm{fp}} = 2$ (simulation run WA02).

origin and the situation just reflects the radial force-equilibrium we have applied for the inlet boundary. This is the hydrodynamic regime.

At the Alfvén point, the residual of the pinch- and toroidal pressure-force ($\mathbf{j_p} \times B_\phi$) is the main collimator, balanced by the centrifugal term. Thermal pressure quickly looses importance. This is the magneto-hydrodynamic regime.

In the asymptotic region beyond the light-cylinder, de-collimation by electric forces overcomes the centrifugal force and is balanced by the poloidal magnetic pressure that changes its sign at the light-cylinder (best seen in WB01). This is the relativistic regime.

To get a global impression on the relative importance of the individual forces we show a radial cut throughout the asymptotic jet in figure 4.8. The strongest forces arise across the inner asymptotic light surface which separates field lines of

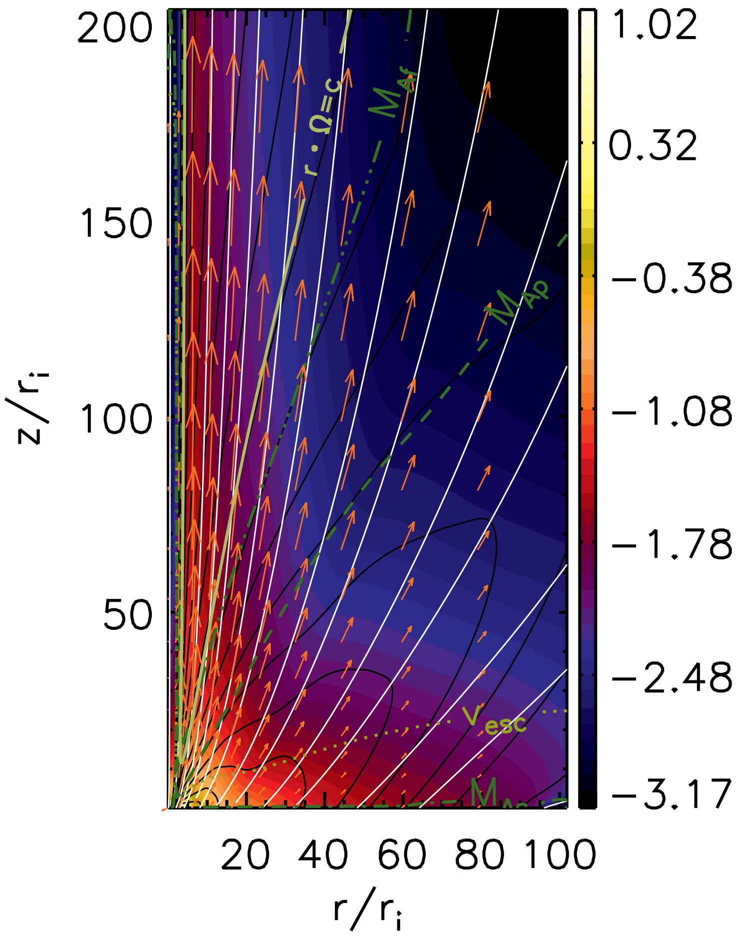

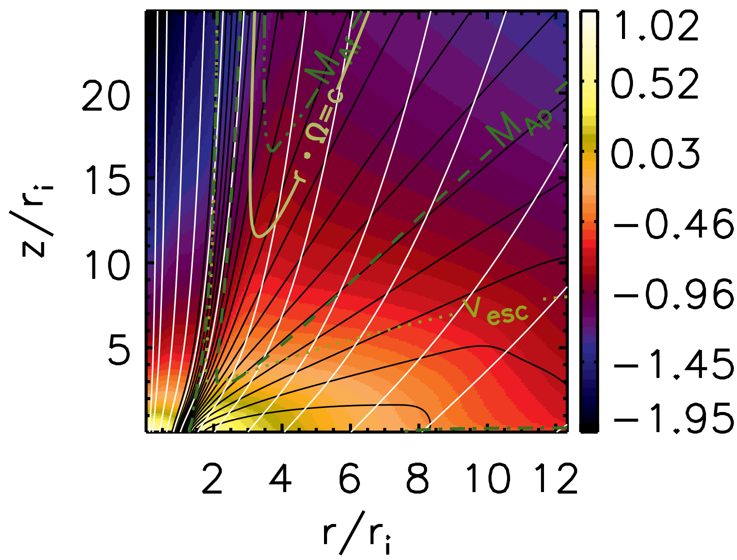

Figure 4.6 Logarithmic (rest-frame) density of the stationary flow (simulation run WA04). Shown are poloidal magnetic field lines (solid white), electric current flow lines (solid black), characteristic MHD surfaces (various dot-dashed green), surface of escape velocity (dotted green), light surface (solid green). Arrows in the top plot indicate the velocity field. The bottom figure is an enlarged picture of the central region indicating the three regimes defined by the light surface.

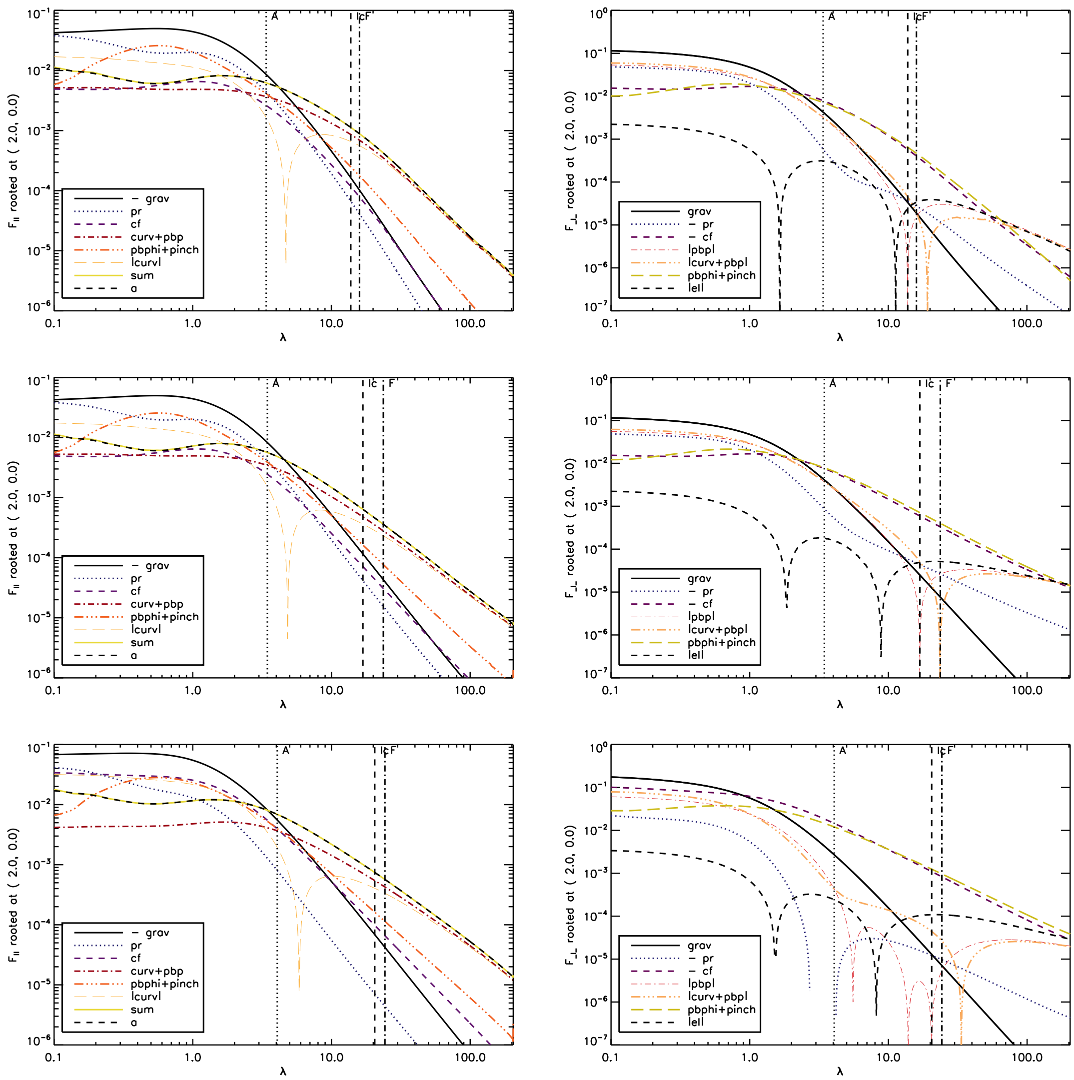

Figure 4.7 Accelerating (left column) and collimating (right column) forces along the field line rooted at $r_{\mathrm{fp}} = 2$ for the three reference simulations (from top to bottom): *WB01* (split monopole), *WA02* (hourglass potential field, hot case), and *WA05* (hourglass potential field, cool case). Shown are the contributions from gravity, gas pressure gradient, centrifugal force, poloidal magnetic field pressure gradient, poloidal field tension and pressure gradient, toroidal magnetic field pressure gradient and tension, and forces due to the electric field. Vertical lines indicate the critical surfaces - the Alfvén point along this field line, denoted by 'A', the light cylinder radius denoted by 'lc', and the fast magnetosonic point denoted by 'F'. In this logarithmic representation a change of sign in the force direction is indicated by the singularities along the graphs.

high angular velocity from those in the non-rotating corona along the axis. Here the electric de-collimation is essential. The $B_\phi(r)$ profile is curled up from the inner disk radius along the outflow - resulting in a magnetic pressure gradient that works in unison with the toroidal field pinch force until at some radius the toroidal field surpasses its maximum and decreases (negative gradient).

The strong gradients in toroidal field and rotation induce a current sheet and give rise to an electric charge. The space charge $\rho_{\rm e} = (1/4\pi)\nabla \cdot \mathbf{E}$ is positive close to the axis and changes its sign at a critical line similar to the case of pulsar winds (Goldreich & Julian 1969).

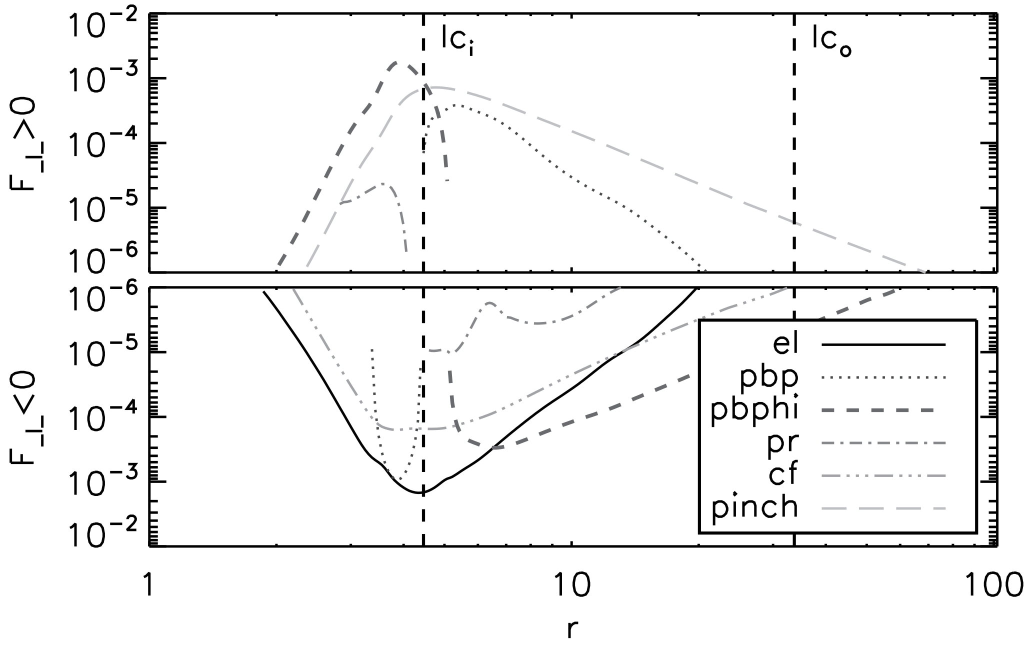

Figure 4.8 Trans-field force cut at $z = 200$, inner (lc_i) and outer (lc_o) light-cylinder. The differentially rotating field lines are fastest at the inner disk-radius, resulting in the inner light-cylinder - here electric de-collimation is important. The $B_\phi(r)$ profile is curled up from the inner disk radius onwards and results in a magnetic pressure gradient that works in unison with the pinch force until the toroidal field surpasses its maximum. Within $r < 3$, we omit the curves for thermal and poloidal pressure. These terms fluctuate around $\pm 10^{-5}$ while balancing each other. (run WA02)

4.4.2.2 Energy Conversion

In the simulations where injection is sub-magnetoslow, the energy flux is not a free parameter, but is consistently determined by the simulation of the disk-wind. It is hence of interest how the partitioning and conversion is realized. From the values of $\mu_{\rm max}$ given in Tab. 4.2 it is obvious that our disk-corona supports only mildly relativistic flows below $\Gamma = 1.5$ (section 2.2.2).

In Fig. 4.9 (top panel) we show the efficiency σ of Poynting flux to kinetic flux conversion along the field line with $r_{\rm fp} = 2$ in the fast component of the jet. Here, σ is below equipartition already at the inlet and it further decreases as Γ approaches μ. In Fig. 4.9 (top panel) the toroidal velocity shows that the flow decouples from co-rotation with the magnetic field at the Alfvén point. Beyond the Alfvén point, angular momentum is then carried predominantly by the magnetic field. The poloidal velocity increases from low injection value (sonic velocity) to $\sim 0.5c$. Further acceleration can not be expected as the bulk of the energy is already in kinetic form. The bottom panel of Figure 4.9 shows the individual energy channels compared to the rest-mass flux for the same field line. At the base of the jet, the strong poloidal electric currents (a strong toroidal field) give rise to an outflow with $\mathcal{K} < \mathcal{T} < -\mathcal{G} < \mathcal{S} < \mathcal{M}$, predominantly transporting energy via rest-mass and Poynting-flux.

The kinetic energy flux surpasses the thermal flux at the Alfvén point and further overcomes the gravitational binding energy term shortly thereafter. This is not surprising, since the escape-surface can be close to the Alfvén surface at least for the inner field lines (see also Fig. 4.6).

Only then, the cold limit $\mu = \Gamma(\sigma + 1)$ is applicable - it is certainly valid in the asymptotical outflow where thermal and gravitational energy fluxes are negligible.

4.4.3 Dependence on the Launching Environment

For the simulations described up to now, we have performed in addition several parameter runs in order to investigate how the resulting jet dynamics depends on the (prescribed) launching conditions - the disk corona (see Tab. 4.2). We now focus on the impact of the plasma β and the disk temperature parameter ϵ.

In general, a low β (a stronger magnetic field) we find that the outflow tends to collimate more, as indicated by the higher average collimation degree ξ and a lower momentum weighted jet radius $r_{\rm jet}$. This in principle decreases the MHD acceleration efficiency which critically depends on the divergence of flux surfaces. It is straightforward to define the mass flux-weighted (half-) opening angle of outflow,

$$\theta_{\dot{M}} = \operatorname{atan} \xi^{-1}, \tag{4.22}$$

which translates to angles of $3^\circ < \theta_{\dot{M}} < 7^\circ$ for the outflows under consideration.

The impact of the magnetic field strength on the amount of mass flux is not clearly visible, as the two simulations with $\epsilon = 1/6, 2/3$ show a different trend. As the ϵ-parameter is simply a proxy for the disk corona density, it will affect the

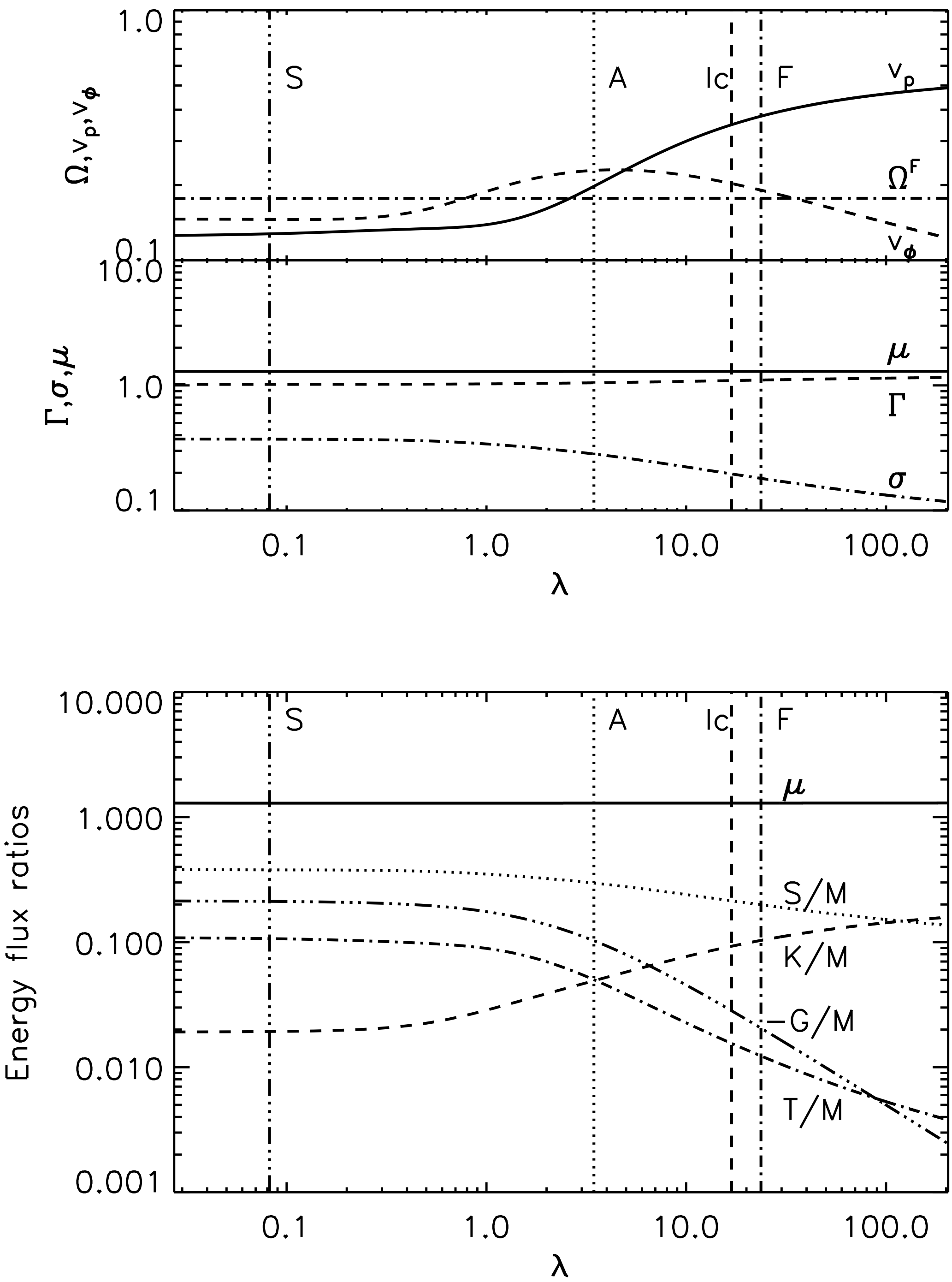

Figure 4.9 Dynamical quantities as a function of the distance along the field line rooted at $r_{\rm fp} = 2$ for the model WA02. Vertical lines indicate the slow-magnetosonic, Alfvén, light surface and fast magnetosonic transitions (from top to bottom). *Left:* Isorotation parameter Ω, poloidal and toroidal velocity are shown in the top panel. Lorentz factor Γ, energy conversion efficiency σ, and normalized total energy flux μ in the bottom panel. The flow is below equipartition already at the base of the jet. *Right:* Complete energy flux ratios. In the asymptotic region, thermal and gravitational fluxes are obviously negligible.

collimation in the following manner: A higher inflow density lowers the Alfvén surface towards the disk surface which in turn broadens the current topology and therefore widens the flow. This is also the trend that we observe in the indicators ξ and $r_{\rm jet}$. Given that the injection speed calculated iteratively from the outflow simulation approaches the slow-magnetosonic speed, we expect the mass flux to scale as $\dot{M} \propto \sqrt{p\rho}$. In fact, this is approximately realized since we have $\dot{M}(\epsilon = 1/6)/\dot{M}(\epsilon = 2/3) = \sqrt{2.5} \simeq 1.6$.

The change of the initial split-monopole inclination θ has little effect on the overall jet collimation angle. In particular, we observe an opposite trend as the wider initial field with $\theta = 77°$ ends up slightly more collimated than the one with $\theta = 85°$. Clearly a wider initial field leads to a larger jet radius $r_{\rm jet}$. Here, we like to stress the point that for the final steady state solutions in our simulations the initial field structure is important only insofar as it also prescribes the poloidal magnetic field profile along the outflow launching boundary. The field structure is completely changed from the initial steady structure to a new dynamic equilibrium. Thus it makes no sense to compare the collimation of the initial field with the collimation of the outflow field distribution.

The parametrization adopted in this study forbids a direct specification of the critical energy flux parameters μ and σ. As a result, the coronal winds obtained are heavily mass-loaded and unable to accelerate beyond $\Gamma < 1.5$. In order to explore also highly relativistic flows, we need to change the parametrization allowing to give the full energy fluxes as boundary conditions. This will be pursued in the following chapter.

4.5 Summary and Conclusions

We have presented ideal MHD simulations of the formation of special relativistic disk winds using the PLUTO 3.0 code. On the technical side, the key points are:
i) The inclusion of (Newtonian) gravity allows us to specify an astrophysically sensible boundary condition of a hydrodynamically stable disk corona. We can thus consistently follow the acceleration from initially sub-escape velocity winds.
ii) Much dedication has been put in the development and testing of a novel realization for the outflow boundary that enables us to simulate for hundreds of inner disk rotations while minimizing spurious collimation due to artificial boundary currents. Our detailed study of jet collimation is possible only through this effort.

As a general result we obtain well collimated jets with a mass flux weighted half-opening angle of $3 - 7°$ and mildly relativistic velocities depending on the launching conditions for the outflow. The flow collimation happens mainly in the classical (non-relativistic) regime before the light surface. A major result of our simulations is that we - for the first time - self-consistently calculated the shape of that light surface. The light surface determines the "relativistic" charater of the flow. Material which traverses the light surface experiences the full relativistic effects.

We can identify three dynamically distinct regions in terms of flow collimation.
i) In the hydrodynamic regime upstream of the Alfvén surface, gravity balances thermal and magnetic pressure, respectively the centrifugal force in the colder case.
ii) In the magneto-hydrodynamic regime following the the Alfvén surface downstream, the residuals of magnetic pinch and the toroidal magnetic pressure gradient balances the centrifugal force.
iii) In the relativistic regime located downstrem of the light surface, the poloidal magnetic pressure gradients now impose a collimating force against electric field de-collimation. Electrodynamic forces ultimately overcome the classical magneto-centrifugal contribution.

A steep rotation profile of the field line as given by a Keplerian disk results in a light surface geometry which steepens for large radii. Depending on the magnetic field profile, the light surface may even collimate along the flow for large radii. In such a case the relativistic core inside the light surface is naturally confined by a non-relativistic wind. The ability of both the relativistic jets and the non-relativistic disk winds to collimate may provide confining agents for an axial ultra-relativistic funnel which could probably be launched by the Blandford-Znajek process.

The relatively slow winds found to arrise at large distances of around 100 Schwarzschild radii may be observed as X-ray absorption winds in radio-quiet AGN.

In the case of Blandford-Payne disk winds, the outflow is kinetic energy-dominated with the ratio of electromagnetic energy flux to kinetic energy flux $\sigma < 1$ already at the jet base and with this ratio further de-creasing downstream the outflow. These disk winds start out with near sonic speed and reach only mildly relativistic speeds up to Lorentz factors $\Gamma < 1.5$.

Chapter 5

Poynting Dominated Flows

5.1 Introduction

In order to accelerate to highly relativistic velocities via MHD processes, the base of the flow has to be dominated by Poynting flux. This is true for jets emanating from the innermost region of the accretion disk as well as for jets powered by the spin-energy of the central black hole. The axisymmetric, steady state theories of such ideal MHD jets predict that the conversion to kinetic energy works efficiently only up to the fast magnetosonic surface located a few light cylinder from the base (Sakurai 1985; Li et al. 1992; Beskin & Nokhrina 2006). At this point, the ratio of Poynting flux to kinetic energy σ merely drops to the value $\simeq \mu^{2/3}$ where μ signifies the available Poynting flux at the base of the flow. Therefore, for $\mu \gg 1$, the flow remains strongly Poynting flux dominated at the fast surface. Beyond the fast magnetosonic point, flow acceleration proceeds gradually (e.g. logarithmically for a freely expanding jet: Tomimatsu (1994); Begelman & Li (1994)) and can become susceptible to the environmental pressure. Due to the uncertain boundary conditions at the base of the outflow and along the outermost field-line, the efficiency of asymptotic flow acceleration is a matter of considerable debate (Vlahakis & Königl 2003; Heyvaerts & Norman 2003b; Tchekhovskoy et al. 2009; Lyubarsky 2009). In the context of pulsar wind nebulae where observations of the termination shock require $\sigma \simeq 10^{-3}$, the telltale *σ-problem* remains a challenge for MHD modeling even after 30 years of research (Rees & Gunn 1974; Kennel & Coroniti 1984; Begelman & Li 1992).

To discuss the particular situation in AGN, we mainly follow the line of argument outlined by Sikora et al. (2005). In AGN, observational evidence supports a gradual acceleration on scales of $10^3 - 10^4$ Schwarzschild radii. A cold flow with high bulk Lorentz factor $\Gamma \leq 5$ in the direct vicinity of the accretion disk would Comptonize the disk photons giving rise to a beamed, highly polarized soft X-ray bump (Begelman & Sikora 1987). This up-scattering would also promote X-ray precursors of γ-ray flares produced under the non-thermal shock-in-jet paradigm (Moderski et al. 2004). Absence of such features hints to a large-scale acceleration process in blazars. Attempts to directly observe the bulk flow acceleration process on the parsec scale were made by Sudou et al. (2000) and Jones & Wehrle (2002) at the example of the radio galaxy NGC 6251. Based on the profiles of jet-to-counter jet intensity ratios (see Section 1.4.2), Sudou et al. (2000) derived a velocity of $0.13c$ at a distance of $\simeq 0.53$pc, accelerating to $0.42c$ at $\simeq 1$pc of displacement. However, these results were questioned by Jones & Wehrle (2002) who were unable to detect the counter-jet, despite of comparable angular resolution. Cotton et al. (1999) combined flux-ratios with superluminal motion measurements of the parsec-scale jet in the radio galaxy NGC 315. In their paper, an acceleration of the emitting component from $0.77c$ to $0.95c$ at displacements of 3.3pc and 9.5pc is inferred.

Time-lags between γ-ray flares and accompanying radio flares in blazars can be used to yield an upper limit on the distance between the *blazar zone* (γ-ray production site) and the radio photosphere. Recent observations of (less than) monthly time-lags suggest a displacement of the blazar zone of ~ 10pc supporting a *far dissipation* scenario (Sikora et al. 2008; Marscher et al. 2010; Agudo et al. 2011). Via the simultaneous observation of an optical polarization swing and a γ-ray flare, Abdo et al. (2010b) could pinpoint the flare region in the blazar 3C 279 to displacements of $\sim 10^5$ gravitational radii. This far dissipation is challenged by observations of rapid γ-ray variability which demand an intrinsic scale of the emitting region below 0.01pc (e.g. Tavecchio et al. 2010). Hence rapid variability and displacement can only be reconciled when a highly collimated flow with an opening angle well below $1°$ is assumed even at the parsec scale. The emerging scenario suggests a large ($\sim 10^4 r_{\rm S}$) Poynting dominated acceleration zone where strong shocks necessary for particle acceleration are suppressed. The end of the acceleration and Poynting dominance would then mark the beginning of the blazar zone where kinetic energy can be dissipated efficiently. At this point, the collimation angle needs to be already below $1°$. Although a very appealing scenario, rigorous analysis with large source statistics so far only supports the parsec-scale radio core as a likely location for both γ-ray and radio flares (e.g. Kovalev et al. 2009).

An other promising site for strong particle acceleration is the reconfinement shock where the environmental pressure trumps over the expanding jet. It is educative to view the reconfinement scale as proxy for jet-environment interaction in relation to the acceleration scale for Poynting dominated flows. We can estimate the equipartition scale for a collimating jet of geometry $z \propto r^{1.5}$ following Barkov & Komissarov (2008); Beskin & Nokhrina (2009)

$$z_{\rm eq} = 2.7 \times 10^4 r_{\rm S} \left(\frac{\Gamma_\infty}{30}\right)^3 = 0.2 \left(\frac{\Gamma_\infty}{30}\right)^3 \frac{M_\bullet}{10^8 M_\odot} \text{pc}. \tag{5.1}$$

For a typical AGN, a lateral expansion of $r_{\rm eq} = 900 \ (\Gamma_\infty/30)^2 r_{\rm S} \simeq 7$mpc is obtained. From the equipartition site, the jet enters a coasting zone and widens with near constant opening angle. When we define the reconfinement for magnetically dominated flows as the site where *magnetic* pressure is trumped by thermal pressure of the interstellar medium, the pressure equilibrium radius $r_{\rm p}$ of the coasting jet can be estimated as

$$r_{\rm p} = \left(\frac{\mu m_{\rm p} c^2 \eta}{2 k_{\rm B} T_{\rm ISM}}\right)^{1/2} r_{\rm eq} = 5 \left(\frac{\eta}{10^{-5}}\right)^{1/2} \left(\frac{T_{\rm ISM}}{10^6 \text{K}}\right)^{-1/2} r_{\rm eq} \tag{5.2}$$

depending on the ambient temperature $T_{\rm ISM}$ and inertial ratio $\eta \equiv \Gamma^2 \rho_{\rm j}/\rho_{\rm ISM}$. Relation (5.2) and thus ($r_{eq} \sim r_{\rm p}$) suggests that for a typical choice of parameters (e.g. Kraft et al. 2003; Croston et al. 2007), environmental interaction and acceleration are interrelated processes that can in fact not be considered separately on the parsec scale. For example, for very low inertial ratios $\eta \lesssim 10^{-7}$, the jet could be forced to reconfinement already in the Poynting dominated acceleration phase. The extreme spread between equipartition scale and the size of the central object indicated by Equation (5.1) poses a huge challenge for dynamical simulations. Correspondingly, the equipartition scale for highly relativistic flows can only be reached with very specialized numerical codes. (see the discussion in section 5.3). So far, the magnetic reconfinement is only seen in analytic (e.g. r-self-similar) studies and awaits verification with less severe assumptions by means of numerical simulations.

In the following, we will investigate whether the requirements of large acceleration scales and high collimation can be met for Poynting dominated disk jets. In particular, we will show simulations covering up to four orders of magnitude in linear scale and study various current distributions in the jet. The relativistic solutions obtained in this chapter will then be used for the synthetic synchrotron observations detailed in the next chapter.

5.2 The Relativistic MHD Jet

We perform axisymmetric jet acceleration simulations with the PLUTO 3.01 code (Mignone et al. 2007) solving the special relativistic magnetohydrodynamic equations. As in the previous chapter, the simulations are of the *disk-as-boundary* type, however in the present study the jet starts out with the slow magnetosonic velocity opening the freedom to assign all energy channels as input parameters. The energy of the jet base is dominated by Poynting flux, driving a large-scale poloidal current circuit. This current distribution is prescribed as a boundary condition in the toroidal magnetic field component. We investigate three cases for $B_\phi(r) \propto r^{-s}$ with $s \in \{1, 1.25, 1.5\}$, where r is the cylindrical radius, resulting in asymptotic jets which are either in a current-carrying (one of them) or current-free (two others) configuration. Injected initially with slow magnetosonic velocity, the jet material accelerates through Alfvèn and fast magnetosonic surfaces within the simulated domain.

5.2.1 Numerical Grid Setup

To eradicate any artificial collimation effect from the outflow boundaries, we decided to move the domain boundaries to such large distance that they are out of causal contact with the region of interest. An inner equidistant grid of 20 cells extends to the scale radius r_1 corresponding to the inner radius of the accretion disk. Beyond r_1 the grid is linearly stretched to $(r, z) = (500, 500)$ with a scaling factor of 1.0013, and for $(r, z) > (500, 500)$ with a larger scaling factor of 1.0047. So far, we apply a square box of 2000^2 scale radii corresponding to 2555^2 grid cells. Magnetic fields are advanced on a staggered grid using the method of constrained transport (Balsara & Spicer 1999) supplied by PLUTO.

The first possible contamination by boundary effects takes place when the bow shock reaches the upper outflow boundary after $t_{c1} < z_{\rm end}/c = 2000$. A typical simulation is terminated after maximally $t_{c2} = 3000$ time units when a signal traveling at the speed of light could have returned from the $z_{\rm end}$ boundary to the subdomain. This conservative treatment ensures that no spurious boundary effects can occur.

In order to test this we have re-run one of our simulations on a five times larger computational domain with comparable resolution. This simulation provided the same result as the lower grid size simulation and acquired a nearly stationary state when terminated. Thus, the region of interest is not at all affected by any outflow boundary effects on account of an increased computational overhead.

5.2.1.1 Inflow Boundary Conditions

In a well posed MHD boundary, the number of outgoing waves (i.e. seven minus the downstream critical points) must equal the number of boundary constraints provided. Thus, in addition to the $B_\phi(r)$ and $v_p(r)$ profiles, we choose to prescribe the thermal pressure $p(r)$ and density $\rho(r)$ as boundary conditions for the jet injection (the jet inlet). The fifth condition sets $v_p || B_p$ and thus constrains the toroidal electric field $E_\phi(r) \equiv 0$. This is a necessary condition for a stationary state to be reached by the axisymmetric simulation.

The remaining primitive MHD variables v_ϕ and B_r are extrapolated linearly from the computational domain, while the component B_z (which determines the magnetic flux) follows from the solenoidal condition.

Specifically, the fixed profiles read

$$\rho(R) = \rho_1 \left[(1-\theta)R + \theta R^{-1.5}\right] \tag{5.3}$$

$$p(R) = p_1 \left[(1-\theta)(1-\rho_1 \ln R) + \theta R^{-2.5}\right] \tag{5.4}$$

$$B_\phi(r) = B_{\phi,1} \left[(1-\theta)r + \theta r^{-s}\right] \tag{5.5}$$

$$v_p(r) = v_{\rm sm}(r) \tag{5.6}$$

where

$$\theta = \begin{cases} 0; & r < 1 \\ 1; & r \geq 1 \end{cases} \tag{5.7}$$

is the step function and r and R denote the cylindrical and spherical radius, respectively. Here and in the following, a subscript 1 indicates the quantity to be evaluated at $(r, z) = (1, 0)$.

The slow magnetosonic velocity profile along the disk $v_{\rm sm}(r)$ of relation (5.6) is updated every time step to account for the variables which are extrapolated from the domain. Within $R < 1$, an inner "black hole corona" with relativistic plasma temperatures is modeled. The physical processes responsible for the formation of an inner hot corona could be an accretion shock or a so-called CENBOL shock (CENtrifugal pressure supported BOundary Layer shock) (see also Kazanas & Ellison 1986; Das & Chakrabarti 1999). Also Blandford (1994) has proposed a mechanism of dissipation near the ergosphere as a consequence of the Lense-Thirring effect. Due to the large enthalpy and decreasing Poynting flux of the inner heat bath, a thermally driven outflow is anticipated from this region (e.g. Meliani et al. 2010b). We apply the causal equation of state introduced by Mignone et al. (2005) to smoothly join the relativistically hot central region to the comparatively cold disk jet. This choice permits a physical solution for both regions of the flow (see also Mignone & McKinney 2007).

5.2.1.2 Outflow boundary conditions

At the outflow boundaries we apply power-law extrapolation for p, ρ and the parallel magnetic field component, while we apply the solenoidal condition to determine the normal magnetic field vector B_z respectively B_r. For the velocities and the toroidal field, zero-gradient conditions are applied. This choice is particularly suited to preserve the initial condition that is well approximated by power laws. A more sophisticated treatment such as force-free (introduced by Romanova et al. 1997) or zero-current boundaries as in the previous chapter is rendered unnecessary by the increased computational grid as detailed before.

5.2.2 Initial Conditions

As initial setup we prescribe a non-rotating hydrostatic corona threaded by a force-free magnetic field. For the initial poloidal field distribution we adopt $B_r = 1/r - z/r\,(r^2+z^2)^{-1/2}$ and $B_z = (r^2+z^2)^{-1/2}$ as in the previous chapter. The hydrostatic corona is balanced by a point-mass gravity in a Newtonian approximation. In order to avoid singularities in the density or pressure distribution, equations (5.3), (5.4), we slightly offset the computational domain from the origin by $(r_0, z_0) = (0, 1/3)$.

5.2.3 Parametrization

In the present setup we focus on effects of the poloidal current distribution and parametrize accordingly. Thus, we set the Kepler speed at $r = 1$ to $v_\mathrm{K} = 0.5c$ for convenience, yielding a sound speed $c_{\mathrm{s},1} = (\gamma p_1/\rho_1)^{1/2} \simeq 0.4c$ from the hydrostatic condition. To further minimize the number of free parameters, we tie the toroidal field strength given by $B_{\phi,1}$ to the poloidal field strength via $B_{\phi,1} = 0.5 B_{p,1}$. This Ansatz is consistent with the sub-Alfvèninc nature of the flow, since at the Alfvèn point $B_{\phi,1} \simeq B_{p,1}$ (e.g. Krasnopolsky et al. 1999) is valid. The two remaining parameters are the poloidal magnetic field strength measured by the plasma-beta $\beta_1^2 = 2p_1/B_{p,1}^2$ and the toroidal field profile power law index s.

Note that with the choice of a fixed in time toroidal field, the injected Poynting flux is controlled via the β_1 parameter, implying the toroidal field being induced in a non-ideal MHD disk below the domain. The conserved total jet energy flux and its partitioning between Poynting and kinetic energy given by the σ-parameter essentially become boundary conditions and determine the terminal Lorentz factor.

5.2.4 Physical Scaling

In order to convert code units to physical units we need to define the two scaling parameters of length and density, while the velocity is naturally normalized to the speed of light c. As before, to obtain an approximate radial scale, we assume that the transition between the inner corona to the disk-driven jet at $r = 1$ corresponds to the innermost stable circular orbit at $3R_\mathrm{S}$ (for a Schwarzschild black hole).

Hence the physical length scale is given by

$$r_{\rm cgs} = 8.9 \times 10^{14} \frac{M_\bullet}{10^9 M_\odot}\; r \text{ cm}. \tag{5.8}$$

The physical density is now obtained by assuming a total jet power $\dot{E}_{43}$ in units of 10^{43}erg s^{-1},

$$\rho_{\rm cgs} = 4.7 \times 10^{-19} \frac{\dot{E}_{43}}{\dot{E}} \left(\frac{M_\bullet}{10^9 M_\odot}\right)^{-2} \rho \text{ g cm}^{-3}, \tag{5.9}$$

where $\dot{E}$ is the corresponding power in code units for a certain simulation run (of order ~ 10). With this, the magnetic field strength follows to

$$B_{\rm cgs} = 73 \left(\frac{\dot{E}_{43}}{\dot{E}}\right)^{1/2} \left(\frac{M_\bullet}{10^9 M_\odot}\right)^{-1} \; B \text{ Gauss} \tag{5.10}$$

and the physical time scale becomes

$$t_{\rm cgs} = 3.1 \times 10^{4} \frac{M_\bullet}{10^9 M_\odot}\; t \text{ s} . \tag{5.11}$$

Unless stated otherwise, we adopt a black hole mass of $M_\bullet = 10^9 M_\odot$ and a total jet power of $\dot{E}_{43}$. In order to calculate the observable radiation fluxes in the next chapter, we assume a photometric distance of $D = 100$ Mpc. The angular scale of the Schwarzschild radius then becomes $\alpha_{\rm rS} = 0.2\ \mu$as. For the case of M87's supermassive black hole with $M_\bullet = 6.6 \times 10^9 M_\odot$ and $D =$ 16 Mpc we would have $\alpha_{\rm rS} = 8\ \mu$as yielding an increase in resolution by a factor of 40 compared to our fiducial scaling.

5.3 Jet Dynamics: Acceleration and Collimation

The large intrinsic scales of the relativistic MHD jet acceleration process require substantial numerical effort when simulated with a dynamical code. Codes optimized for such tasks were developed by Komissarov et al. (2007) or Tchekhovskoy et al. (2008), involving particular grid-extension techniques which can speed up the simulations of a causally de-coupled flow. In both seminal papers the flow acceleration could be followed substantially beyond the equipartition regime to establish tight links to analytical calculations. However, it can be argued that by using a rigid, reflecting boundary of certain shape as done by Komissarov et al. (2007), or a force-free approach as applied by Tchekhovskoy et al. (2008), the rate of jet collimation resulting from those simulations could be altered.

Here we aim at studying MHD *self*-collimation including inertial forces. We therefore solve the full MHD equations omitting the outer fixed funnel around the jet and replace it with a stratified atmosphere which may dynamically evolve due to the interaction with the outflow. By placing the outer boundaries out of causal contact with the solution of interest, we can be certain to observe the intricate balance between jet self-collimation and acceleration that is inaccessible otherwise. We like to emphasize that the density has to be considered in the flow equations for two reasons - one is to take into account the inertial forces which are important for collimation and de-collimation, the other is our aim to consistently treat the Faraday rotation which is given by cold electrons. The latter could in principle be taken into account in magnetodynamic simulations by introducing electron tracer particles as additional degree of freedom, but is not immediately satisfied by applying the force-free limit of ultrarelativistic MHD.

We summarize our parameter runs of different jet models in table 5.1, indicating the maximum Lorentz factor attained, $\Gamma_{\rm max}$ and other dynamical quantities of interest on which our results discussed in the following are based. Although the

Table 5.1 Simulation runs

run ID	s	β_1	$\Gamma_{\rm max}$	Γ_∞	$\theta_{\rm fl,1}$
1h	1	0.005	8.5	25	0.21°
2h	1.25	0.005	7.9	24	0.16°
3h	1.5	0.005	7.9	23	0.17°
1m	1	0.01	5.9	13	0.14°
2m	1.25	0.01	5.6	13	0.16°
3m	1.5	0.01	5.9	13	0.24°

Note. — Columns denote: Simulation ID; Radial power law slope of the toroidal field; Plasma beta at (r,z)=(1,0); Maximal Lorentz factor obtained in the Raycasting domain; Maximal attainable Lorentz factor assuming complete conversion into kinetic energy $\Gamma_\infty \equiv \mu$. Collimation angle of the field line rooted at the inner disk radius evaluated at z=1000.

different electric current distributions applied in the inflow boundary condition promote a distinct jet dynamics as seen for example in the position of the light cylinder shown in figures 5.1 to 5.3, the geometry of the field lines turns out to be quite similar. At a height $z = 750$ (corresponsing to $\approx 2200 r_{\rm S}$), the fast jet component is collimated into an opening angle less than 1° in all our models. More obvious differences are found in the radial distribution of the Lorentz factor which is peaked at the maximum of vertical current density j_z. In the case of closed-current models, the fast jet component becomes narrower as the integral electric current levels off more steeply. We find an acceleration efficiency in terms of the total energy per rest mass energy, μ of $\Gamma/\mu \approx 80\%$ for the axial spine and acceleration efficiencies varying between $20\% < \Gamma/\mu < 40\%$ for the outer parts of the jet (see the outer field lines in the middle panels). Since the flow has not reached equipartition within the considered domain, the acceleration efficiencies we obtain represent only a lower limit to the total efficiency Γ_∞/μ. Energy conversion

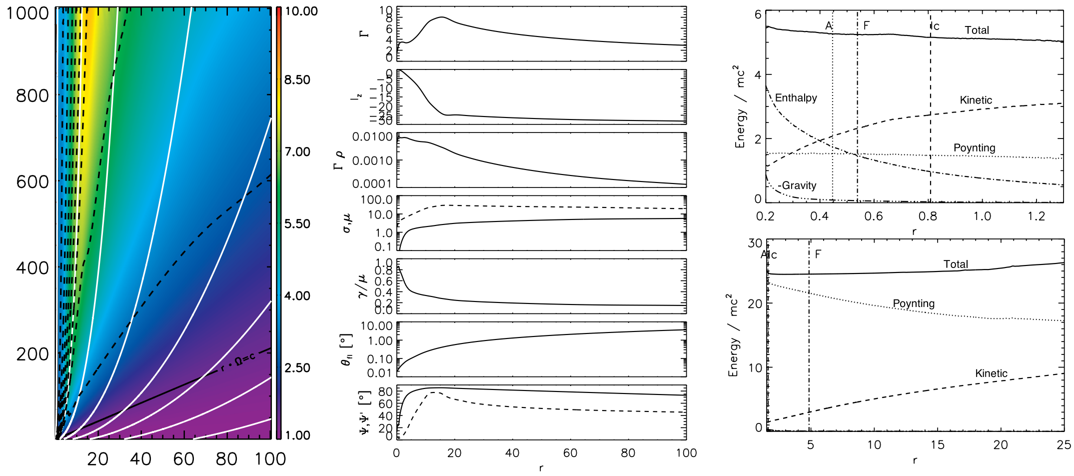

Figure 5.1 Jet model 1h allowing no outgoing current in the disk. *Left:* Current lines (dashed) shown on Lorentz factor color-contours in the (r,z) plane (note the extreme aspect ratio). Field lines are given in solid white and the light-cylinder is indicated by the solid black line. *Center:* Cuts through $z = 750$ for Lorentz-factor Γ, integral current I_z, lab-frame density $\Gamma\rho$, Poynting-to-kinetic energy flux ratio σ (solid) and total normalized energy μ (dashed), acceleration efficiency Γ/μ, field line collimation angle $\theta_{\rm fl}$ and the pitch angles of the co-moving system Ψ' (dashed), respectively the lab-frame Ψ (solid). *Right:* Acceleration along selected field-lines against the cylindrical radius r showing thermal acceleration for a field line in the spine (footpoint $r_{\rm fp} = 0.2$, above) and magnetic acceleration in the jet ($r_{\rm fp} = 1.5$, below). Vertical lines indicate the crossing of the Alfvèn (A) and fast (F) critical point as well as the light cylinder (lc).

is depicted in the right panels of figures 5.1 to 5.3 showing the individual energy channels normalized to the conserved rest mass energy flux $\rho u_p c^2$ along selected field lines. The terms are defined: $E_{\rm Enthalpy} \equiv \Gamma(h-1)$, $E_{\rm Kinetic} \equiv \Gamma$, $E_{\rm Gravity} \equiv \varphi$ and the Poynting flux $E_{\rm Poynting} \equiv -r\Omega B_p B_\phi/(4\pi\rho u_p c^2)$. [1]

5.3.1 Poynting Dominated Flow

We first consider the MHD acceleration of the disk component of the jet flow. Here, the bulk of the acceleration takes place in the relativistic regime beyond the light surface $r_L(r,z) \equiv c/\Omega$, and can therefore be approximated asymptotically $x \equiv r/r_L \gg 1$, $\Gamma \gg 1$. For a cold wind initially dominated by Poynting flux, the

[1]Where ρ denotes the co-moving density, $u_p = \Gamma v_p$ is the poloidal part of the four-velocity and h signifies the specific enthalpy defined through the equation of state.

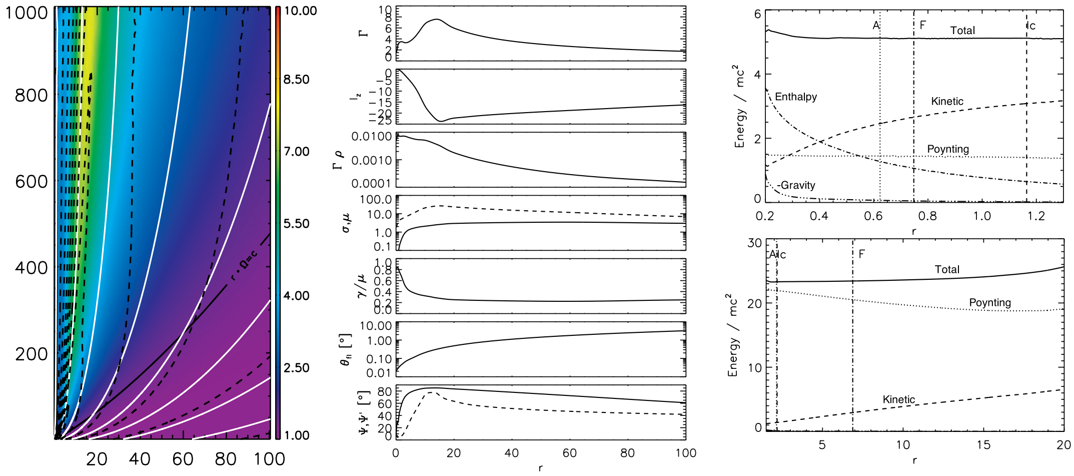

Figure 5.2 As figure 5.1 for model 2h.

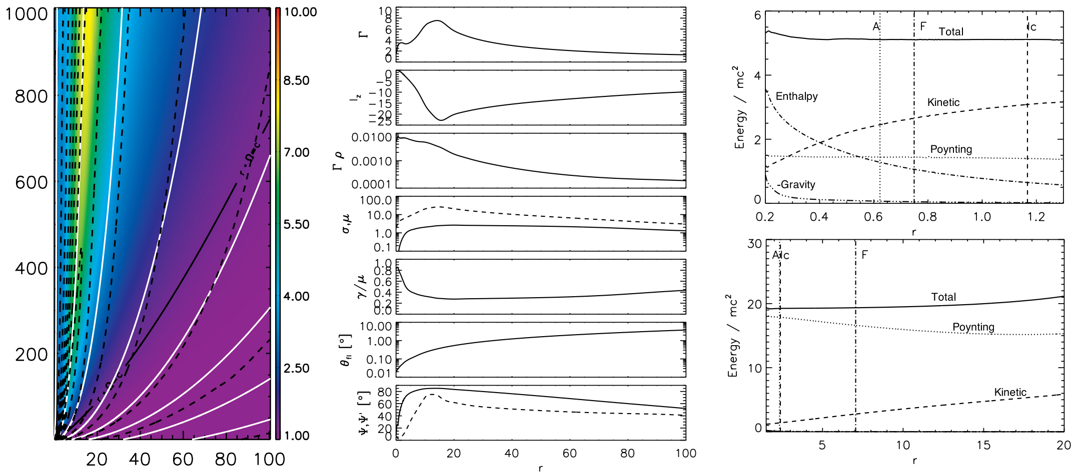

Figure 5.3 As figure 5.1 for model 3h.

total energy flux per rest mass energy flux μ can be expressed as

$$\mu = \Gamma + E_{\text{Poynting}} = \Gamma - \frac{\Omega r B_p B_\phi}{4\pi \rho u_p c^2}, \tag{5.12}$$

Following the asymptotic relations by Camenzind (1986b) we have $v_\phi \to 0\,(x \gg 1)$, and hence $\Omega r \simeq -B_\phi B_p^{-1} v_p$ can be used to eliminate the toroidal field from equation 5.12. With $\Gamma \gg 1$ we can write

$$\mu = \Gamma - \frac{\Omega^2 r^2 B_p}{4\pi k c^3}, \tag{5.13}$$

where μ, $k \equiv \rho u_p / B_p$, and Ω are conserved quantities along the stationary streamline (for details see e.g. Porth & Fendt (2010)). Thus, the asymptotic flow acceleration depends solely on the decrease of

$$\phi \equiv r^2 B_p \tag{5.14}$$

along the flow line by differential fanning out of the field lines.[2] We show the evolution of the ϕ function along selected field lines for the intermediate model 2h in figure 5.4 (left panel). In the non-asymptotic regime, ϕ increases until the $x = 1$

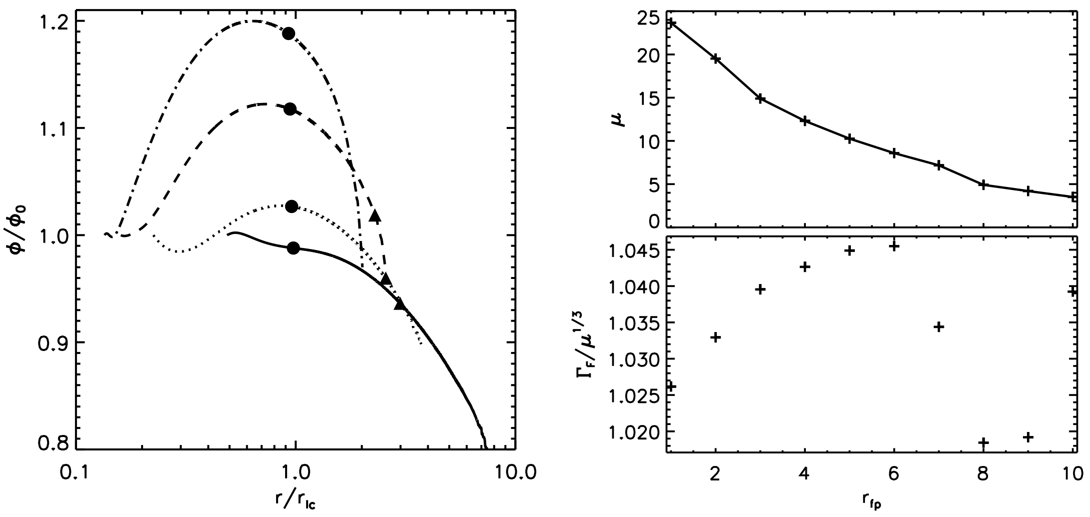

Figure 5.4 Acceleration along field lines $r_{\rm fp} \in \{2,4,6,8\}$ shown respectively as {solid,dotted,dashed,dash-dotted} lines in model 2h. *Left:* The $\phi = B_p r^2$ function of the expanding flux tube normalized by footpoint value against radius in terms of light cylinder radii $r/r_{\rm lc}$. Alfvèn (•) and fast (▲) critical point transitions are marked accordingly. *Right:* Total energy flux ratio μ *(top)* and Lorentz factor at the fast point Γ_F compared to the expected value of $\mu^{1/3}$ for various field line footpoints *(bottom)*. We find Michel's scaling to be satisfied within 5%.

surface, while it is decreasing for $x \gg 1$ as expected.

The second term of (5.13) corresponds to the Michel magnetization parameter $\sigma_{\rm M}$ (Michel 1969) [3] For a critical solution in a monopole field geometry where the fast magnetosonic velocity is reached at infinity ($x_{\rm F} \to \infty$), the terminal Lorentz-factor becomes

$$\Gamma(x_{\rm F}) = \mu^{1/3}. \tag{5.15}$$

Different derivations of this fundamental result are given by Camenzind (1986b); Tchekhovskoy et al. (2009). For small perturbations from the monopole field geometry Begelman & Li (1994); Beskin et al. (1998) could show that x_F can be crossed at a finite distance, where again (5.15) is satisfied. This general scaling was also found by Fendt & Camenzind (1996); Fendt & Greiner (2001); Fendt & Ouyed (2004) for collimating relativistic jets. Our jet solutions quickly accelerate to the fast magnetosonic point and, despite the departure from the monopolar

[2]Sometimes denoted as "field line bunching" in the recent literature.

[3]Where we added the subscript "M" in order to avoid confusion with the parameter $\sigma = \sigma_{\rm M}/\Gamma$ defined previously.

shape, follow Michel's scaling there remarkably well. As illustrated in figure 5.4 (right panel), the deviation from the expectation of $\mu^{1/3}$ is less than 5%.

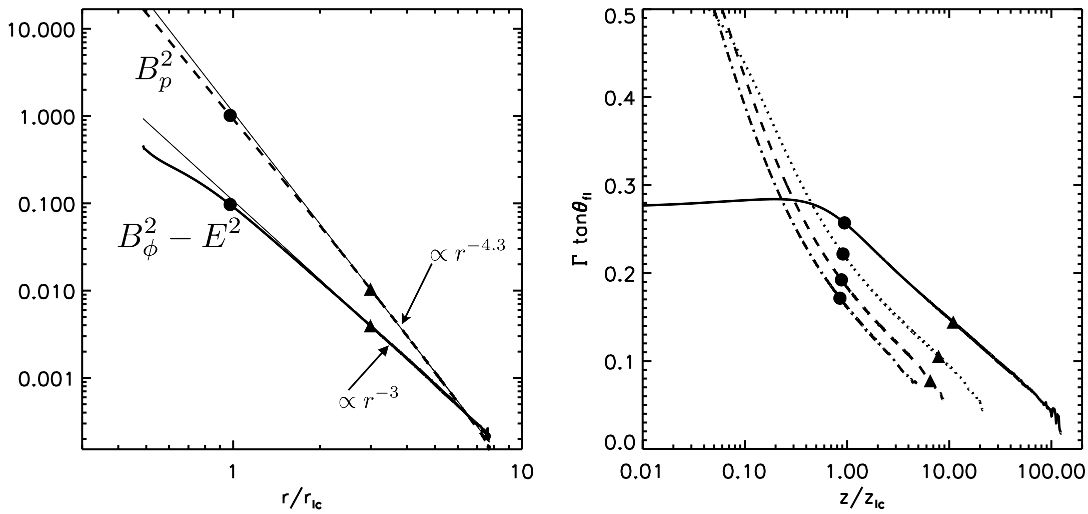

Figure 5.5 Characterization of the acceleration in model 2h. *Left:* Comparison of the field strengths for $r_{\rm fp} = 2$ along the flux tube. We find $B_p^2 > B_\phi^2 - E^2$ for the most part of the domain yielding the linear acceleration regime. Also shown are power-law fits to the super-fast regime (thin solid lines). *Right:* The quantity $\Gamma \tan\theta_{\rm fl}$ along the same field lines of figure 5.4. Efficient acceleration in the power-law regime would yield $\Gamma \tan\theta_{\rm fl} \simeq$ *const*. Alfvèn (●) and fast (▲) critical point transitions are marked accordingly.

Insight into the ongoing acceleration process can be gained by an analysis of the trans-field force equilibrium as performed for example by Chiueh et al. (1991); Vlahakis (2004). The asymptotic relativistic force balance can conveniently be decomposed into "curvature", "electromagnetic" and "centrifugal" contributions. Depending on the dominating terms, at least two regimes are possible (see also the discussion by Komissarov et al. 2009): When the curvature term is negligible, the equilibrium is maintained by balancing of the centrifugal force with the electromagnetic contribution. This constitutes the first or linear acceleration regime. The transition to the second regime occurs when field line tension begins to dominate over the centrifugal force, maintaining the equilibrium between purely electromagnetic forces. The occurrence of curvature in the force equilibrium leads to a tight correlation between collimation and acceleration since the tension force also becomes the governing accelerating force[4].

As far as a stationary state is reached, we find that the acceleration is well

[4]The latter was demonstrated using the parallel field force-balance in application to relativistic disk wind simulations by Porth & Fendt (2010).

described by the linear acceleration regime $\Gamma \propto r$, or

$$\Gamma^2 \approx \frac{B_\phi^2}{B_p^2} \tag{5.16}$$

as suggested for the initial acceleration of rotating flows by various authors (e.g. Beskin et al. (1998), Narayan et al. (2007), Tchekhovskoy et al. (2008) and Komissarov et al. (2009)). This corresponds to

$$B_p^2 \gg B_\phi^2 - E^2 \tag{5.17}$$

which is satisfied for the most part of the flow in our simulation domain. Figure 5.5 (left panel) shows B_p^2 and $B_\phi^2 - E^2$ for a sample field line in the fast jet. We find that the critical field strengths are fairly well approximated by power-laws in the asymptotic super fast-magnetosonic regime. For the particular case shown, we have $B_p^2 \propto r^{-4.3}$ and $B_\phi^2 - E^2 \propto r^{-3}$ such that the flow experiences a transition to the second, or power-law acceleration regime where the inverse of relation 5.17 becomes true.

For the power-law regime, a correlation between Lorentz factor Γ and half-opening angle of the jet $\theta_{\rm fl}$,

$$\Gamma \tan \theta_{\rm fl} \simeq 1 \tag{5.18}$$

was discovered by Komissarov et al. (2009) in the context of ultra-relativistic gamma-ray bursts. Figure 5.5 (right panel) illustrates the run of $\Gamma \tan \theta_{\rm fl}$ along a set of field lines in our fiducial model. Compared to the suggestion of equation 5.18, our simulation setup shows efficient MHD self-collimation, but appears less efficient in terms of acceleration.

We note that only when a substantial part of flow acceleration takes place in the power-law regime, relation 5.18 will hold. Our AGN jet models are however collimated to $\simeq 1^\circ$ and accelerated with efficiencies of 40% ($\Gamma \simeq 8$) already in the linear regime. Even if the flow acceleration is followed indefinitely, $\Gamma \theta_{\rm lf} \simeq 1$ can not be recovered as this would require terminal Lorentz factors of $\Gamma_\infty > 60$ and thus violate energy conservation.

It could be argued that the low acceleration efficiency is due to the loss of causal connection for the relativistic flow. In this case, the bunching of field-line can not be communicated across the jet anymore, thus stalling the acceleration process. This should in fact occur when the fast Mach-cone half opening-angle $\theta_{\rm MF} \simeq \pi/2\sqrt{\mu/\Gamma^3}$ does not comprise the jet axis, hence $\theta_{\rm MF} < \theta_{\rm fl}$ (see also Zakamska et al. 2008; Komissarov et al. 2009). We have checked this conjecture by comparing both angles and found our still moderate Lorentz factor, highly collimated, jet models to be in causal connection throughout the whole acceleration domain.

5.3.2 Thermal Spine Acceleration

In this work, the very inner jet spine is modeled as a thermal wind. An alternative approach would be to prescribe a Poynting dominated flow originating in the Blandford & Znajek (1977) process. In this case, the toroidal field would be generated by the frame dragging in the black hole ergosphere below our computational domain similar to the induction in the disk. However, our attempts to increase the central magnetization σ by further decreasing the coronal density failed at the inability of the numerical scheme to handle the steep density gradients emerging at the boundary. Due to the vanishing toroidal field at the axis, also the Blandford & Znajek (1977) mechanism is not able to provide acceleration of the axial region (see also McKinney 2006).

In principle, it would be possible to convert the thermal enthalpy first into Poynting flux when the jet is expanding, and then back into kinetic energy via the Lorentz force as observed by Komissarov et al. (2009). However, as we see in figures 5.1 to 5.3 (right top panels), this does in fact not occur in our simulations since the Poynting flux is approximately conserved along the inner flux lines that show little expansion. It is the magnetic field distribution and the collimated structure of the outer (disk-jet) component which merely provide the shape of the trans-sonic nozzle for the thermal wind. We can thus understand the acceleration in the jet spine by using the relativistic Bernoulli equation, which we cast in the form

$$h^2 \left[1 + 2\varphi + (u/c)^2\right] = c^4 \Gamma_\infty^2 = \text{const.} \tag{5.19}$$

An order of magnitude estimate sufficiently far from the compact object yields $h\Gamma \simeq const.$ Using mass conservation $\Gamma \rho r^2 = const$ $(v \to c)$ and a polytropic equation of state with the enthalpy $h = c^2 + \gamma/(\gamma-1)\, p/\rho$, we obtain a scaling relation $\Gamma \propto r^{-2+2/(2-\gamma)}$ $(p/\rho \gg c^2)$. For a relativistic polytropic index of $\gamma = 4/3$ this results in $\Gamma \propto r$.

Applying a non-relativistic index of $\gamma = 5/3$, the latter relation would yield $\Gamma \propto r^4$, however, the non-relativistic limit also implies $p/\rho \ll c^2$, and thus $h \to c^2$ $(\gamma \to 5/3)$ and the acceleration ceases.

Our simulations are performed employing the causal equation of state (obeying the Taub (1948) inequality) introduced by Mignone et al. (2005). Thus we obtain a variable effective adiabatic index

$$\gamma_{\text{eff}} = \frac{(h-1)\rho/p}{(h-1)\rho/p - 1} \tag{5.20}$$

between 4/3 and 5/3. Figure 5.6 (top panel) shows the effective adiabatic index along a stream line / flux surface. In the sample stream line we find γ_{eff} to vary between $1.45 < \gamma_{\text{eff}} < 1.65$ as the plasma adiabatically cools from relativistic to

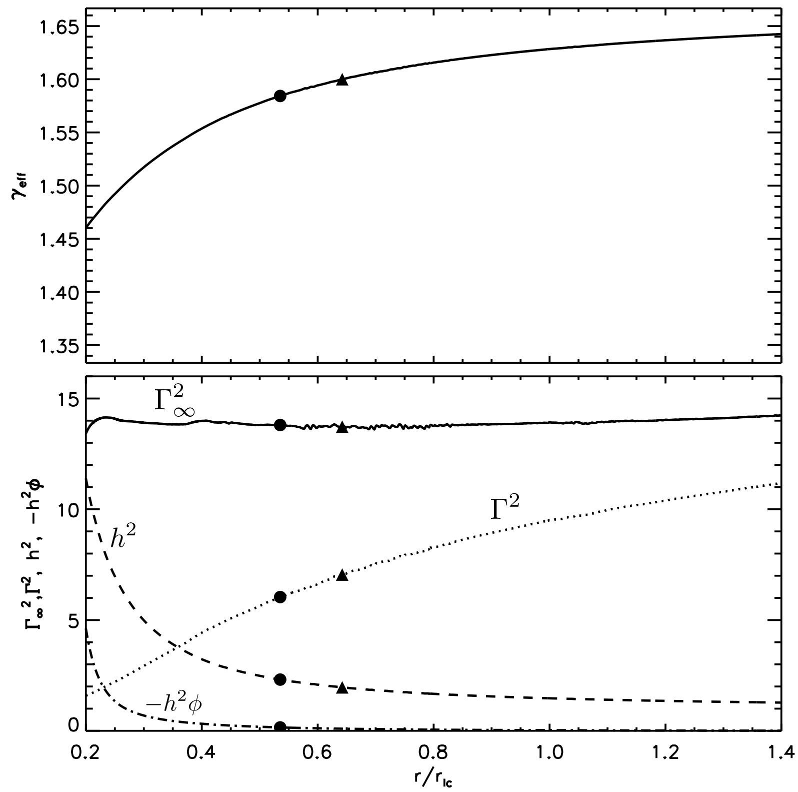

Figure 5.6 Thermal acceleration along the field line $r_{\rm fp} = 0.2$ in model 2h. *Top:* Effective polytropic index $\gamma_{\rm eff}$ along the flow. *Bottom:* Individual terms of equation 5.19 showing thermal energy conversion and the conservation of $\Gamma_\infty \simeq 3.7$. In this plot, we normalized to c=1. Alfvèn (•) and fast (▲) critical point transitions are marked accordingly.

non-relativistic temperatures. Thermal acceleration saturates for $\gamma_{\rm eff} \to 5/3$ as the enthalpy approaches the specific rest mass energy c^2 (see also Fig. 5.6, bottom panel). The maximum attainable Lorentz factor Γ_∞ is given by the footpoint values at the sonic point to $\Gamma_\infty = h_0(\Gamma_0 + 2\phi_0)^{1/2}$ and depends on the detailed modeling of the inner corona. In our approach the jet spine Lorentz factor is thus limited to values of $\Gamma_\infty < 4$.

5.4 Summary and Conclusions

Our jets are realistically modeled to consist of two components: an inner thermal spine assumed to originate in the a black hole corona, and a surrounding self-collimating disk jet driven by Poynting flux.

We follow the flow acceleration for more than 3000 Schwarzschild radii reaching Lorentz factors in the disk jet of $\Gamma \sim 8$ within the AGN "blazar zone" where we will calculate the synchrotron emission maps in the next chapter. In application to a $10^9 M_\odot$ black hole this translates to a distance of 0.3pc.

Although the Poynting dominated jet flow becomes super fast-magnetosonic within the domain, it has not yet reached equipartition between Poynting and kinetic energy - jet acceleration is still ongoing. According to the available energy budget, in the case of high energy disk jets terminal Lorentz factors of $\Gamma_\infty \sim 20$ would be acquired asymptotically. At the fast magnetosonic point we find the Michel scaling $\Gamma(x_{\rm F}) = \Gamma_\infty^{1/3}$ to be satisfied within 5%. We find that the jet acceleration up to a distance $z \sim 3000 r_{\rm S}$ is well described by the linear relation $\Gamma \propto r$ as proposed by Tchekhovskoy et al. (2008) and Komissarov et al. (2009). We do however not reproduce the tight coupling of acceleration and collimation $\Gamma \tan\theta_{\rm fl} \simeq 1$ observed in the latter communications but instead find $\Gamma \tan\theta_{\rm fl}$ to monotonically decrease along the flow. The fast jet component in all models under consideration collimates to half-opening angles of $\lesssim 0.3°$. We find the causal connection within the flow - its ability to communicate with the axis via fast magneto-sonic waves - to be well maintained in our simulations.

Also the thermal spine acceleration is shown to be efficient with $\Gamma \propto r$ and limited only by the amount of enthalpy available at the sonic point, in our case to $\Gamma_\infty < 4$.

We have placed the location of the outflow boundaries out of causal contact with the propagating jet beam of interest. Thus, we can be sure that the calculated jet structure is purely self-collimated, and does not suffer from spurious boundary effects leading to an artificial collimation. We have investigated jets with a variety of poloidal electric current distributions. We find - somewhat surprisingly - that the topology of the current distribution, e.g. closed current circuits in comparison to current-carrying models, has little influence on the jet collimation.

Chapter 6

Synthetic Synchrotron Observations

6.1 Introduction

The existence of an ordered large-scale μG- mG magnetic field in extragalactic jets is well established by the detection of radio synchrotron emission, however the exact geometry of the field structure is under debate. The recent observational literature strongly suggests *helical magnetic fields* (e.g. O'Sullivan & Gabuzda (2009)), a scenario which is consistent with theoretical models and numerical simulations of MHD jet formation (see e.g. (Blandford & Payne 1982; Ouyed & Pudritz 1997; Krasnopolsky et al. 1999; Fendt & Čemeljić 2002; Fendt 2006; Porth & Fendt 2010)). The wavelength dependent rotation of the polarization plane known as Faraday rotation provides a valuable diagnostic of magnetic field structure in astrophysical jets. Consistent detections of $\Delta\chi \propto \lambda^2$ are found in resolved jets as well as in unresolved radio *cores* (Zavala & Taylor 2003). Helical magnetic fields are generally perceived to promote transversal Faraday rotation measure (RM) *gradients* owing to the toroidal field component. Observationally, such gradients were first detected by Asada et al. (2002) and Zavala & Taylor (2005) in the jet of 3C 273. The RMs are generally found to follow a monotonic profile across BL Lac and Blazar jets (Gabuzda et al. 2004; O'Sullivan & Gabuzda 2009; Croke et al. 2010) and also across the jets of radio galaxies observed at larger viewing angles (Kharb et al. 2009).

While the magnetic field structure of pc and Kpc-scale jets can in principle be derived from radio observations, not much is known about the field structure within the jet forming region very close to black hole - mainly because of two reasons. Firstly, this very core region cannot be spatially resolved and, thus, cannot readily be compared with expected RM profiles of helical jets. This is somewhat unfortunate, as in the Poynting dominated region close to the jet origin we expect the magnetic field helix to be well preserved and not much affected by environmental effects. Secondly, the observed rotation measures are so high that it is impossible to draw firm conclusions about the intrinsic field geometry from the polarization vector with mere radio observations.

Only very few cases exist where this core of jet formation could be resolved observationally. Among them is the close-by galaxy M87, where the VLBI/VLBA resolution of $\simeq 0.1\,\mathrm{mas}$ is sufficient to resolve about $0.01\,\mathrm{pc}$ within the central region, and allows to trace the jet origin down to $\simeq 20$ Schwarzschild radii r_S when the recent mass estimate of $6.6 \times 10^9 M_\odot$ by Gebhardt et al. (2011) is adopted. This pinpoints the launching area within $\simeq 30 r_\mathrm{S}$ (Junor et al. 1999; Kovalev et al. 2007). The radio maps clearly show limb brightening and indicate an initial jet opening angle of about $60°$.

Despite a vast amount of observational data spanning over a huge frequency scale, and also time series of these multifrequency observations, rather little is known about the dynamical status of relativistic jets. There are no direct unambiguous observational tracers of jet velocity or density as only (if at all) the pattern speed of radio knots is detected. Kinematic modelling of knot ejection suggests pc-scale Lorentz factors of typically $\Gamma \simeq 10$, while Kpc-jet velocities are believed to be definitely lower and of the order of 0.1c. Kinematic modeling of jet propagation has been combined with synchrotron emission models of nuclear flares, resulting in near perfect fits of the observed, time-dependent radio pattern of jet sources such as 3C 279 (Lindfors et al. 2006).

However, what was missing until recently is a consistent combination of *dynamical models* with *radiation models* of synchrotron emission resulting in theoretical radiation maps which can then be compared with observations. Zakamska et al. (2008) and Gracia et al. (2009) have taken a step into this direction by providing optically thin synchrotron and polarization maps from self-similar MHD solutions. Broderick & McKinney (2010) presented synchrotron ray-castings from 3D general relativistic jet formation simulations that also include the evolution of a turbulent accretion disk performed by McKinney & Blandford (2009). In their approach, the MHD solution is extrapolated by means of an essentially self-similar scheme in order to reach distances up to 10pc. Their study focussed on the rotation measure provided by Faraday rotation in the disk wind *external* to the emitting region in the Blandford-Znajek jet.

In comparison, using axisymmetric large scale simulations, we do not rely on an extrapolation within the AGN core (up to 0.3pc) and treat the Faraday rotation also internal (but not exclusively) to the emitting region in the fast jet that

gradually transforms into a sub-relativistic disk wind. The observational signatures obtained in our work are derived entirely from the (beam convolved) Stokes parameters which allows us to also investigate the breaking of the λ^2 law due to opacity effects.
As the above studies, we also rely on post-hoc prescriptions for the relativistic particle content. Towards a more consistent modeling of the non-thermal particles, Mimica et al. (2009) have presented a method to follow the spectral evolution of a seed particle distribution due to synchrotron losses within a propagating relativistic hydrodynamic jet. The question of particle acceleration and cooling is in fact essential to close the loop for a fully self-consistent treatment of jet dynamics, jet internal heating, and jet radiation.

To derive signatures of synchrotron emission from relativistic MHD jet formation is the main goal of this chapter. We apply the dynamical variables derived from the simulations discussed in the previous chapter to calculate the synchrotron emission from these jets, taking into account proper beaming and boosting effects for different inclination angles. In particular, we apply the relativistically correct polarized radiation transfer along the line of sight throughout the jet.

6.2 Synchrotron Radiation and Faraday Rotation

The numerical MHD simulations discussed before provide an intrinsic dynamical model for the parsec-scale AGN core. In the following we will use this information - kinematics, magnetic field distribution, plasma density and temperature - to calculate consistent synchrotron emission maps. What is still missing for a fully self-consistent approach is the acceleration model for the highly relativistic particles which actually produce the synchrotron radiation. However, we have compared a few acceleration models and discuss differences in the ideal resolution synchrotron maps (see below).

Radio observations of nearby AGN-cores show optically thick and thin emission features with a high degree of Faraday rotation (e.g. Zavala & Taylor 2002). The nature of the Faraday rotation could either be internal, thus directly produced in the emitting volume, or due to an external Faraday sheet, possibly comprised of a magnetized disk-wind as ventured e.g. by Broderick & McKinney (2010), or an ambient jet cocoon. On these scales, even with global VLBI experiments, the radio emission is barely resolved for most of the known sources. Therefore we apply beam averaging to examine the resolution dependence of the results. For a grid of lines of sight, each corresponding to one pixel in the final image, we solve for the parameters of linear polarization $\mathbf{I} = \{I^l, I^r, U^{lr}\}$ as defined e.g. by

Pacholczyk (1970b). This treatment provides the equivalent information as the Stokes parameters $\{I, Q, U\}$. Within the aforementioned notation, the transport equation is a linear system of equations

$$\frac{d\mathbf{I}}{dl} = \boldsymbol{\mathcal{E}} - \underline{\mathbf{A}}\ \mathbf{I} \tag{6.1}$$

where $\boldsymbol{\mathcal{E}}$ denotes the emissivity vector and $\underline{A}$ the opacity matrix, taking into account relativistic beaming, boosting and swing of the polarization as outlined in Section 3.3 and derived in Appendix A. Assuming an electron-proton plasma, the electron number density follows from the mass density of the simulations. We assume further that a small subset of these "thermal" electrons is accelerated to a power-law distribution and thus responsible for the non-thermal emission of synchrotron radiation. The modeling of particle acceleration is detailed further in section 6.2.1.

A fraction of the Faraday rotation thus takes place already in the emitting region of the relativistic jet, such that the radiation undergoes depolarization due to *internal* Faraday rotation. In this case, the angular difference $\Delta\chi_{\rm obs}$ between the observed polarization angle $\chi_{\rm obs}$ and the $(\lambda \to 0)$ case can depart from the integral

$$\Delta\Psi \propto \int n_e \nu^{-2} \mathbf{B} \cdot \mathbf{dl}, \tag{6.2}$$

which is customarily used in the diagnostics of jet observations. For example, in a uniform optically thin medium with internal Faraday rotation, the value of $\Delta\chi_{\rm obs}$ is just half of relation (6.2). Non-uniform optically thin media will break the λ^2-law and exhibit depolarization once $\Delta\chi_{\rm obs}$ exceeds $\sim 45°$ (e.g. Burn 1966). For optically thin media with $\Delta\chi_{\rm obs} < 45°$, λ^2-law rotation measures can be recovered also in the non-uniform case, however the observed rotation angle is always less than $\Delta\Psi$.

We show the effect of internal Faraday rotation along an individual ray compared to the case with no Faraday rotation in Figure 6.1. In the emitting volume the polarization degree oscillates as expected for an optically thin medium with Faraday rotation (see also Section 3.3.2.1). As a consequence, the observed polarization degree is lowered. Following the density and magnetic field strength, the differential Faraday depth $d\chi_{\rm F}/dl$ decreases fast enough towards the observer, such that we can be confident not to miss a substantial part of the Faraday screen in the ray-casting domain.

To speed up the computation in cases of high optical or Faraday depths, we (i) limit the integration to $\tau < 100$, and (ii) solve the polarized transport only for the last 200 internal Faraday rotations $\tau_{\rm F} < 200\pi$. Both optimizations do not at all affect the resulting emission maps, as the observed radiation typically originates

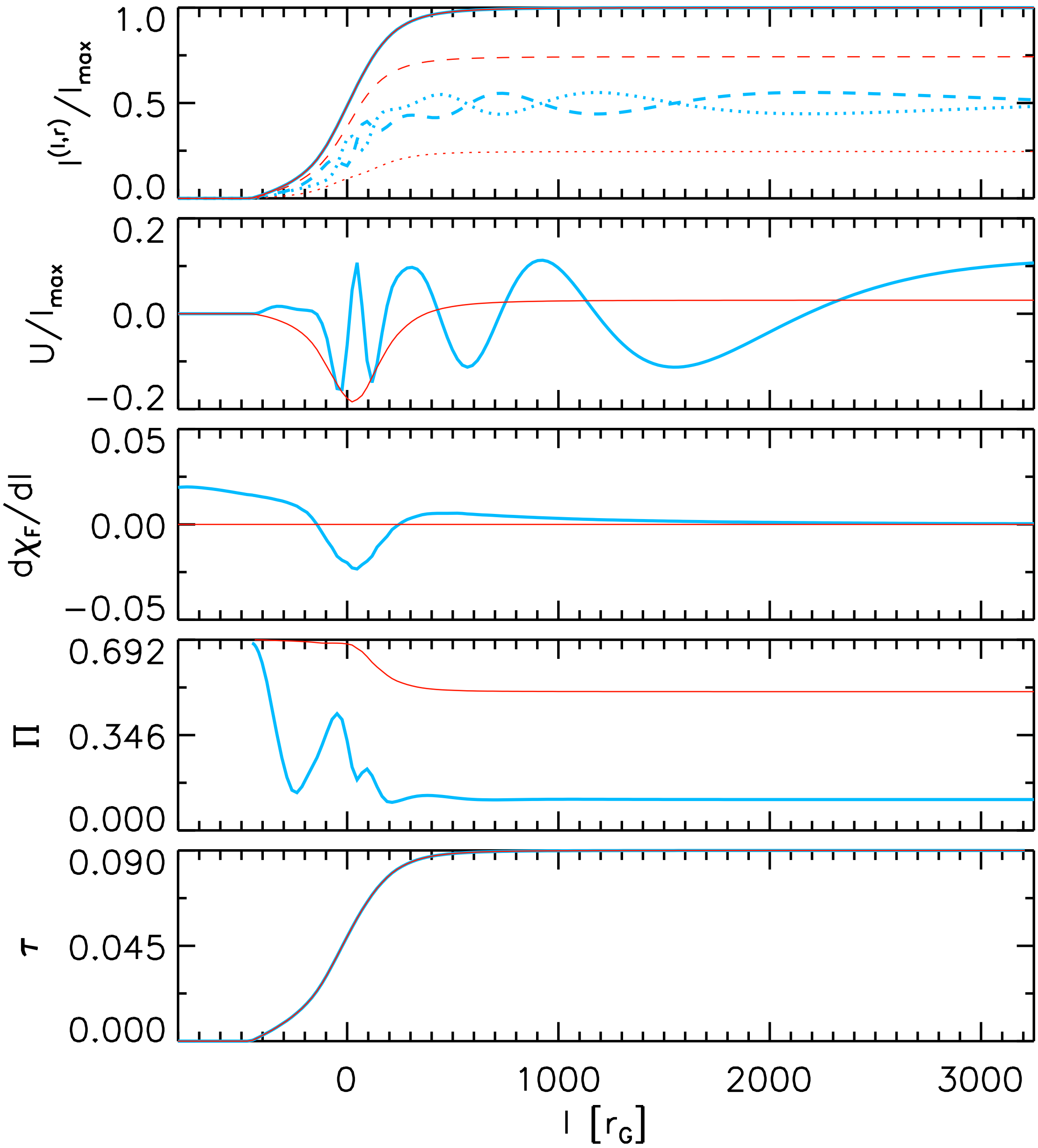

Figure 6.1 Raytracing for an individual line of sight. Thick blue lines including Faraday rotation compared to a case where the latter was neglected - illustrated by thin red lines. The upper panels show intensity (I^{tot}) and the Stokes parameters I^l (dotted), I^r (dashed) and U (second panel). Faraday depth $d\chi_F/dl$ [rad/r$_\mathrm{G}$], polarization degree Π and the optical depth τ is shown in the subsequent panels. Internal Faraday rotation and the accompanying depolarization is observed in the emitting region near the $x = 0$ plane ($l = 0$).

in the photosphere of $\tau = 1$, and only a few internal Faraday rotations suffice to depolarize the radiation in the models under consideration.

Once $\mathbf{I}$ is recovered, we obtain beam-averaged quantities via the convolution

$$\langle \mathbf{I} \rangle(\mathbf{x}) = \int d^2\mathbf{x}' \, \mathcal{G}(\mathbf{x} - \mathbf{x}')\mathbf{I}(\mathbf{x}') \tag{6.3}$$

with a Gaussian beam $\mathcal{G}$. The beam-averaged Stokes parameters are then used for mock observations providing spectral indices, polarization maps, rotation measure maps, and spectra to be compared to the model parameters.

6.2.1 Particle Acceleration Recipes

Within the MHD description of the jet plasma, knowledge about the relativistic particle distribution, which is needed as input for the synchrotron emission model, is not available. To recover the information from the velocity-space averaged quantities of MHD, we have to rely on further assumptions. To mention other approaches, Mimica et al. (2009) were able to follow the spectral evolution of an ensemble of relativistic particles embedded in a hydrodynamic jet simulation. Their treatment includes synchrotron losses, assuming a power-law seed distribution derived from the gas thermal pressure and density at the jet inlet.

Alas, for our purposes a consistent prescription for in-situ acceleration and cooling would be required - which seems unfeasible at the time. We therefore take a step back and assume that relativistic electrons are distributed following a global power law with index p as $dn_{\mathrm{e}} = N_0 E^{-p} dE$ for $E_{\mathrm{l}} \leq E \leq E_{\mathrm{u}}$ where N_0 signifies the overall normalization of the distribution and E_{l}, E_{u} denote the lower and upper cutoffs. The optically thin flux density for the synchrotron process then reads $S_\nu \propto \nu^{-\alpha}$ with $\alpha = (p-1)/2$. Optically thick regions radiate according to the source function $S_\nu = \epsilon_\nu / \kappa_\nu \propto \nu^{2.5}$.

This choice of particle distribution is justified by observations as well as theoretical expectations for the particle acceleration. The major physical mechanisms capable of producing non-thermal relativistic electrons are (internal) shock acceleration of relativistic seed electrons (e.g. Kirk et al. 2000) and MHD processes like magnetic reconnection (Lyubarsky 2005) or hydromagnetic turbulence (Kulsrud & Ferrari 1971). Considering differential rotation in relativistic jets, Rieger & Mannheim (2002), Rieger & Duffy (2004) and Aloy & Mimica (2008) suggested particle acceleration by shear or centrifugal effects.

In addition to E_l and E_u, the normalization N_0 depends highly on the mechanism under consideration. A straight-forward recipe is to connect the particle energy to the overall mass density (similar to Gracia et al. 2009)

$$\rho = m_p \int_{E_l}^{E_u} N_0 E^{-p} dE, \tag{6.4}$$

where an ionic plasma consisting of equal amounts of protons and relativistic electrons is assumed. Thus, all available electrons are distributed following this relation and the Faraday effect is maintained by the "equivalent density of cold electrons" $\propto n_e E_l^{-2}$ (e.g. Jones & Odell 1977) in contrast to relation (3.11) where we assumed that the most part of electrons is non-relativistic.

An alternative to (6.4) is to specify the integral particle energy density and thus the first moment of the distribution function. For their leptonic jet models, Zakamska et al. (2008) have assumed that the internal energy is carried by relativistic particles, hence the relation

$$\epsilon = 3p = \int_{E_l}^{E_u} N_0 E^{1-p} dE \tag{6.5}$$

can be used to provide N_0 from the gas pressure resulting from the simulations.

In contrast to relativistic shock acceleration where the energy reservoir for the particles is the bulk kinetic energy of the flow, MHD processes directly tap into the co-moving magnetic energy density, and can effectively accelerate the particles up to equipartition. Accordingly, for the equipartition fraction ϵ_{B},

$$\epsilon_{\mathrm{B}} \frac{B'^2}{8\pi} = n_{\mathrm{e}} \langle E \rangle = \int_{E_l}^{E_u} N_0 E^{1-p} dE \tag{6.6}$$

is customarily used to estimate jet magnetic field strength from the observed emission (e.g. Blandford & Königl 1979) or vice versa (Lyutikov et al. 2005; Broderick & McKinney 2010). To obtain peak fluxes in the Jy range, we have applied $\epsilon_{\mathrm{B}} = 0.1$ for our fiducial model. For the following discussion we have adopted $\alpha = 0.5$ ($p = 2$), $E_{\mathrm{u}} = 10^6 E_{\mathrm{l}}$ and specified $E_{\mathrm{l}} = \gamma_{\mathrm{t}} m_e c^2$ for application with relation (6.4). For $\alpha = 0.5$ and applying the recipes (6.5,6.6), only the cutoff *energy ratio* $E_{\mathrm{u}}/E_{\mathrm{l}}$ enters logarithmically into the determination of N_0. Within these assumptions, the influence of the cutoff values on resulting jet radiation is marginal. The magnitude of E_{l} then merely determines the number density of relativistic particles, to be chosen consistent with the number of particles available for acceleration. In this first study, we neglect the spectral changes introduced by the cutoff energies as this would require a more detailed modeling of the particle content which is beyond the scope of this work.

The observed morphology of the intensity maps is mainly determined by the various prescriptions for N_0 mentioned above. In the following we briefly compare the resulting radio maps.

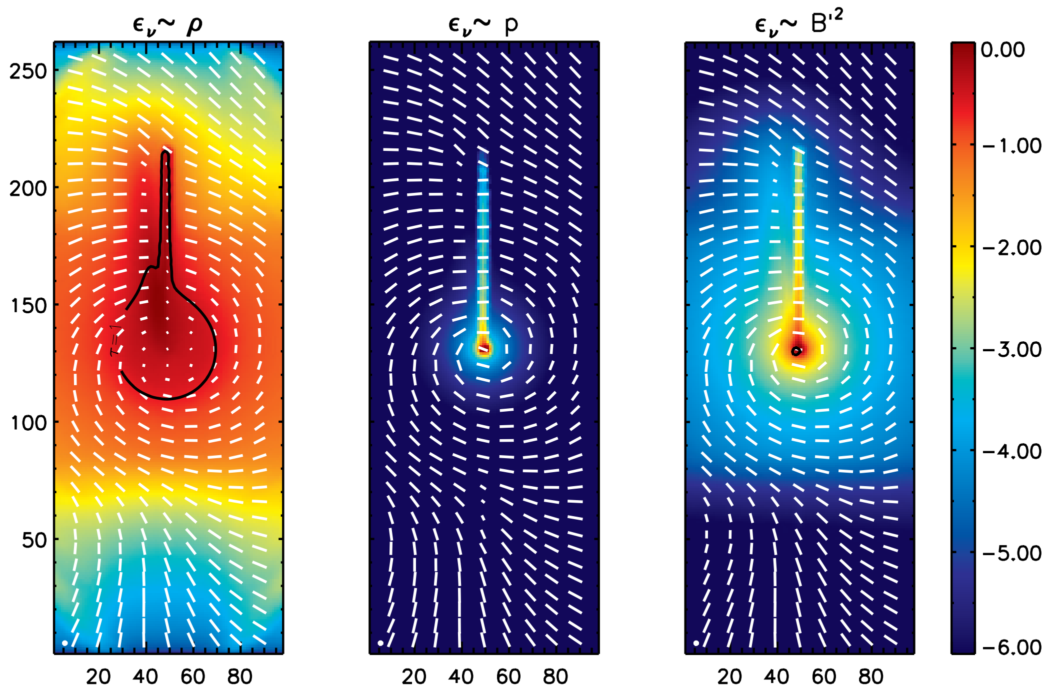

Figure 6.2 Ideal resolution logarithmic $I_\nu/I_{\nu,\max}$ maps for model 2h at $\nu = 43$ GHz, $i = 30°$ using various tracers for the relativistic particles: Density *(left)*, thermal pressure *(center)* and magnetic energy density *(right)*. Linear ($\hat{\mathbf{e}}$) polarization vectors are overlaid as white sticks. The (x-) scale is given in terms of ray-casting footpoint and corresponds to a physical extent of $1200 r_\mathrm{S}$.

6.2.2 Radio Maps for Different Particle Acceleration Models

Figure 6.2 shows ideal resolution maps for the aforementioned particle acceleration tracers. For the sake of comparison, Faraday rotation is neglected and with 43GHz we choose a high radio frequency to penetrate through the opaque jet base.

All tracers show an almost identical polarization structure, and highlight a thin "needle" owing to the cylindrically collimated axial flow with high density, and high magnetic and thermal pressure. The axial flow is slower than the Poynting dominated disk wind which is de-beamed and, thus, not visible at this inclination. Since the axial flow features $\boldsymbol{\beta} || \mathbf{B}$ (cf. 3.9), the resulting $\hat{\mathbf{e}}$ polarization vector reduces to the classical case, and points in direction perpendicular to the projected vertical field of the axial spine. In the case of the density tracer, the emission becomes optically thick, as indicated by the $\tau = 1$ contour. Correspondingly, the polarization degree is lowered and the direction of the spine polarization turns inside the $\tau = 1$ surface. Depending on the radial density and pressure profiles $\rho \propto r^{-3/2}$, $B^2 \propto r^{-2}$ and the pressure distribution in the disk corona $p \propto r^{-5/2}$, the emission at the base of the jet is more or less extended, it dominates the flux in all three cases. Relativistic beaming cannot overcome the energy density which is present in the disc corona, and therefore necessitates a more elaborate modeling of the accelerated particles in the jet. This will be provided in section 6.3.

6.2.3 Relativistic Swing and Beaming

In optically thin, non-relativistic synchrotron sources, the observed $\hat{\mathbf{b}}$ polarization vector directly corresponds to the projected magnetic field direction of the emitting region and thus carries geometric information about the jet. This allows us to interpret parallel $\hat{\mathbf{e}}$ vectors in terms of toroidal fields, while perpendicular $\hat{\mathbf{e}}$ vectors indicate a poloidal field (e.g. Laing 1980). Similar to all realistic models of MHD jet formation, our simulations feature a helical field structure that is tightly wound within the fast jet, but increasingly poloidal further out. Hence, the resulting polarization structure is that of the telltale *spine and sheath* geometry - across the jet, the polarization $\hat{\mathbf{e}}$ direction flips from being perpendicular to parallel and eventually returns to a perpendicular orientation.

Due to aberration and the accompanying swing of the polarization (e.g. Blandford & Königl 1979), an interpretation in terms of pure geometrical effects is not longer applicable in flows with relativistic velocities, instead a kinematic jet model is required. For cylindrical (i.e. (z, ϕ)-symmetric) relativistic jets, Pariev et al. (2003) have demonstrated how the optically thin polarization follows a strictly bimodal distribution, since the inclined polarization vector from the front of each annulus cancels with the corresponding polarization vector from the back side (see also Section 3.3.2.3). This remains also valid for differentially rotating jets.

For the case of a collimating and accelerating jet as shown here, we loosen the constraint of cylindrical symmetry to mere axisymmetry in the ϕ direction. Additionally, our simulations feature a non-constant pitch of the magnetic field and a small degree of rotation. Together, this results in inclined polarization vectors which deviate from the strict bimodality observed in (z, ϕ)-symmetry. Figure 6.3 shows the optically thin polarization structure in the presence of relativistic effects (left panel), and in absence thereof (right panel). To produce the non-relativistic map, we had simply set $\mathbf{v} \equiv 0$ before conducting the radiation transport. At the base of the outflow where the velocities are only mildly relativistic, the polarization vectors are found predominantly perpendicular to the collimating poloidal magnetic field in both cases. Further downstream, the bimodal spine-and-sheath polarization structure prevails as the jet dynamics becomes increasingly cylindrical. The figure clearly demonstrates how the relativistic swing skews the spine towards the approaching side of the jet. Note that the jet rotation is also apparent in the beamed asymmetric intensity contours. At high inclination $i = 60°$, the main emission from the high-speed jet is de-beamed and only the low-velocity "needle"

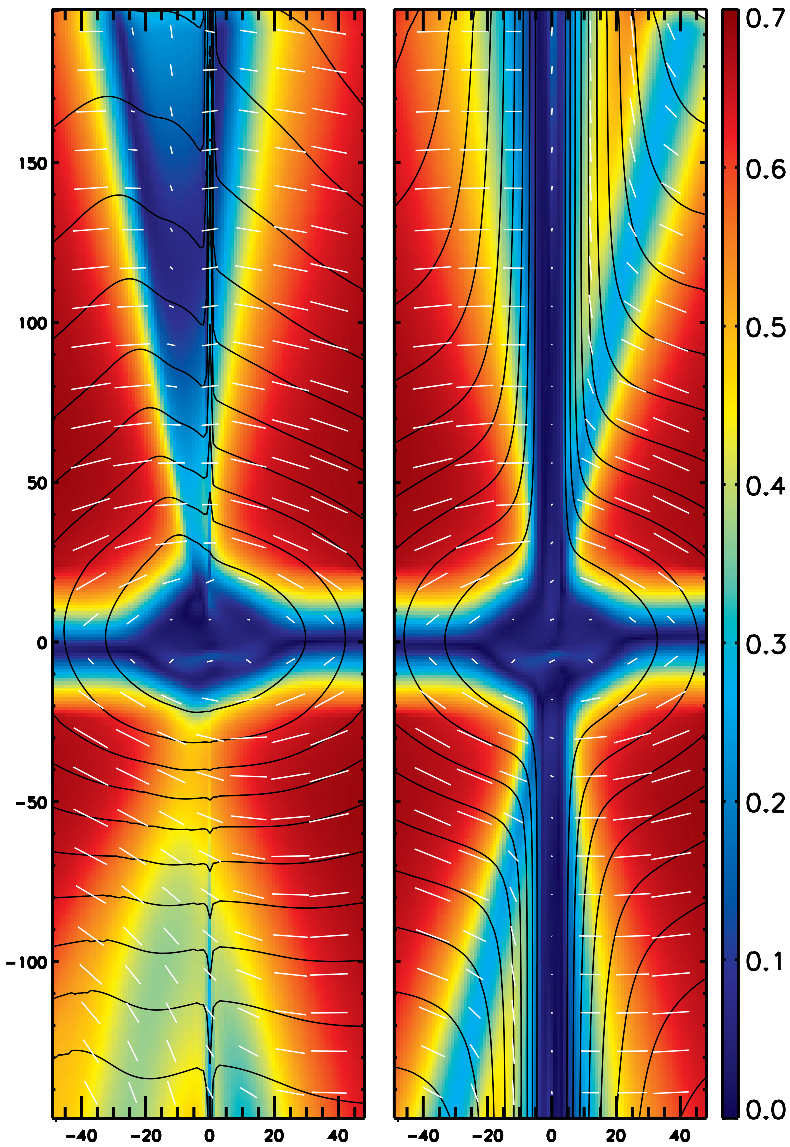

Figure 6.3 Relativistic effect on optically thin polarization (run 2h) at $i = 60°$. The polarization degree is indicated by the background coloring, black contours show total intensity levels spaced by factors of two. *Left:* Including relativistic aberration. At this high inclination, the jet is de-beamed and rotation is apparent in the asymmetry of the intensity contours. *Right:* In the absence of relativistic effects, the polarization pattern is point symmetric about the origin and the intensity clearly promotes the jet.

of the thermal spine along the axis can be recognized. It is worthwhile to note that both intensity and polarization of axisymmetric non-relativistic synchrotron sources exhibit a point symmetry about the origin as illustrated in Fig. 6.3.

6.2.4 Pitch-Angle Dependence

Several Authors (Marscher et al. 2002; Lister & Homan 2005) found indications for a bimodal distribution of the electric vector position angles (EVPA) of quasars and BL-Lac objects either aligned or perpendicular to the jet direction. It was also supposed that BL-Lacs tend to aligned $\hat{\mathbf{e}}$ vectors and overall higher degree of polarization. In a recent 86 GHz polarimetric survey however, Agudo et al. (2010) found no such correlation in their flat-radio-spectrum AGN sample, rather are their data consistent with an isotropic (mis-)alignment. Alignment is customarily attributed to oblique shocks, while perpendicular EVPAs are then interpreted in terms of a shearing of the magnetic field with the surrounding. Another possible explanation for the bimodality is due to large-scale helical fields as shown in the previous section. By varying the emitting region within the collimating jet volume, we investigate to which degree the polarization still conveys the geometric information of the emitting region. As before, Faraday rotation is neglected and we introduce the co-moving pitch angle $\tan\Psi' \equiv B'_\phi/B'_p$ in analogy to Lyutikov et al. (2005). As shown in Section 3.3.2.3 at the example of a non-rotating cylindrical jet, the co-moving fields appear much less twisted than their laboratory frame counterparts. We find that substantially higher pitches than

$$B'_\phi/B'_p \simeq 1 \tag{6.7}$$

are not realized within the simulations. An impression on the pitch angle distribution throughout the jet can be obtained with the cuts shown in the middle panels of figures 5.1 to 5.3. We restrict the emission to originate from $B'_\phi/B'_p \geq \{1, 2\}$, corresponding to $\Psi' \geq \{45°, 63°\}, (\Psi > \{83°, 86°\})$ where equipartition particle energy density (eq. 6.6) is assumed. This way, only the regions of the current driven jet contribute to the emission and no radiation is observed from the spurious axis where B_ϕ must vanish. Figure 6.4 shows the polarization for the two cases and various viewing angles.

In the high pitch-angle case $B'_\phi/B'_p > 2$, the resulting EVPA become parallel for viewing angles $i > 10°$ while for the standard case $B'_\phi/B'_p > 1$, this happens only at viewing angles $i > 30°$. Most structure is observed at moderate viewing angles where we can find the core polarization perpendicular to the ridge line polarization for the case $i = 30°, B'_\phi/B'_p > 1$ as observed in some sources (e.g. Pushkarev et al. 2005). Here we also see a spine and sheath polarization profile across the jet. In

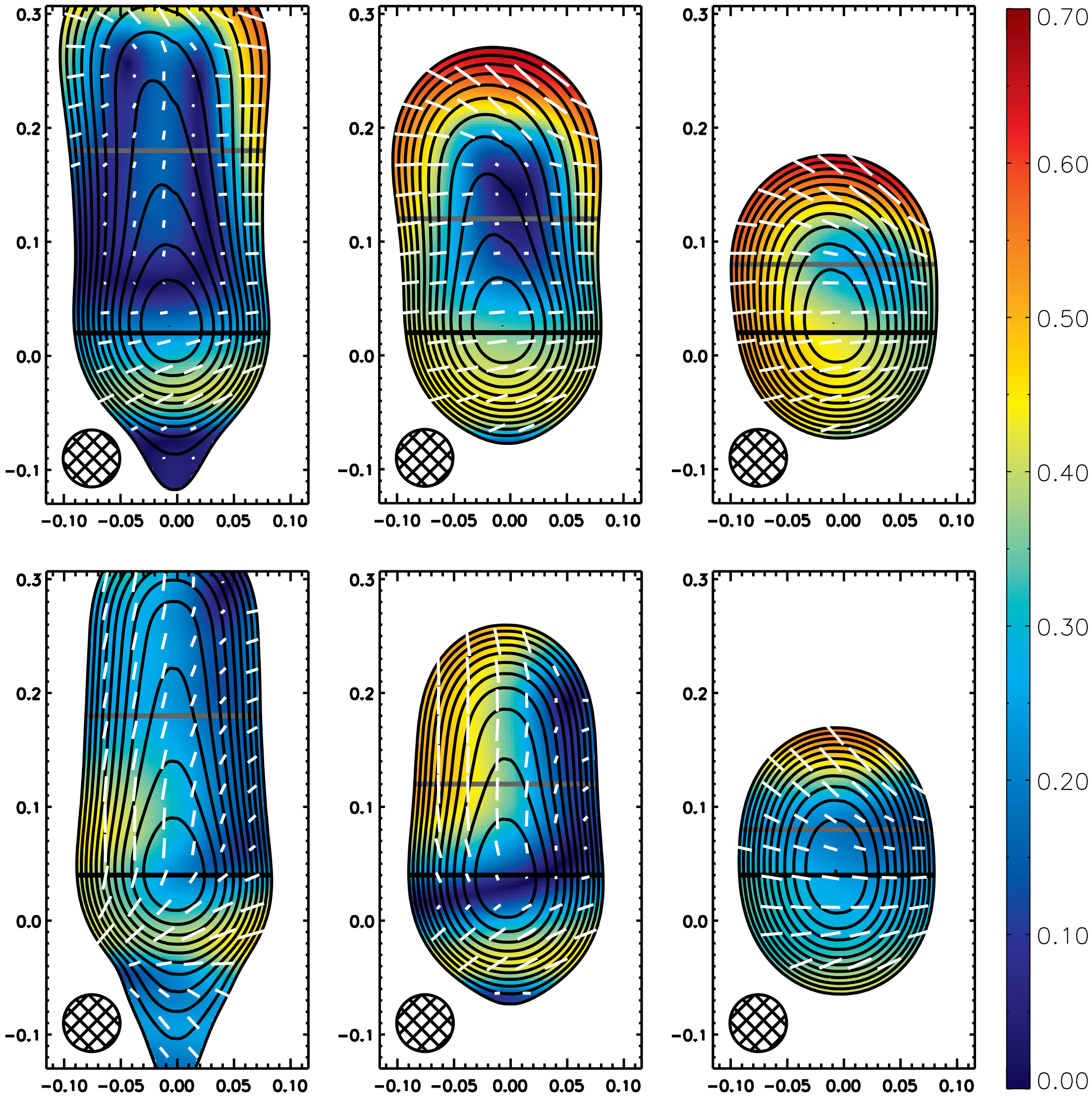

Figure 6.4 Polarizations for $i \in \{30°, 20°, 10°\}$ *(from left to right)* emitted from regions with co-moving pitches $B'_\phi/B'_p > 1$ *(above)* and $B'_\phi/B'_p > 2$ *(below)*. The polarization degree $\Pi_{43\mathrm{GHz}}$ is color-coded and $I_{43\mathrm{GHz}}$ contours are shown. Contours are spaced by a factor of 2 out to $\simeq 5 \cdot 10^{-4} I_{\nu,\mathrm{peak}}$ where the image is cropped. Spatial scale is given in milli arcseconds and a restoring beam with FWHM=0.05 mas was used.

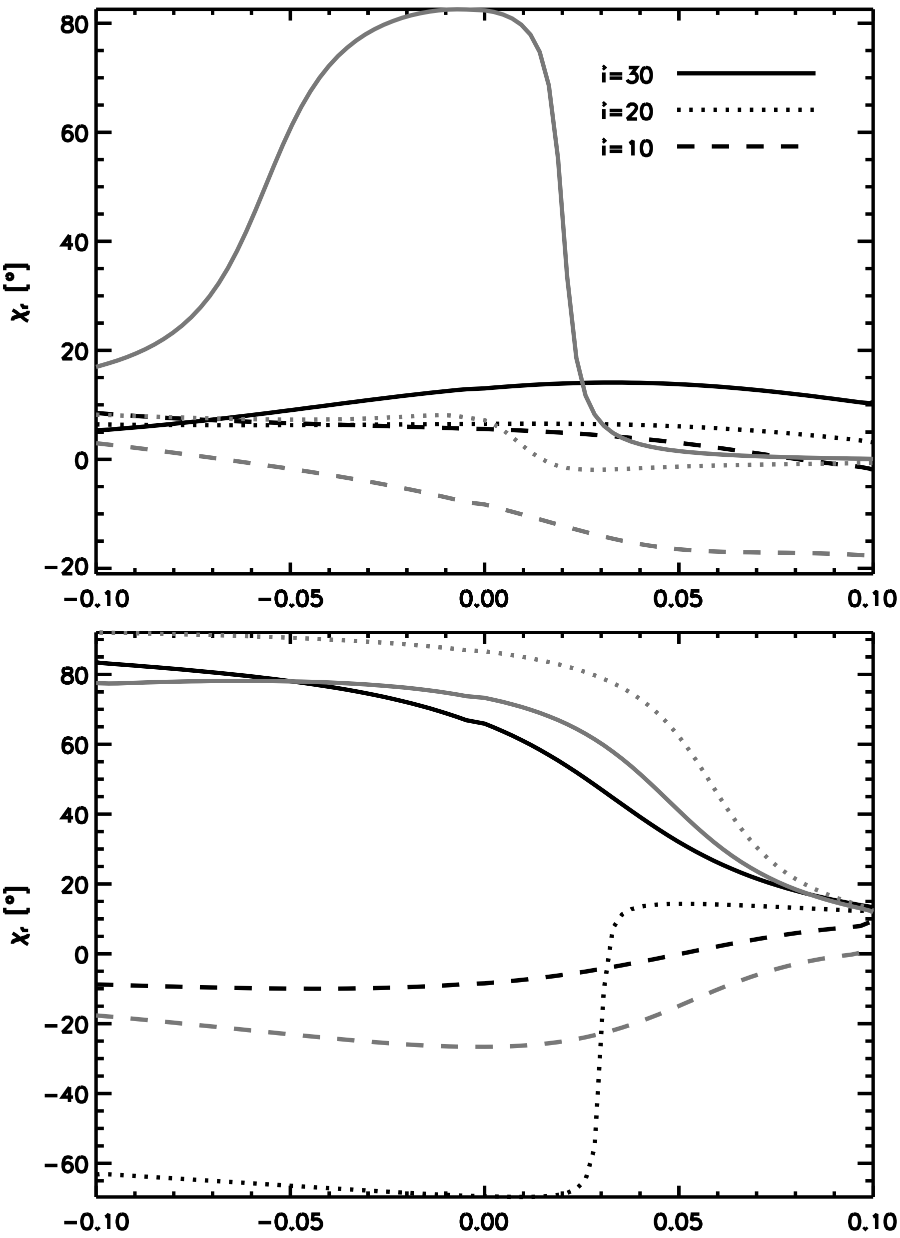

Figure 6.5 Polarization angles for the cuts along core *(black)* and jet *(gray)* emitted from regions with co-moving pitches $B'_\phi/B'_p > 1$ *(above)* and $B'_\phi/B'_p > 2$ *(below)* as in Figure 6.4.

the adopted parametrization of the emission region, the spine and sheath structure is only observed for $B'_\phi/B'_p \sim 1$ as higher pitches tend to alignment and lower pitches tend to counter align.

Beam depolarization is apparent in regions where the polarization turns and, consistent with most observations, the degree of polarization increases towards the boundary of the jet. In the high-pitch case, a left-right asymmetry is most significant with parallel vectors on the approaching side of the rotating jet and perpendicular ones at the receding one (Figure 6.5). Lyutikov et al. (2005) have proposed that based on the asymmetric polarization signal, the handedness of the magnetic field and thus the spin direction of the black hole / accretion disk can be inferred. Our results support this finding. Clearly, when increasing the pitch, the EVPAs turns from the perpendicular to the parallel direction as a general trend. However, pitches $B'_\phi/B'_p > 4$ were not realized by our simulations, such that the emitting region would vanish. Thus for the models under consideration, when approaching the Blazar case, the intrinsic polarization always appears perpendicular. In the following we will mostly characterize the emission region by $B'_\phi/B'_p \geq 1$ as this best selects the relativistic jet contribution.

6.3 Radiation in the Jet Models

We have now introduced all parameters to build models for the synthetic observations. A radiation model comprises a MHD simulation run, a particular physical scaling given by $M_\bullet, \dot{E}$ and the specific parameters of the radiation transport $\Psi', \epsilon_{\rm B}$ and i. Note that the thermal electrons responsible for Faraday rotation are assumed to follow the flow density everywhere and hence the parameter Ψ' determining the region of emission is also responsible for the divide between internal and external Faraday rotation. To normalize the flux, a photometric distance $D = 100\,\mathrm{Mpc}$ is assumed in all models. Table 6.1 summarizes the parameters adopted in this work. We will mostly report results for the fiducial model A and consult the other models only for comparison with the standard case.

For the interpretation of the results, an understanding of the qualitative dependence of the observables on our parametrization is helpful and therefor discussed in the following. In terms of the physical scaling and equipartition fraction, we have

$$\epsilon_\nu \propto \epsilon_{\rm B}\ \dot{E}^{7/4}\ M_\bullet^{-7/2}\ \nu^{-\alpha} \tag{6.8}$$

$$\kappa_\nu \propto \epsilon_{\rm B}\ \dot{E}^{2}\ M_\bullet^{-4}\ \nu^{-\alpha-5/2} \tag{6.9}$$

$$\frac{d\chi_{\rm F}}{dl} \propto \dot{E}^{3/2}\ M_\bullet^{-3}. \tag{6.10}$$

Table 6.1 Jet radiation models

model ID	run ID	$M_\bullet[M_\odot]$	$\dot{E}$[erg/s]	$\epsilon_{\rm B}$	$\tan\Psi'$	i[deg]	$\frac{\dot{M}}{\dot{M}_{\rm Edd}}$
A	2h	10^9	10^{43}	0.1	1	20	1.3×10^{-6}
B	2h	10^9	10^{44}	0.001	0.5	20	1.3×10^{-5}
C	1h	10^9	10^{43}	0.1	1	20	5.5×10^{-7}
D	3h	10^9	10^{43}	0.1	1	20	1.1×10^{-6}

Note. — Columns denote: Model ID; Simulation ID; Black hole mass; Total energy flux rate; Equipartition fraction; Minimal co-moving pitch angle of emission; Standard inclination; Resulting jet mass loss rate in terms of the Eddington accretion rate (with a radiative efficiency of 0.1).

The observable quantities then become

$$I_\nu^{\rm thin} \propto \epsilon_\nu \times l \propto \epsilon_{\rm B}\ \dot{E}^{7/4}\ M_\bullet^{-5/2}\ \nu^{-\alpha} \tag{6.11}$$

$$I_\nu^{\rm thick} \propto \epsilon_\nu/\kappa_\nu \propto \dot{E}^{1/4}\ M_\bullet^{3/2}\ \nu^{2.5} \tag{6.12}$$

and the opacities follow to

$$\tau_\nu \propto \alpha_\nu \times l \propto \epsilon_{\rm B}\ \dot{E}^2\ M_\bullet^{-3}\ \nu^{-\alpha-2.5} \tag{6.13}$$

$$\chi_{\rm F} \propto \dot{E}^{3/2} M_\bullet^{-2}. \tag{6.14}$$

In reverse, based on the latter relations, spectrum and Faraday rotation measurements will allow us to constrain the physical parameters.[1]

We deliberately chose model B to feature ~ 32 times higher Faraday depth compared to model A by increasing the jet energy $\dot{E}$, while maintaining a similar spectrum with the choice of $\epsilon_{\rm B}$ (although the total flux is thus decreased by a factor of ~ 1.8).

6.3.1 Core Shift

Lobanov (1998) showed how opacity effects in optically thick jet cores provide valuable information that can help to constrain the dynamical jet quantities. As the bulk of the radiation originates in the photosphere $\tau = 1$, the projected distance of the $\tau = 1$ surface will result in a specific core offset. Due to the frequency dependent opacity of a synchrotron self absorbing radio source, the measured core position varies systematically with the observing frequency. In simple model jet where the magnetic field and relativistic particle density is modeled as $B \propto r^{-m}$ and $N \propto r^{-n}$ (Königl 1981), this projected distance becomes

[1] In practice this is further complicated by the dependences introduced by the doppler factor which we omitted here as we will compare only dynamically identical models at a given inclination.

$$r_{\rm core} \propto \nu^{-1/k_r} \tag{6.15}$$

where k_r is a combination of the parameters m, n and the spectral index α

$$k_{\rm r} = \frac{(3+2\alpha)m + 2n - 2}{5+2\alpha}. \tag{6.16}$$

In a conical jet, the (predominantly toroidal) magnetic field strength will follow $m = 1$ due to approximate conservation of magnetic energy flux. Conservation of relativistic particles sets for the number density $n = 2$. It is noteworthy that in this most reasonable case, the exponent k_r becomes independent of the spectral index $k_{\rm r} \equiv 1$. Although our jet models are collimating and thus not exactly conical, qualitatively we expect $k_{\rm r}$ close to unity when equipartition particle energy (eq. 6.6) and thus $n = 2m$ is assumed. The observed core shift is illustrated in figure 6.6 for the fiducial model A. Fits of the $k_{\rm r}$ exponent for all runs are shown in the right panel.

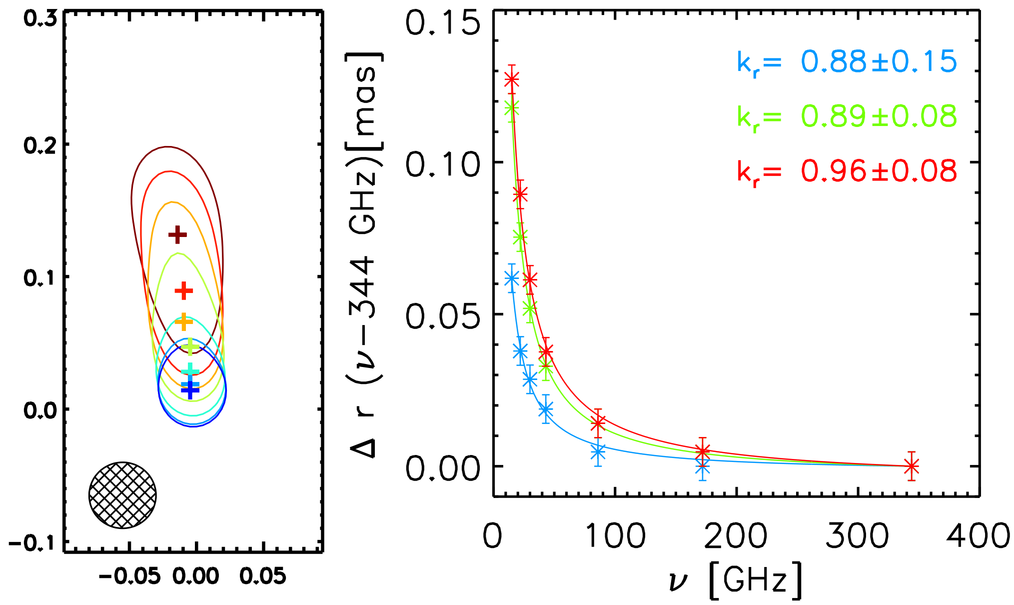

Figure 6.6 *Left:* Half maximum intensity contours and peak positions illustrating the core shift in mas in model A for different frequencies: 344GHz (blue) to 15 GHz (maroon). The images are aligned with respect to the imaginary black hole line of sight located at the origin. *Right:* Fit of the core distances relative to the 344 GHz peak for models C,A,D (top to bottom). The fit function reads $\Delta r = A(\nu^{-1/k_{\rm r}} - 344^{-1/k_{\rm r}})$ with free parameters A and $k_{\rm r}$.

The best fits are slightly steeper than the conical expectation of $k_{\rm r} = 1$. Within the fitting error, models C and D are however still consistent with $k_{\rm r} = 1$ while the deviation in model A becomes significant. It is tempting to interpret this behavior as a consequence of jet collimation which increases the shift for larger distances from the origin. As the far regions are probed by lower frequencies, the distance law of a collimating jet is expected to systematically steepen towards the low frequency side. The quality of the fits for our model jets suggests that core shifts can provide a robust diagnostic of the AGN jet acceleration region. Unfortunately, core shift largely complicates the interpretation of the Faraday rotation maps, as we will show in section 6.3.3.

6.3.2 Depolarization

To understand the polarization signal of the simulated jets, let us briefly review some considerations on the polarization degree in general (e.g. Pacholczyk 1970b), in the presence of Faraday rotation (e.g. Burn 1966) and when an observing beam is used.

The high polarization degrees obtained for the uniform field cases (Equations (3.22), (3.23)) are rarely observed in AGN cores which go down to the percentage level. This clearly necessitates a mechanism for depolarization.

Already Burn (1966) considered the admixture of a isotropic random field component $B_{\rm r}$ to an otherwise ordered field B_0 in the emitting region. He found the simple relation for depolarization relating the energies of the fields $\Pi_r \simeq \Pi_0 B_0^2 (B_0^2 + B_{\rm r}^2)^{-1}$ where $\Pi_{\rm r}$ is now the reduced polarization due to the additional random component. In result, to obtain significant depolarization the random component needs to be comparable to the ordered field. The accompanying dissipation of energy would notably decrease the efficiency of the jet acceleration process, increasing the scales of jet acceleration possibly beyond the parsec scale. The occurrence of turbulence and thus randomly oriented fields in the AGN core can serve as an explanation for various multifrequency observations as ventured by Marscher (2011). Under additional compression, even a completely randomized field structure can account for the high and low observed polarization degrees as demonstrated by Laing (1980). However, the complex physics of turbulence *within the jet* can not be incorporated into MHD simulations of relativistic jet formation at this time. [2] Our current MHD simulation models thus provide highly ordered near force-free fields around which relativistic electrons following an isotropic distribution are assumed to gyrate. We propose that the most promising site for finding such ordered (helical) fields is in fact the Poynting dominated regime of the jet acceleration region that is modeled here.

Under the influence of Faraday rotation within the emitting volume, the polarization degree will also depend on the Faraday opacity $\beta_{\rm F} \equiv d\chi_F/ds$.

[2] Note on the other hand that simulations featuring turbulent slow disk winds serving as Faraday screen were presented by Broderick & McKinney (2010).

We first consider optically thick radiation where the polarization degree is governed by the ratio of ordinary to Faraday opacity $\delta \equiv \kappa_\nu/\beta_{\mathrm{F}}$. Specifically, with $\kappa_\nu \propto \nu^{-p/2-2}$ and $\beta_{\mathrm{F}} \propto \nu^{-2}$ it becomes $\delta \propto \nu^{-p/2} \to \nu^{-1}\,(p=2)$. Once the photon mean free path is smaller than the correlation length of the field and the mean rotation length β_{F}^{-1} in the low frequency limit ($\delta \to \infty$), we expect Π to approach the uniform magnetic field case Π_{l}. Accordingly, for a small value of δ, the radiation is depolarized $\Pi \to 0\,(\delta \to 0)$.

For optically thin radiation, the impact of Faraday rotation can be parametrized by $\eta \equiv \beta_{\mathrm{F}} l$ describing the angular change during the emission length l. The polarization degree will then decrease and oscillate according to $\Pi = \Pi_{\mathrm{h}}|\sin\eta/\eta|$. This is known as *differential Faraday rotation* and its influence on Π is shown in figure 6.1 along a line of sight in the simulation. Since $\eta \propto \nu^{-2}$, internal Faraday rotation has vanishing influence also in the high frequency limit and Π approaches the maximal polarization degree Π_{h}. In a non-uniform field, changes in the emitting geometry lower the maximal polarization degree and Π_{h} can only be assumed at the edges of the emission region. The direction of preferred emission perpendicular to the projected magnetic field is also the direction of dominant absorption, such that in the uniform field case the optically thick polarization direction is flipped by 90° with respect to the optically thin polarization.

Additional depolarizing effects occur when an extended source is observed with finite resolution. The radiation is depolarized when the beam encompasses *(1)* intrinsic changes in the emitting geometry, *(2)* optical depth transitions leading to 90° flips and *(3)* varying Faraday depths, known as (internal or external) *Faraday dispersion* (see also Gardner & Whiteoak 1966; Sokoloff et al. 1998).

For completeness, we should also mention depolarization via "blending" - contamination with an unpolarized (thermal) component - for example radiation from the torus in the infrared. This occurs when the intensity of the contaminant becomes a notable fraction of the total intensity and thus imprints on the spectral energy distribution as well. Naturally, our results are only valid as long as the jet-synchrotron radiation is dominating the total flux.

6.3.2.1 Low Faraday Rotation Case

Spectrum and core polarization degree for model A is shown in figure 6.7. The observable core polarization degree is defined as

$$\langle \Pi_\nu \rangle \equiv \frac{\int d\Omega\ \langle I_\nu(\Omega)\rangle\ \Pi(\langle \mathbf{I}_\nu(\Omega)\rangle)}{\int d\Omega I_\nu(\Omega)} \tag{6.17}$$

where the quantities under the integral are themselves subject to beam convolution. In absence of the latter, the averaged polarization degree increases monotonically

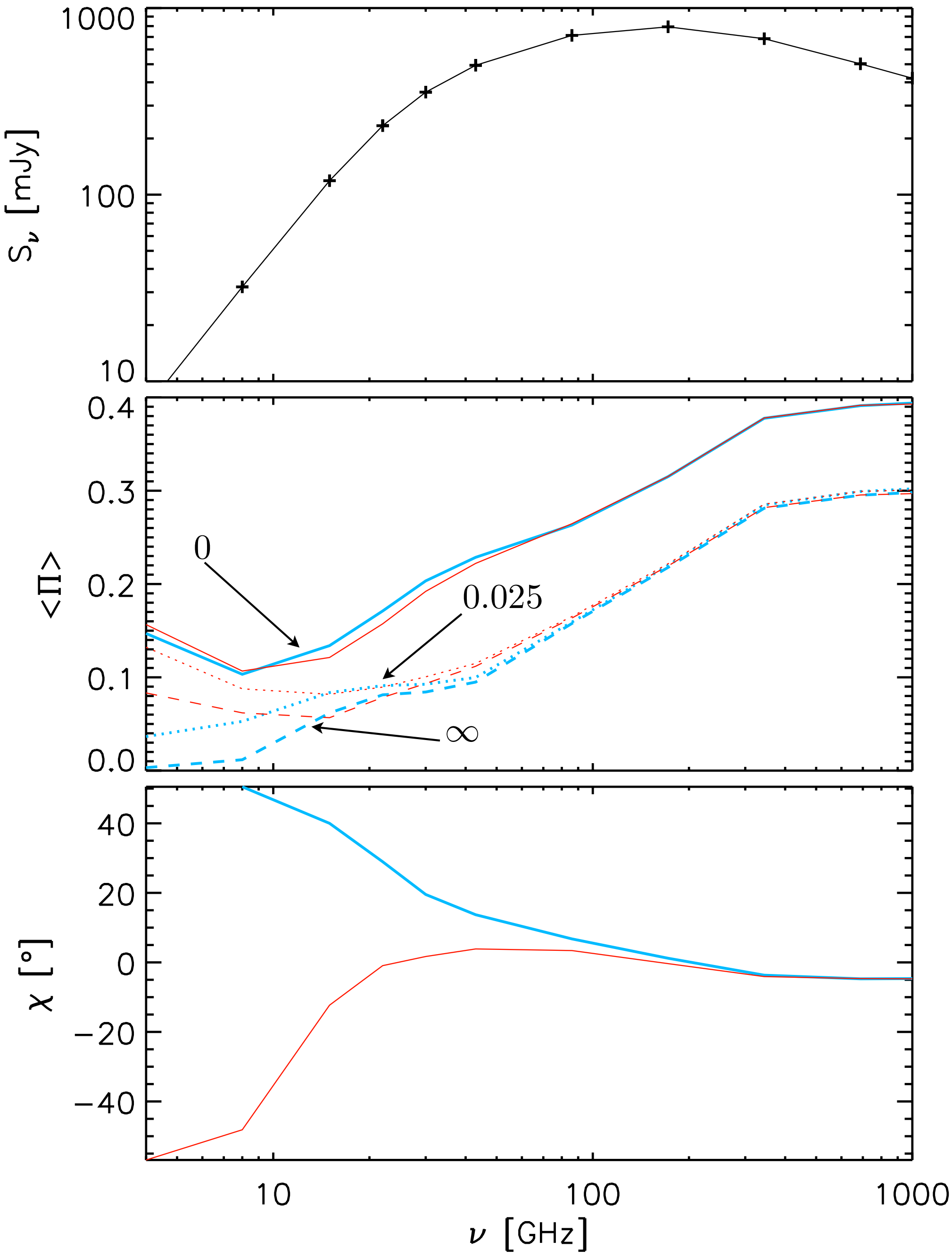

Figure 6.7 Spectrum, core polarization degree and core polarization direction in model A showing depolarization due to beam- and Faraday effects. The curves in the middle panel are shown for increasing beam-FWHM in mas as indicated and converge towards the unresolved case. The unresolved polarization direction is shown in the lower panel. Thick blue lines take Faraday rotation into account and thin red lines are calculated in its absence.

from the expected value of ~ 0.1 in the low frequency range to 0.4 in the optically thin case. Due to the varying emitting geometry, the theoretical maximum of $\Pi_{\mathrm{h}} = 0.69$ is not realized. The influence of differential Faraday rotation seen in the ideal resolution case is in fact small. Depolarization occurs through ordinary beam depolarization and through Faraday dispersion, once the angle between the (unresolved) emitted polarization direction and the Faraday rotated polarization becomes larger than $\sim 45°$ (compare with lower panel of Fig. 6.7). We note that also for the unrotated polarization direction, a flip of $\sim 90°$ between the thick and thin case is not observed. This is also expected, since the photosphere probes various pitch angles as the frequency is decreased and so the simple uniform field case does not apply.

With increasing beam size, the polarization degree ultimately converges to the unresolved case. The convergence is faster for the optically thin regime where the intrinsic emission is less extended and thus quickly masked by the beam.

6.3.2.2 High Faraday Rotation Case

To observe the effect of depolarization due to internal Faraday rotation, we perform the same analysis as before for the high Faraday rotation model B. Figure 6.8 shows the resulting quantities. As anticipated, a similar spectrum is obtained but the polarization degree and direction behave differently. Even when observed with ideal resolution, the polarization degrees of the two cases (Faraday active vs. neglected Faraday rotation) separate clearly as a result of internal depolarization. Also the unresolved polarization angles separate at higher frequencies. Due to multiple rotations, the polarization angle appears to fluctuate below observing frequencies of 100 GHz. In principle, the ideal resolution polarization degree is expected to rise again for lower frequencies as $\delta \to \infty$. However, this did not yet occur at frequencies above 4 GHz that were under investigation.

6.3.3 Rotation Measure

A helical field geometry is generally perceived to promote transversal rotation measure (RM) gradients owing to its toroidal field component. First evidence for RM gradients was found by Asada et al. (2002) and Zavala & Taylor (2005) in the jet of 3C 273. In several unresolved radio cores, λ^2 law RMs have been detected and are found to follow a monotonic profile for example by Gabuzda et al. (2004); O'Sullivan & Gabuzda (2009); Croke et al. (2010).

Taylor & Zavala (2010) point out the observational requirements of a RM gradient detection as follows: *1.* At least three resolution elements across the jet. *2.* A change in the RM by at least three times the typical error. *3.* An optically thin

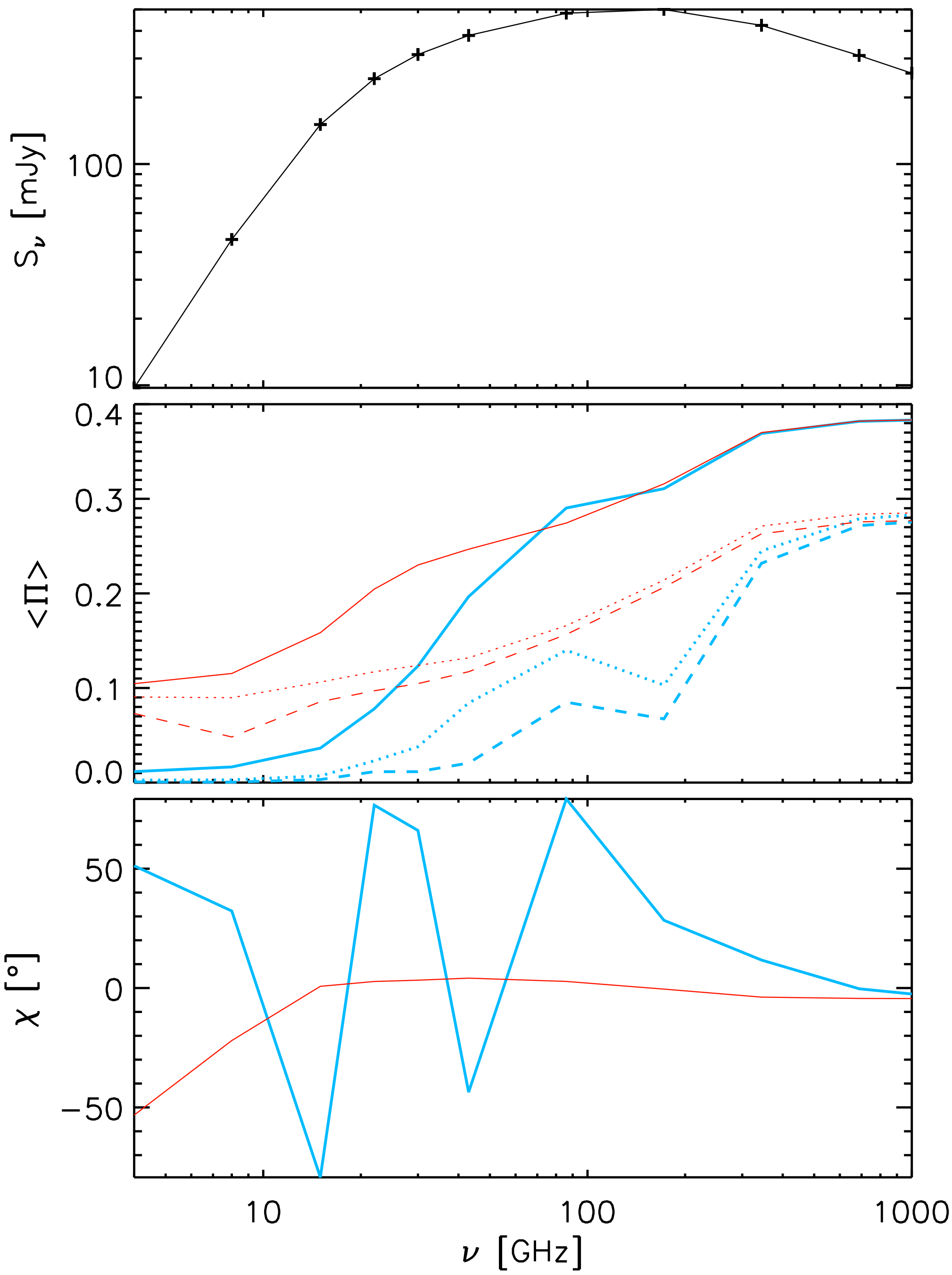

Figure 6.8 As figure 6.7 but for model B with high Faraday rotation.

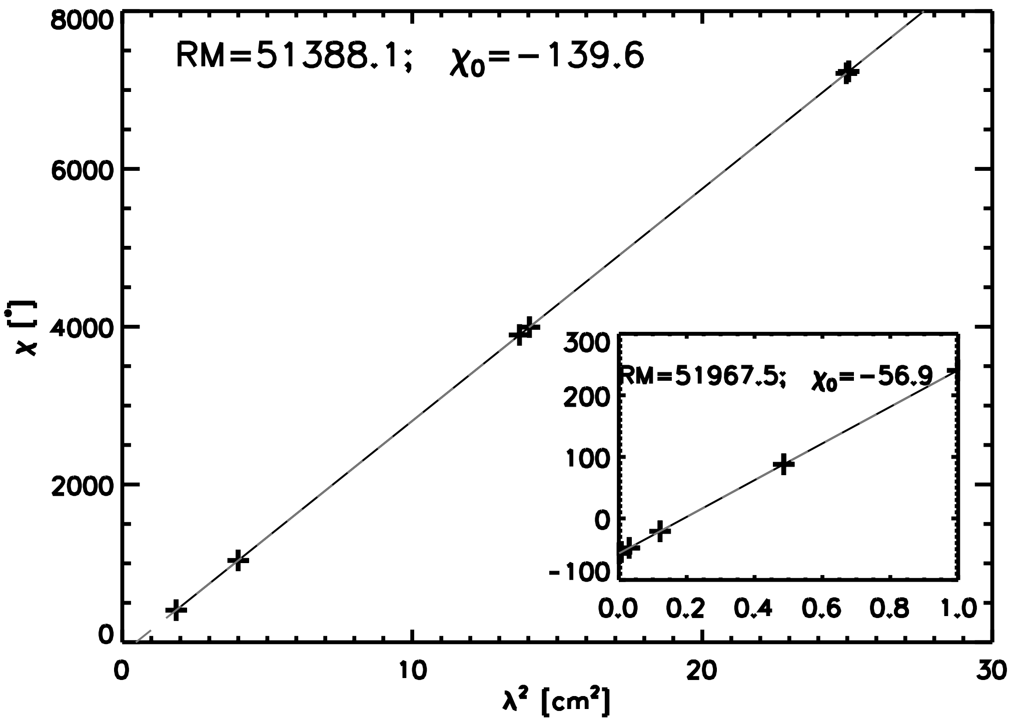

Figure 6.9 Determination of the rotation measure for an ideal resolution line of sight with little internal Faraday rotation. The value of RM (indicated in rad/m^2) necessitates multiple rotations by π for the high λ^2 case. In the inlay, a different fit for the optically thin regime is shown. Between the two cases, the effective angle of emission χ_0 (indicated in deg) is rotated by 83°.

synchrotron spectrum at the location of the gradient. *4.* A monotonically smooth change in the RM from side to side (within the errors).

In the following paragraphs we will touch up on each of the aforementioned points. Due the flip between the optically thick and thin polarization direction, the measurement of λ^2-law RM around the spectral peak require extra caution. Using sufficiently small spacings in $\Delta\lambda^2$ to recover $n\pi$ rotations, we can fit the rotation measure law

$$\chi(\lambda^2) = \chi_0 + \mathrm{RM}\lambda^2 \tag{6.18}$$

to the optically thick and thin cases, where χ_0 now denotes the effective angle of emission. The fits are shown for a particular line of sight that features little internal rotation in figure 6.9. Here, χ_0 differs by almost 90°, whereas RM is of comparable size. However, the latter two findings are not necessarily true for all lines of sight, since the optically thin photons can originate in higher Faraday depths and different emitting geometry, as mentioned previously. We stress that with ideal resolution, consistent λ^2-laws are found both for optically thick and thin photons. Alas, if taken together, we would not be able to fit a linear function for the whole range.

The two-dimensional RM maps shown in Figure 6.10 demonstrate the effect of beam averaging on the low- and high frequency regime. In the high frequency case, the intensity is strongly peaked close to the central object where the Faraday depth is highest, leading to steep radial gradients also in the rotation measure. As the emission is more extended, the RM is lower and smoother in the low frequency case. We find an interesting relation between the core shift and the rotation measure: As the photosphere moves outwards with decreasing frequency, the flux tends to originate further away from the central object leaving systematically less Faraday active material between the observer and the source. [3] After beam convolution, the polarization angle is biased towards the outward moving photosphere, resulting in a shallower rotation measure for lower frequencies which ultimately breaks the λ^2-law that is valid for each ideal resolution line of sight, (e.g. figure 6.9).

Once the core shift distance is large compared to the scale of typical changes in the Faraday depth or emission angle, a λ^2-law will not be observed when the observations are aligned according to the core position. Even absolute positioning as done here[4] can successfully reestablish the λ^2-law only when the beam size is smaller than the core shift. In practice, unresolved core shifts could well be the origin of optically thick λ^2-law breakers.
To this end, we find a striking resemblance of the λ^2-profile shown in Figure 16 with the λ^2-breaking core of the quasar 4C +29.45 given in Figure 2b of O'Sullivan & Gabuzda (2009). Further investigation is needed to quantify this effect in detail.

6.3.4 Resolution, mm-VLBI

In order to observe the helical fields of the jet acceleration region via the associated rotation measure, beam sizes able to resolve the dynamics are essential. In addition, the frequency must be sufficiently high to peer through the self-absorption barrier. With the advance of global mm-VLBI experiments, substantial progress will be made on both of these fronts. The theoretical resolution of a 10^4km mm-observatory (at 300GHz) evaluates to 10μas, similar to the resolution of space-VLBI at 86GHz. Corresponding to a physical scale of $\sim 60\ r_{\rm S}$, our reference object is thus entering the regime of interest for RM studies.

At present, the record holders in terms of physical and angular resolution are the 1.3mm observations of the radio source Sgr A* near the galactic center black hole that were reported by Doeleman (2008) and Fish et al. (2011). Coherent

[3] As a limitation of our direct ray tracing method, the photosphere can in principle shift to the outer boundary (the "lid") of our domain, such that the very optically thick regime below 8GHz can not reliably be probed.

[4] Our images are aligned with respect to the imaginary black hole line of sight. In practice, optically thin features should be used as indicators for an absolute alignment.

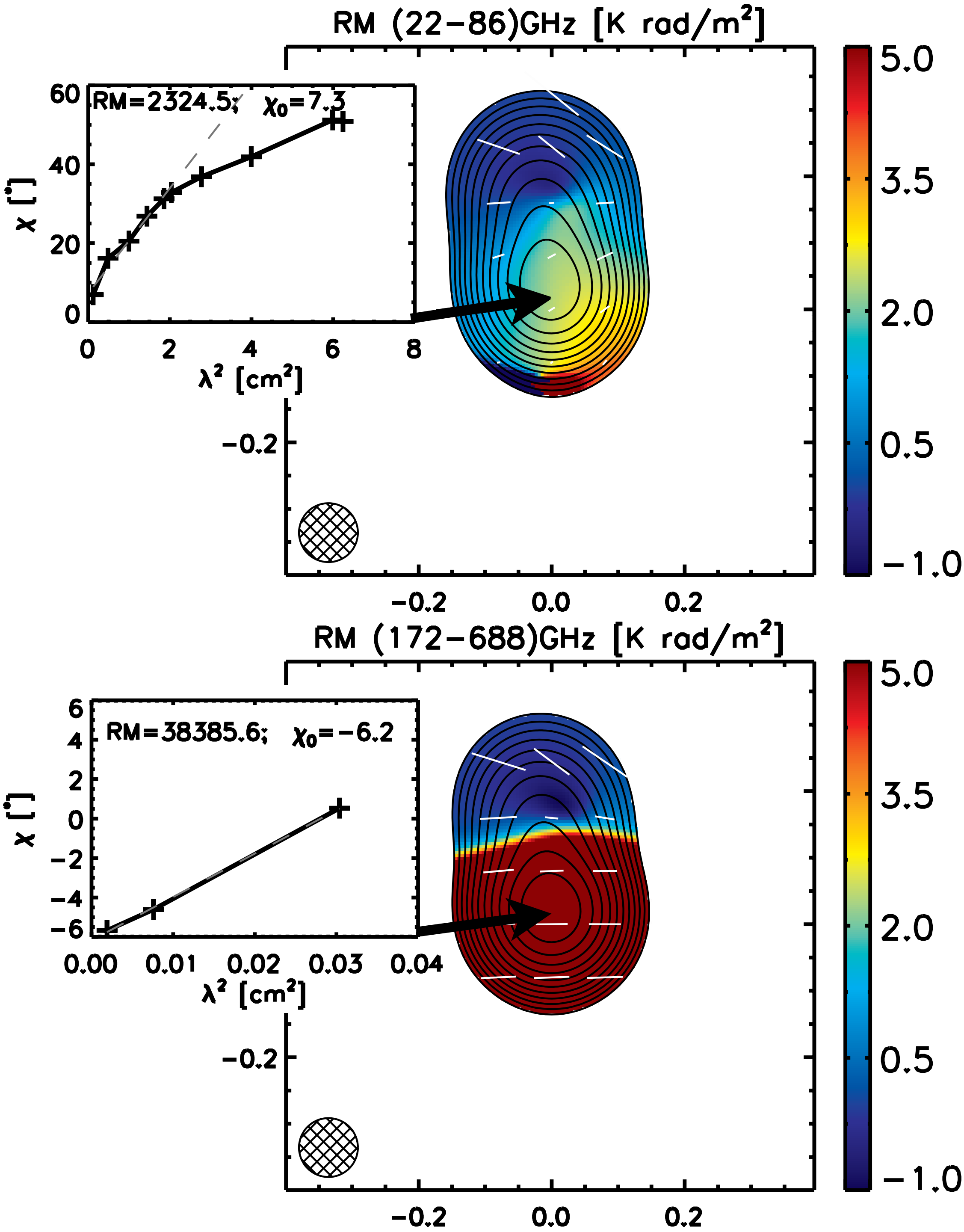

Figure 6.10 Rotation measure maps ($i = 20°$) in the optically thick *(top)* and in the optically thin regime *(bottom)*. White sticks indicate the direction of effective emission, χ_0. In the top plot inlay, only the $22 - 86$GHz region is fitted while the additional points illustrate the λ^2-law breaking due to the core shift (see text).

structures on scales less than 45μas or $\sim 4r_\mathrm{S}$ could already be detected[5] and sub-mm rotation measure magnitudes in excess of 4×10^5rad/m^2 were discovered and confirmed by Macquart et al. (2006) and Marrone et al. (2007).

For the prominent case of M87, Broderick & Loeb (2009a) elaborate that the inner disk and black hole silhouette at 5 r_S could be observed with (sub) mm-VLBI. In M87, high frequency radio observations are already pushing towards the horizon scale (e.g. Krichbaum et al. 2006; Ly et al. 2007), only the important core polarization signal is still inconclusive (e.g. Walker et al. 2008). Rotation measures at core distances of $\approx$ 20mas vary between -5000 and 10^4 rad/m^2 depending on the location in the jet (e.g. Zavala & Taylor 2002). It is tempting to extrapolate these values to the μas scale, assuming the observed RM values are non-local enhancements due to cold electron over densities. Following this argument that was put forward by Broderick & Loeb (2009a), the resulting core RM's would be on the order of 10^8rad/m^2, enough to account for the low observed polarization degree via Faraday depolarization.

In the mm wavelength range, large rotation measures are needed to produce detectable deviations in the polarization angle due to the decreasing coverage of λ^2 space. Typical calibration errors of $\sim 1^\circ$ require RM $> 18 \times 10^3$rad/m^2 for a 3σ detection between 172 and 688 GHz and RM $> 4.3 \times 10^3$rad/m^2 when 86 GHz observations are added. The steep spectrum synchrotron flux of the jet rapidly declines when higher frequencies are considered, however, opacity and Faraday depth also decrease to yield a higher contribution of polarized flux from the core (e.g. Figure 6.7). Also the deviations introduced by the core-shift as described in the previous section will pose lesser problems in (sub-) mm observations.

6.3.4.1 Sub-mm Rotation Measure Maps

To obtain detectable deflections of the polarization angle also at short wavelengths, we now focus on the high Faraday depth model B. As discussed in section 6.3.2.2, at frequencies beyond 172 GHz, the unresolved polarization vector exhibits changes below 45° and internal depolarization is not observed (see also Figure 6.8), such that we find consistent λ^2-law rotation measures in the mm wavelength range. For an increasing beam FWHM from 6.25μas to 100μas, sub-mm RM maps for the optically thin radiation are shown in figure 6.11. The corresponding physical resolution is $31r_\mathrm{S} - 500r_\mathrm{S}$. Steep gradients of RM across the jet axis and "spine and sheath" polarization structures are observable down to a resolution of 125 r_S, below which most information is destroyed by the beam. With increasing beam size, only

[5] Given several Jansky flux in the mm-range, imaging the black hole shadow in Sgr A* becomes a mere problem of visibility in the southern hemisphere (e.g. Miyoshi et al. 2007).

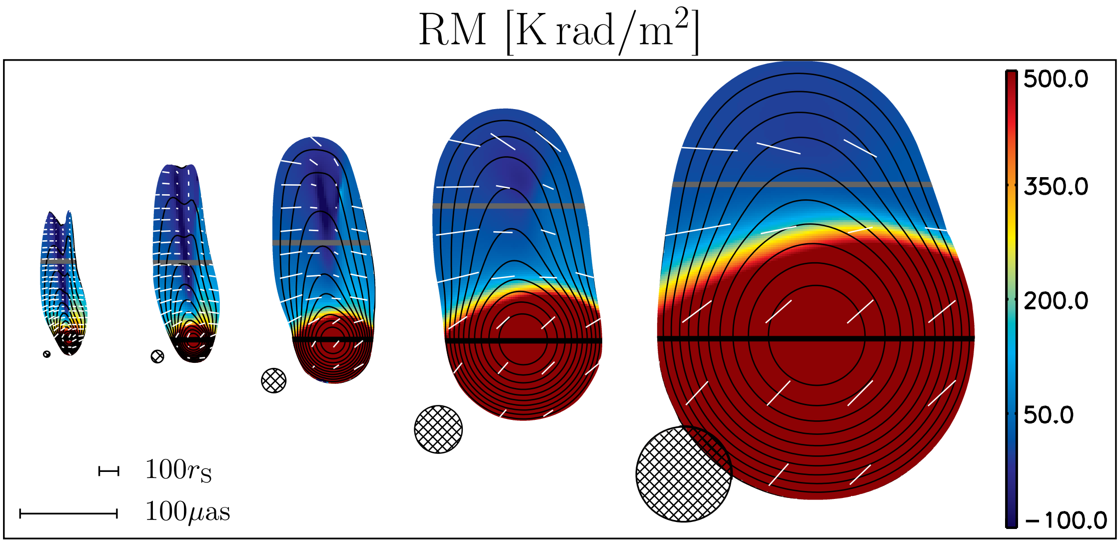

Figure 6.11 RM maps in the optically thin wavelength range (344 – 688 GHz) of model B when observed with decreasing resolution from 6.25μas to 100μas doubling the beam size for each image. The effective emission angle χ_0 is indicated by white sticks.

the central Faraday pit remains detectable. Here the core rotation measure reaches values as high as 10^6rad m^{-2}.

We show the transversal cuts along the core and jet in figure 6.12. At a beam size of 500r_S and observing frequencies between 172 – 688GHz the transversal RM gradients of the jet fall below the assumed detection limit of 3° and become consistent with a constant. Interestingly, beam convolution decreases the magnitude of RM not only in the cuts exhibiting a sign change, but also for the cuts across the intensity peak. We note that the intrinsic jet RM profiles are non-monotonic. Only when under-resolved, the RM features the monotonic profiles "from side to side" that are typically observed.

6.3.5 Viewing Angle

To investigate the viewing angle dependence on the observations we show radio observables for different inclinations from 0.01° to 40° in figure 6.13. With a resolution of 50μas in the 43-86 GHz frequency range these images preview the next generation space VLBI experiments. We observe asymmetric features in the spectral index as proposed by Clausen-Brown et al. (2011). Due to the core shift, the maximum of the spectral index appears "behind" the low frequency intensity peak. When seen right down the jet, the polarization vectors are radially symmetric and show an inclination about the radial direction. With increasing viewing angle, the predominating polarization direction with respect to the jet flips from perpendic-

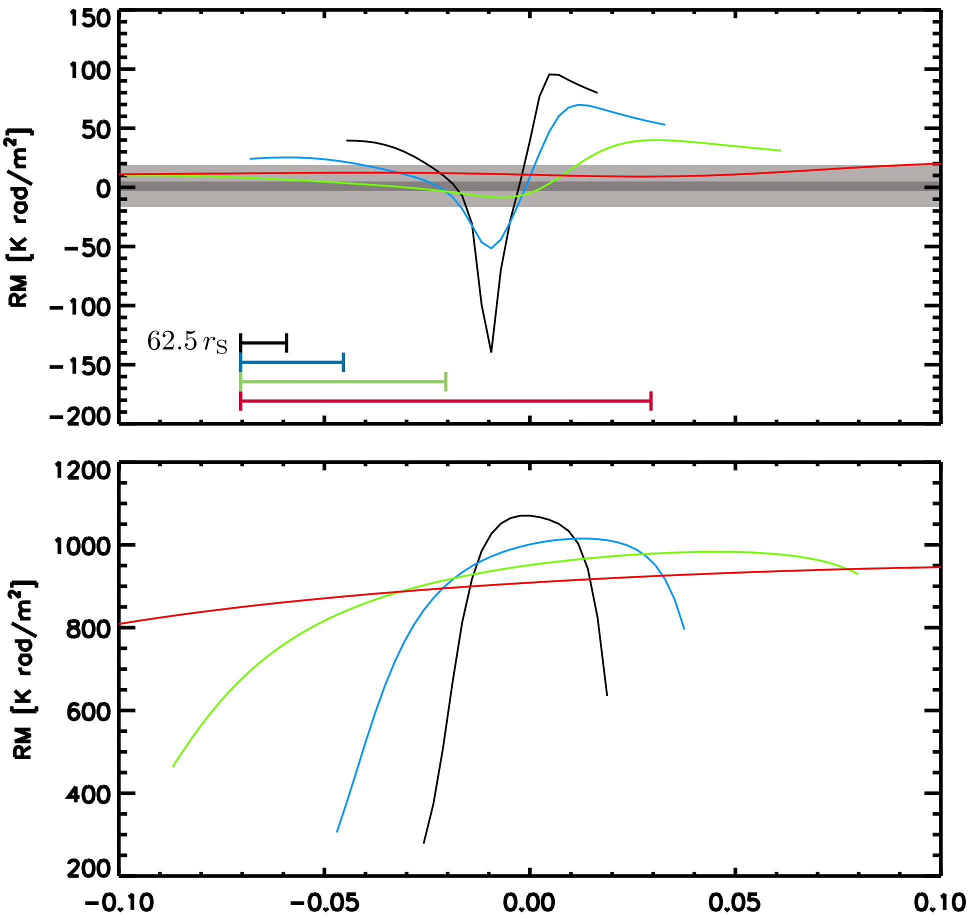

Figure 6.12 RM cuts along the paths indicated in figure 6.11 for various beam sizes. The physical resolution of the cuts is $62.5r_S - 500r_S$ as indicated and 3° detection limits for $86 - 688\,$GHz and $172 - 688\,$GHz observations are shaded grey in the top panel. Curves are cropped where the intensity falls below $5 \times 10^{-4} I_{\nu,\mathrm{peak}}$ as in figure 6.11.

ular to parallel orientation. Also the transversal polarization structure exhibits asymmetries as mentioned in section 6.2.4. To produce rotation measure maps, we fitted the λ^2 law to observations at 43, 85 and 86 GHz. In order to avoid the problems due to optical depth effects (see section 6.3.3) we exclude regions of spectral index between $0 < \alpha < 2$ in the maps. The strong feature in the 20° RM map at $(0, 0.15)$mas is most likely an artifact from the finite ray-casting domain and corresponds to the region where the axis pierces through the "lid" of the domain. For $i = 40°$ this region is excluded from the RM map and for $i = 0.01$ the problem does not arise. At high inclinations, we observe steep RM gradients that coincide with the spine-sheath flip of polarization.

As such high resolution data are not readily available, we also quantify the integral values that should reflect unresolved core properties. The viewing angle

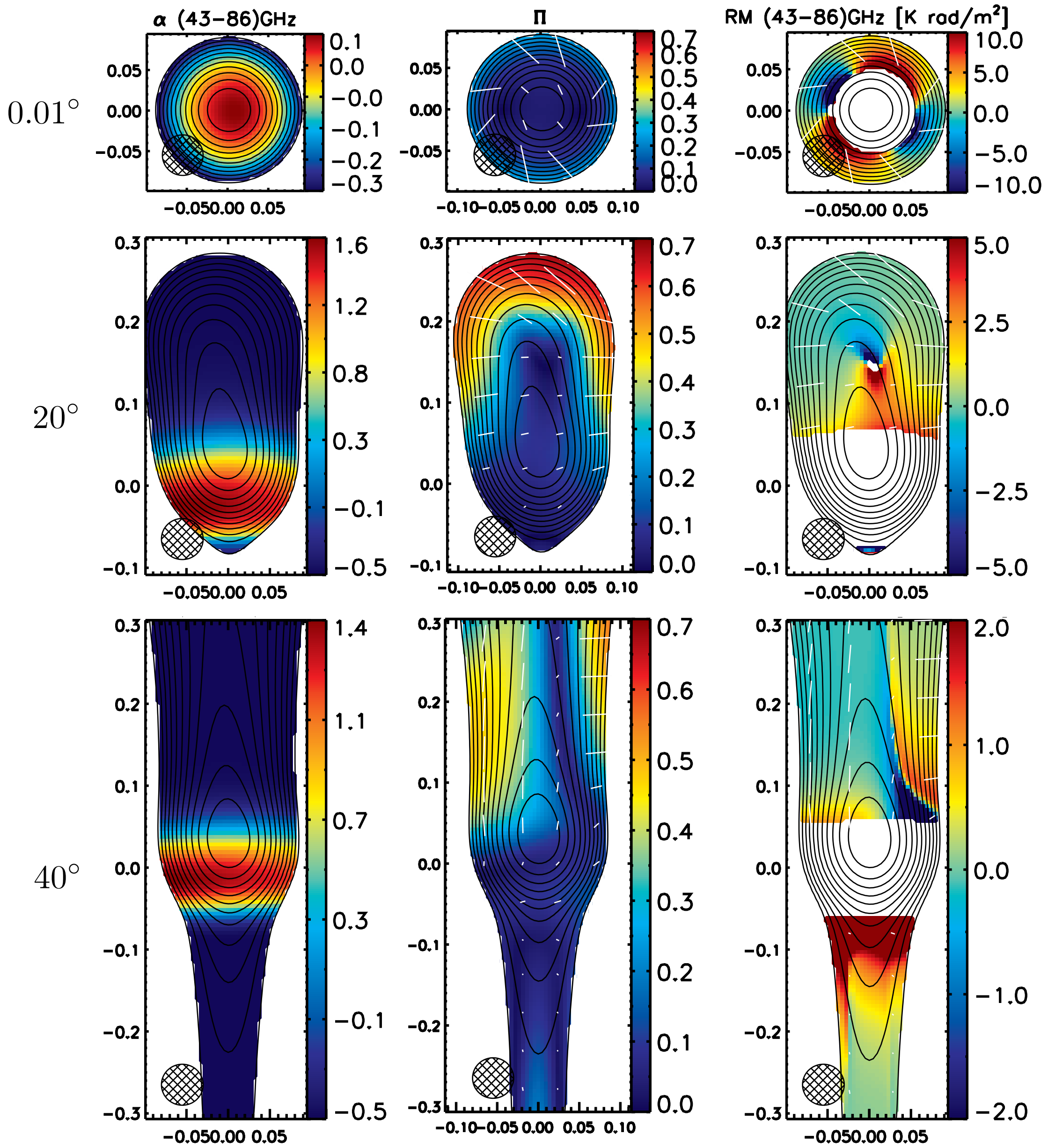

Figure 6.13 Mock observations based on model A at 43GHz and 86GHz for viewing angles $i \in (0.01°, 20°, 40°)$ with resolution of 50μas. Contours according to 43GHz intensity and spaced by factors of two. From left to right: Spectral index α, 43GHz polarization degree Π and rotation measure in optically thin regions.

dependence of flux, spectral index, unresolved polarization degree, polarization direction and rotation measure are shown in figure 6.14. The flux peaks at viewing

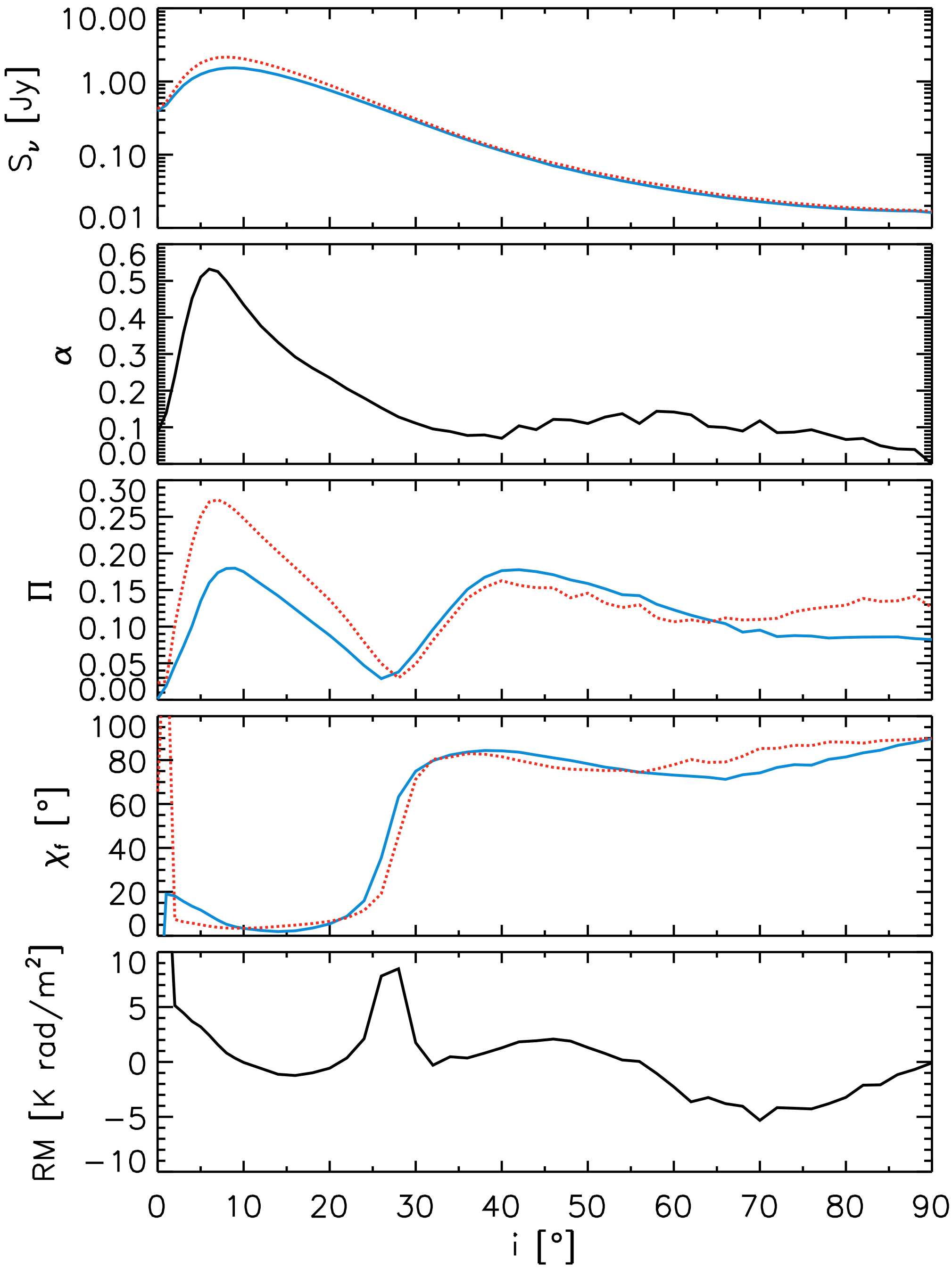

Figure 6.14 The dependence on viewing angle i of unresolved quantities for 86 GHz (dotted, colored red in the online version) and 43 GHz (solid, colored blue in the online version). Top to bottom: Beamed flux, spectral index, integral polarization degree, observed polarization vector $\chi_{\rm f}$ and apparent rotation measure derived from $\Delta\chi_{\rm f}$.

angles of roughly 5° and not when looking directly down the jet as would be the case for simplified cylindrical flows with toroidal fields. This reflects the fact that our jet solutions are not perfectly collimated and exhibit a small degree of rotation such that the Doppler factor attains its maximum value of $D \simeq 15$ at $i \simeq 5°$. The dominating polarization direction flips from perpendicular (0°) to parallel (90°) for viewing angles $i > 25°$. At this flip, the polarization degree shows a local minimum through beam depolarization. In the framework of the unified model proposed by Urry & Padovani (1995), this suggests that the core polarization direction in the radio galaxy case (viewed at high inclination) should be clearly distinct from the blazar case (looking down the jet). For $i = 0°$, the polarization degree approaches zero and its direction fluctuates between 0° and 90° due to the axial symmetry.

6.3.6 Towards Modeling Actual Observations

Individual sources are modeled by constraining all free parameters (tables 5.1 and 6.1) with observations of spectra, core shift, polarization and rotation measures. Taken together, we obtain seven interrelated parameters in our radiation models. Two of these are related to jet dynamics, parametrizing the energy partitioning with β_1 and the current distribution with the parameter s. We find that the current distribution has little influence on the observables and hence this dependence can eventually be dropped, which reduces the number of free parameters but at the same time looses predictive power.
Two parameters are related to the physical scaling of the simulations, namely the total energy flux $\dot{E}$ and the black hole mass $M_\bullet$. With the scale free nature of the underlying MHD, a single dynamical simulation can be used to construct a multitude of objects for arbitrary total energy flux and black hole mass. Thus in principle a library of physical jet models can be constructed from a few dynamically distinct simulations (see also: Physical scaling, section 5.2.4).
Compared to the simulations, the raytracing is fast and can be used to vary the remaining parameters $\epsilon_{\mathrm{B}}, \Psi'$ and i.

An alternative to modeling individual sources is to compare the statistical properties of a set of models with a sample of AGN cores as observed e.g. by Agudo et al. (2010).

We have to postpone such an effort for future investigation. However, already with the acquired data (e.g. figure 6.14), our simulations strongly suggest a bimodal distribution of the polarization angle.

6.4 Summary and Conclusions

In chapter 5, we have performed axisymmetric, special relativistic MHD simulations of jet acceleration and collimation. The resulting dynamical variables are now applied to calculate polarized synchrotron radiation transport in postprocessing, providing dynamically consistent emission maps to predict VLBI radio and (sub-) mm observations of nearby AGN cores. For this purpose, we have developed a special relativistic synchrotron transport code fully taking into account self-absorption and (internal) Faraday rotation. Since the acceleration of non-thermal particles can not be followed self-consistently within the framework of pure MHD, it remains necessary to resort the particle energy distribution to simple recipes. We have compared three prescriptions of the non-thermal particle energy distribution. We found good agreement in the alignment of the polarization structure, but considerable differences in the intensity maps. Thus, the polarization maps derived in this work can be considered as robust, while the intensities distribution should be regarded with caution.

The strict bi-modality of the polarization direction suggested by Pariev et al. (2003); Lyutikov et al. (2005) and others can be circumvented when the structure of a collimating jet is considered. However, the efficient collimation to near-cylindrical jet flows in general confirms the results obtained for optically thin cylindrical flows when the fast jet is considered. Thus, depending on the pitch angles of the emission region, also a spine-and-sheath polarization structure is observed. The relativistic swing effect skews the polarization compared to the non-relativistic case. Our radiation models affirm the finding of Lyutikov et al. (2005) and Clausen-Brown et al. (2011) that relativistic aberration promotes asymmetries in the polarization (half spine-sheaths) and also in the spectral index. The observational detection of such features would allow to determine the spin direction of the jet driver, be it the accretion disk or the central black hole.

The frequency-dependent core shift in the radiation maps following our jet simulations is consistent with analytical estimates of conical jets by Lobanov (1998) in two jet models and slightly steeper in the third case considered. We attribute this discrepancy to fact of jet *collimation*. The overall good agreement with the analytical estimate suggests that the standard diagnostics should provide robust results capable of determining the jet parameters. With our radiation models we have confirmed the intuition that unresolved core shifts should lead to a breaking of the λ^2 rotation measure law. Further, we have demonstrated that that law can be restored again as soon as the resolution is increased. Opacity effects do not allow to obtain a consistent λ^2-law across the spectral peak. Once the regimes are separated however, we obtain two valid relations for which the optically thin rotation measure is substantially increased over the optically thick case as it peers deeper into the Faraday pit.

The interpretation of observations featuring both internal Faraday rotation and changes in opacity is one of the most challenging aspects in polarimetric imaging of jets. With our detailed modeling, we were able to disentangle the depolarizing effects of opacity transition, differential Faraday rotation, and also beam effects such as ordinary beam depolarization or Faraday dispersion for two exemplary jet models. We find that the unresolved, optically thin mm-wavelength radiation is depolarized due to both the changing emission geometry (down to $\sim 40\%$), and the additional beam depolarization (down to $\sim 30\%$). Increasing the Faraday opacity by observing at lower frequencies would lead to depolarization below the 1% level due to *1.* Faraday dispersion and *2.* differential Faraday rotation.

We have also investigated the influence of resolution on the detectability of rotation measure (RM) gradients in the optically thin parsec-scale jet-core previewing mm-VLBI observations. To detect the intrinsic non-monotonic profiles across the jet, a resolution of $\sim 100 r_{\rm S}$ would be required. Increasing the beam size leads to more monotonic transversal RM profiles and the detection of a "RM-gradient" can be claimed until the jet is resolved by only two beam sizes across. We find the peak magnitude of the RM to increase with resolution. High RMs beyond $10^4 \mathrm{rad\,m^{-2}}$ are required to obtain a noticeable deflection in the mm-wavelength range. From the sources where high resolution data is already available, namely Sgr A* and M87, such high rotation measures are in fact observed, and we predict that many more objects in this class will be found at the advent of ALMA and global mm-VLBI.

Finally, we have presented mock observations of spectral index, polarization degree and rotation measure for various inclinations. Asymmetries in the spectral index and polarization degree can be observed most clearly at high inclinations $> 30°$. The necessary resolution for this detection in a fiducial low Faraday rotation case (our model A) amounts to 50μas, which could be reached with the next generation space-VLBI. At $\sim 30°$, the predominant polarization vector flips from perpendicular alignment (with respect to the projected jet direction) for the blazar case to parallel alignment for the radio galaxy case at high inclinations. The flip in polarization is clearly detectable also from unresolved quantities. In summary, these findings suggest a bimodal distribution of the observed polarization direction of AGN core jets. However, by adding a substantial amount of Faraday rotation (our model B), this signature will be scrambled unless the observing frequency is chosen high enough - confirming the popular intuition.

In this chapter, we have focussed on general signatures of the synchrotron radiation in the large-scale helical fields in the acceleration region of relativistic MHD jets. With the developed tool set in hand, further progress can be made when calibrating the observational diagnostics with the mock observations that are detailed here. We expect a substantial improvement from a more consistent treatment of the non-thermal particles, taking into account particle acceleration and cooling. Potentially, also modeling of individual sources, or the cumulative statistics of AGN surveys applying dynamical simulations could be undertaken in the future.

Chapter 7

Three Dimensional Structure of Jet Formation

7.1 Introduction

So far, we investigated in detail the acceleration and collimation of axisymmetric relativistic jets. This is largely justified by the observational appearance and ease of the modeling. However, since nature does not obey axisymmetry, 2D modeling falls short in two important aspects:

1. It can easily be shown that the axisymmetric induction equation ($\partial_\phi \equiv 0$) lacks a mechanism to transform toroidal magnetic field back into poloidal field. Therefore the toroidal field can only be amplified, leading to a potential overproduction of B_ϕ and the collimating pinch force. This might cast a shadow of doubt on the validity of axisymmetric results, however, we should stress that as long as axisymmetry of the flow is preserved, also a fully three-dimensional simulation features this property.

2. In order to also study the stability of jets, a three dimensional treatment is necessary. The instability of current carrying plasmas is connected to non-axisymmetric perturbations of the toroidal magnetic field (Bateman 1978). Among these current driven instabilities, the $m = 1$ mode known as the "kink" is the most violent one. It leads to a helical displacement from the axis of the plasma-cylinder.

In the context of young stellar objects, the helical Kink can yield an explanation for the wiggly structure observed at some stellar jets (e.g. HH 46/47) (Todo et al. 1993; Lery et al. 2000). If not brought to a halt by regulating non-linear mechanisms, the exponential instability growth must lead to complete disruption of the jet. At the presence of instability, jets can dissipate magnetic energy via reconnection (e.g.

Drenkhahn & Spruit 2002; Lyutikov & Uzdensky 2003) and shocks (e.g. Blandford & Königl (1979)), leading to heating, acceleration of high-energy particles and radiation. As noted by Heinz & Begelman (2000) and Drenkhahn & Spruit (2002), the dissipation into a fully tangled magnetic field could also promote efficient quasi-thermal acceleration of the bulk flow out of magnetic enthalpy. In principle, the current-driven instabilities can be accompanied by other types of instabilities such as the Kelvin-Helmholtz instability (KH) caused by shear between jet and ambient material. The KH instability can thus lead to an efficient mixing of the jet and environment. However, in the presence of strong magnetic fields, growth of the KH modes is strongly suppressed (Keppens et al. 1999). In particular, toroidal fields appear to hinder mixing and thus exert a stabilizing influence (Appl & Camenzind 1992; Mignone et al. 2010).

As pointed out by McKinney & Blandford (2009), when the well-known Kruskal-Shafranov (KS) instability criterion

$$\left|\frac{B_\phi}{B_p}\right| > \frac{2\pi r}{z} \tag{7.1}$$

for cylindrical force-free equilibria is applied to relativistic jets, we obtain the result that jets become unstable already at the Alfvén point $z_A \simeq 10 r_{\rm S}$ (where $B_\phi \gtrsim B_p$ and $z \gtrsim r$) - before accelerating to highly relativistic velocities. This is in stark contrast to the finding of some AGN FR-II jets propagating unperturbed out to distances of $10^7 r_{\rm S}$.

Linear stability analysis in non-relativistic, but otherwise complete MHD was conducted for current-free and current-carrying jets with helical magnetic fields by Appl & Camenzind (1992). The stability of *relativistic* MHD jets on the other hand is still not fully addressed in linear analysis and subject of ongoing research. Considering linear analysis of *force-free* cylindrical configurations, Istomin & Pariev (1994) and Istomin & Pariev (1996) concluded stability of $B_z = const.$ jets with respect to axisymmetric and helical perturbations. Begelman (1998) on the other hand demonstrated the violent instability of the $m = 1$ mode which he postulated as a possible solution to the long-standing $\sigma-$problem. Also Lyubarskii (1999) stressed the importance of the $m = 1$ mode by considering more realistic configurations with decreasing flux. However, Lyubarskii (1999) and recently Narayan et al. (2009) note the time-delated slow growth rate of the kink which could lead to a displacement of launching and dissipation sites - supporting the far dissipation scenario mentioned before.

Tomimatsu et al. (2001) could extend the classical KS criterion and demonstrated a stabilizing effect of the relativistic field line rotation. Their analysis

(TKS) yields the simple criterion for instability

$$\left|\frac{B_\phi}{B_p}\right| > \frac{2\pi r}{z} \qquad \text{and} \qquad \left|\frac{B_\phi}{B_p}\right| > \frac{r\Omega}{c} \tag{7.2}$$

such that the toroidal field strength also has to overcome the stabilizing electric field. The asymptotic relation for relativistic jets $B_\phi \simeq -r\Omega/cB_p$ suggests marginal stability of the unperturbed flow.[1] Taken at face value, the TKS criterion thus suggests that relativistic jets are always on the verge of instability with the ultimate fate strongly depending on details of the modeling. For example, several authors investigated the stabilizing influence of environmental effects such as shear (e.g. Mizuno et al. 2007), external wind with relativistic bulk motion (Hardee & Hughes 2003) and sideways expansion (Rosen & Hardee 2000), emphasizing the influence of modeling details for jet and ambient material. While there is now growing consensus that the kink instability can also operate in the relativistic regime, to answer whether it can grow indefinitely to finally disrupt the jet or rather saturate, requires a study of the non-linear evolution via numerical simulations (e.g. Mizuno et al. 2009; Mignone et al. 2010; Mizuno et al. 2011).

We like to point out that jet stability can best be studied by including the initial acceleration and collimation region of the jet. Thereby, self-consistent helical magnetic fields are obtained and the number of ad-hoc assumptions for the jet base can be reduced to a minimum of physically well motivated choices. McKinney & Blandford (2009) were the first to present 3D simulations of jet formation including a turbulent accretion disk. In their seminal paper, no significant disruption or dissipation out to scales of $10^3 r_{\rm S}$ was observed, however by using comparatively low resolution GRMHD simulations. Although the launching directly from the turbulent accretion flow promises the most realism, a systematic study of instability growth can hardly be performed this way. For non-relativistic disk jets, Ouyed et al. (2003), Anderson et al. (2006), Moll et al. (2008) and Staff et al. (2010) followed an alternative approach by treating the rotating magnetosphere as a fixed-in time injection boundary. As a natural generalization of previous axisymmetric work, the boundary can be used to model the corona of a Keplerian accretion disk. Also we will follow this strategy for the case of relativistic jets, as it allows to systematically control the fixed in time and time variable injection conditions.[2]

In this chapter, we show our first results concerning the stability of relativistic jets near the launching region. We will discuss 3D RMHD simulations exposed to non-axisymmetric perturbations triggered by the accretion disk and due to jet-

[1] However, this result should be handled with care, since the TKS criterion strictly only applies in the sub-Alfvénic region of the flow; see also the discussion by McKinney & Blandford (2009).

[2] To our knowledge, the only study addressing stability of the jet formation region in the relativistic case was presented by McKinney & Blandford (2009).

cloud interactions. To complement the previous considerations of 2D jet formation, we focus mainly on non-axisymmetric features within the jet.

7.2 Model Setup

In our model, the jet is launched from a rotating inlet resembling the corona of an accretion disk similar to the setup outlined in chapter 4. The initially purely poloidal magnetic field is thus transformed into a helical shape giving rise to a global electric current system which accelerates and collimates the flow. Due to the increased complexity of the three dimensional treatment, we have to resort to a slightly simplified setup neglecting stratification due to a gravitational source term.

7.2.1 Initial and Boundary Conditions

We initialize the domain with constant values for density and pressure $\rho \equiv \rho_0 = 0.01$, $p \equiv p_0$, threaded by a split-monopole field (Equations (4.7), (4.8)) with the "source" at $y = -4$. The domain-pressure follows from the plasma β parameter at the inner disk edge $r = 1$ to $p_0 = \beta/2B_1^2$, where B_1 denotes the corresponding poloidal magnetic field strength at $(r, y) = (1, 0)$.

It proved necessary to truncate the disk inlet at r_{out} in order to avoid the poorly determined states where disk-boundary and outflow boundary meet. Not truncating the disk lead to additional $m = 4$ noise triggered predominantly at the corners of the domain. At the $y = 0$ plane and within $r < r_{\mathrm{out}}$ we assign boundary conditions for a rotating magnetosphere injecting a sonic flow along the field-lines. To provide the axisymmetric boundary constraints, we transform to cylindrical coordinates around the $y-$axis, compute the required quantities and subsequently transform back to the cartesian domain to assign the updated boundary conditions. In our particular implementation, we measure the ϕ-angle from the $x-$axis to the positive $z-$direction and thus the disk revolves around the opposite direction when compared to the previous chapters. This also implies that the current circuit turns around such that the axial ("return") current is now pointed in direction of propagation. We specify fixed-in time axisymmetric profiles for the five quantities $p \equiv p_0, \rho \equiv 100\rho_0, v_\phi = r\omega(r), v_p \equiv c_{\mathrm{s}}, E_\phi \equiv 0$ in accordance with corollary 2. In addition, the magnetic flux B_y is fixed to the initial profile. Since the evolution of B_y is already suppressed via the choice of $E_\phi \equiv 0$, this does not represent an additional boundary constraint. The radial field component is obtained by potential field extrapolation ($j_\phi = 0$) of the domain values B_r, given the fixed profile of the vertical field component B_y. The toroidal field B_ϕ follows from the domain via zero gradient extrapolation to yield also $j_r = 0$. This way, the boundary current is largely under control, in particular, no spurious current sheets are allowed to arise at the injection boundary. For the rotation profile, we adopt

$$\omega(r) = 0.5c \begin{cases} 1 & ; \quad r < 1 \\ r^{-3/2} & ; \quad 1 \leq r < r_{\mathrm{out}} \end{cases} \tag{7.3}$$

representing an inner solid-body rotation law and an outer Keplerian profile as in Tchekhovskoy et al. (2008). Beyond r_{out}, we apply equatorial reflecting boundary conditions for all variables. Due to the numerical errors introduced by the coordinate-transformation and decreased resolution compared to the previous axisymmteric studies, steep gradients of the rotation law as in chapter 4 must be avoided if no special treatment for the velocity profile is given.[3] It is also for similar stability reasons that we specify ω instead of the field rotation law Ω as before. The assignment of Ω increases the numerical error in ω due to the accumulation of errors in B_ϕ and B_p involved in the computation of $v_\phi = r\Omega + v_p B_\phi / B_p$. Specifying a fixed value for Ω lead to a spurious evolution of the vertical magnetic field which gets "evacuated" from the axis; an effect also discussed by Ouyed et al. (2003). The causal TM equation of state is employed (see section 2.1.7). Three additional passive tracer scalars $\iota_1 - \iota_3$ are advanced with the flow for the purposes of refinement and post-processing. The $x < 0$ part of the disk inlet is colored by $\iota_1 = 1$, the $x > 0$ part of the disk features $\iota_2 = 1$ and the initial domain is filled with $\iota_3 = 1$.

7.2.2 Numerical Grid Setup

We perform simulations in a cartesian adaptive grid using the AMRVAC detailed in section 3.1.2. Although a natural extension of the previous 2D studies would imply adoption of a cylindrical grid, the peculiarities in direction and resolution of an axial grid let us refrain from this option. With the adaptive mesh refinement in a cartesian domain, a uniform resolution for all regions of interest is obtained without the directional biases present in stretched grid simulations (e.g. Moll et al. 2008; Mignone et al. 2010), especially, a high resolution can be achieved also at the jet head which will prove necessary to resolve the helically displaced tip of the jet. The cartesian discretization and quadrantal symmetry introduces notable noise leading to a "pumping" of the $m = 4$ mode. We comment on the measures taken to analyze and circumvent the spurious modes further in section 7.3.2.

The largest domain size considered in the following extends over $x \in [-32, 32]$, $y \in [0, 128]$ and $z \in [-32, 32]$ in units of the inner disk radius. A base resolution of $48 \times 96 \times 48$ cells is chosen, adaptively refined by four additional grid levels

[3] See also the discussion in Appendix 3 of Ouyed et al. (2003).

(three for the smaller domain case). Thus 12 grid cells per inner disk radius are achieved, totaling in 240 cells across the entire jet inlet radius. To our knowledge this high resolution is unprecedented in 3D jet formation simulations. The effective resolution for the domain is $768 \times 1536 \times 768 = 9.06 \times 10^8$ cells and we observe a grid filling with roughly $\simeq 3 \times 10^8$ cells at the termination time. Refinement to the highest level is enforced for the disk inlet $r < r_{\rm out}; y < 1$ and for the region around the axis $x, z < 1; y < 10$ to resolve the steep gradients of the split monopole field. We use the passive tracers $\iota_1 + \iota_2$ for the coarsening strategy of the jet-less domain as described in section 3.1.2.

7.2.3 Perturbations

In order to investigate the behavior upon instability and to break the quandrantal symmetry of the grid, the initially axisymmetric setup needs to be distorted by non-axisymmetric perturbations. The physical origin of the perturbation can be easily be found in a non-axisymmetric evolution of the accretion disk, for example due to orbit of vortices and quasi-periodic oscillations (van der Klis et al. 1985), or in a non-homogenous external medium. In active galactic nuclei, the presence of such a medium within the central region is well established as the broad line region that is possibly comprised of clouds orbiting the black hole at high velocity ($\sim 0.1c$) (e.g. Davidson & Netzer 1979; Araudo et al. 2010) or in manifestation of a clumpy torus surrounding the accretion disk (e.g. Dullemond & van Bemmel 2005). The eventual collision of such clouds with a relativistic jet was already proposed by Blandford & Königl (1979) as a mechanism to explain transient features in compact radio sources. The scenario of jet-cloud collision is thus of interest not only in respect to jet stability, but also concerning the triggering of particle acceleration at the shock surface. We take the presence of a clumpy ambient medium as a motivation for our second setup of jet perturbations, where we model how the emerging jet funnels through such a density structure.

7.2.3.1 Mode Injection

To model non-axisymmetric features of the accretion disk, we employ perturbations to the rotation velocity $\omega + \Delta\omega$ following a mode decomposition. This method was already successfully applied by Rossi et al. (2008) and Mignone et al. (2010). In particular, we adopt

$$\Delta\omega(r,t) = \frac{\epsilon_\omega \omega_0(r)}{(m_{\rm max}+1)l_{\rm max}} \sum_{m=0}^{m_{\rm max}} \sum_{l=1}^{l_{\rm max}} \cos(m\phi + \omega(l)\omega_0(r)t + bl(l)) \tag{7.4}$$

to obtain modes up to $m_{\rm max} = 3$ with $l_{\rm max} = 8$ sub- and super-Keplerian frequencies $\omega(l) \in \{0.5, 1, 2, 3, 0.03, 0.06, 0.12, 0.25\}$ featuring a random phase offset $bl(l)$. The maximum amplitude of the perturbation is set to $\epsilon_\omega = 2\%$.

7.2.3.2 Clumpy medium

A static clumpy medium is modeled as density perturbation by prescribing the size spectrum in Fourier space and subsequent transformation of the random-phased Fourier coefficients to real space. To obtain a particular cloud size, the following spectrum is adopted:

$$f(k) = k_{\rm min}^{-s-1} \frac{s+1}{2s} \begin{cases} k^s & ; \quad k \geq k_{\rm min} \\ k_{\rm min}^s & ; \quad k < k_{\rm min} \end{cases} \tag{7.5}$$

where $k_{\rm min}$ relates to the cloud size λ and domain size via $\lambda = \max(\Delta x, \Delta y, \Delta z)/k_{\rm min}$. The highest frequency $k_{\rm max}$ is limited by the base-level resolution of the grid to $k_{\rm max} < 0.5 \min(\rm nx, ny, nz)$. We adopt a slope of the cloud size function $s = 5/3$ reminiscent of the power spectrum index of MHD turbulence. In the following, the maximal cloud density is set to $100\rho_0$.

7.3 Results and Discussion

We now describe the simulations performed and the analysis of non-axisymmetric features. The non-linear temporal and spatial evolution of angular modes is discussed and we show evidence for jet self-stabilization in the launching region.

7.3.1 Overview of the Simulations

The large simulations L3D and L3Dm described in the following were run under the HPC-Europa2 project on the JADE machine; for this purpose 150K cpu hours have been granted. The data to be analyzed amounts to 3TB and a single snapshot of the unstructured grid can demand up to 120GB of RAM. Analysis of such large quantities of data is made possible by employing the visualization cluster of the Max-Planck Society at the Rechenzentrum Garching. Table 7.1 summarizes our parameter runs and Figure 7.1 shows a rendering of our fiducial unperturbed solution.

Various flow quantities in the $x = 0$ plane are shown in Figure 7.2. The poloidal field lines tend to over-collimate and converge back towards the axis at $y \simeq 12$. This is also where a high temperature axial spine develops, while the high-σ disk wind itself is cold. The tendency of over-collimation is also observed as a transient feature in the axisymmetric simulations featuring a split-monopole flux distribution

Table 7.1 Parameter summary of the 3D simulations

ID	β	ϵ_ω	$r_{\rm out}$	λ	Domain	# levels	$T_{\rm end}$
L3D	0.01	0	20	-	$64 \times 128 \times 64$	5	168
L3Dm	0.01	0.02	20	-	$64 \times 128 \times 64$	5	168
M3D	0.01	0	10	-	$32 \times 64 \times 32$	4	103
M3Dd	0.01	0	10	16	$32 \times 64 \times 32$	4	189
M3Dmd	0.01	0.02	10	16	$32 \times 64 \times 32$	4	222

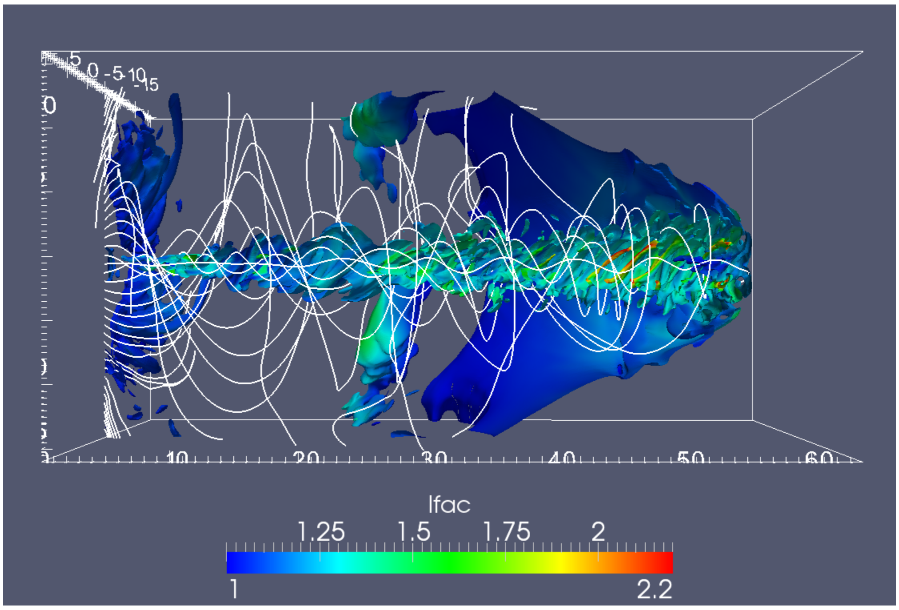

Figure 7.1 Rendering of the simulation, cut open pressure isocontour with magnetic field lines (run M3D).

described in chapter 4 (c.f. Figure 4.3). Hence we suspect that the over-collimation will vanish with longer simulation times. At this scale, the Lorentz factor of the disk wind is still moderate ($\Gamma < 1.5$), it rises above $\Gamma \simeq 2$ only in rare locations at the high pressure backbone. We note that at late times in the simulation, the imperfect treatment of the injection boundary might cause a numerical evacuation of the axial region accompanied with a high speed axial flow due to the effects described in section 7.2.1. We report results only before the spurious boundary effect propagates to the domain of interest. Unfortunately, this hinders us to follow the simulations for longer evolutionary time spans as would be needed to acquire a near-stationary state.

7.3.2 Mode Analysis

We now evaluate the impact of $m = 4$ pumping due to the quadrantal symmetry and quantify the growth of non-axisymmetric modes within the jet formation

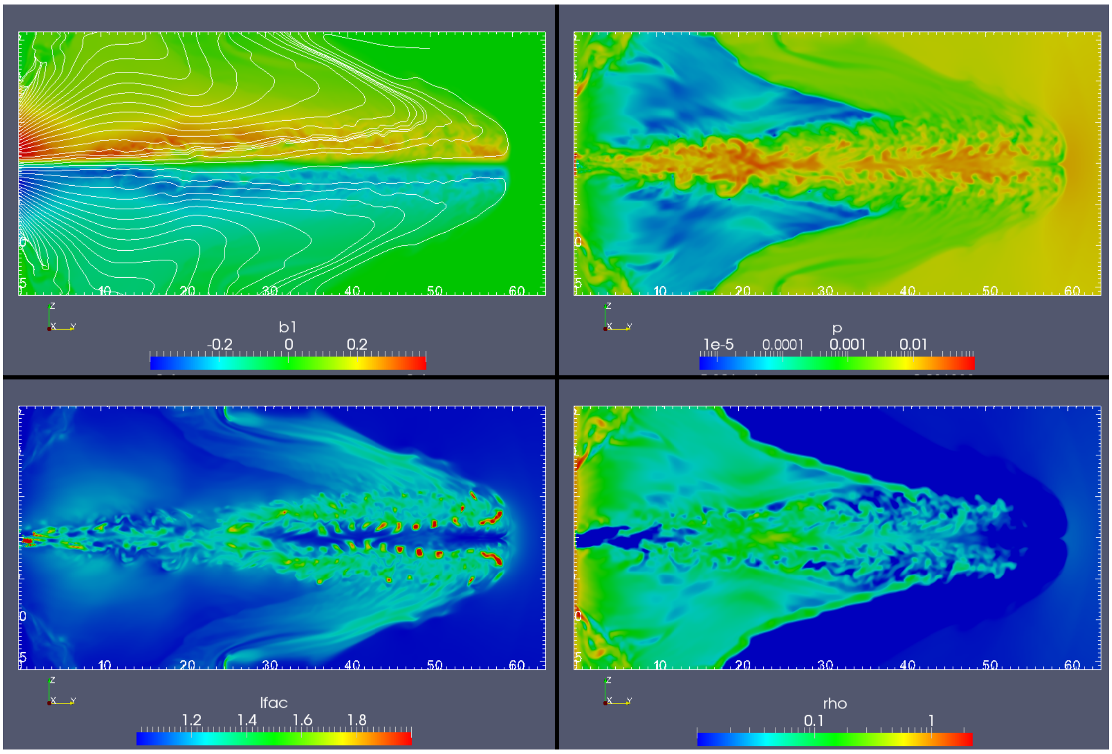

Figure 7.2 Simulation M3D at $t = 103$ $x = 0$. Shown are: (Toroidal) Magnetic field strength across the plane with field lines within the plane; thermal pressure; Lorentz factor and co-moving density.

region. To first give an impression of the azimuthal variations, a qualitative comparison of the unperturbed simulation L3D with run L3Dm is shown in slices of selected quantities across the jet in Figures 7.3 and 7.4. When no measure of perturbing the quadrantal symmetry is taken, we observe a strong favoritism of multiples of the $m = 4$ mode in all flow quantities. Higher order modes are most apparent in the density ρ and vertical current density j_y. In the mode injected slices on the other hand, we observe a slight dominance of the $m = 3$ mode.

To quantify the growth of non-axisymmetric modes within the jet, we calculate the fast Fourier transformation of the variables on the slice in cylindrical (r, ϕ) representation. For this purpose, we re-grid the unstructured slice data $x \in [-12, 12]$, $z \in [-12, 12]$ containing the jet spine using a uniform grid before transformation to the cylindrical coordinates $r \in [0, 12]$, $\phi \in [0, 2\pi]$. Thereafter, the Fourier-transformation of the (r, ϕ)-plane

$$\tilde{f}(n, m) = \frac{1}{N_r N_\phi} \sum_{n_r=0}^{N_r-1} \sum_{n_\phi=0}^{N_\phi-1} f(n_r, n_\phi) \exp\left(-2\pi i \left(m\frac{n_\phi}{N_\phi} + n\frac{n_r}{N_r}\right)\right) \tag{7.6}$$

is executed which yields the radial (n) and angular (m) Fourier amplitudes of the input scalar via $A(n, m) \equiv |\tilde{f}(m, n)|^2$. To quantify fluctuations of the angular part

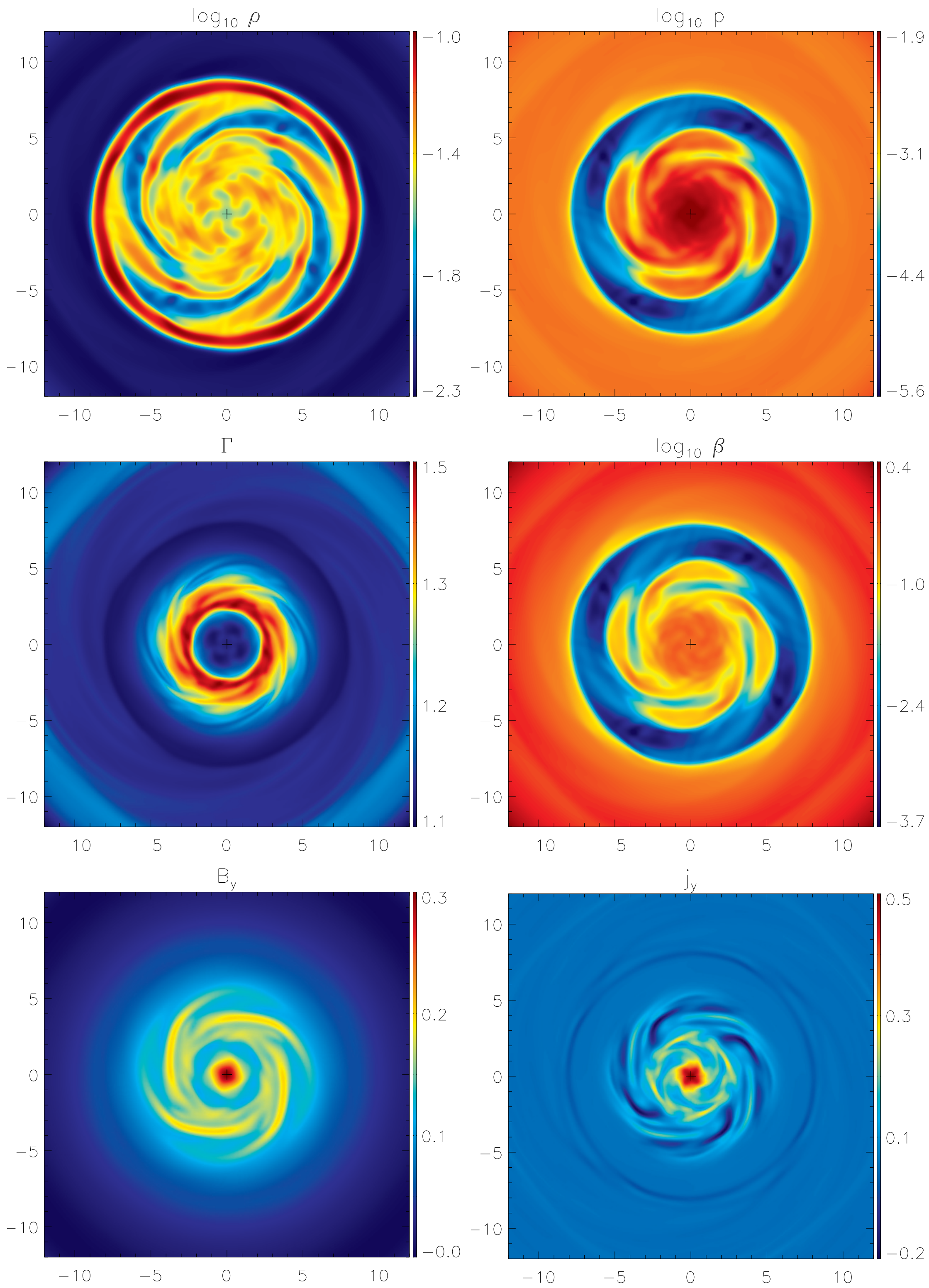

Figure 7.3 Two-dimensional slices in the $x - z$ plane at $y = 32$ for $t = 100$ in the unperturbed run L3d. The center is marked by “+″.

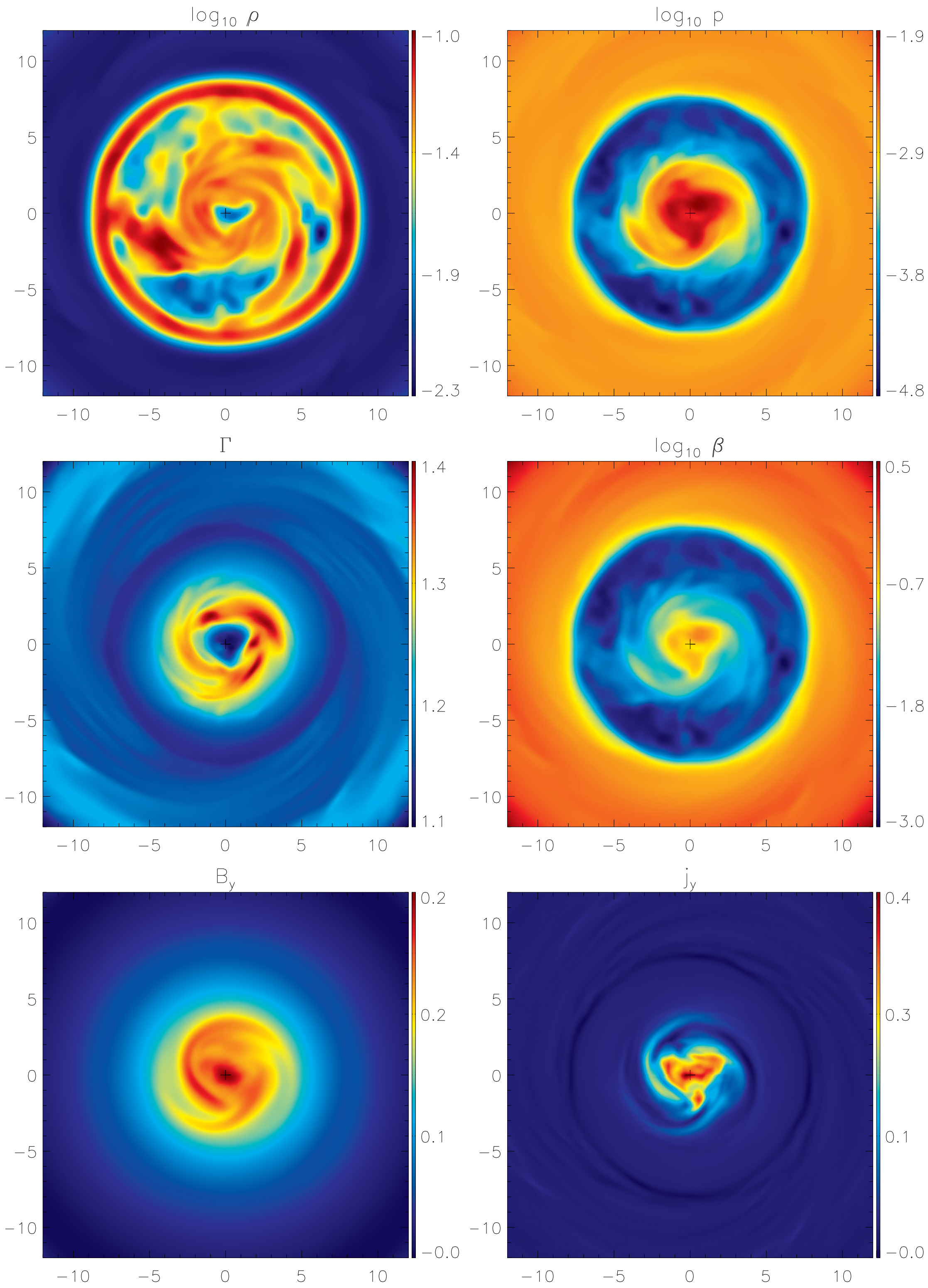

Figure 7.4 As Figure 7.3 but for the run featuring mode-injection.

alone, we define the normalized cumulative Fourier amplitudes

$$A(m) \equiv \frac{1}{|\tilde{f}(0,0)|^2} \sum_{n=0}^{N_n-1} |\tilde{f}(n,m)|^2 \tag{7.7}$$

which measures the fluctuations with angular frequency m in relation to the squared mean of the scalar f expressed by $|\tilde{f}(0,0)|^2$. The Fourier amplitude planes of the density fluctuations of Figure 7.3 and 7.4 are shown in Figure 7.5. The $m = 4$

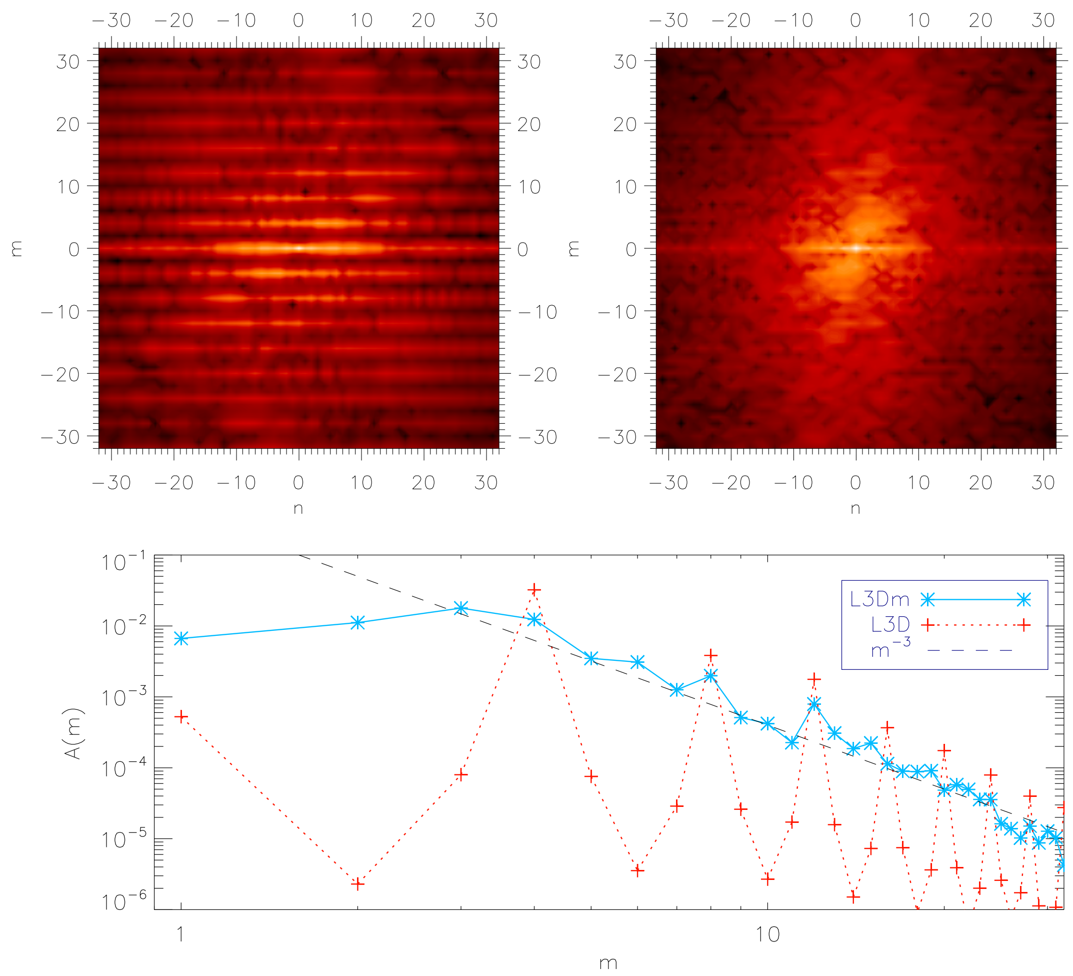

Figure 7.5 *Top:* Radial (n) and angular (m) Fourier amplitudes of density across $y = 32$ at $t = 100$ for the unperturbed case L3D *(left)* and for the perturbed case L3Dm *(right)* . *Bottom:* Cumulative modes for the two cases. To guide the eye, we show the empirical mode-decay following the power-law m^{-3}.

pollution of the unperturbed run is clearly visible, mode injection on the other hand can be used to get rid of this effect almost entirely as shown in the lower panel of Figure 7.5.

7.3.2.1 Temporal Evolution

To quantify the temporal growth of the modes, we calculate the Fourier amplitudes at the $y = 32$ slice in run L3Dm for various snapshots. At this altitude, the magnetic "backbone" B_y becomes distorted at $t > 80$ with dominating $m = 1$ and $m = 2$ modes, however the amplitudes grow no further. The evolution of the $A(m)$ function across the slices is shown in Figure 7.6. After an exponential rise where the growth time in $m = 1$ is shortest, followed by the $m = 4$ mode, the perturbations saturate at $t \simeq 80$ and subsequently fluctuate about a mean value. Mostly, the amplitudes are ordered according to $A(m) > A(m+1)$ although the $m = 2$ occasionally surpasses the $m = 1$ contribution. Also the motion of the jet barycenter oscillates, with an amplitude below 0.2 inner disk radii. For this analysis, a finer time-sampling would be desirable. This is however restricted by the disk-space limitations of the computational facilities.

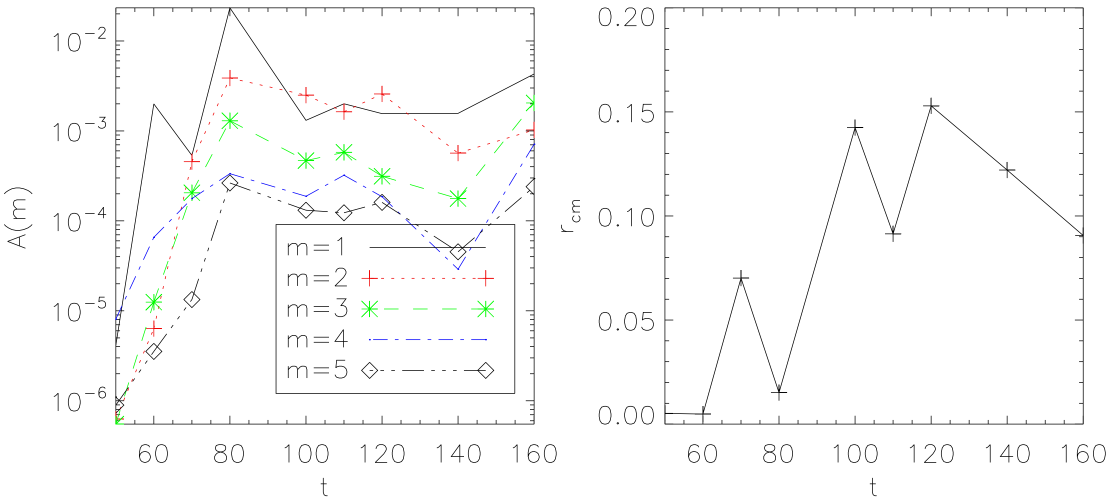

Figure 7.6 *Left:* Mode growth of B_y at $y = 32$ in simulation L3Dm. After initial exponential rise, the modes tend to saturate. Due to grid-noise, the $m = 4$ mode is initially comparable to the dominant $m = 1$ mode. *Right:* Barycenter motion on the $y = 32$ slice.

7.3.2.2 Spatial Evolution

The clearest indicator of the kink instability can be observed in the deflection of the jet barycenter. For this purpose we define the barycenter $\bar{r} = \sqrt{\bar{x}^2 + \bar{z}^2}$ of the quantity Q

$$\bar{x} \equiv \frac{\int x \; Q \; dx \; dz}{\int Q \; dx \; dz}; \qquad \bar{z} \equiv \frac{\int z \; Q \; dx \; dz}{\int Q \; dx \; dz} \tag{7.8}$$

in analogy with Mignone et al. (2010). For the density-displacement $r_{\rm cm}$, we define $Q_{\rm cm} = \chi \Gamma \rho$, where the tracer $\chi \equiv 1 - \iota_3$ picks out the jet contribution alone.

For the current displacement $r_{jy>0}$ we set $Q_{jy>0} = \chi j_y^+$ taking only the positive values of the current j_y^+. Finally, the motion of the magnetic flux is defined via $Q_{By>0} = \chi B_y^+$, taking into account only the positive flux B_y^+. Barycenter motion and mode population along the jet is shown in Figure 7.7 for run L3D and in Figure 7.8 for the mode-injected run L3Dm. Let's first focus on run L3D. The barycenter displacement is small compared to the inner disk radius and even tends to decrease along the jet. Only near the jet-head, a significant displacement can be observed. The modes are dominated by ubiquitous $m = 4$ noise, which seems to suppress all other fluctuations starting at height $y = 20$. The $m = 4$ dominance prevails all the way to the jet head.

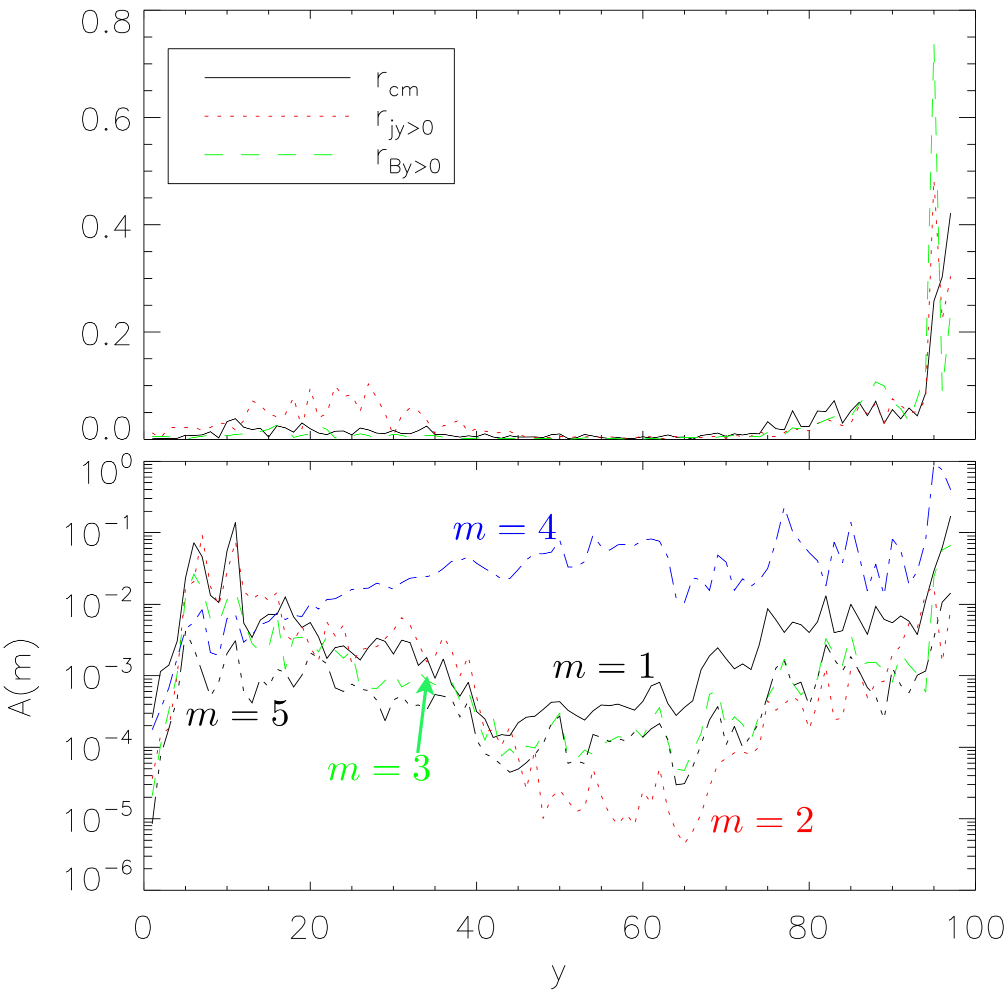

Figure 7.7 Barycenter displacements in units of inner disk radius and cumulative Fourier amplitudes of density ρ along the unperturbed jet L3D at time $t = 168$.

The behavior of run L3D is different, here, the kink mode surpasses the $m = 4$ at $y \simeq 10$. The angular fluctuations saturate around $y = 20$. Until $y = 60$, the displacements in current and magnetic flux stay roughly constant. This hints to a self-stabilization of the jet formation region. The kink mode starts to rise again towards the jet head, accompanied with a notable barycenter motion. We note that the magnetic field configuration near the jet head is strongly toroidally dominated as the magnetic flux necessarily reverses to connect to the initial split monopole field in front of the jet (see e.g. Figure 7.1). This toroidal dominance could yield an explanation for the strong growth of the kink mode at the jet head. To quantify

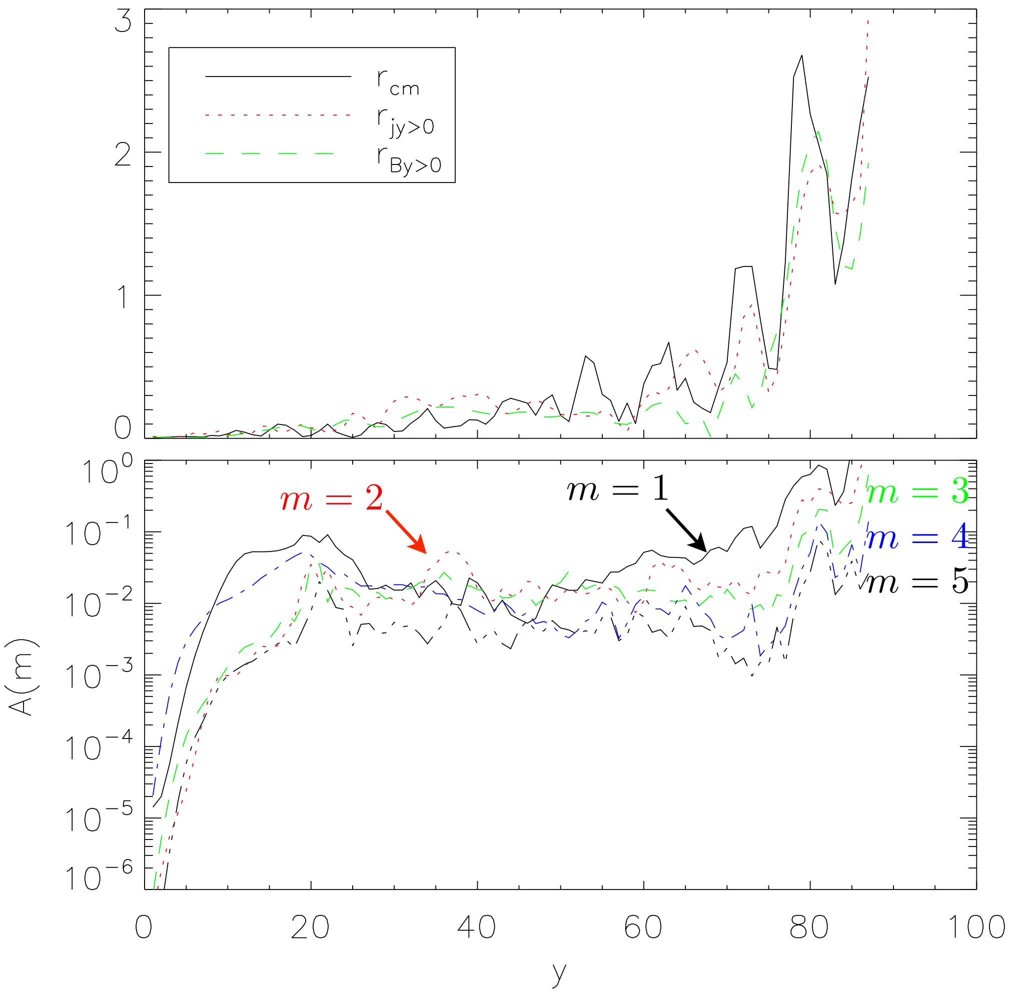

Figure 7.8 As Figure 7.7 but for run L3Dm at time $t = 160$.

this further, we introduce the co-moving magnetic pitch defined as

$$P \equiv -2\pi r \frac{B'_p}{B'_\phi} \tag{7.9}$$

which plays a major role in the stability of current carrying plasmas in the laboratory (e.g. Bateman 1978) and astrophysical jets (e.g. Appl et al. 2000; Lery et al. 2000). Small values of $P/r < 1$ and thus toroidally dominated configurations are particularly susceptible to the kink instability. The radius r and the fields B_ϕ, B_p involved in the definition of the pitch are well-defined however only in axisymmetry. For small perturbations from the cylindrical shape, we can re-orient the symmetry axis on the magnetic backbone at the position $(\bar{x}, \bar{z})$ and define effective values for $\bar{r}$, $B_{\bar{\phi}}$ and $B_{\bar{r}}$ with respect to the new origin. To define the magnetic backbone position using equations (7.8), we apply the kernel $Q_{\mathrm{BB}} = \chi B_y^2$ which reliably finds the peak of magnetic flux. Similarly, we can define an effective light surface via the comparison of the field strengths

$$x = \frac{E}{B_{\bar{p}}} \tag{7.10}$$

where $x = 1$ marks the light surface and $B_{\bar{p}} = \sqrt{B_{\bar{r}}^2 + B_y^2} \simeq B_y$ is the poloidal field strength with respect to the magnetic backbone. The co-moving fields are obtained by applying the standard Lorentz transformation rule (3.25). Since the jet is well collimated $B_y \gg B_{\bar{r}}$, the location of the backbone is in fact only of secondary importance for the definition of the light surface and we obtain similar results when considering only the vertical field B_y in Equation (7.10). We show the pitch profiles along the jet in combination with the light surface in Figure 7.9. To visualize the Lorentz force across the flow, we show force vectors of the electric field $\rho_e \mathbf{E} = \boldsymbol{\nabla} \cdot \mathbf{E}\ \mathbf{E}$ and of the current $\boldsymbol{\nabla} \times \mathbf{B} \times \mathbf{B}$ where we neglected the displacement-current for simplicity.

The three-fold structure of the light surface discussed in section 2.2.4 is recovered, however, the motion of the magnetic backbone induces a spiral pattern on the light surface such that inner and outer surfaces eventually merge. The magnetic backbone is markedly seen also in the pitch and we note that electric forces exhibit a de-collimating contribution at the central core while they tend to collimate near the outer light cylinder. As a general trend, we obtain a radially decreasing pitch profile from the backbone to is minimal value $P/r \lesssim 1$, from where the pitch increases again to the boundary of the jet. The regions of low pitch coincide with the locations of super-luminal field-line rotation and the stabilizing effect of electric forces becomes apparent as they tend to counter-act the magnetic contribution. The Fourier plane of the magnetic flux is shown in Figure 7.10. The modes are stunningly well described by a power-law and we find a filling of the low-order modes in according to m^{-3}.

7.3.3 Jet-Cloud interaction

We now study how the jet reacts to external perturbations exerted by a clumpy ambient medium. As the jet head funnels its way through the in-homogenous environment, also the upstream flow becomes deflected. Figure 7.11 shows a rendering of the simulation M3Dmd in comparison to M3D with field lines colored according to the magnetic pitch. The dense clouds represent a strong perturbation and we

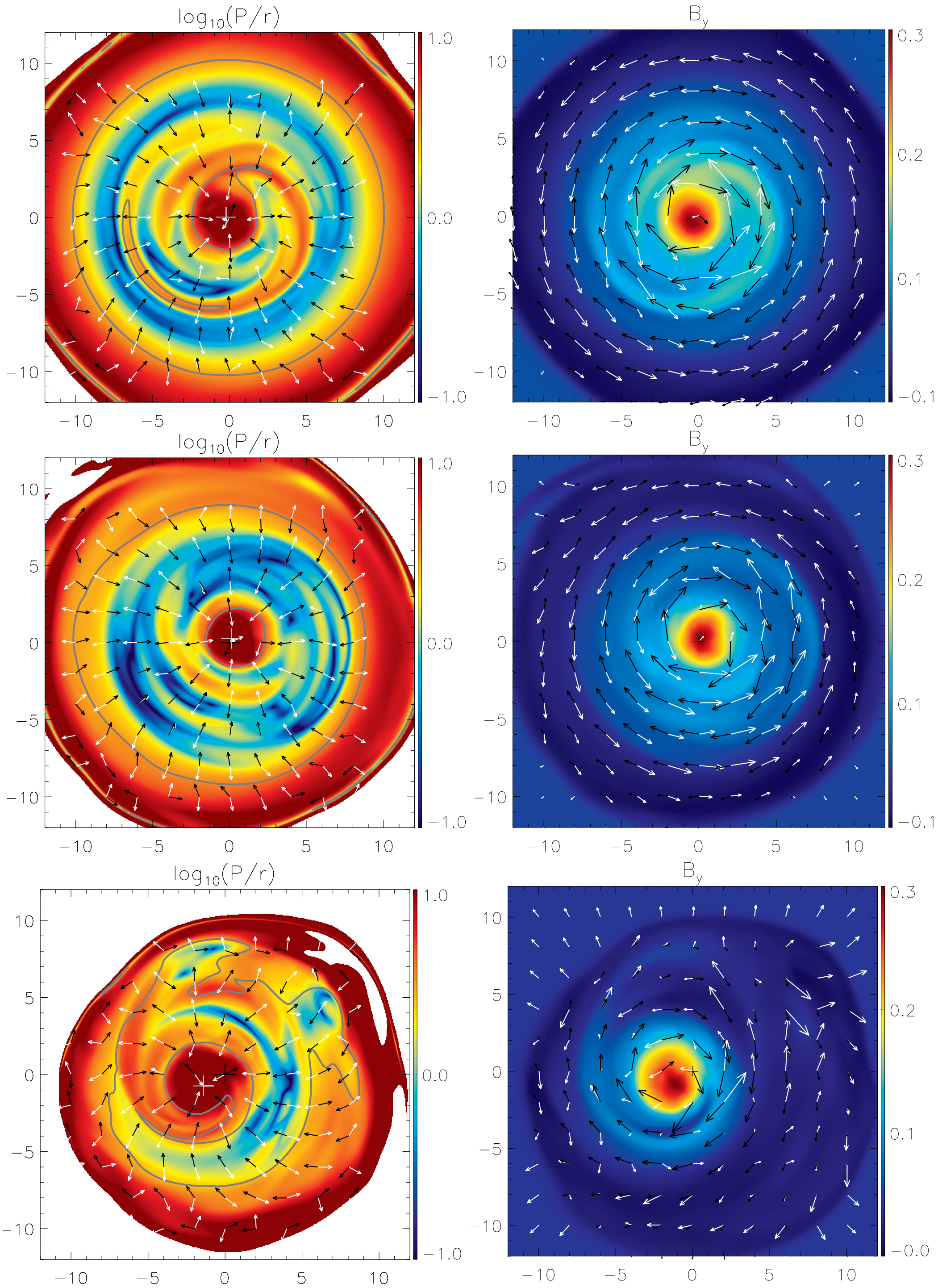

Figure 7.9 *Left:* Co-moving pitch and effective light surface with respect to the center of magnetic flux (shown as grey contours) through the surfaces $y \in \{60, 70, 80\}$ *(top to bottom)* for run L3Dm at $t = 160$. Black arrows indicate the direction of the electric force $\rho_e \mathbf{E}$ and white arrows show the direction of the Lorentz force $\nabla \times \mathbf{B} \times \mathbf{B}$. The axis is marked by a black "+" and the center of magnetic flux is shown as gray "+". *Right:* Corresponding magnetic flux B_y with velocity (white) and magnetic field vectors (black) in the plane.

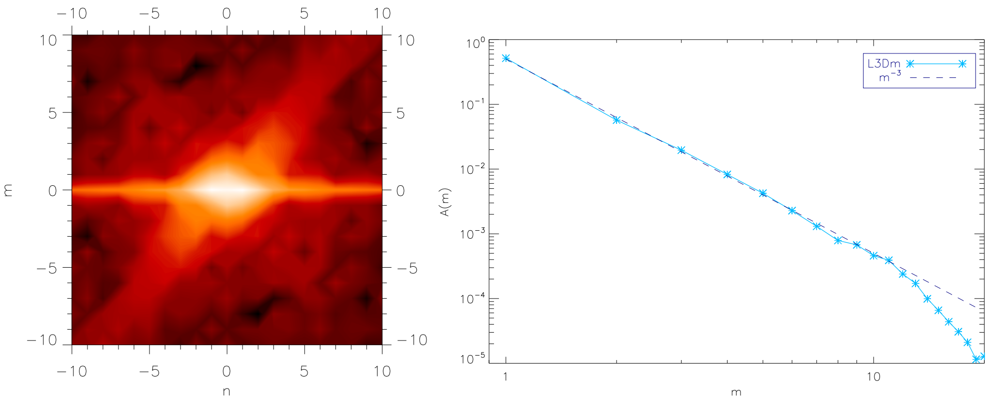

Figure 7.10 Fourier amplitudes corresponding to $B_y(y = 80, t = 160)$ in run L3Dm. Empirically, we find that the low-order modes are populated according to m^{-3}.

find the jet heavily distorted. Accordingly, the motion of the jet barycenter is increased and we find a strong dominance of the $m = 1$ mode along the whole jet (Figure 7.12). Due to the increased density of the external medium, the jet prop-

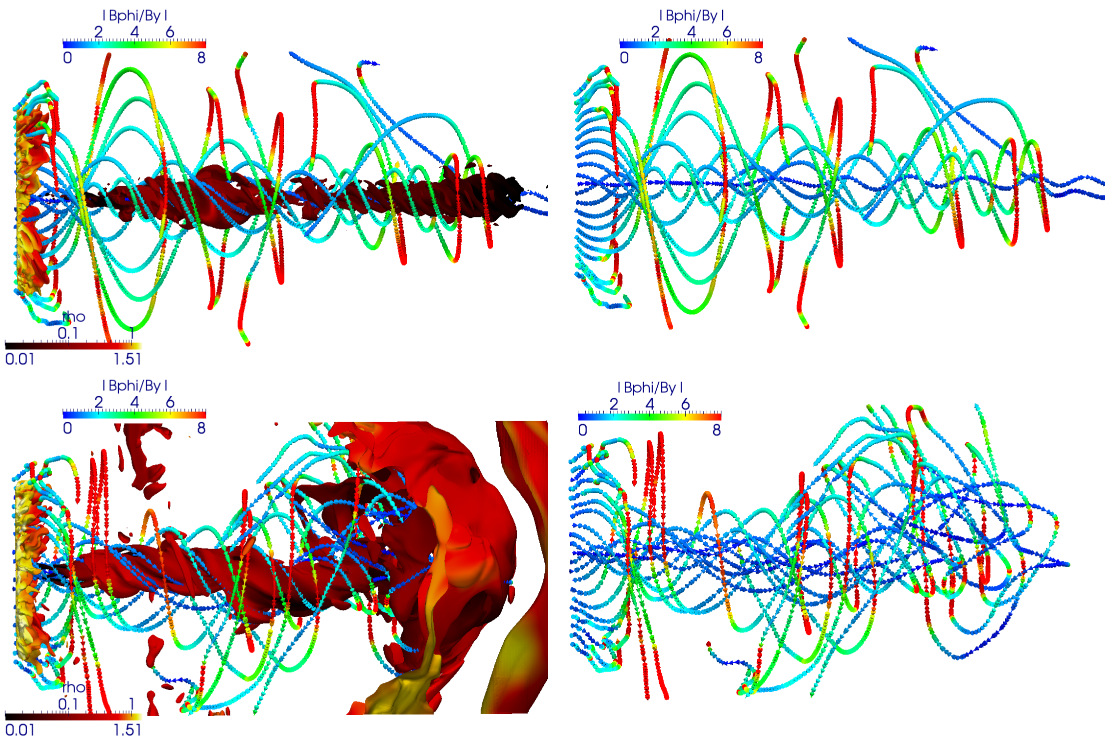

Figure 7.11 Field lines of the unperturbed *(top)* and perturbed *(bottom)* simulations at times $t = 103$ and $t = 194$, respectively. To guide the eye along the bent jet, pressure isocontours are added in the left-hand figures. The perturbed run shows a wider magnetic backbone and decreased toroidal field.

agation speed is reduced and the bow-shock is much wider (compare with Figure 7.1). We therefore compare the jet morphology between runs M3D and M3Dmd

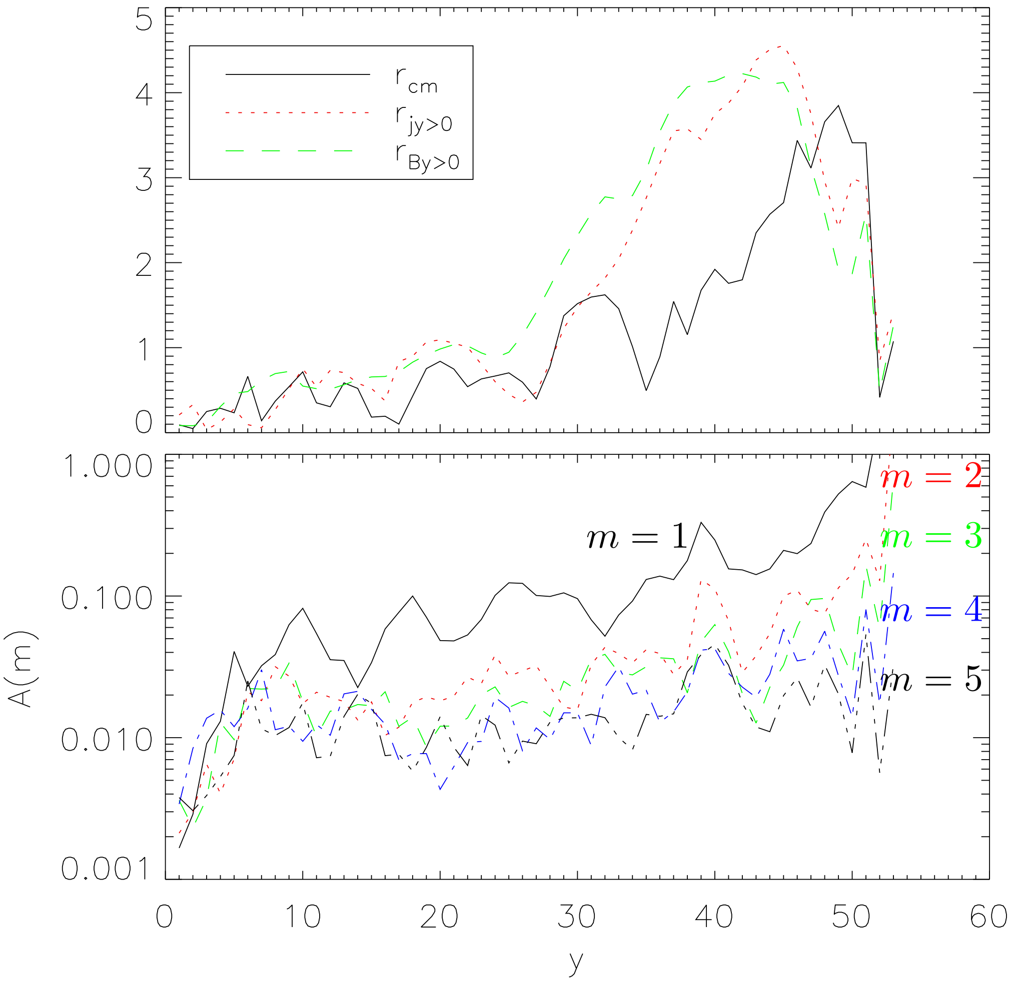

Figure 7.12 Barycenter motion and low order angular modes in density of simulation M3Dmd at $t = 194$.

at times of roughly equal jet propagation length. The precession of the magnetic backbone against the toroidal magnetic field direction tends to "smear" out the high-pitched axial region and the tightly would helix is effectively unwound. This represents an efficient mechanism of jet self-stabilization also noted by Ouyed et al. (2003). In their study the effect was described as follows: "The appearance of the $|m| = 1$ modes pumps energy into the poloidal magnetic field, causing the jet Alfvèn Mach number to fall below unity and stabilize the jet". From our simulations we come to a similar conclusion, in addition, we note that the "unwinding" of the helical field also decreases the field-line rotation Ω and thus also the influence of electric fields. We show the increase in magnetic pitch compared to simulation L3D is shown in Figure 7.13. Regions of low pitch are reduced to a thin sheet where the effective light cylinder is found. In this regime, electric stabilization can not be of importance since the typical value of the light-cylinder x is only of order unity or below.

The instability leads to cascade of energy to smaller scales and thus a population of high order modes of the thermal energy density. The violent jet motion triggered by the kink instability could thus seed turbulence within the jet medium. This could facilitate turbulent particle acceleration and should be focus of future studies.

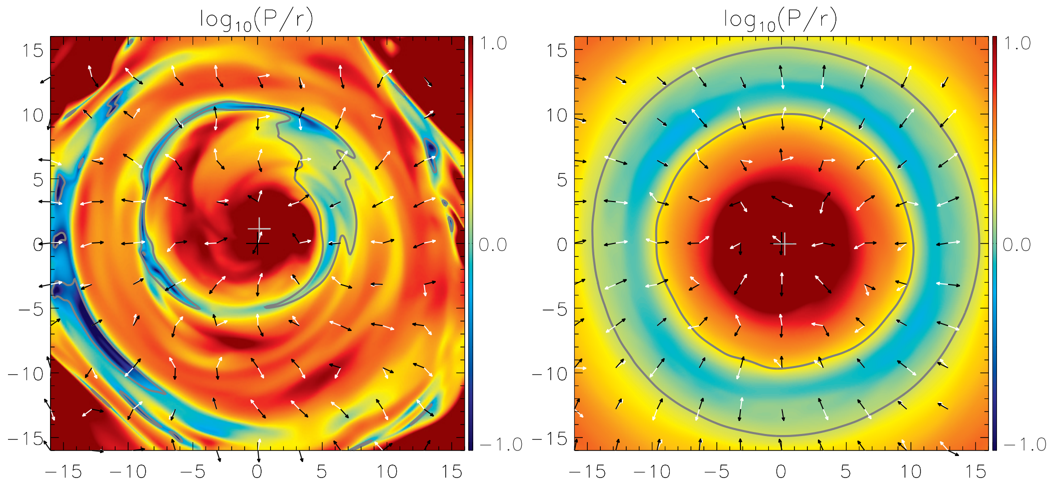

Figure 7.13 As in Figure 7.9; comparison of the pitch at $y = 32$ in runs M3Dmd *(left)* and L3Dm *(right)* at times $t = 194$ respectively $t = 160$. The motion of the backbone in the heavily perturbed simulation increases the poloidal field on account of the toroidal field.

7.4 Summary and Conclusions

We have presented first results of high-resolution 3D simulations of relativistic jet formation from magnetospheres in Keplerian rotation. When the flow is perturbed by non-axisymmetric internal perturbations of the accretion disk corona, the modes first grow exponentially at the base, approach saturation along the jet and grow again towards the jet head. The $m = 1$ kink is the dominant mode of departure from axisymmetry. At a given height above the accretion disk, the temporal evolution of the modes was considered. Also here we find a saturation of perturbations before a notable dissipation or even disruption is encountered. As an aside, we also performed simulations where the only measure of perturbation is the ubiquitous discretization noise of the grid. In result, the modes are dominated by multiples of $m = 4$ which grow along the flow on account of other modes and we observe virtually no motion of the jet barycenter.

To further investigate the stability of the jet structure, we considered the co-moving magnetic pitch. As in the axisymmetric case, a stabilizing backbone of high pitch $P \gg 1$ develops, surrounded by an intermediate, toroidally dominated region $P < 1$ and an outer high-pitch region at the border of the jet. The locations of super-luminal field line rotation (the light surface) approximately coincide with the low-pitch region. Forces due to the electric field $\rho_e\mathbf{E}$ oppose the classical magnetic Lorentz force $\boldsymbol{\nabla} \times \mathbf{B} \times \mathbf{B}$ which could thus add to jet stabilization in the relativistic case. Near the jet-head, we find that the squared Fourier amplitudes of low order modes are populated according to m^{-3} which yields $m^{-3/2}$ for the power-spectra. It is currently unclear how this result can be reconciled with theory of MHD turbulence on the one side and the growth-rates of the unstable modes on the other side.

In order to study external perturbations, we initialized the domain with a static clumpy ambient medium following a power-law spectrum in Fourier space. While this should not be mistaken for a fully developed MHD-turbulent medium, it allows us to investigate perturbations "external" to the jet as a general scenario. The amplitude in cloud density was chosen as 100 which thus represent a strong perturbation to the jet.

In result, the jet funnels its way through the path of least resistance which leads to large departures of the barycenter from the axis and dominating $m = 1$ modes. When compared to the unperturbed case, the magnetic pitch is largely increased which can be interpreted as a mechanism of jet self-stabilization. Due to the precession of the magnetic backbone against the toroidal magnetic field direction, the helical structure tends to be "unwound" leading to an increase of poloidal field which also reduces the amount of field-line rotation. The external perturbation and accompanying motion of the magnetic backbone also gives rise to filamentary small-scale structure, reminiscent of turbulence. The accompanying dissipation could facilitate turbulent particle acceleration within the jet. Further investigation with high-resolution 3D simulations is needed to fully quantify this effect.

Chapter 8

Conclusions and Outlook

In this thesis, models of relativistic jet formation are developed by means of special relativistic MHD simulations. In order to confront the simulations with existing high resolution radio observations and to make predictions for upcoming (sub-) mm wavelength studies of active galactic nuclei, the relativistically beamed synchrotron radiation transport is conducted in the dynamical models. Thus dynamically consistent intensity maps and spectra of the self-absorbed radio core are obtained and signatures of the helical magnetic field are derived in linear polarization and Faraday rotation.

We now summarize our main conclusions, further results are noted in the corresponding sections of the individual chapters.

Summary of Main Conclusions

In chapter 4, mildly relativistic jets from hot accretion disk coronae are obtained. To provide a realistic inflow boundary in dynamical equilibrium, a central point-mass gravity is added as a source term to the equations of RMHD. Therefore, the flow is allowed to consistently transcend all critical points within in the simulation domain. To facilitate this study, the disk corona boundary is provided causally consistent with the sub-magnetosonic nature of the inflow and a current-free outflow boundary is developed which allows a detailed study of the delicate jet self-collimation process. Some key results are:

- The disk winds are heavily mass-loaded and sub-equipartition between the electromagnetic energy and the kinetic energy prevails already at the base of the flow. However, the flow originating at the inner part of the accretion disk traverses the light-cylinder whose shape is self-consistently obtained by the simulations.

- Flows with initial paraboloidal and split-monopole field configurations collimate well with mass-weighted opening angles of $3° - 7°$ where the largest change of the field-line opening angle is acquired already before traversing the light surface.
- In the region beyond the light-cylinder, an intricate balance of electrodynamic forces is acquired across the field with the electric lab-frame charge separation force balancing the traditional Lorentz force almost entirely.

These disk jets could potentially provide collimating agents for inner ultra-relativistic jets possibly launched by the Blandford-Znajek mechanism.

To also cover the regime of highly relativistic jets, in chapter 5, Poynting dominated flows of various pre-described electric current distributions at the injection boundary are considered. The flow acceleration is followed for more than 3000 Schwarzschild radii allowing to obtain Lorentz factors of $\Gamma \simeq 8$ within the simulation domain. By providing outflow boundaries out of causal contact with the jet, again pure MHD self-collimating solutions are obtained. To list some key results:

- The relativistic flow becomes highly collimated with half-opening angles of the fast component $< 0.3°$.
- Michel's scaling of the Lorentz factor at the fast magnetosonic point $\Gamma \propto \mu^{1/3}$ is verified within 5% and the initial acceleration proceeds in the linear regime according to $\Gamma \propto r$.
- Scaled to a $10^9 M_\odot$ black hole, the simulations extend to 0.3pc where we find the flow still dominated by Poynting flux.
- Within the scales under our consideration, the electric current distribution at the jet base has little influence on the jet collimation.

The obtained jets maintain causal connection throughout the whole outflow evolution and are thus potentially susceptible to global jet instabilities.

In chapter 6, the dynamical simulations are applied to perform synthetic observations of synchrotron radiation from the core jet. For this purpose, a synchrotron transport code was developed that takes into account the Stokes-parameters I,Q,U of linear polarization, relativistic beaming, self-absorption and Faraday rotation. While the intensity maps of the synthetic observations bear the uncertainty of the particle distribution which can only be modeled post-hoc, the polarization structure is largely independent of the particular choice for non-thermal particle tracer. The standard diagnostics of radio observations can be applied to the near-stationary model-jets and predictions for high resolution interferometric observations of nearby AGN are made. To list the key results of the polarization:

- Depending on the viewing angle and the pitch of the emitting region, the helical fields of the jet formation site give rise to spine and sheath polarization structures observed in some AGN.
- Asymmetries found in polarization and spectral index hint to the handedness of the magnetic helix and thus reveal the sense of rotation of the central engine.
- The unresolved polarization direction of the core depends on the inclination: for small viewing angles (blazar case) the dominating polarization direction of the electric field (EVPA) is oriented perpendicular to the jet direction, while for larger inclinations $i > 30°$, the EVPA is directed along the jet.

As a further diagnostic of the field geometry, also the rotation measures (RM) across jets is considered. Since the core-RM can attain values as high as $10^6 \mathrm{rad/m^2}$, mm-wavelength observations are needed to unambiguously detect λ^2-law rotation measures in AGN core jets. The key results of the rotation measure study are:

- When the Faraday rotation occurs within the emitting region of the core, consistent λ^2-law rotation measures can only be detected in a small window of frequencies where the rotation angle is below $\sim 45°$ but still above the detection limit.
- Starting at a resolution of two beam-radii across the jet, RM gradients can be detected as monotonous profiles.
- The intrinsic profile of the RM across the core-jet is non-monotonous and a resolution of $\sim 100 r_{\mathrm{S}}$ is required to observe its non-monotonous run.

In chapter 7, we have considered the three-dimensional structure of the jet launching region by means of high resolution adaptive mesh refinement simulations. If the jet is perturbed by small internal perturbations exerted on the field line foot-points, the non-axisymmetric modes saturate quickly along the flow and rise only towards the jet-head. Here, the $m = 1$ kink is the dominant non-axisymmetric mode. Conversely, no significant additional dissipation of magnetic energy is observed in the stable jet-base. The electric fields tend to oppose the classical magnetic Lorentz force which thus add to the stabilization of relativistic jets. We also considered external perturbations to the emerging jet exerted by a clumpy ambient medium. The jet reacts to strong external perturbations by developing a wider magnetic backbone of increased pitch. This “unwinding” of the helical field-structure also leads to a decreased field-line rotation and the influence of electric fields is therefore reduced. The strong external perturbations lead to a filamentary flow structure and the development of current sheets within the jet. This could give rise to non-thermal particle acceleration as required by the synchrotron process.

Outlook

Within this thesis, dynamical MHD models of relativistic jets in conjunction with post-hoc synchrotron transport calculations are developed. Given the wealth of physics at play in natures fascinating realization of relativistic jets, the presented study can only provide a humble starting point for future research. To be the first to criticize our own work, let us mention the most important elements that deserve improving and outline how further progress can be achieved.

A key issue of jet formation is the mass-loading of the flow. This determines the final Lorentz factor to be attained and the scale of acceleration itself. One attempt to solve this problem without taking the entire disk into account is to launch the flow sub-sonically; this is followed in chapter 4. In result, heavily mass-loaded disk-jets could be obtained which alas can not serve as models for highly relativistic jets observed in AGN. The mass-loading issue is circumvented in the subsequent chapter where the energy fluxes effectively enter as a modeling parameter. Consequently, dynamical models in the regime of extragalactic jets are obtained and the observational signatures of the models are further discussed in chapter 6. The interesting question which now comes to mind is: *what determines the mass-loading of the jet?* To answer this question satisfactory requires to take the evolution of the accretion disk into account. While the physics of accretion disks itself is an active field of research with numerous unanswered questions, progress can be made in two ways: Either a thin accretion disk is treated by means of a mean-field resistivity as customary in the context of young stellar objects (YSO), or a turbulent disk susceptible to the magneto-rotational instability (MRI) is considered where the resistivity follows naturally form the turbulent stresses.

We note here that relativistic effects are presumably less important at the very base of the *disk jet*, such that we do not expect substantial differences in mass-loading between the non-relativistic thin disk case as in YSOs and the fully relativistic treatment of resistivity and viscosity as needed for the application to AGN or $\mu-$quasars. However, a consistent study of such magnetized accretion-ejection structures in the relativistic case is still missing and would allow a systematic investigation of the outflow in dependence of the disk parameters. This will certainly contribute to our understanding of the jet phenomenon. Such direct insight is not as easily obtained in MRI turbulent disks where no obvious "steering parameters" exert control over the simulation. In this case however, the widespread mass-loading of the tentative Blandford-Znajek jet with ad-hoc created pair plasma (by means of a density floor value) leaves an opportunity of improvement. Future investigations in this field should therefore address the issues of pair- and baryon-loading of the jet.

In our approach, only the Blandford-Payne (BP) type disk jets could be considered, leaving the Blandford-Znajek (BZ) jets that emerge in the black holes ergosphere untouched. Naturally, for a thorough investigation of the BZ process, a general relativistic treatment in the Kerr-metric is inevitable. Within the last years, several authors already presented results of general relativistic magnetohydrodynamic (GRMHD) simulations showing jets created by the BZ process, however, the results could so far not be reproduced due to the unavailability of advanced GRMHD codes. With the recent publication of the HARM2D simulation code originally developed by Gammie et al. (2003)[1], this situation changed - allowing anyone to reproduce and refine present GRMHD models. The burning questions in this field are connected to the influence and evolution of black hole spin leading to the well known "spin paradigm" discussed already in the introduction of this thesis. Also a consistent dynamical treatment of thin-disk accretion in GRMHD is still missing completely, which would provide a valuable counterweight to the existing approaches. As discussed earlier, progress in this direction is mostly hampered by the increased resolution requirements of thin disks, this technical problem however is likely to be solved within the next years.

Another important issue is connected to the treatment of non-thermal particles in the jet. With little additional effort, the simple post-hoc modeling that we have adopted can be augmented by considering cooling due to adiabatic and radiation losses. A major challenge however is to answer the fundamental question: *how are particles accelerated in jets?* The subject of astrophysical particle acceleration at shocks (via Fermi I/II processes) or due to dissipating current sheets is in itself a very active field of research and no adequate recipes suitable for post-hoc particle modeling are to be expected in the near future. Some progress can be made by the inclusion of passive tracer particles to an MHD flow (via "particle movers") or by adopting a two-fluid formulation. For a fully consistent treatment however, the fluid approximation ultimately has to be relaxed in favor of a kinetic approach. Despite ever increasing computational capabilities, global kinetic simulations of relativistic jets are not likely to become feasible in the foreseeable future due to the demand of resolving a multitude of scales, starting at the electron gyro-radius. In the meantime, re-simulations of small regions of interest, either to improve the resolution or to adopt a more realistic (e.g. kinetic) treatment could lead to further progress. This is a common approach followed in other fields of astrophysics where

[1] http://rainman.astro.illinois.edu/codelib/

a large disparity in scales is involved, for example in cosmology, solar physics or accretion disk research (in the form of “shearing boxes”).

To extend the existing radiation modeling, the next logical step is to focus on non-axisymmetric effects as obtained for example in the 3D simulations of the last chapter. Of equal importance is the modeling of radiation from time-dependent processes. These can be found in the form of superluminal knots ejected from the jet formation site or via the evolution of 3D jet instabilities. Also dynamical scenarios leading to intra-day variability could be explored. For a consistent treatment of time-dependent effects, time-dilation needs to be implemented to the transport code which can be done in a straight-forward way. To complete the non-thermal spectrum of jets, including inverse Compton radiation in the radiation modeling would also be desirable. Since this is obtained by a scattering process, an extension of the existing treatment is however a non-trivial task.

An interesting class of objects has been left largely unexplored by us: the X-ray binaries also known as $\mu-$quasars. Harnessing the scale-free nature of the MHD approach, our dynamical models can equally well be applied to the “steady jets” of these galactic sources. We note however that the electron gyro-frequency in the strong magnetic field environments of stellar mass black holes can surpass the GHz radio frequency, such that plasma refraction is likely to play a role in the radiation transport (see section 1.3.2). This effect could safely be neglected in the AGN case that we have considered here. Due to the increased time-resolution of processes around stellar mass black holes, the focus in the modeling of $\mu-$quasars should be set on time-dependent state transitions of the accretion flow and the accompanying development of jets.

The experiences on jet formation gained in this work can be capitalized in many ways. For example, the obtained jet solutions can serve to replace the ad-hoc assumptions on the jet inlet customarily adopted in present Kpc scale jet propagation simulations that investigate the feedback between jet and galactic medium. Preliminary work in this direction has already been carried out by us. A technical obstacle on this path however is the difficulty to connect the magnetic flux of the jet solution divergence free to a realistic ambient galactic field. In particular, how and when the magnetic field lines close on themselves needs to be considered. A more promising approach would be to directly simulate from the launching site to the scale where jet-environment interactions become important for the dynamics of the flow. As discussed in section 5.1, this is likely to comprise five orders of magnitude in radial scale which poses a challenge for dynamical simulations. However, by employing adaptive mesh-refinement techniques, the challenge can be mastered, at least within the axisymmetric approximation.

Finally, fully three-dimensional simulations of the jet formation site as presented in chapter 7 promise great insights into the conditions in the heart of AGN. Via the "disk as boundary" treatment, a systematic study of jet stability in the trans-Alfvénic region of the accelerating jet can be conducted. Such a coherent analysis of the non-linear evolution of relativistic jet stability is still missing and is under way. Also realistic scenarios such as the collision of a jet with individual broad-line region clouds (reminiscent of the "lighthouse model") can be studied by means of dynamical simulations. To this end, we have performed preliminary simulations that need to be analyzed further. An other prospect of 3D simulations is to answer how robust the jet formation paradigm is upon departure from axisymmetry. This could give insights into jet formation in X-ray binaries ($\mu-$quasars) and shed light on extreme conditions as present for example in cataclysmic variables. Such a study would allow to develop dynamically consistent models of strongly perturbed, e.g. precessing jets.

All that is done throughout this thesis and proposed in this final chapter might help to catch a glimpse of the captivating phenomenon of relativistic jets. But certainly, jets will continue to fascinate and puzzle astrophysicists for years to come!

Appendix A

Appendix 1

A.1 Most General State of Polarization

Considering a plane-wave solution of Maxwell‘s equations in vacuum with arbitrary (elliptic) polarization. The electric vector may be represented by

$$\mathbf{E} = \mathfrak{Re}\left[E_l \mathbf{l} + E_r \mathbf{r}\right] \tag{A.1}$$

where the direction of propagation is given by $\mathbf{n} = \mathbf{r} \times \mathbf{l}$ and $E_l = a_l e^{-i\epsilon_1} e^{-ikz+i\omega t}$, $E_r = a_r e^{-i\epsilon_2} e^{-ikz+i\omega t}$ are the complex oscillating functions of a wave solution with positive amplitudes a_l, a_r and phases ϵ_1, ϵ_2. The four Stokes parameters are customarily defined by

$$I = E_l E_l^* + E_r E_r^* \tag{A.2}$$
$$Q = E_l E_l^* - E_r E_r^* \tag{A.3}$$
$$U = E_l E_r^* + E_r E_l^* \tag{A.4}$$
$$V = i\left(E_l E_r^* + E_r E_l^*\right). \tag{A.5}$$

In this convention, the first parameter can directly be identified with the intensity I. Q and U describe the orientation of the ellipse and V parametrizes its semi-major axis. $V = -I$ gives left-handed circular light while $V = +I$ corresponds to right-handed circular light. In the geometric representation

$$\mathbf{E} = a\mathbf{p}\cos\beta\sin(\omega t - kz + \alpha) + a\mathbf{q}\sin\beta\cos(\omega t - kz + \alpha) \tag{A.6}$$

the Stokes parameters read

$$I = a^2 \tag{A.7}$$
$$Q = a^2\cos 2\beta\ \cos 2\chi \tag{A.8}$$
$$U = a^2\cos 2\beta\ \sin 2\chi \tag{A.9}$$
$$V = a^2\sin 2\beta \tag{A.10}$$

indtroducing the inclination angle χ as

$$\tan(\epsilon_1 - \epsilon_2) = \frac{\tan 2\beta}{\sin 2\chi}. \tag{A.11}$$

$\chi \in (-\pi/4, \pi/4]$ is measured in the clockwise direction from **l** respectively **r** depending on the quadrant where the vector of polarization **p** is found (see Figure A.1). It is important to keep this ambiguity in mind when reproducing **p** from the Stokes parameters.

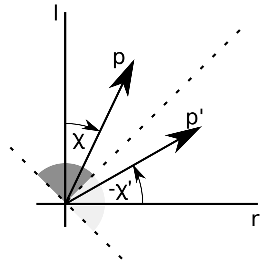

Figure A.1 On the definition of the angle χ.

For the transport of linearly polarized light, it is convenient to work in the parameters $\{I_l = E_l E_l^*,\ I_r = E_r E_r^*,\ U_{lr}\}$ leaving three independent quantities

$$\begin{aligned} I &= I^l + I^r && \text{(A.12)}\\ Q &= I^l - I^r && \text{(A.13)}\\ U^{lr} &= \left(I^l - I^r\right)\tan 2\chi && \text{(A.14)} \end{aligned}$$

since $V = 0$ for purely linear light. As **p** rotates around the half-circle, $\tan 2\chi$ experiences four sign-changes, while U^{lr} shows only two (see also: van de Hulst 1957).

A.2 Synchotron Radiation

The emissivities and absorption coefficients for synchrotron radiation are customarily derived in the comoving (dashed) system. For an isotropic powerlaw distribution of relativistic electrons $dn_{\rm rel} = N_0 E_e^{-2\alpha-1} dE_e$ for $E_l \le E \le E_u$ of number density

$$n_{\rm rel} = \frac{N_0}{2\alpha}\left(m_e \Gamma_l c^2\right)^{-2\alpha}\left[1 - \left(\frac{\Gamma_u}{\Gamma_l}\right)^{-2\alpha}\right] \tag{A.15}$$

($\alpha > 0$), one finds for the emission and absorption coefficients

$$\begin{aligned} \epsilon_{\nu'}^{\prime(e,b)} &= \frac{1}{2} c_5(\alpha) N_0 (B' \sin\vartheta')^{\alpha+1}\left(\frac{\nu'}{2c_1}\right)^{-\alpha}\left[1 \pm \frac{2\alpha+2}{2\alpha+10/3}\right] && \text{(A.16)}\\ \kappa_{\nu'}^{\prime(e,b)} &= c_6(\alpha) N_0 \left(B' \sin\vartheta'\right)^{\alpha+3/2}\left(\frac{\nu'}{2c_1}\right)^{-\alpha-5/2}\left[1 \pm \frac{2\alpha+3}{2\alpha+13/3}\right] && \text{(A.17)} \end{aligned}$$

depending on the constants

$$c_1 = \frac{3e}{4\pi m^3 c^5} = 6.27 \times 10^{18} \quad \mathrm{cm}^{-7/2}\mathrm{g}^{-5/2}\mathrm{s}^4 \tag{A.18}$$

$$c_3 = \frac{\sqrt{3}}{4\pi}\frac{e^3}{mc^2} = 1.87 \times 10^{-23} \quad \mathrm{cm}^{5/2}\mathrm{g}^{1/2}\mathrm{s}^{-1} \tag{A.19}$$

$$c_5(\alpha) = \frac{1}{4}c_3\Gamma\left(\frac{6\alpha+2}{12}\right)\Gamma\left(\frac{6\alpha+10}{12}\right)\Gamma\left(\frac{2\alpha+10/3}{2\alpha+2}\right) \tag{A.20}$$

$$\to 1.37 \times 10^{-23}\mathrm{cm}^{5/2}\mathrm{g}^{1/2}\mathrm{s}^{-1} \ (\alpha \to 0.5) \tag{A.21}$$

$$c_6(\alpha) = \frac{1}{32}\left(\frac{c}{c_1}\right)^2 c_3\,(2\alpha + 13/3)\,\Gamma\left(\frac{6\alpha+5}{12}\right)\Gamma\left(\frac{6\alpha+13}{12}\right) \tag{A.22}$$

$$\to 8.61 \times 10^{-41}\mathrm{cm}^{5/2}\mathrm{g}^{1/2}\mathrm{s}^{-1} \ (\alpha \to 0.5) \tag{A.23}$$

in Gauss cgs units where $\Gamma(\cdot)$ denotes the Gamma-function (Pacholczyk 1970b). The upper sign corresponds to the direction of the main polarization axis ($\hat{\mathbf{e}}'$).

A.2.1 Polarization of Synchrotron Radiation

For synchrotron radiation of a moving source, the direction of polarization depends on the two factors:

1. The electric field vector of the photon in the co-moving system of emission $\hat{\mathbf{e}}' = \hat{\mathbf{n}}' \times \hat{\mathbf{B}}'$ is perpendicular to the local magnetic field and the line-of-sight. The corresponding magnetic field of the photon is given by $\hat{\mathbf{b}}' = \hat{\mathbf{n}}' \times \hat{\mathbf{e}}'$.

2. Relativistic aberration adds a velocity-dependent "swing" to the orientation (Blandford & Königl 1979), satisfying $\hat{\mathbf{n}} = \hat{\mathbf{e}} \times \hat{\mathbf{b}}$ also in the observers system. This results a different transformation behavior for $\hat{\mathbf{b}}$ and $\hat{\mathbf{B}}$.

Due to the various orientations of the magnetic fields $\hat{\mathbf{B}}$ along the photon path, it is useful specify two rotated reference systems in order to describe the polarization: The final "observers system" (l, r) aligned for example with the symmetry axis of the jet and the "emitting system" (e, b) given by the directions of $\hat{\mathbf{e}}$ and $\hat{\mathbf{b}}$ in a volume element within the line of sight. It is important to note that both systems are stationary with respect to the observer and merely rotated around the line-of sight. To specify the system (e,b), we consider a photon being emitted in the *co-moving emitting system* with polarization $\hat{\mathbf{e}}' = \hat{\mathbf{n}}' \times \hat{\mathbf{B}}'$. Boosted to the emitting system, one finds for the directions

$$\hat{\mathbf{e}} = \frac{\mathbf{n} \times \mathbf{q}}{\sqrt{q^2 - (\mathbf{n}\cdot\mathbf{q})^2}}\ ; \qquad \mathbf{q} = \hat{\mathbf{B}} + \mathbf{n} \times (\mathbf{v} \times \hat{\mathbf{B}}) \tag{A.24}$$

(Lyutikov et al. 2003). The two reference systems are thus rotated by an angle χ_e given as

$$\cos\chi_e = \hat{\mathbf{l}} \cdot \hat{\mathbf{e}}\ ; \qquad \sin\chi_e = \hat{\mathbf{n}} \cdot \left(\hat{\mathbf{l}} \times \hat{\mathbf{e}}\right) \tag{A.25}$$

and illustrated in figure A.2.

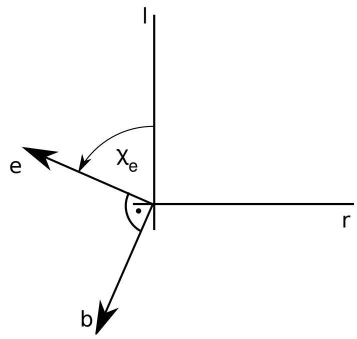

Figure A.2 On the definition of the angle χ_e.

A.3 Linearly Polarized Radiation Transfer

In the emitting system (e,b), absorption adds to the differential Stokes parameters as follows:

$$dI^{(a,e)} = -\kappa^{(e)} I^{(e)} ds \tag{A.26}$$
$$dI^{(a,b)} = -\kappa^{(b)} I^{(b)} ds \tag{A.27}$$
$$dU^{(a,eb)} = -\kappa U^{(eb)} ds \tag{A.28}$$

where the superscript a should remind us of the absorption character of the differentials and $\kappa = 1/2(\kappa^{(e)} + \kappa^{(b)})$ is the average absorption coefficient. We first consider the unpolarized part of the incoming radiation with $U = 0$. Depending on the ratio of $\kappa^{(e)}/\kappa^{(b)}$, the resulting polarization will be either along the $\hat{e}$ ($\chi = 0$) or $\hat{b}$ ($\chi = \pi$) direction. In both cases, $\tan(2\chi) = 0$ and therefor $U = 0$ also for the outgoing radiation. Hence dU accounts only for the change in the completely polarized part. Here one can use the identity $I^2 = Q^2 + U^2$, to obtain $U^2 = 4I^{(e)}I^{(b)}$ which leads to equation (A.28) after differentiation and use of the previous relations (A.26) and (A.27).

For the emissivity, the relations read:

$$dI^{(e,e)} = \epsilon^{(e)} ds \tag{A.29}$$
$$dI^{(e,b)} = \epsilon^{(b)} ds \tag{A.30}$$
$$dU^{(e,eb)} = 0 \tag{A.31}$$

where the last relation follows again from the fact that the emitted light has $\chi = 0$.

To incorporate the Faraday effect, we need to explore the change of $(\mathbf{I}) = (I^{(l)}, I^{(r)}, U^{(lr)})^T$ under rotations. Following Chandrasekhar (1960), a rotation of the axis by the angle ϕ in clockwise direction results in the linear transformation

$$L(\phi) = \begin{pmatrix} \cos^2\phi & \sin^2\phi & \frac{1}{2}\sin 2\phi \\ \sin^2\phi & \cos^2\phi & -\frac{1}{2}\sin 2\phi \\ -\sin 2\phi & \sin 2\phi & \cos 2\phi \end{pmatrix} \tag{A.32}$$

for the three parameters while V remains unchanged. As expected for a rotation, L satisfies the group relations $L(\phi_2) \circ L(\phi_1) = L(\phi_1 + \phi_2)$ and $L^{-1}(\phi) = L(-\phi)$. When the Faraday rotation measure $d\chi_F$ per unit dl is given, the differential Stokes parameters for the first order in $d\chi_F$ read

$$dI^{(f,l)} = U^{(lr)} d\chi_F \tag{A.33}$$
$$dI^{(f,r)} = -U^{(lr)} d\chi_F \tag{A.34}$$
$$dU^{(f,lr)} = -2I^{(l)} d\chi_F + 2I^{(r)} d\chi_F \tag{A.35}$$

in the observers system.

Now we use the transformation (A.32) to convert the previously derived relations for absorption and emission from the local lab system to the observers system. We rotate by the angle χ_e to obtain

$$\begin{pmatrix} dI^{(l)} \\ dI^{(r)} \\ dU^{(lr)} \end{pmatrix} = L(\chi_e) \begin{pmatrix} dI^{(e)} \\ dI^{(b)} \\ dU^{(eb)} \end{pmatrix}; \qquad \begin{pmatrix} I^{(l)} \\ I^{(r)} \\ U^{(lr)} \end{pmatrix} = L(\chi_e) \begin{pmatrix} I^{(e)} \\ I^{(b)} \\ U^{(eb)} \end{pmatrix}. \tag{A.36}$$

We can then write down the radiation transport equation in the observers system

$$dI^{(l)} = dI^{(a,l)} + dI^{(e,l)} + dI^{(f,l)} \tag{A.37}$$
$$dI^{(r)} = dI^{(a,r)} + dI^{(e,r)} + dI^{(f,r)} \tag{A.38}$$
$$dU^{(lr)} = dU^{(a,lr)} + dU^{(e,lr)} + dU^{(f,lr)}. \tag{A.39}$$

After some algebra, we arrive at

$$\begin{aligned}
\frac{dI^{(l)}}{ds} &= I^{(l)}\left[-\kappa^{(e)}\cos^4\chi_e - \kappa^{(b)}\sin^4\chi_e - \frac{1}{2}\kappa\sin^2 2\chi_e\right] \\
&+ U^{(lr)}\left[\frac{1}{4}\left(\kappa^{(e)} - \kappa^{(b)}\right)\sin 2\chi_e + \frac{d\chi_F}{ds}\right] \\
&+ \epsilon^{(e)}\cos^2\chi_e + \epsilon^{(b)}\sin^2\chi_e
\end{aligned} \tag{A.40}$$

$$\begin{aligned}
\frac{dI^{(r)}}{ds} &= I^{(r)}\left[-\kappa^{(e)}\sin^4\chi_e - \kappa^{(b)}\cos^4\chi_e - \frac{1}{2}\kappa\sin^2 2\chi_e\right] \\
&+ U^{(lr)}\left[\frac{1}{4}\left(\kappa^{(e)} - \kappa^{(b)}\right)\sin 2\chi_e - \frac{d\chi_F}{ds}\right] \\
&+ \epsilon^{(e)}\sin^2\chi_e + \epsilon^{(b)}\cos^2\chi_e
\end{aligned} \tag{A.41}$$

$$\begin{aligned}
\frac{dU^{(lr)}}{ds} &= I^{(l)}\left[\frac{1}{2}\left(\kappa^{(e)} - \kappa^{(b)}\right)\sin 2\chi_e - 2\frac{d\chi_F}{ds}\right] \\
&+ I^{(r)}\left[\frac{1}{2}\left(\kappa^{(e)} - \kappa^{(b)}\right)\sin 2\chi_e + 2\frac{d\chi_F}{ds}\right] \\
&- \kappa U^{(lr)} - \left(\epsilon^{(e)} - \epsilon^{(b)}\right)\sin 2\chi_e
\end{aligned} \tag{A.42}$$

the transport equations for the Stokes parameters (Pacholczyk 1970b).

A.4 Relativistic Beaming

So far, we used the relativistic swing to rotate the emitted direction of polarization to the observer system where the transport is conveniently conducted. However, we did not specify how the emissivities and opacities that are defined in the co-moving system (A.16, A.17) transform to the observer system. Here we give the corresponding transformations of the remaining quantities involved in radiation transport.

A.4.1 Doppler Boosting

Given a photon emitted in the source frame with the four-momentum

$$(p'^{\mu}) = (p'^0, p'^1, p'^2, p'^3)^T. \tag{A.43}$$

An observer moving towards the source with velocity $v = -v_z$ will measure the photon as

$$p^{\mu} = \Lambda'^{\mu}_{\ \nu} p'^{\nu}; \qquad \left(\Lambda'^{\mu}_{\ \nu}\right) = \begin{pmatrix} \Gamma & 0 & 0 & \beta\Gamma \\ 0 & 1 & 0 & 0 \\ 0 & 0 & 1 & 0 \\ \beta\Gamma & 0 & 0 & \Gamma \end{pmatrix} \tag{A.44}$$

and hence

$$(p^{\mu}) = \left(\Gamma p^0 + \beta\Gamma p^3, p^1, p^2, \beta\Gamma p^0 + \Gamma p^3\right)^T \tag{A.45}$$

with the energy

$$E = h\nu = cp^0 = \Gamma E' \left(1 + \beta \cos\theta'\right); \qquad \cos\theta' = \frac{p'^3}{p'^0}. \tag{A.46}$$

Due to relativistic aberration, the photon will be detected from an angle that relates to the angle of emission as

$$\cos\theta = \frac{p^3}{p^0} = \frac{\beta + \cos\theta'}{1 + \beta\cos\theta'}. \tag{A.47}$$

After inserting equation (A.47) into (A.46) we obtain

$$\nu = \frac{\nu'}{\Gamma\left(1 - \beta\cos\theta\right)} \equiv D\nu' \tag{A.48}$$

introducing the all-important "Doppler factor" D.

A.4.2 Transformation of Radiation Quantities

From the invariance of the photon occupation number it follows the well known relation for the specific intensity

$$\frac{I_\nu}{\nu^3} = inv. \tag{A.49}$$

The optical depth τ is a Lorentz invariant as well, since it represents the fraction of transmitted photons which involves simple counting. From similar considerations, the quantities involved in radiative transfer relate to their source-frame values via

$$\begin{aligned}
\nu &= D\nu' \\
d\Omega &= D^{-2} d\Omega' \\
I_\nu &= D^3 {I'}_{\nu'} \\
T &= DT' \\
dl &= Ddl' \\
dV &= DdV' \\
\epsilon_\nu &= D^2 {\epsilon'}_{\nu'} \\
\kappa_\nu &= D^{-1} {\kappa'}_{\nu'} \\
\tau_\nu &= \tau'_{\nu'},
\end{aligned} \tag{A.50}$$

as demostrated for example by Rybicki & Lightman (1986) and Begelman et al. (1984).

A.5 Unpolarized Transfer in the Observers System

In case of a continuous jet, the radiative transfer is best performed directly in the observers system by solving

$$\frac{dI_\nu}{ds} = \epsilon_\nu - \kappa_\nu I_\nu \tag{A.51}$$

along the line-of-sight. The observed intensity I_ν in terms of the local co-moving coefficients (for the observed frequency ν) becomes with the transformations (A.50)

$$\frac{dI_\nu}{dl} = D^{2+\alpha}\epsilon'_\nu - D^{\alpha+1.5}\kappa'_\nu I_\nu. \tag{A.52}$$

The additional factor D^α arises from the necessity to specify ϵ_ν, κ_ν in terms of the *observed* frequency ν.

A.6 Polarized Transfer in the Observers System

Summarizing the previous considerations, we now give the transfer equations for linearly polarized Synchotron radiation in the observers system. Writing (A.40-A.42) in analogy to (A.52), we have the set of linear equations

$$\frac{d\mathbf{I}}{dl} = \mathcal{E} - \underline{\mathbf{A}}\ \mathbf{I} \tag{A.53}$$

with the coefficients

$$(\underline{\mathbf{A}}) = \begin{pmatrix} a_{11} & 0 & a_{13} \\ 0 & a_{22} & a_{23} \\ 2a_{23} & 2a_{13} & a_{33} \end{pmatrix}; \qquad (\mathcal{E}) = \begin{pmatrix} D^{2+\alpha}\epsilon'^{(e)}\cos^2\chi_e + D^{2+\alpha}\epsilon'^{(b)}\sin^2\chi_e \\ D^{2+\alpha}\epsilon'^{(e)}\sin^2\chi_e + D^{2+\alpha}\epsilon'^{(b)}\cos^2\chi_e \\ -D^{2+\alpha}\left(\epsilon'^{(e)} - \epsilon'^{(b)}\right)\sin 2\chi_e \end{pmatrix} \tag{A.54}$$

$$a_{11} = D^{\alpha+1.5}\left[\kappa'^{(e)}\cos^4\chi_e + \kappa'^{(b)}\sin^4\chi_e + \frac{1}{2}\kappa\sin^2 2\chi_e\right] \tag{A.55}$$

$$a_{13} = -\left[\frac{1}{4}D^{\alpha+1.5}\left(\kappa'^{(e)} - \kappa'^{(b)}\right)\sin 2\chi_e + \frac{d\chi_F}{dl}\right] \tag{A.56}$$

$$a_{22} = D^{\alpha+1.5}\left[\kappa'^{(e)}\sin^4\chi_e + \kappa'^{(b)}\cos^4\chi_e + \frac{1}{2}\kappa'\sin^2 2\chi_e\right] \tag{A.57}$$

$$a_{23} = -\left[\frac{1}{4}D^{\alpha+1.5}\left(\kappa'^{(e)} - \kappa'^{(b)}\right)\sin 2\chi_e - \frac{d\chi_F}{dl}\right] \tag{A.58}$$

$$a_{33} = D^{\alpha+1.5}\kappa'. \tag{A.59}$$

This is solved by the numerical transport code by ray-casting for a grid of lines of sight.

Appendix B

Appendix 2

B.1 Zero Current Outflow Boundary

One of the major goals of this work is to investigate the collimation behavior of relativistic outflows. It is therefore essential to exclude any numerical artifacts leading to a spurious flow collimation. We find that the standard zero-gradient outflow boundary conditions may lead to an un-physical Lorentz force in radial direction implying such spurious collimation (or de-collimation).

Thus, we put substantial effort in implementing and testing an enhanced outflow boundary condition to the numerical code.

To get a handle on the Lorentz-force $j_\phi \times B_p$, one has to address the toroidal electric currents at the grid boundary. In principle there are (at least) two options. One is the possibility to copy the toroidal electric current across the boundary. While this approach should minimize spurious collimation efficiently, we observed that the overall stability of the simulation was decreased. Thus we decide to use the following zero-toroidal current outflow boundaries in our simulations.

In this case we take advantage of the staggered grid by enforcing zero toroidal currents while simultaneously satisfying the solenoidal condition $\nabla \cdot \mathbf{B} = 0$. In the following our procedure is described in detail. We consider computational grid cells (i_{end}, j), adjunct to the domain boundary at $(i_{\mathrm{end}}+1, j)$, as illustrated in Fig. B.1. The magnetic field components of the domain, $B_{\mathrm{t}}(i_{\mathrm{end}}, j+1/2)$, $B_{\mathrm{n}}(i_{\mathrm{end}}+1/2, j)$, $B_{\mathrm{n}}(i_{\mathrm{end}}+1/2, j+1)$, together with the transverse field component $B_{\mathrm{t}}(i_{\mathrm{end}}+1, j+1/2)$ of the first ghost zone, constitute a toroidal corner-centered electric current $I_\phi(i_{\mathrm{end}}+1/2, j+1/2)$. Utilizing Stokes theorem, $I_\phi = \int d\mathbf{S} \cdot \nabla \times \mathbf{B_p} = \oint d\mathbf{l} \cdot \mathbf{B_p}$, we then solve for the unknown field component $B_{\mathrm{t}}(i_{\mathrm{end}}+1, j+1/2)$ under the constraint that $I_\phi = 0$,

$$B_{\mathrm{t}}|_{i_{\mathrm{end}}+1,j+1/2} = B_{\mathrm{t}}|_{i_{\mathrm{end}},j+1/2} + \frac{\Delta r}{\Delta z}\left[B_{\mathrm{n}}|_{i_{\mathrm{end}}+1/2,j+1} - B_{\mathrm{n}}|_{i_{\mathrm{end}}+1/2,j}\right] \tag{B.1}$$

where we have assumed an equally spaced grid for clarity of the argument. Once $B_{\rm t}(i_{\rm end}+1, j+1/2)$ is known for all j, the next layer of normal field components $B_{\rm n}(i_{\rm end}+3/2, j)$ can be inferred from the $\nabla \cdot \mathbf{B} = 0$ constraint in its integral form,

$$B_{\rm n}|_{i_{end}+3/2,j+1} = \frac{\Delta S_{\rm n} B_{\rm n}|_{i_{\rm end}+1/2,j+1} + \left(\Delta S_{\rm t} B_{\rm t}|_{i_{\rm end}+1,j+1/2} - \Delta S_{\rm t} B_{\rm t}|_{i_{\rm end}+1,j+3/2}\right)}{\Delta S_{\rm n}|_{i_{\rm end}+3/2,j+1}}. \tag{B.2}$$

For the next grid layer, the transverse field components can again be found applying Eq. B.1, and the process is repeated for the each layer.

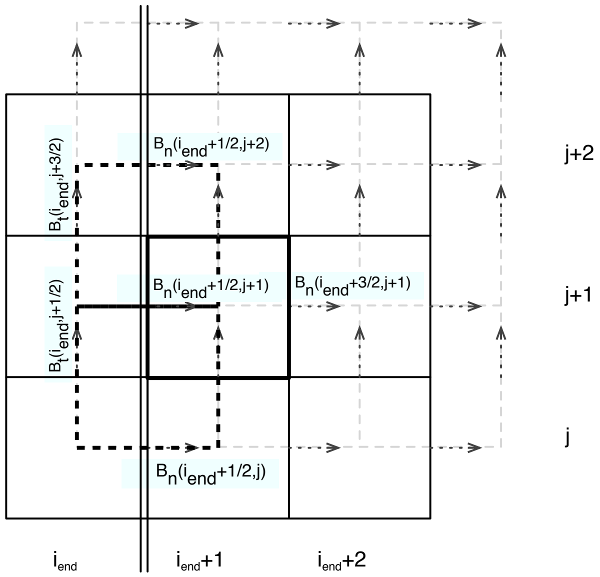

Figure B.1 Construction of the $\nabla \times \mathbf{B_p} = \mathbf{0}$ and $\nabla \cdot \mathbf{B} = 0$ boundary condition. Shown is the last grid slab of the domain $(i_{\rm end}, j)$ and a ghost zone of two elements.

Some words of caution. We find that the current-free magnetic field boundary condition can only be realized when the grid cell aspect ratio $\Delta z/\Delta r$ is not too large. An aspect ratio of e.g. 12/1 resulted in errors of 100% in $B_{\rm n}$ at the most critical areas close to the symmetry axis leading to an overall unstable flow evolution. We find that as a rule of thumb, an aspect ratio of 3/1 should not be exceeded. We also emphasize that it is essential to treat the grid corners consistently. This is because field components in the corner, $B_{\rm t}(i_{\rm end}+1, j_{\rm end}+1/2)$, and $B_{\rm n}(i_{\rm end}+1/2, j_{\rm end}+1)$, are interrelated which would lead to an ambiguity. In order to avoid this ambiguity, we decided to extrapolate the values in question which does provide the information that is missing otherwise.

We demonstrate quality of our approach by showing results of simulations which *do not* apply the zero current but the zero-gradient or the zero second derivative outflow condition with otherwise the same flow parameters as in simulation WA04 of chapter 4 (Fig. B.2). As it can be seen, for zero-gradient boundary conditions, the effect of collimation by artificial currents is so strong that no steady-state can be reached and the flow is continuously squeezed towards the axis. Also in zero second derivative, we observe an artificial alignment with the grid geometry.

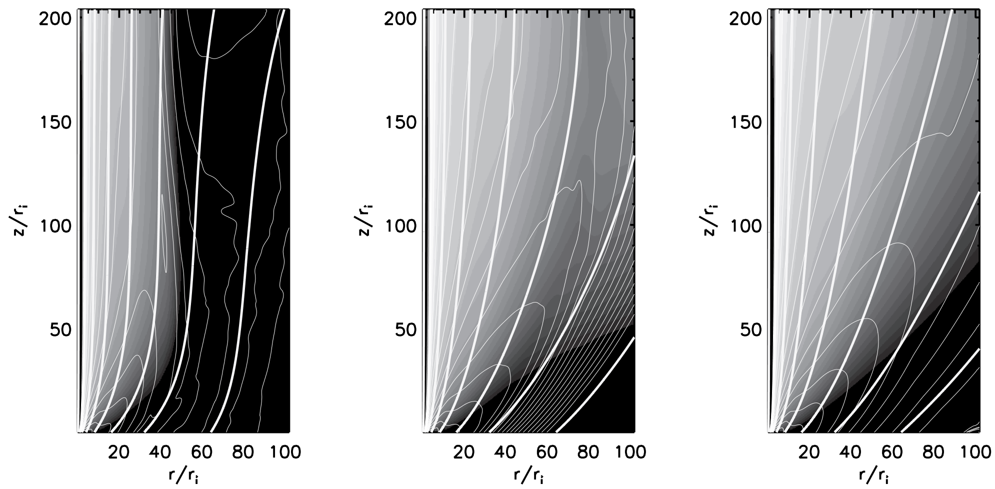

Figure B.2 Comparison of simulations applying a variation of outflow boundary conditions for the magnetic fields at the time of 100 inner disk rotations. The parameters are equal to those in simulation WA04. The grayscale indicates the Lorentz factor $log(\Gamma - 1)$ as in figure 4.3, the poloidal magnetic field (the poloidal electric current) is shown in thick (thin) white contours. Standard zero gradient, zero second derivative, zero current boundary condition, respectively (from left to right).

B.1.1 Geometry and Convergence

We check the geometry dependence of the zero current outflow boundary by several realizations of the fiducial run WA04, each with the same resolution but with a different grid size or shape. Figure B.3 (left panel) compares the steady state flow characteristics for various boxes with ratios $\Delta z/\Delta r \in \{1/1, 2/1, 4/1\}$. While geometries and sizes with $\Delta z/\Delta r \geq 2/1$ are in excellent agreement, the quadratic domains show significantly thinner characteristics. The reason for this discrepancy is the sub Alfvénic flow that traverses the $Z_{\rm end}$ boundary in "broad" domains. In these underdetermined simulations, current circuits start to open at the sub Alfvénic part of Z_{end} which ultimately destroys the Butterfly shape in the entire domain. As also noticed and extensively discussed by Krasnopolsky et al. (1999), a sub Alfvénic (vertical) outflow can not obtain the proper critical point information and leads to erroneous extensive collimation. This problem can be avoided by taking the position of the critical Alfvén surface into account, hence we choose a ratio of 2/1 for the simulations in question.

Finally we check convergence by comparison to a half-resolution run with 256×512 grid elements. The solutions are in good agreement, indicated by contours of the Alfvén Mach number in figure B.3 (right panel). In conclusion we use a grid of 512×1024 cells with a domain size of $(r, z) = (102, 204)$ inner disk radii, ensuring that the presented results are independent of the numerical discretization and depend mostly on the disk corona boundary.

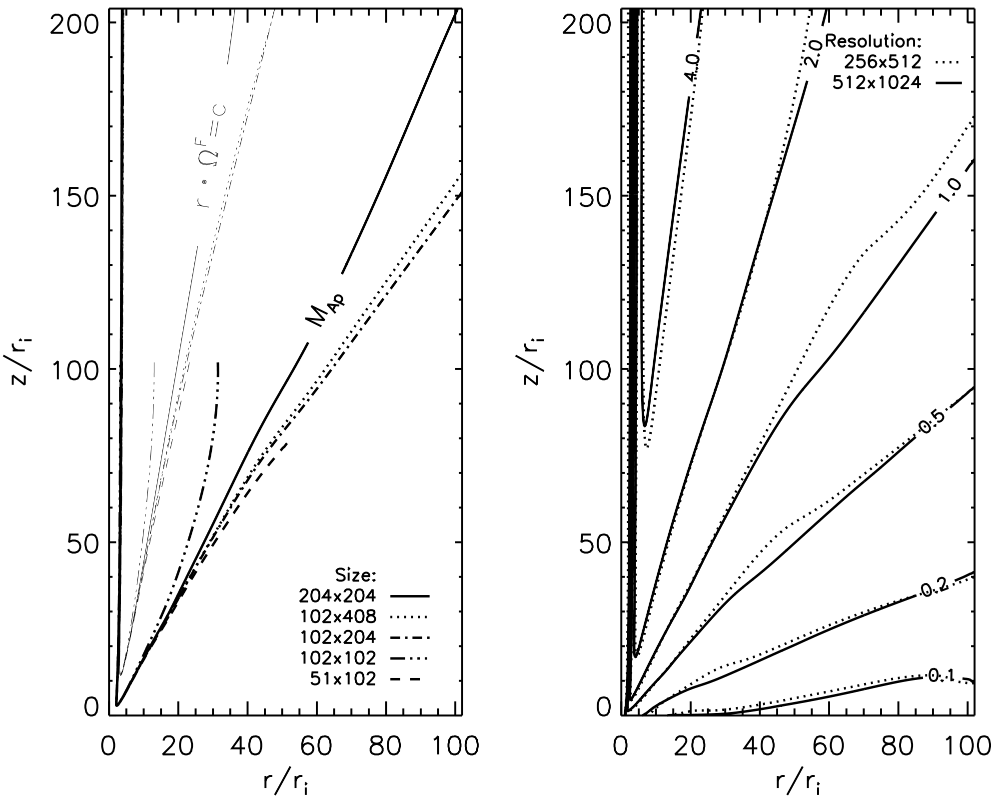

Figure B.3 Comparison of different grid realisations with zero current outflow boundaries after 200 inner disk rotations. Parameters as in simulation WA04. *Left:* Various geometries and sizes. Shown is the critical Alfvén surface and the light cylinder. *Right:* Convergence test with two grid resolutions. Shown are contours of the Alfvén mach number M for 256×512 and for 512×1024 grid elements.

Appendix C

List of Publications

During the course of this work, results detailed in this thesis were presented at international conferences and workshops. Here we list all the scientific communications related this thesis.

C.1 Peer Review Journals and Books

- **Porth O.**, Fendt C., Meliani Z. & Vaidya B. (2011), *Synchrotron radiation of self-collimating relativistic MHD jets*, **ApJ 737, p. 42.**

- **Porth O.** & Fendt C. (2010), *Acceleration and Collimation of Relativistic Magnetohydrodynamic Disk Winds*, **ApJ 709, p. 1100.**

- **Porth O.** & Fendt C. (2010), *From disk winds to relativistic jets*, Proceedings of the Workshop HEPRO II, **Modern Physics D, Volume 19, Number 6, p. 677**

C.2 Publication in Journals or Books Without Peer Review

- **Porth O.** (2011), *Two component relativistic acceleration and polarized radiation of the parsec-scale AGN jet*, Proceedings of the International Astronomical Union, IAU Symposium 274

- Fendt C., Vaidya B., **Porth, O.**, Sheikh Nezami S. (2011), *MHD simulations of jet formation - protostellar jets & applications to AGN jets*, Proceedings of the

International Astronomical Union, IAU Symposium 275

• **Porth O.** (2011), *Simulations and synchrotron radiation from the relativistic jet base*, Proceedings of the Workshop "Steady Jets and Transient Jets", Memorie della Societa Astronomica Italiana, 82, p. 125

C.3 Abstracts of Scientific Talks

• *Signatures of synchrotron radiation from the relativistic jet base*
Conference "The Central Kiloparsec in Galactic Nuclei (AHAR11)", Bad Honnef, Germany, August 29 – September 2, 2011

> *We show the results of large scale axisymmetric simulations of two-component jet acceleration in special relativistic magnetohydrodynamics. Within one parsec from the accretion disk, the component dominated by Poynting flux accelerates to relativistic velocities $\Gamma \sim 8$ but is still far from equipartition. In the near-stationary end-state, we solve the polarized Synchrotron radiation transport incorporating self-absorption and (internal) Faraday rotation. With mock-observations of the parsec scale jet base in radio and sub-mm wavelength we obtain observational signatures of the model. These comprise radio maps, spectra, polarization structure (revealing spin direction), frequency dependent depolarization, core shift and Faraday rotation measure. We also specify the detectability of such features depending on the available resolution, predicting the discovery of rotation measure gradients with the advance of space-VLBI and global mm-VLBI featuring resolutions of 100 Schwarzschild radii. The presented work represents a near complete toolbox to test the present diagnostics used in radio observations of AGN cores.*

• *Two component acceleration and polarized emission of the inner parsec-scale jet*
Conference "Accretion and Outflow in Black Hole Systems", Kathmandu, Nepal, October 11–15, 2010

We show the results of large scale axisymmetric simulations of two-component jet acceleration in special relativistic magnetohydrodynamics. Within one parsec from the accretion disk, the component dominated by Poynting flux accelerates to relativistic velocities $\Gamma \sim 10$ *but is still far from equipartition. Thermal acceleration of the inner component saturates quickly after the sonic point but is delimited to* $\Gamma \sim 3$ *by the amount of enthalpy available in the black hole corona. In the near-stationary end-state, we solve the polarized Synchrotron radiation transport incorporating self-absorption and (internal) Faraday rotation. With mock-observations of the jet base in radio and sub-mm wavelength we show the resolution dependence of the transversal rotation measure gradients. Models that seem to break the* λ^2*-law in the radio band can yield consistent rotation measures when observed in the ALMA frequency range.*

- *From disk winds to relativistic jets*

Workshop "High Energy Phenomena in Relativistic Outflows II", Buenos Aires, Argentina, October 26–30, 2009

We investigate the relativistic acceleration and collimation of a wind launched from a magnetized accretion disk corona. Time-dependend simulations of the full set of special relativistic magneto hydro dynamic (RMHD) equations are performed with the publicly available PLUTO code. In order to provide an injection boundary in dynamical equilibrium, Newtoninan gravity was added as source term. The flow starts out with sub-escape velocity and we allow for sub magnetoslow injection to consistently prescribe the mass-loading. The detailed trans field and parallel field force-balances are shown with highlights on the relativistic contribution due to electric fields. Generally we find collimated flows with mass-weighted half-opening angles of 3-7 degrees and mildly relativistic velocities. The outer subrelativistic flow is a promising candidate for the X-ray absorption winds that are observed in many radio-quiet active galactic nulei (AGN).

- *MHD simulations of relativistic jet formation*

Workshop "The high-energy astrophysics of outflows from compact objects", Ringberg, Germany, December 7–13, 2008

We show the first results of jet acceleration and self-collimation simulations in the relativistic regime where the jet is launched from an accretion disk corona. The jet starts out as a sub-escape velocity wind and is accelerated to mildly relativistic velocities with $\Gamma \sim 3$ *by the magnetocentrifugal force. We can follow the evolution until a stationary state is reached within the computational domain and find both of the initially paraboloidal and split monopole field geometries to collimate well with half-opening angles* $\sim 1^\circ$.

Bibliography

Abdo, A. A., Ackermann, M., Agudo, I., et al. 2010a, ApJ, 716, 30

Abdo, A. A., Ackermann, M., Ajello, M., et al. 2010b, Nature, 463, 919

Abramowicz, M. A. 2009, A&A, 500, 213

Agudo, I., Jorstad, S. G., Marscher, A. P., et al. 2011, ApJ, 726, L13+

Agudo, I., Thum, C., Wiesemeyer, H., & Krichbaum, T. P. 2010, ApJS, 189, 1

Aharonian, F., Akhperjanian, A. G., Bazer-Bachi, A. R., et al. 2007, ApJ, 664, L71

Albert, J., Aliu, E., Anderhub, H., et al. 2007, ApJ, 669, 862

Alfvén, H. & Herlofson, N. 1950, Physical Review, 78, 616

Aloy, M. A. & Mimica, P. 2008, ApJ, 681, 84

Anderson, J. M., Li, Z., Krasnopolsky, R., & Blandford, R. D. 2006, ApJ, 653, L33

Anile, A. M. 1989, Relativistic fluids and magneto-fluids: With applications in astrophysics and plasma physics (Cambridge University Press)

Antonuccio-Delogu, V. & Silk, J. 2008, MNRAS, 389, 1750

Appl, S. & Camenzind, M. 1992, A&A, 256, 354

Appl, S. & Camenzind, M. 1993, A&A, 270, 71

Appl, S., Lery, T., & Baty, H. 2000, A&A, 355, 818

Araudo, A. T., Bosch-Ramon, V., & Romero, G. E. 2010, A&A, 522, A97+

Armitage, P. J., Reynolds, C. S., & Chiang, J. 2001, ApJ, 548, 868

Asada, K., Inoue, M., Uchida, Y., et al. 2002, PASJ, 54, L39

Balbus, S. A. & Hawley, J. F. 1998, Reviews of Modern Physics, 70, 1

Bally, J. 2007, Ap&SS, 311, 15

Balsara, D. 2001, ApJS, 132, 83

Balsara, D. S. & Spicer, D. S. 1999, Journal of Computational Physics, 149, 270

Baring, M. G. & Harding, A. K. 1997, ApJ, 491, 663

Barkov, M. V. & Komissarov, S. S. 2008, International Journal of Modern Physics D, 17, 1669

Bateman, G. 1978, MHD instabilities (MIT Press)

Baum, S. A., Zirbel, E. L., & O'Dea, C. P. 1995, ApJ, 451, 88

Begelman, M. C. 1998, ApJ, 493, 291

Begelman, M. C., Blandford, R. D., & Rees, M. J. 1984, Reviews of Modern Physics, 56, 255

Begelman, M. C. & Li, Z. 1994, ApJ, 426, 269

Begelman, M. C. & Li, Z.-Y. 1992, ApJ, 397, 187

Begelman, M. C., McKee, C. F., & Shields, G. A. 1983, ApJ, 271, 70

Begelman, M. C. & Sikora, M. 1987, ApJ, 322, 650

Belloni, T., Homan, J., Casella, P., et al. 2005, A&A, 440, 207

Beskin, V. S., Kuznetsova, I. V., & Rafikov, R. R. 1998, MNRAS, 299, 341

Beskin, V. S. & Nokhrina, E. E. 2006, MNRAS, 367, 375

Beskin, V. S. & Nokhrina, E. E. 2009, MNRAS, 397, 1486

Best, P. N., Kauffmann, G., Heckman, T. M., & Ivezić, Ž. 2005, MNRAS, 362, 9

Bicknell, G. V. & Begelman, M. C. 1996, ApJ, 467, 597

Biretta, J. A., Owen, F. N., & Cornwell, T. J. 1989, ApJ, 342, 128

Blackman, E. G. & Pessah, M. E. 2009, ApJ, 704, L113

Blandford, R. D. 1994, in Astronomical Society of the Pacific Conference Series, Vol. 54, The Physics of Active Galaxies, ed. G. V. Bicknell, M. A. Dopita, & P. J. Quinn, 23–+

Blandford, R. D. & Königl, A. 1979, ApJ, 232, 34

Blandford, R. D. & Payne, D. G. 1982, MNRAS, 199, 883

Blandford, R. D. & Rees, M. J. 1974, MNRAS, 169, 395

Blandford, R. D. & Znajek, R. L. 1977, MNRAS, 179, 433

Blundell, K. M., Rawlings, S., & Willott, C. J. 1999, AJ, 117, 677

Boettcher, M. & Schlickeiser, R. 1996, A&A, 306, 86

Bogovalov, S. V. 1994, MNRAS, 270, 721

Bogovalov, S. V. 1997, A&A, 323, 634

Boris, J. P. 1970, Naval Research Laboratory, Washington

Broderick, A. E. & Loeb, A. 2009a, ApJ, 697, 1164

Broderick, A. E. & Loeb, A. 2009b, ApJ, 703, L104

Broderick, A. E. & McKinney, J. C. 2010, ApJ, 725, 750

Broderick, J. W. & Fender, R. P. 2011, ArXiv e-prints

Burn, B. J. 1966, MNRAS, 133, 67

Burnham, S. W. 1890, MNRAS, 51, 94

Camenzind, M. 1986a, A&A, 156, 137

Camenzind, M. 1986b, A&A, 162, 32

Camenzind, M. 1989, in Astrophysics and Space Science Library, Vol. 156, Accretion Disks and Magnetic Fields in Astrophysics, ed. G. Belvedere, 129–143

Camenzind, M. & Krockenberger, M. 1992, A&A, 255, 59

Cappi, M. 2006, Astronomische Nachrichten, 327, 1012

Carilli, C. L. & Barthel, P. D. 1996, A&A Rev., 7, 1

Casse, F. & Ferreira, J. 2000, A&A, 361, 1178

Casse, F. & Keppens, R. 2002, ApJ, 581, 988

Casse, F. & Keppens, R. 2004, ApJ, 601, 90

Chakrabarti, S. K. & Khanna, R. 1992, MNRAS, 256, 300

Chakrabarti, S. K. & Wiita, P. J. 1993, ApJ, 411, 602

Chandrasekhar, S. 1960, Radiative transfer, ed. Chandrasekhar, S.

Chang, K. & Refsdal, S. 1979, Nature, 282, 561

Chaty, S., Mirabel, I. F., Duc, P. A., Wink, J. E., & Rodriguez, L. F. 1996, A&A, 310, 825

Chelouche, D. & Netzer, H. 2005, ApJ, 625, 95

Chiaberge, M., Celotti, A., Capetti, A., & Ghisellini, G. 2000, A&A, 358, 104

Chiueh, T., Li, Z.-Y., & Begelman, M. C. 1991, ApJ, 377, 462

Clausen-Brown, E., Lyutikov, M., & Kharb, P. 2011, MNRAS, 1041

Cocke & Holm. 1972, Nature, 240, 161

Codella, C., Cabrit, S., Gueth, F., et al. 2007, A&A, 462, L53

Cohen, M. H., Cannon, W., Purcell, G. H., et al. 1971, ApJ, 170, 207

Colella, P. & Woodward, P. R. 1984, Journal of Computational Physics, 54, 174

Contopoulos, J. 1994, ApJ, 432, 508

Contopoulos, J. 1995, ApJ, 446, 67

Corbel, S., Fender, R. P., Tzioumis, A. K., et al. 2000, A&A, 359, 251

Cotton, W. D., Feretti, L., Giovannini, G., Lara, L., & Venturi, T. 1999, ApJ, 519, 108

Courant, R., Friedrichs, K., & Lewy, H. 1928, Mathematische Annalen, 100, 32

Cowie, L. L., Songaila, A., Hu, E. M., & Cohen, J. G. 1996, AJ, 112, 839

Croke, S. M., O'Sullivan, S. P., & Gabuzda, D. C. 2010, MNRAS, 402, 259

Croston, J. H., Kraft, R. P., & Hardcastle, M. J. 2007, ApJ, 660, 191

Curtis, H. D. 1918, Publications of Lick Observatory, 13, 31

Czerny, B., Goosmann, R., & Janiuk, A. 2008, Chinese Journal of Astronomy and Astrophysics Supplement, 8, 302

Das, T. K. & Chakrabarti, S. K. 1999, Classical and Quantum Gravity, 16, 3879

Davidson, K. & Netzer, H. 1979, Reviews of Modern Physics, 51, 715

De Villiers, J.-P., Hawley, J. F., & Krolik, J. H. 2003, ApJ, 599, 1238

De Young, D. S. 1993, ApJ, 405, L13

Dedner, A., Kemm, F., Kröner, D., et al. 2002, Journal of Computational Physics, 175, 645

Del Zanna, L., Bucciantini, N., & Londrillo, P. 2003, A&A, 400, 397

Della Ceca, R., Maccacaro, T., Caccianiga, A., et al. 2004, A&A, 428, 383

Dhawan, V., Mirabel, I. F., & Rodríguez, L. F. 2000, ApJ, 543, 373

Di Matteo, T., Springel, V., & Hernquist, L. 2005, Nature, 433, 604

Doeleman, S. 2008, Journal of Physics Conference Series, 131, 012055

Drenkhahn, G. & Spruit, H. C. 2002, A&A, 391, 1141

Dullemond, C. P. & van Bemmel, I. M. 2005, A&A, 436, 47

Dunn, R. J. H., Fabian, A. C., & Celotti, A. 2006, MNRAS, 372, 1741

Edge, D. O., Shakeshaft, J. R., McAdam, W. B., Baldwin, J. E., & Archer, S. 1959, MmRAS, 68, 37

Eisenstein, D. J., Weinberg, D. H., Agol, E., et al. 2011, ArXiv e-prints

Evans, C. R. & Hawley, J. F. 1988, ApJ, 332, 659

Falcke, H., Körding, E., & Markoff, S. 2004, A&A, 414, 895

Falle, S. A. E. G. 1991, MNRAS, 250, 581

Falle, S. A. E. G. & Komissarov, S. S. 1996, MNRAS, 278, 586

Fan, X., Strauss, M. A., Schneider, D. P., et al. 2003, AJ, 125, 1649

Fanaroff, B. L. & Riley, J. M. 1974, MNRAS, 167, 31P

Fanidakis, N., Baugh, C. M., Benson, A. J., et al. 2011, MNRAS, 410, 53

Fath, E. A. 1909, Lick Observatory Bulletin, 5, 71

Fender, R. P. 2001, MNRAS, 322, 31

Fender, R. P., Gallo, E., & Russell, D. 2010, MNRAS, 406, 1425

Fender, R. P., Garrington, S. T., McKay, D. J., et al. 1999, MNRAS, 304, 865

Fendt, C. 1997a, A&A, 319, 1025

Fendt, C. 1997b, A&A, 323, 999

Fendt, C. 2006, ApJ, 651, 272

Fendt, C. 2009, ApJ, 692, 346

Fendt, C. & Camenzind, M. 1996, A&A, 313, 591

Fendt, C. & Greiner, J. 2001, A&A, 369, 308

Fendt, C. & Memola, E. 2001, A&A, 365, 631

Fendt, C. & Ouyed, R. 2004, ApJ, 608, 378

Fendt, C. & Čemeljić, M. 2002, A&A, 395, 1045

Fenimore, E. E., Epstein, R. I., & Ho, C. 1993, A&AS, 97, 59

Feretti, L., Comoretto, G., Giovannini, G., Venturi, T., & Wehrle, A. E. 1993, ApJ, 408, 446

Ferrarese, L. & Merritt, D. 2000, ApJ, 539, L9

Ferreira, J. 1996, in Lecture Notes in Physics, Berlin Springer Verlag, Vol. 471, Jets from Stars and Galactic Nuclei, ed. W. Kundt, 82–+

Ferreira, J. 1997, A&A, 319, 340

Ferreira, J. & Pelletier, G. 1993, A&A, 276, 625

Ferreira, J. & Pelletier, G. 1995, A&A, 295, 807

Fish, V. L., Doeleman, S. S., Beaudoin, C., et al. 2011, ApJ, 727, L36+

Fossati, G., Maraschi, L., Celotti, A., Comastri, A., & Ghisellini, G. 1998, MNRAS, 299, 433

Fruchter, A. S., Thorsett, S. E., Metzger, M. R., et al. 1999, ApJ, 519, L13

Gabuzda, D. C., Mullan, C. M., Cawthorne, T. V., Wardle, J. F. C., & Roberts, D. H. 1994, ApJ, 435, 140

Gabuzda, D. C., Murray, É., & Cronin, P. 2004, MNRAS, 351, L89

Gammie, C. F., McKinney, J. C., & Tóth, G. 2003, ApJ, 589, 444

Gardner, F. F. & Whiteoak, J. B. 1966, ARA&A, 4, 245

Garrington, S. T., Leahy, J. P., Conway, R. G., & Laing, R. A. 1988, Nature, 331, 147

Gebhardt, K., Adams, J., Richstone, D., et al. 2011, ApJ, 729, 119

Gebhardt, K., Bender, R., Bower, G., et al. 2000, ApJ, 539, L13

Georganopoulos, M. & Kazanas, D. 2003, ApJ, 594, L27

Ghisellini, G., Tavecchio, F., & Chiaberge, M. 2005, A&A, 432, 401

Ghosh, P. & Abramowicz, M. A. 1997, MNRAS, 292, 887

Ghosh, S. 2004, A&A, 418, 795

Giacomazzo, B. & Rezzolla, L. 2006, Journal of Fluid Mechanics, 562, 223

Goedbloed, J., Keppens, R., & Poedts, S. 2010, Advanced Magnetohydrodynamics (Cambridge University Press)

Goedbloed, J. P. H. & Poedts, S. 2004, Principles of Magnetohydrodynamics, ed.

Goedbloed, J. P. H. & Poedts, S.

Goldreich, P. & Julian, W. H. 1969, ApJ, 157, 869

Gopal-Krishna, Dhurde, S., & Wiita, P. J. 2004, ApJ, 615, L81

Gorosabel, J., Pérez-Ramírez, D., Sollerman, J., et al. 2005, A&A, 444, 711

Gracia, J., Vlahakis, N., Agudo, I., Tsinganos, K., & Bogovalov, S. V. 2009, ApJ, 695, 503

Granato, G. L., Silva, L., Monaco, P., et al. 2001, MNRAS, 324, 757

Grazian, A., Fontana, A., de Santis, C., et al. 2006, A&A, 449, 951

Gregg, M. D., Becker, R. H., White, R. L., et al. 1996, AJ, 112, 407

Greiner, J., Cuby, J. G., & McCaughrean, M. J. 2001, Nature, 414, 522

Gubbay, J., Legg, A. J., Robertson, D. S., et al. 1969, Nature, 224, 1094

Haardt, F. & Maraschi, L. 1991, ApJ, 380, L51

Hardee, P. E. 2007, ApJ, 664, 26

Hardee, P. E. & Hughes, P. A. 2003, ApJ, 583, 116

Häring, N. & Rix, H.-W. 2004, ApJ, 604, L89

Hawley, J. F., Beckwith, K., & Krolik, J. H. 2007, Ap&SS, 311, 117

Hawley, J. F. & Krolik, J. H. 2001, ApJ, 548, 348

Heinbockel, J. H. & Landry, J. G. 1995, NASA STI/Recon Technical Report N, 96, 10685

Heinz, S. & Begelman, M. C. 2000, ApJ, 535, 104

Henri, G., Pelletier, G., & Roland, J. 1993, ApJ, 404, L41

Henri, G. & Saugé, L. 2006, ApJ, 640, 185

Heyvaerts, J. & Norman, C. 1989, ApJ, 347, 1055

Heyvaerts, J. & Norman, C. 2003a, ApJ, 596, 1240

Heyvaerts, J. & Norman, C. 2003b, ApJ, 596, 1256

Hirschmann, M., Khochfar, S., Burkert, A., et al. 2010, MNRAS, 407, 1016

Ho, L. C. 2002, ApJ, 564, 120

Ho, L. C., Filippenko, A. V., & Sargent, W. L. W. 1997, ApJ, 487, 568

Huang, L., Liu, S., Shen, Z., et al. 2008, ApJ, 676, L119

Israel, F. P. 1998, A&A Rev., 8, 237

Istomin, Y. N. & Pariev, V. I. 1994, MNRAS, 267, 629

Istomin, Y. N. & Pariev, V. I. 1996, MNRAS, 281, 1

Jahnke, K. & Macciò, A. V. 2011, ApJ, 734, 92

Jester, S. 2008, MNRAS, 389, 1507

Jones, D. L. & Wehrle, A. E. 2002, ApJ, 580, 114

Jones, T. W. & Odell, S. L. 1977, ApJ, 214, 522

Jones, T. W., O'dell, S. L., & Stein, W. A. 1974, ApJ, 188, 353

Jorstad, S. G., Marscher, A. P., Lister, M. L., et al. 2005, AJ, 130, 1418

Jorstad, S. G., Marscher, A. P., Mattox, J. R., et al. 2001, ApJS, 134, 181

Junor, W., Biretta, J. A., & Livio, M. 1999, Nature, 401, 891

Kato, Y. 2007, Ap&SS, 307, 11

Kato, Y., Mineshige, S., & Shibata, K. 2004, ApJ, 605, 307

Kazanas, D. & Ellison, D. C. 1986, ApJ, 304, 178

Kellermann, K. I. & Pauliny-Toth, I. I. K. 1969, ApJ, 155, L71+

Kennel, C. F. & Coroniti, F. V. 1984, ApJ, 283, 694

Keppens, R. & Meliani, Z. 2008, Physics of Plasmas, 15, 102103

Keppens, R., Meliani, Z., van Marle, A., et al. 2011, Journal of Computational Physics, In Press, Corrected Proof,

Keppens, R., Nool, M., Tóth, G., & Goedbloed, J. P. 2003, Computer Physics Communications, 153, 317

Keppens, R., Tóth, G., Westermann, R. H. J., & Goedbloed, J. P. 1999, Journal of Plasma Physics, 61, 1

Kharb, P., Gabuzda, D. C., O'Dea, C. P., Shastri, P., & Baum, S. A. 2009, ApJ, 694, 1485

Kirk, J. G., Guthmann, A. W., Gallant, Y. A., & Achterberg, A. 2000, ApJ, 542, 235

Klamer, I. J., Ekers, R. D., Sadler, E. M., & Hunstead, R. W. 2004, ApJ, 612, L97

Knigge, C., Woods, J. A., & Drew, J. E. 1995, MNRAS, 273, 225

Koide, S., Shibata, K., & Kudoh, T. 1998, ApJ, 495, L63+

Koldoba, A. V., Kuznetsov, O. A., & Ustyugova, G. V. 2002, MNRAS, 333, 932

Komissarov, S. S. 1999, MNRAS, 303, 343

Komissarov, S. S. 2005, MNRAS, 359, 801

Komissarov, S. S. 2007, MNRAS, 382, 995

Komissarov, S. S. 2009, Journal of Korean Physical Society, 54, 2503

Komissarov, S. S. 2011, Mem. Soc. Astron. Italiana, 82, 95

Komissarov, S. S., Barkov, M. V., Vlahakis, N., & Königl, A. 2007, MNRAS, 380, 51

Komissarov, S. S. & Falle, S. A. E. G. 1997, MNRAS, 288, 833

Komissarov, S. S., Vlahakis, N., & Königl, A. 2010, MNRAS, 407, 17

Komissarov, S. S., Vlahakis, N., Königl, A., & Barkov, M. V. 2009, MNRAS, 394, 1182

Königl, A. 1981, ApJ, 243, 700

Körding, E., Rupen, M., Knigge, C., et al. 2008, Science, 320, 1318

Kormendy, J. & Richstone, D. 1995, ARA&A, 33, 581

Kovalev, Y. Y., Aller, H. D., Aller, M. F., et al. 2009, ApJ, 696, L17

Kovalev, Y. Y., Lister, M. L., Homan, D. C., & Kellermann, K. I. 2007, ApJ, 668, L27

Kraft, R. P., Vázquez, S. E., Forman, W. R., et al. 2003, ApJ, 592, 129

Krasnopolsky, R., Li, Z., & Blandford, R. 1999, ApJ, 526, 631

Krichbaum, T. P., Graham, D. A., Bremer, M., et al. 2006, Journal of Physics Conference Series, 54, 328

Krolik, J. H. 1998, Active Galactic Nuclei: From the Central Black Hole to the Galactic Environment, ed. Krolik, J. H.

Krolik, J. H. & Hawley, J. F. 2010, in Lecture Notes in Physics, Berlin Springer Verlag, Vol. 794, Lecture Notes in Physics, Berlin Springer Verlag, ed. T. Belloni, 265–+

Kulsrud, R. M. & Ferrari, A. 1971, Ap&SS, 12, 302

Kuncic, Z. & Bicknell, G. V. 2004, ApJ, 616, 669

Laing, R. A. 1980, MNRAS, 193, 439

Laing, R. A. 1988, Nature, 331, 149

Landau, L. D. & Lifshitz, E. M. 1959, Fluid mechanics (Pergamon Press)

Landau, L. D. & Lifshitz, E. M. 1960, Electrodynamics of continuous media, ed. Landau, L. D. & Lifshitz, E. M.

Ledlow, M. J. & Owen, F. N. 1996, AJ, 112, 9

Lery, T., Baty, H., & Appl, S. 2000, A&A, 355, 1201

Li, Z.-Y. 1993, ApJ, 415, 118

Li, Z.-Y. 1995, ApJ, 444, 848

Li, Z.-Y., Chiueh, T., & Begelman, M. C. 1992, ApJ, 394, 459

Lindfors, E. J., Türler, M., Valtaoja, E., et al. 2006, A&A, 456, 895

Lister, M. L., Cohen, M. H., Homan, D. C., et al. 2009, AJ, 138, 1874

Lister, M. L. & Homan, D. C. 2005, AJ, 130, 1389

Lister, M. L. & Marscher, A. P. 1997, ApJ, 476, 572

Lithwick, Y. & Sari, R. 2001, ApJ, 555, 540

Lobanov, A. P. 1998, A&A, 330, 79

Lohner, R. 1987, Computer Methods in Applied Mechanics and Engineering, 61, 323

Lundquist, S. 1950, Arkiv. fysik, 2, 35

Ly, C., Walker, R. C., & Junor, W. 2007, ApJ, 660, 200

Ly, C., Walker, R. C., & Wrobel, J. M. 2004, AJ, 127, 119

Lynden-Bell, D. 1978, Phys. Scr, 17, 185

Lyubarskii, Y. E. 1999, MNRAS, 308, 1006

Lyubarsky, Y. 2009, ApJ, 698, 1570

Lyubarsky, Y. E. 2002, MNRAS, 329, L34

Lyubarsky, Y. E. 2005, MNRAS, 358, 113

Lyutikov, M. & Lister, M. 2010, ApJ, 722, 197

Lyutikov, M., Pariev, V. I., & Blandford, R. D. 2003, ApJ, 597, 998

Lyutikov, M., Pariev, V. I., & Gabuzda, D. C. 2005, MNRAS, 360, 869

Lyutikov, M. & Uzdensky, D. 2003, ApJ, 589, 893

Machida, M. & Matsumoto, R. 2003, ApJ, 585, 429

Macquart, J., Bower, G. C., Wright, M. C. H., Backer, D. C., & Falcke, H. 2006, ApJ, 646, L111

Magorrian, J., Tremaine, S., Richstone, D., et al. 1998, AJ, 115, 2285

Maiolino, R. & Rieke, G. H. 1995, ApJ, 454, 95

Malkan, M. A. & Sargent, W. L. W. 1982, ApJ, 254, 22

Markoff, S., Nowak, M., Corbel, S., Fender, R., & Falcke, H. 2003a, A&A, 397, 645

Markoff, S., Nowak, M., Corbel, S., Fender, R., & Falcke, H. 2003b, New Astronomy Review, 47, 491

Markoff, S., Nowak, M., Young, A., et al. 2008, ApJ, 681, 905

Marrone, D. P., Moran, J. M., Zhao, J., & Rao, R. 2007, ApJ, 654, L57

Marscher, A. P. 2005, Mem. Soc. Astron. Italiana, 76, 168

Marscher, A. P. 2006, in American Institute of Physics Conference Series, Vol. 856, Relativistic Jets: The Common Physics of AGN, Microquasars, and Gamma-Ray Bursts, ed. P. A. Hughes & J. N. Bregman, 1–22

Marscher, A. P. 2011, in Bulletin of the American Astronomical Society, Vol. 43, American Astronomical Society Meeting Abstracts 217, 142.64–+

Marscher, A. P. & Gear, W. K. 1985, ApJ, 298, 114

Marscher, A. P., Jorstad, S. G., Larionov, V. M., et al. 2010, ApJ, 710, L126

Marscher, A. P., Jorstad, S. G., Mattox, J. R., & Wehrle, A. E. 2002, ApJ, 577, 85

Martí, J. M. & Müller, E. 2003, Living Reviews in Relativity, 6, 7

Mathews, W. G. 1971, ApJ, 165, 147

Matsakos, T., Tsinganos, K., Vlahakis, N., et al. 2008, A&A, 477, 521

Matthews, T. A. & Sandage, A. R. 1963, ApJ, 138, 30

McKinney, J. C. 2006, MNRAS, 368, 1561

McKinney, J. C. & Blandford, R. D. 2009, MNRAS, 394, L126

McKinney, J. C. & Gammie, C. F. 2002, ApJ, 573, 728

McKinney, J. C. & Narayan, R. 2007, MNRAS, 375, 513

McNamara, B. R., Wise, M., Nulsen, P. E. J., et al. 2000, ApJ, 534, L135

Meisenheimer, K. & Roeser, H.-J. 1986, Nature, 319, 459

Meliani, Z., Casse, F., & Sauty, C. 2006a, A&A, 460, 1

Meliani, Z. & Keppens, R. 2009, ApJ, 705, 1594

Meliani, Z. & Keppens, R. 2010, A&A, 520, L3+

Meliani, Z., Sauty, C., Tsinganos, K., Trussoni, E., & Cayatte, V. 2010a, A&A, 521, A67+

Meliani, Z., Sauty, C., Tsinganos, K., Trussoni, E., & Cayatte, V. 2010b, ArXiv e-prints

Meliani, Z., Sauty, C., Tsinganos, K., & Vlahakis, N. 2004, A&A, 425, 773

Meliani, Z., Sauty, C., Vlahakis, N., Tsinganos, K., & Trussoni, E. 2006b, A&A, 447, 797

Melrose, D. B. 1997, Journal of Plasma Physics, 58, 735

Merloni, A., Heinz, S., & di Matteo, T. 2003, MNRAS, 345, 1057

Mészáros, P. 2001, Science, 291, 79

Michel, F. C. 1969, ApJ, 158, 727

Mignone, A. & Bodo, G. 2006, MNRAS, 368, 1040

Mignone, A., Bodo, G., Massaglia, S., et al. 2007, ApJS, 170, 228

Mignone, A. & McKinney, J. C. 2007, MNRAS, 378, 1118

Mignone, A., Plewa, T., & Bodo, G. 2005, ApJS, 160, 199

Mignone, A., Rossi, P., Bodo, G., Ferrari, A., & Massaglia, S. 2010, MNRAS, 402, 7

Mignone, A., Ugliano, M., & Bodo, G. 2009, MNRAS, 393, 1141

Miller, K. A. & Stone, J. M. 2000, ApJ, 534, 398

Mimica, P., Aloy, M., Agudo, I., et al. 2009, ApJ, 696, 1142

Mirabel, I. F. & Rodríguez, L. F. 1994, Nature, 371, 46

Mirabel, I. F. & Rodríguez, L. F. 1998, Nature, 392, 673

Miyoshi, M., Kameno, S., Ishitsuka, J. K., et al. 2007, Publications of the National Astronomical Observatory of Japan, 10, 15

Mizuno, Y., Hardee, P., & Nishikawa, K. 2007, ApJ, 662, 835

Mizuno, Y., Hardee, P. E., & Nishikawa, K.-I. 2011, ApJ, 734, 19

Mizuno, Y., Lyubarsky, Y., Nishikawa, K., & Hardee, P. E. 2009, ApJ, 700, 684

Moderski, R., Sikora, M., Madejski, G. M., & Kamae, T. 2004, ApJ, 611, 770

Moll, R., Spruit, H. C., & Obergaulinger, M. 2008, A&A, 492, 621

Mukhopadhyay, B. & Misra, R. 2003, ApJ, 582, 347

Murphy, G. C., Ferreira, J., & Zanni, C. 2010, A&A, 512, A82+

Mushotzky, R. F., Done, C., & Pounds, K. A. 1993, ARA&A, 31, 717

Nagataki, S. 2009, ApJ, 704, 937

Narayan, R., Li, J., & Tchekhovskoy, A. 2009, ApJ, 697, 1681

Narayan, R., McKinney, J. C., & Farmer, A. J. 2007, MNRAS, 375, 548

Nicotra, O. E., Baldo, M., Burgio, G. F., & Schulze, H.-J. 2006, A&A, 451, 213

Noble, S. C., Gammie, C. F., McKinney, J. C., & Del Zanna, L. 2006, ApJ, 641, 626

Nowak, M. A. & Wagoner, R. V. 1991, ApJ, 378, 656

Nowak, M. A., Wilms, J., & Dove, J. B. 2002, MNRAS, 332, 856

Ohsuga, K. & Mineshige, S. 2011, ArXiv e-prints

Okamoto, I. 1978, MNRAS, 185, 69

Orosz, J. A., Groot, P. J., van der Klis, M., et al. 2002, ApJ, 568, 845

Ostriker, E. C. 1997, ApJ, 486, 291

O'Sullivan, S. P. & Gabuzda, D. C. 2009, MNRAS, 393, 429

Ouyed, R., Clarke, D. A., & Pudritz, R. E. 2003, ApJ, 582, 292

Ouyed, R. & Pudritz, R. E. 1997, ApJ, 482, 712

Ouyed, R. & Pudritz, R. E. 1999, MNRAS, 309, 233

Pacholczyk, A. G. 1970a, Radio astrophysics (W. H. Freeman and Co)

Pacholczyk, A. G. 1970b, Radio astrophysics (W. H. Freeman and Co)

Paczynsky, B. & Wiita, P. J. 1980, A&A, 88, 23

Palenzuela, C., Lehner, L., Reula, O., & Rezzolla, L. 2009, MNRAS, 394, 1727

Pariev, V. I., Istomin, Y. N., & Beresnyak, A. R. 2003, A&A, 403, 805

Peng, C. Y. 2007, ApJ, 671, 1098

Penrose, R. 1969, Nuovo Cimento Rivista Serie, 1, 252

Peterson, B. M. 1997, An Introduction to Active Galactic Nuclei, ed. Goméz de Castro, A. I. & Franqueira, M.

Phinney, E. S. 1982, MNRAS, 198, 1109

Piran, T. 1999, Phys. Rep., 314, 575

Piran, T. 2004, Reviews of Modern Physics, 76, 1143

Polko, P., Meier, D. L., & Markoff, S. 2010, ApJ, 723, 1343

Porth, O. & Fendt, C. 2010, ApJ, 709, 1100

Porth, O., Fendt, C., Meliani, Z., & Vaidya, B. 2011, ApJ, 737, 42

Powell, K. G. 1994, Approximate Riemann solver for magnetohydrodynamics (that works in more than one dimension), Tech. rep.

Price, P. A., Fox, D. W., Kulkarni, S. R., et al. 2003, Nature, 423, 844

Proga, D. 2007, in Astronomical Society of the Pacific Conference Series, Vol. 373, The Central Engine of Active Galactic Nuclei, ed. L. C. Ho & J.-W. Wang, 267–+

Proga, D. & Begelman, M. C. 2003, ApJ, 582, 69

Pudritz, R. E. & Norman, C. A. 1983, ApJ, 274, 677

Pudritz, R. E., Ouyed, R., Fendt, C., & Brandenburg, A. 2007, in Protostars and Planets V, ed. B. Reipurth, D. Jewitt, & K. Keil, 277–294

Pudritz, R. E., Rogers, C. S., & Ouyed, R. 2006, MNRAS, 365, 1131

Pushkarev, A. B., Gabuzda, D. C., Vetukhnovskaya, Y. N., & Yakimov, V. E. 2005, MNRAS, 356, 859

Quilis, V., Bower, R. G., & Balogh, M. L. 2001, MNRAS, 328, 1091

Quirrenbach, A., Witzel, A., Kirchbaum, T. P., et al. 1992, A&A, 258, 279

Quirrenbach, A., Witzel, A., Krichbaum, T., Hummel, C. A., & Alberdi, A. 1989, Nature, 337, 442

R. D. Blandford, H. Netzer, & L. Woltjer. 1990, Active Galactic Nuclei, ed. R. D. Blandford, H. Netzer, L. Woltjer, T. J.-L. Courvoisier, & M. Mayor

Ramsey, J. P. & Clarke, D. A. 2011, ApJ, 728, L11+

Rees, M. J. 1966, Nature, 211, 468

Rees, M. J. 1967, MNRAS, 135, 345

Rees, M. J. 1978, MNRAS, 184, 61P

Rees, M. J. & Gunn, J. E. 1974, MNRAS, 167, 1

Reid, M. J., Schmitt, J. H. M. M., Owen, F. N., et al. 1982, ApJ, 263, 615

Reipurth, B. & Bally, J. 2001, ARA&A, 39, 403

Reipurth, B. & Heathcote, S. 1997, in IAU Symposium, Vol. 182, Herbig-Haro Flows and the Birth of Stars, ed. B. Reipurth & C. Bertout, 3–18

Reynolds, C. S., Fabian, A. C., Celotti, A., & Rees, M. J. 1996, MNRAS, 283, 873

Rieger, F. M. & Duffy, P. 2004, ApJ, 617, 155

Rieger, F. M. & Mannheim, K. 2002, A&A, 396, 833

Romanova, M. M., Ustyugova, G. V., Koldoba, A. V., Chechetkin, V. M., & Lovelace, R. V. E. 1997, ApJ, 482, 708

Romero, R., Martí, J. M., Pons, J. A., Ibáñez, J. M., & Miralles, J. A. 2005, Journal of Fluid Mechanics, 544, 323

Rosen, A. & Hardee, P. E. 2000, ApJ, 542, 750

Rossi, P., Mignone, A., Bodo, G., Massaglia, S., & Ferrari, A. 2008, A&A, 488, 795

Ruderman, M. 1975, in Annals of the New York Academy of Sciences, Vol. 262, Seventh Texas Symposium on Relativistic Astrophysics, ed. P. G. Bergman, E. J. Fenyves, & L. Motz, 164–180

Rybicki, G. B. & Lightman, A. P. 1986, Radiative Processes in Astrophysics (Wiley-vch)

Ryu, D., Chattopadhyay, I., & Choi, E. 2006, ApJS, 166, 410

Sakurai, T. 1985, A&A, 152, 121

Sakurai, T. 1987, PASJ, 39, 821

Sandage, A. 1965, ApJ, 141, 1560

Sanders, R. H. 1983, ApJ, 266, 73

Sauty, C., Tsinganos, K., & Trussoni, E. 2002, in Lecture Notes in Physics, Berlin Springer Verlag, Vol. 589, Relativistic Flows in Astrophysics, ed. A. W. Guthmann, M. Georganopoulos, A. Marcowith, & K. Manolakou , 41–+

Sazonov, S., Revnivtsev, M., Krivonos, R., Churazov, E., & Sunyaev, R. 2007, A&A, 462, 57

Schmidt, M. 1963, Nature, 197, 1040

Schmidt, W. K. H. 1978, Nature, 271, 525

Schwinger, J. 1949, Physical Review, 75, 1912

Semerák, O. & Karas, V. 1999, A&A, 343, 325

Seyfert, C. K. 1943, ApJ, 97, 28

Shakura, N. I. & Syunyaev, R. A. 1973, A&A, 24, 337

Shcherbakov, R. V. 2008, ApJ, 688, 695

Shklovsky, I. I. 1953, Dokl. Akad. Nauk. SSSR, 90

Sikora, M., Begelman, M. C., Madejski, G. M., & Lasota, J.-P. 2005, ApJ, 625, 72

Sikora, M., Moderski, R., & Madejski, G. M. 2008, ApJ, 675, 71

Sikora, M., Stawarz, Ł., & Lasota, J.-P. 2007, ApJ, 658, 815

Silk, J. & Rees, M. J. 1998, A&A, 331, L1

Sim, S. A., Long, K. S., Miller, L., & Turner, T. J. 2008, MNRAS, 388, 611

Singal, J., Petrosian, V., Lawrence, A., & Stawarz, L. 2011, ArXiv e-prints

Sokoloff, D. D., Bykov, A. A., Shukurov, A., et al. 1998, MNRAS, 299, 189

Sramek, R. A. & Weedman, D. W. 1980, ApJ, 238, 435

Staff, J. E., Niebergal, B. P., Ouyed, R., Pudritz, R. E., & Cai, K. 2010, ApJ, 722, 1325

Stone, J. M. & Norman, M. L. 1992, ApJS, 80, 753

Strittmatter, P. A., Hill, P., Pauliny-Toth, I. I. K., Steppe, H., & Witzel, A. 1980, A&A, 88, L12

Sudou, H., Taniguchi, Y., Ohyama, Y., et al. 2000, PASJ, 52, 989

Synge, J. L. 1957, The relativistic gas. (North-Holland Pub. Co)

Takamoto, M. & Inoue, T. 2011, ApJ, 735, 113

Takeuchi, S., Ohsuga, K., & Mineshige, S. 2010, PASJ, 62, L43+

Taub, A. H. 1948, Physical Review, 74, 328

Tavecchio, F., Ghisellini, G., Bonnoli, G., & Ghirlanda, G. 2010, MNRAS, 405, L94

Taylor, G. B. & Zavala, R. 2010, ApJ, 722, L183

Taylor, J. B. 1974, Physical Review Letters, 33, 1139

Tchekhovskoy, A., McKinney, J. C., & Narayan, R. 2008, MNRAS, 388, 551

Tchekhovskoy, A., McKinney, J. C., & Narayan, R. 2009, ApJ, 699, 1789

Tchekhovskoy, A., Narayan, R., & McKinney, J. C. 2010a, ApJ, 711, 50

Tchekhovskoy, A., Narayan, R., & McKinney, J. C. 2010b, New A, 15, 749

Tingay, S. J., Jauncey, D. L., Preston, R. A., et al. 1995, Nature, 374, 141

Titarchuk, L. & Shrader, C. R. 2002, ApJ, 567, 1057

Todo, Y., Uchida, Y., Sato, T., & Rosner, R. 1993, ApJ, 403, 164

Tomimatsu, A. 1994, PASJ, 46, 123

Tomimatsu, A., Matsuoka, T., & Takahashi, M. 2001, Phys. Rev. D, 64, 123003

Tornikoski, M., Valtaoja, E., Terasranta, H., et al. 1993, AJ, 105, 1680

Toro, E. F. 1999, Riemann Solvers and Numerical Methods for Fluid Dynamics (Springer)

Tóth, G. 2000, Journal of Computational Physics, 161, 605

Tremaine, S., Gebhardt, K., Bender, R., et al. 2002, ApJ, 574, 740

Tsang, O. & Kirk, J. G. 2007, A&A, 463, 145

Tsinganos, K., Sauty, C., Surlantzis, G., Trussoni, E., & Contopoulos, J. 1996, MNRAS, 283, 811

Turner, T. J. & Miller, L. 2009, A&A Rev., 17, 47

Tzeferacos, P., Ferrari, A., Mignone, A., et al. 2009, MNRAS, 1371

Urry, C. M. & Padovani, P. 1995, PASP, 107, 803

Ustyugova, G. V., Koldoba, A. V., Romanova, M. M., Chechetkin, V. M., & Lovelace, R. V. E. 1995, ApJ, 439, L39

Ustyugova, G. V., Koldoba, A. V., Romanova, M. M., Chechetkin, V. M., & Lovelace, R. V. E. 1999, ApJ, 516, 221

van Breugel, W., Fragile, C., Croft, S., et al. 2004, in IAU Symposium, Vol. 222, The Interplay Among Black Holes, Stars and ISM in Galactic Nuclei, ed. T. Storchi-Bergmann, L. C. Ho, & H. R. Schmitt, 485–488

van de Hulst, H. C. 1957, Light Scattering by Small Particles, ed. van de Hulst, H. C.

van der Klis, M., Jansen, F., van Paradijs, J., et al. 1985, Nature, 316, 225

Vlahakis, N. 2004, ApJ, 600, 324

Vlahakis, N. & Königl, A. 2003, ApJ, 596, 1104

Vlahakis, N., Tsinganos, K., Sauty, C., & Trussoni, E. 2000, MNRAS, 318, 417

von Rekowski, B., Brandenburg, A., Dobler, W., Dobler, W., & Shukurov, A. 2003, A&A, 398, 825

Wagner, S. J. & Witzel, A. 1995, ARA&A, 33, 163

Walker, R. C., Ly, C., Junor, W., & Hardee, P. J. 2008, Journal of Physics Conference Series, 131, 012053

Wang, Y. & Sheeley, Jr., N. R. 2003, ApJ, 599, 1404

Wardle, M. & Koenigl, A. 1993, ApJ, 410, 218

Whitney, A. R., Shapiro, I. I., Rogers, A. E. E., et al. 1971, Science, 173, 225

Wilkinson, P. N., Polatidis, A. G., Readhead, A. C. S., Xu, W., & Pearson, T. J. 1994, ApJ, 432, L87

Wilson, A. S. & Colbert, E. J. M. 1995, ApJ, 438, 62

Yan, R., Ho, L. C., Newman, J. A., et al. 2011, ApJ, 728, 38

Zakamska, N. L., Begelman, M. C., & Blandford, R. D. 2008, ApJ, 679, 990

Zanni, C., Ferrari, A., Rosner, R., Bodo, G., & Massaglia, S. 2007, A&A, 469, 811

Zavala, R. T. & Taylor, G. B. 2002, ApJ, 566, L9

Zavala, R. T. & Taylor, G. B. 2003, ApJ, 589, 126

Zavala, R. T. & Taylor, G. B. 2005, ApJ, 626, L73

Zinnecker, H., McCaughrean, M. J., & Rayner, J. T. 1998, Nature, 394, 862